Thermalization of matter decay products and non-thermal dark matter production in the early universe

Dissertation
zur
Erlangung des Doktorgrades (Dr. rer. nat.)
der
Mathematisch-Naturwissenschaftlichen Fakultät
der
Rheinischen Friedrich-Wilhelms-Universität Bonn

von
Bardia Najjari Farizhendi
aus
Tehran, Iran

Bonn, August 2025

Angefertigt mit Genehmigung der Mathematisch-Naturwissenschaftlichen Fakultät der Rheinischen Friedrich-Wilhelms-Universität Bonn

Gutachter/Betreuer:	Prof. Dr. Manuel Drees
Gutachter:	Prof. Dr. Herbert Dreiner
Tag der Promotion:	27.11.2025
Erscheinungsjahr:	2025

Acknowledgements

I would like to thank all the people who made my years in Bonn, and particularly during my PhD years, rich, pleasant and memorable.

I would like to start by sincerely thanking Manuel Drees for his supervision and for sharing his knowledge; I deeply appreciate his openness and support, on and off academic grounds, both during the time I was in Bonn, and afterwards. I will always think fondly especially of the many coffees (including occasional ice-cubes in my case) and conversations I enjoyed in Manuel's office together with other colleagues. I would also like to thank Herbi Dreiner, for his open and friendly support throughout the years, for everything that I learned from him, and for lending me his Santa Clause costume for the BCTP Christmas gathering, one of my many fond memories of the BCTP.

I would like to continue by expressing my gratitude to Andreas Wißkirchen, Petra Weiß, Patricia Zündorf, and Christa Börsch for their continuous support, for the many pleasant chats we had, and for organising and helping organise our lives in the BCTP. I would particularly like to thank Christa for introducing me to some of her -and now also my- favourite books, starting with lending me her own copy of The Dragonbone Chair.

I had the pleasure of knowing and befriending many colleagues in the BCTP; I would like to thank Urmi, Paul, Zhongyi, Yong, Sadra, Raghuveer, Rahul, Cesar, Mahsa, Reza, Thorsten, Amitayus, Wenbin, Chenhuan, Dominik, Max, Simon, and... for their friendship, their support, and the many contributions they've had to my life; from studying to correcting exercise sheets together, and from teaching me how to skateboard to sharing their favourite songs with me. Special thanks to Chenhuan, Wenbin and Yong for taking the time to proofread my thesis and for their feedback.

Thesis abstract

Thermalization of matter decay products and non-thermal dark matter production in the early universe

Bardia Najjari Farizhendi

Submitted as a part of the requirements for admission to the doctoral examination procedure at the Faculty of Mathematics and Natural Sciences at the University of Bonn

The evolution history of the early universe is closely tied with the evolution history of its contents. Various studied cosmological histories include periods where the energy content of the non–relativistic matter component is converted to relativistic radiation via decay processes. The particles resulting from these decays often have energies close to the mass of the decaying matter component and significantly larger than the temperature of the radiation component. These highly energetic particles will subsequently be replaced by a larger number of particles with a distribution compatible with the thermal radiation component; a process referred to as thermalization. During thermalization, the highly energetic particles can interact with other particles in the universe to contribute to observable phenomena, including e.g. production of non–thermal dark matter. Studying these effects requires an understanding of the thermalization process.

In this thesis, we study the thermalization process of highly energetic decay products, focusing on the initial phase of kinetic equilibration, in which the high energy of the initial decay products is distributed among newly generated particles. We begin by briefly reviewing some of the tools used throughout this thesis, including effective kinetic theory.

We then move on to use these tools to study thermalization in a simplified setup, in which thermalization proceeds via interactions of a single species of non–Abelian gauge bosons. We identify nearly collinear splitting processes as the dominant contribution to the equilibration process and show that one should include the Landau–Pomeranchuk–Migdal (LPM) effect for a consistent effective kinetic theory treatment. We formulate and solve the Boltzmann equation governing the spectrum of out–of–equilibrium particles resulting from the cascade of splittings in the thermalization process. After comparing our spectrum to previous approximate solutions from the literature, we present how this could be used to calculate cosmological observables by studying the example of non–thermal dark matter production.

We then expand our study of thermalization by including all non–scalar species of the Standard Model in our cascade of nearly collinear splitting processes. We use LPM suppression rates from the literature to write down the Boltzmann equations governing the spectra of these species after a decay of a matter component particle and solve these numerically. Finally, we analyze the resulting spectra and discuss how these can be used for more precise calculations of cosmological observables by revisiting the example of non–thermal dark matter production.

Contents

1 Introduction **1**
- 1.1 Dark matter and the composition of the universe . . . 2
- 1.2 Dark matter candidates, production, and detection . . . 4
- 1.3 Cosmological expansion history . . . 5
- 1.4 Thermalization of matter decay products and dark matter production . . . 8

2 Physics of the early universe plasma **15**
- 2.1 The Friedmann–Lemaître–Robertson–Walker universe . . . 15
- 2.2 The Friedmann Equation . . . 17
- 2.3 The Thermal Plasma . . . 18
- 2.4 Thermal field theory and thermal mass . . . 21
- 2.5 Coherence effects and effective kinetic theory of gauge–interactions . . . 25
- 2.6 Summary and recap . . . 31

3 Particle thermlization in the early universe: pure gauge boson treatment **33**
- 3.1 Formulation of the problem . . . 34
  - 3.1.1 The Basic Setup . . . 34
  - 3.1.2 The Thermalization of Energetic Particles . . . 35
  - 3.1.3 Coherent interference and LPM resummation . . . 38
- 3.2 The thermalization cascade and the Boltzmann equation . . . 42
  - 3.2.1 The quasi–static Boltzmann equation . . . 43
  - 3.2.2 Model parameters and the dimensionless Boltzmann equation . . . 45
- 3.3 Solution of the Boltzmann equations . . . 46
  - 3.3.1 Generic features and approximate solutions . . . 47
  - 3.3.2 Numerical solution . . . 50
  - 3.3.3 Analytical parameterization of the numerical solution . . . 54
- 3.4 Applications of the spectrum of out–of–equilibrium particles: an example . . . 57
- 3.5 Summary . . . 64

4 The Standard Model of particle physics and thermalization cascades in the early universe **69**
- 4.1 A cascade of Standard Model particles . . . 69
- 4.2 Thermalization via a splitting cascade of multiple particles . . . 72
- 4.3 The LPM effect for multiple species and interactions . . . 74
  - 4.3.1 LPM suppressed splitting rates in leading logarithmic approximation . . . 77
  - 4.3.2 Particle content and the treatment of chirality . . . 82
- 4.4 System of Boltzmann equations . . . 83

4.5 Numerical calculation of the spectra . . . 87
4.5.1 Solutions for $x_M = 10^4$ . . . 88
4.5.2 The role of x_M and scaling behavior . . . 97
4.6 Example of applications: Revisiting non–thermal production of heavy dark matter . . . 102
4.7 Summary and discussion . . . 104

5 Summary **107**

A Running of the coupling constants, and the treatment of couplings for the standard model (SM) **111**

B Standard Model gauge boson thermal masses **113**

C Analytic approximate solution the single–species splitting driven spectrum **115**

Bibliography **119**

List of Figures **127**

List of Tables **129**

Acronyms **131**

CHAPTER 1

Introduction

"It was a still night, tinted with the promise of dawn. A crescent moon was just setting. Ankh-Morpork, largest city in the lands around the Circle Sea, slept.

That statement is not really true.

On the one hand, those parts of the city which normally concerned themselves with, for example, selling vegetables, shoeing horses, carving exquisite small jade ornaments, changing money and making tables, on the whole, slept. Unless they had insomnia. Or had got up in the night, as it might be, to go to the lavatory. On the other hand, many of the less law-abiding citizens were wide awake and, for instance, climbing through windows that didn't belong to them, slitting throats, mugging one another, listening to loud music in smoky cellars and generally having a lot more fun. But most of the animals were asleep, except for the rats. And the bats, too, of course. As far as the insects were concerned...

The point is that descriptive writing is very rarely entirely accurate [...]"

Terry Pratchett, The Light Fantastic

The standard model (SM) of particle physics and the Λ cold dark matter (ΛCDM) model of cosmology are two cornerstones of our modern understanding of the physics of the universe on both the smallest and largest length scales. The SM contains the fundamental building blocks and non–gravitational interactions of the "visible" universe, i.e. the part of the universe observed via its interactions with the electromagnetic radiation. The ΛCDM, on the other hand, incorporates Einstein's theory of general relativity together with the SM particles and interactions to describe the evolution of the universe from an "early time" up to the "present".

According to the SM, the fermionic quarks and leptons are organized in three *generations* with identical coupling to the force carrier gauge bosons. The gauge bosons in turn correspond to the gauge group $SU(3)_C \times SU(2)_L \times U(1)_Y$; the constituents are, respectively, the $SU(3)_C$ color gauge group of the *strong* interactions, the left–chiral *weak* interactions, and the abelian $U(1)_Y$ hypercharge. The latest element of the SM to be discovered, namely the scalar Higgs boson, is responsible for breaking the symmetry group of the SM into $SU(3)_C \times U(1)_{\mathrm{EM}}$ at low scales; the Higgs boson is further responsible for generating the elementary fermion masses, thereby differentiating the three SM fermionic generations. All members of the SM are, directly or indirectly, observable via their

interactions with the matter on earth and are therefore sometimes collectively referred to as "luminous", or as belonging to the "visible sector".

Turning our attention to cosmological scales, the ΛCDM assumes the universe to have been filled with a cosmological *fluid* and in a state of thermal equilibrium with a temperature T at early times. The energy density contained in the perfect fluid dictates an expansion of the universe, resulting, in turn, in a universal cooling of its content. The evolution of the universe can then be parameterized in terms of an increasing time parameter t or, equivalently, a decreasing temperature T.

Both models have been strikingly successful in predicting and explaining a wide range of physical observables [1]. In particular, the ΛCDM framework successfully predicts the production and ratios of *light* atomic nuclei in a process known as big–bang nucleosynthesis (BBN); this serves to guarantee, amongst others, that at the time of nucleosynthesis, i.e. with the universe being ~ 1 s old or having a temperature of ~ 3 MeV [2], the perfect fluid was dominated by relativistic *radiation* with a composition very well predicted by the SM particle content and interactions. The subsequent evolution of this radiation–dominated (RD) fluid leads to the "matter–radiation decoupling" and the formation of the cosmic microwave background radiation (CMB); the latter serves as a treasure–trove of information regarding the history and composition of the universe at early times [3]. The small density fluctuations in the resulting largely homogenous universe are then enhanced in the process of structure formation to shape the highly non–homogenous universe observed at late times. Finally, the *cosmological constant* (Λ) element of the ΛCDM accounts for the observation of *accelerated expansion* of the present universe.

Despite their unprecedented success, both the SM and the ΛCDM need to be further modified to accommodate observations [1]. The SM, for example, predicts all three neutrinos to be massless; a prediction found to be incompatible with the observation of neutrino oscillations. Another example is universe being flat, homogenous, and isotropic on large scales as deduced, e.g., from the observation of the CMB. These observations cannot be easily explained by ΛCDM + SM, giving rise to the so–called "flatness" and "horizon" *problems* in cosmology. One, therefore, modifies the SM of particle physics by the addition of new particles and interactions to allow for an explanation of these observations; in the latter case, e.g., this is often accomplished by the introduction of additional fields and interactions leading to a period of cosmological "inflation".

The set of theories and models considered to address the shortcomings of the SM are collectively referred to as physics beyond the standard model (BSM). The successful description of cosmology by the concordance ΛCDM model, therefore, suggests and relies on the existence of BSM physics; in particular, the SM in its present form cannot accommodate the dominant matter component present in the universe; the cold dark matter.

1.1 Dark matter and the composition of the universe

The existence of cold dark matter (DM), i.e., a massive, non-relativistic, and non–luminous (non–baryonic) component in the energy content of the universe, has been well established by independent cosmological observations of gravitational effects on different length–scales [1, 4, 5]. The independence and variety of these scales and observations make it non–trivial for them to be explained economically by modifications of the dynamics and laws of motion (see the review on dark matter in [1]); as such, we will not be focusing on these scenarios.

Early hints for the existence of DM came from the observation of *flat* rotation curves of galaxies,

where the radial variation of the tangential velocity of the occupied orbits *flattens out* as one moves away from the central luminous regions of the galaxy, suggesting the existence of a gravitating non–luminous component extending far outside the luminous matter distribution [6, 7]. It is, moreover, worth noting that a class of *old* galaxies point to the presence of a sizable DM presence by their mere existence; without a DM contribution, the density perturbations observed in the CMB would be too small to account for the formation of galaxies at these early times [8].

The next length–scale to provide evidence for DM is that of clusters of galaxies, where several independent observational measures for the mass distribution within the cluster point to the existence and properties of a non–luminous matter component [9, 10]. The velocity dispersion of the galaxies in the cluster, as well as the temperature of the cluster's gas content observed via its X–ray signature, are functions of the gravitational potential; a measurement of the velocity dispersion or the X–ray spectrum, therefore, allows for probing the matter content of the lensing cluster. The gravitational lensing effect further delivers an independent measurement of the total mass contained in the cluster. Independent mass measurements of galaxy clusters yield a mass that is larger than that explained by the baryonic matter content of the cluster.

On the scale of galaxy clusters, a somewhat special role is reserved for the "bullet cluster" system; a high–velocity (hence the term "bullet") encounter of two galaxy clusters. At impact, the luminous baryonic gas content of the two clusters interact, pushing back and therefore heating up one another as observed from their X-ray emission; gravitational lensing observations, however, reveal a dominant contribution of non-luminous matter in each cluster undisturbed by the impact, resulting in the DM distribution being displaced relative to the baryonic matter distribution. The latter observation has been used to derive an upper bound on the strength of DM self–interactions parameterized as the DM–DM interaction cross section of $\sigma_{\mathrm{DM-DM}} \simeq \mathcal{O}\,(1\,\mathrm{b})\ m_{\mathrm{DM}}/1\,\mathrm{GeV}$ [11].

Finally, evidence for the existence of DM on *cosmological* scales is found in the CMB anisotropy data [3]; as mentioned earlier, the CMB is predicted by the ΛCDM to provide us with a snapshot of the universe at a temperature $T \sim 0.3\,\mathrm{eV}$. The angular spectrum of these anisotropies provides us with our most precise measurement of the *abundance* of DM in the universe. The result can be formulated as the present–day fraction of DM (see e.g. the review on cosmological parameters in [1])

$$\Omega_{\mathrm{DM}} h^2 = 0.1198 \pm 0.0012, \tag{1.1}$$

where Ω_{x} is defined as the ratio of the energy density of a component x and the *critical* energy density ρ_{C} of a *spatially flat* universe. Together with luminous baryonic matter Ω_{B}, relativistic photon radiation Ω_{R}, neutrinos Ω_{ν} and the cosmological constant Ω_{Λ}, they provide the critical density for a *spatially flat* universe, formulated as

$$\sum_{\mathrm{x}} \Omega_{\mathrm{x}} h^2 \ = \ 1. \tag{1.2}$$

The dimensionless parameter h, defined as the Hubble expansion rate in units of 100 km/sMpc, encodes the uncertainty in the expansion rate of the universe and applies universally to all contributing components x; the current measurements are in tension but imply $h \sim 0.7$ [12]. As mentioned before, the cold DM further allows for the growth of structures following from the anisotropies already present at the CMB decoupling.

1.2 Dark matter candidates, production, and detection

The established presence of a DM component in the universe provides an unequivocal signature for BSM physics and model building. One, therefore, needs to extend the SM to provide one or more massive species that are *stable* on cosmological time–scales and interact weakly with the SM particles; criteria that depend on the nature and particle interactions of the DM species. A DM model must additionally reproduce the precisely measured abundance (1.1) of *cold* relics, i.e., DM particles that are nonrelativistic by the onset of the process of structure formation at a temperature $T \sim 1\,\mathrm{eV}$. Satisfying the latter two criteria relies not only on the DM species and its interactions but also on the evolution history of the universe and the DM *production mechanism*.

A plethora of BSM models and production mechanisms have been proposed to address the shortcomings of the SM and the ΛCDM. An indicator for the diversity of proposed DM models is the wide available mass–range: as an example, *fuzzy* DM models, with bosonic dark matter as light as $10^{-22}\,\mathrm{eV}$ [13, 14], have been proposed to produce light relics via a *misalignment* mechanism. On the other hand, primordial black hole (PBH) candidates as heavy as $1 \times 10^3\,\mathrm{M}_\odot$, with $1\,\mathrm{M}_\odot \equiv (1.9884 \pm 0.0002) \times 10^{30}\,\mathrm{kg}$ [1] denoting a solar mass, are devised to form by the gravitational collapse of overdense regions (density fluctuations) of the cosmic fluid [4, 5].

A subgroup of proposed BSM extensions have the advantage of simultaneously addressing or explaining several observations, and are therefore sometimes considered to be better motivated. An example of such models is the theory of supersymmetry (SUSY) (see e.g. the review section in [1]); addressing, among other issues, the "hierarchy" problem of the SM, while at the same time providing a viable DM candidate in the form of the lightest supersymmetric particle (LSP) whose stability is guaranteed by symmetry. Typical supersymmetric DM models predict the LSP to have a mass in the range $100\,\mathrm{GeV} - 10\,\mathrm{TeV}$, and serve as a well–motivated realization of weakly interacting massive particles (WIMPs): new particles with mass and interaction strengths of weak–scale physics.

WIMPs arise in many BSM scenarios and, under generic circumstances, reproduce a relic abundance in the ballpark of the observed value (1.1), earning the title of the *WIMP miracle*. The corresponding production mechanism, the *thermal* freeze out (FO) (see e.g. [15]), starts with the DM in thermal equilibrium with the luminous component of the universe at temperatures larger than the WIMP mass. As the universe cools down to a temperature below the mass, WIMP particles continue annihilating into lighter particles from the visible sector; the annihilation reduces the number of WIMP particles and, consequently, the rate of the annihilation process until the annihilation process is effectively stopped by the ongoing cosmic expansion. A population of WIMPs thus freezes out to provide the relic abundance (1.1). It is important to note that unlike the case of fuzzy DM or PBHs, the FO starts with a thermal population of DM and is in this sense independent of initial conditions the universe might have at earlier times.

The relatively sizeable interactions of the WIMP with the visible sector allow us to search for them in terrestrial and astrophysical experiments (see e.g. [5]). *Direct detection* experiments look for the signal resulting from the DM particles interacting with the detector to transfer a fraction of its momentum to the detector material. *Indirect detection* experiments look for a signal in visible particles resulting from the annihilation of DM particles. Finally, *collider experiments* aim to detect signatures of DM particles being produced in the high–energy interactions of SM particles at particle colliders. A collection of direct, indirect, and collider experiments have failed to detect (or managed to exclude) a large fraction of well–motivated WIMPs [16]; while this tension does not mean that WIMPs are ruled out, it does motivate modifying and going beyond the WIMP paradigm.

One available avenue for modifying the thermal WIMP paradigm is to relax the criterion of the DM starting out in thermal equilibrium with the visible sector. Assuming that the DM's interactions with the visible sector are too "feeble" for it to ever reach thermal equilibrium, one may gradually freeze in (FI) a population of feebly interacting massive particle (FIMP) from the interaction of the SM particles in the thermal bath [17]. The production continues until the cosmic expansion and cooling cut off the production at a temperature slightly below the FIMP's mass. Such a FI population of FIMPs could once again be independent of initial conditions, and could arise generically in some BSM scenarios. A key feature of FIMPs is that the feeble coupling required by the production mechanism will also make an observable signal considerably weaker, allowing it to evade the constraints applying to the WIMP.

Another possible variation to the DM production we have not yet addressed arises from modification to the cosmological expansion history [18]; note that cosmological expansion and the resulting cooling play a key role in both FO and FI mechanisms as discussed. As an example, If one were to increase the rate of expansion during the process of FO, the DM annihilations to the visible sector would become less efficient, resulting in an enhancement of the produced population of DM from FO; If the enhanced rate of expansion is to result from a nonrelativistic component, however, the produced number density can get strongly diluted by the eventual decay of these particles, leading to a suppression of FO relic density. With the DM content of the universe being fixed (1.1), the latter suppression can be balanced out by a larger FO production i.e. a heavier WIMP with weaker couplings to the visible sector. Such cosmological histories, therefore, open up new regions in the parameter space for the scrutinized thermal WIMPs. Interestingly, an enhanced rate of expansion affects the thermal FI in the opposite direction; an enhanced expansion rate during FI production results in a smaller accumulation of FIMPs which is then further suppressed by entropy dilution after FI. The suppression can again be compensated by larger FI production corresponding to larger interactions of the FIMP with the visible sector. The modified expansion history, therefore, improves the detection perspectives for FI DM at experiments [19].

We have so far remained agnostic to the mechanism responsible for changes to the expansion history of the universe, while the different potential candidates, e.g., extra light degrees of freedom (DoF), extra matter component, etc., affect the cosmic history differently. It is therefore helpful to study the variety of possible expansion histories and how it can affect other cosmological processes, and in particular, the production of DM.

1.3 Cosmological expansion history

We saw that extending the SM by extra stable particles allows for a solution to the DM problem and allows the ΛCDM to describe observations such as cosmological structure formation or features of the CMB. Similarly, one may extend the standard model of cosmology by including new components and phases, to address the observations that are not explained within the ΛCDM.

The theory of *cosmic inflation*, i.e., an early period of accelerated expansion of the universe, is the most prominent extension of the ΛCDM. According to the theory of inflation, the universe underwent a phase of accelerated *superluminal* expansion at very early times. The expansion stretches a small *patch* of a pre-existing vacuum by more than 60 e–folds (see e.g. the review on inflation in [1]). In this picture, the "causally independent" patches of the present universe have been in causal contact before the end of inflation, a fact reflected in the high degree of isotropy in the CMB; this provides an explanation for the horizon problem of the ΛCDM. The flatness of the universe is similarly explained

to result from the enormous stretching resulting from the exponential expansion. As mentioned earlier, the inflationary paradigm further uses the quantum fluctuations of fields during the inflation to "seed" the primordial density perturbations imprinted in the CMB and the cosmic structure data.

The inflationary paradigm allows for a large variety of models and constructions. In a typical *slow–roll* realization of inflation, the exponential expansion results from the *flat* potential of a scalar field, i.e. the *inflaton*, dominating the energy density of the universe; the result mimics a cosmological constant and can further be written as a fluid with the equation of state

$$\omega \equiv \frac{\langle p \rangle}{\langle \rho \rangle} \tag{1.3}$$

of $\omega \approx -1$, where p denotes the pressure of a fluid with a corresponding energy density ρ, and $\langle \ldots \rangle$ denotes spatial averaging[1]. Inflation ends when ω departs significantly from -1, corresponding to the scalar field leaving the flat section of the potential to settle in the minimum of the potential function. The subsequent evolution of the composition of the universe (1.2) as described by the ΛCDM involves the universe being dominated by radiation with $\omega = 1/3$ at BBN, followed by the domination of dark and luminous matter with $\omega = 0$ before finally entering the present era of accelerated expansion with $\omega = -1$.[2] [3]

The inclusion of an inflationary era, therefore, calls for an *eventual* reheating (RH): the transfer of energy from the inflaton field to mostly visible relativistic particles in order to *repopulate* the universe with radiation with an equation of state $\omega = 1/3$. The reheated universe will subsequently expand *subluminally* to shape the present observable universe. A widely–studied realization of post–inflationary dynamics involves the inflaton oscillating around the potential minimum with a dominant quadratic *mass* term; the oscillating field mimics a matter component with $\omega = 0$ dominating the energy density of the universe. The massive inflatons eventually decay perturbatively and predominantly to "light" relativistic visible sector particles to reheat the universe. This basic scenario, therefore, predicts a period of early matter–dominated era (EMD) after the end of inflation and prior to RD. In the simplest case, the RD phase at the end of inflation persists through the BBN, in which case the scenario is often referred to as a "standard cosmological history".

The details of the inflationary model, and therefore the expansion history of the universe prior to reheating, are strongly model–dependent. The form of the inflationary potential could, e.g., disallow a quadratic form, and therefore, an effective inflaton mass. This could result in the inflaton condensate mimicking a radiation component with $\omega = 1/3$ leading to an RD state [23]. While such scenarios still rely on a reheating phase to populate the SM radiation component of the universe, an inflationary EMD phase could be absent. Another key aspect of inflationary models is the coupling of the inflaton to other bosonic and fermionic fields (see e.g. section 2.1.2 in [20] and references therein). A coupling to bosonic species can lead to efficient *resonant* particle production and the transfer of energy from the inflaton to a radiation component via the non–linear *preheating* process. A sizable fraction of the energy density of the inflaton field can be converted to radiation before the "parametric resonance"

[1] For an overview of fragmentation phenomena potentially leading to large spatial inhomogeneities and the effect on the equation of state parameter see e.g. [20]

[2] As $\omega = -1$ represents both the late accelerated expansion era dominated by the cosmological constant component, as well as the inflationary period, similar constructions, known as *quintessence* [21] models, have been suggested to explain the late–time accelerated expansion. For an overview of the topic, see e.g. the review on *dark energy* in [1].

[3] For completeness, see also the recently emerging results from [22], reportedly pointing to dynamical dark energy.

behavior is disrupted by backreaction and decoherence effects. The fraction of energy left behind in the inflaton field will in the most general case again constitute a matter component with $\omega = 0$. An interesting expansion history results from a long–lived subdominant population of massive inflaton particles surviving an efficient resonant production of radiation. The inflation, in such a scenario, ends in an era of RD, while the subdominant matter contribution will get to dominate the universe at later times due to its softer equation of state. As before, the matter component should decay prior to the BBN to be consistent with observations. The result is an intermediate matter–dominated era (IMD); a matter–domination (MD) era proceeded and followed by RD eras [24].

IMDs are further motivated by post–inflationary physics [25]. A large class of BSM physics models predict new scalar fields (sometimes referred to as *moduli* irrespective of their physical origin) initially displaced from their effective potential minima in an RD universe and at high temperatures. The moduli approach their minima at late times, mimicking a matter equation of state, and therefore get to dominate the energy density of the universe prior to their decay, should they live long enough. Incidentally, moduli decays typically rely on gravitational interaction, so that "light" (as compared to the scale of the high–energy BSM theory) moduli can be sufficiently long–lived; as a matter of fact, the long lifetime and post BBN decay of the moduli is often regarded as a potential problem to be addressed in BSM model–building [26]. Other realizations of an IMD rely on FO or FI of heavy long–lived states from the thermal bath or from inflation decays. Even if initially subdominant, these decoupled contributions once more grow merely due to the matter equation of state; moreover, the decoupled sector can acquire [27] and develop [4] its own temperature, e.g. due to number changing processes, affecting the onset of matter equation of state in the decoupled sector and therefore the IMD.

A dominant matter component present prior to the BBN potentially affects the cosmological history and observations in multiple ways [20]. As mentioned earlier, the change in the expansion rate of the universe affects the efficiency of DM production from FO and FI. The different equation of state further allows for the linear growth of density perturbations during the MD era; if these perturbations survive, they may modify the matter power–spectrum at small scales or allow for more efficient formation of PBHs from large overdense regions. Modifications of the cosmological expansion history further affect the reentry time of density perturbation modes into the Hubble horizon; the latter results in modifications in the CMB and serves to potentially constrain deviations from the standard cosmic history.

In cosmological histories with an EMD phase, a special role is reserved for the eventual out of equilibrium (OoE) decays of the matter component. In addition to the dilution of DM abundance discussed above, the entropy dilution resulting from matter decays similarly affects the *matter asymmetry* parameter and allows for models of large baryon and lepton asymmetry production prior to matter decays [28]. In fact, the generation of matter asymmetry requires OoE processes as one of the Sakharov conditions for the successful generation of matter asymmetry; CP–violating OoE decays of the matter component are therefore often used as a key component of models of matter asymmetry production.

In a majority of models with a MD era the matter component consists of "heavy" particles; i.e. particles with a mass much larger than the temperature of the radiation component. Decays of the matter component, therefore, result in *non–thermal* OoE visible sector particles with energies much larger than their counterparts from the *thermal radiation bath*. In order not to interfere with the

[4] See e.g. section 2.3.3 of [20] and the references therein.

success of BBN, the standard cosmological history requires the radiation component to have a thermal distribution prior to the BBN. The OoE decay products are, therefore, required to attain thermal equilibrium in a process of *thermalization* to reach kinetic and chemical equilibrium with the thermal bath.

1.4 Thermalization of matter decay products and dark matter production

In the previous section, we established the appearance of an EMD in generic cosmological histories, without the need for parameter "fine–tuning". At the end of the MD era, the matter component of mass M is bound to decay to highly–energetic (HE) visible sector particles to reheat the SM radiation bath of temperature T. The scale M is typically much larger than that of the SM particle masses so that the initial decay products constitute an OoE radiation component with particle energies well above T. Moreover, the chemical composition of the initial decay products depends strongly on the coupling between the matter component and the visible sector species and can, therefore, largely deviate from that of the standard thermal bath of temperature T.

As an example, let us assume that at the end of the EMD era, the matter particles of mass M undergo two–body decays into an electron–positron pair with energies $M/2 \gg T$. The thermal radiation bath at the time of the decay will consist of all visible sector particles s with masses $m_s \lesssim T$. In order to reach thermal equilibrium, the electron–positron pair of energy $M/2$ need to be replaced with $\mathcal{O}(M/T)$ SM particles, each with an energy of $\mathcal{O}(T)$; moreover, the initial electron–positron pair needs to be replaced by a collection SM particles.

The process of thermalization of HE decay products involves the production of many new particles, and the redistribution of energy from the HE particles to the particles in the radiation thermal bath (TB). The dynamics of the thermalization process, therefore, relies on the particle processes dominated by the SM particles and interactions. On the other hand, apart from the effects of the decaying matter component, the post–inflationary cosmological evolution of the TB is governed by the gravitational expansion of the universe and, therefore, at a typically much smaller rate in comparison to the SM particle processes.

The strong hierarchy between the SM thermalization particle rates and the rate of cosmic expansion has motivated the treatment of *instantaneous thermalization* [5] . In this framework, so long as one is interested in the evolution of the TB as a whole, one may assume the energetic decay products to be instantaneously replaced by a thermal distribution of visible sector particles. The assumption of instant thermalization has been widely used to study a variety of cosmological phenomena and in particular in the study of DM production in an EMD era [29–31]. Within this assumption, the effect of MD era is effectively reduced to modifications of the expansion rate; the reheating process and the decay of the matter component are similarly reduced to a process of entropy injection or production of secondary particles as direct decay products of the decaying matter component.

In reality, the process of thermalization will occur with a finite rate and, therefore, on a finite *thermalization time–scale* given by the visible sector particle interactions. Consequently, the instantaneous thermalization treatment is likely to break down once we are interested in the study of processes occurring on time–scales comparable to that of thermalization. Before their thermalization is complete, HE decay products form a population of OoE visible sector particles with energies larger

[5] Not to be confused with *instantaneous reheating*, denoting a scenario where the energy contained in the inflaton/matter component is instantanouesly converted, e.g. via decays, to a relativistic radiation component.

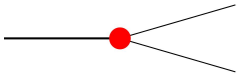

Figure 1.1: Schematic of $2 \rightarrow 3$ "splitting" process for a high energy particle (left incoming) interacting with a particle from the TB (red blob) to split into two outgoing particles (outgoing right), increasing the number of particles by one. The thickness of the lines is meant to imply a larger incoming energy being distributed among the two outgoing particles.

than that of the TB. Similar to SM particles within the TB, these visible sector particles can therefore contribute to many cosmological processes of interest.

The thermalization process relies on the interactions of the HE decay products with other particles in the environment to produce new particles and redistribute energy. As these particles belong to the visible sector, they are able to partake in a large variety of elastic and inelastic interactions. A first step towards studying the thermalization process would then be to find a small subset of particle processes with the largest contribution. As the SM is a *weakly coupled* theory in the early universe, one may systematically classify the many contributing processes by their order in the *perturbation theory* [6].

A natural starting point is the study of $2 \rightarrow 2$ processes as they are of the lowest order in the weak couplings of the SM. *Elastic* and *inelastic* $2 \rightarrow 2$ processes allow the HE decay products to transfer part of their energy to the *soft* particles from the TB; *inelastic* $2 \rightarrow 2$ processes additionally allow the particle composition the OoE particles to change. Historically, $2 \rightarrow 2$ processes were considered to be the primary means of thermalization [32, 33]; a closer look at the dynamics of $2 \rightarrow 2$ processes, however, reveals them as an inefficient means of energy transfer between the HE particles and the TB. The reason is that the large energy of the OoE particles suppresses the rate of the majority of $2 \rightarrow 2$ processes; an exception for this rate–suppression is provided by the *forward* limit of elastic scattering processes mediated by massless gauge bosons. In the latter processes, the rate of the process becomes independent of the energy of the OoE particles; the absence of rate suppression comes, however, at the price of the negligibly small momentum transfer associated with a forward scattering process, so that the contribution to the thermalization process is once again suppressed.

The next logical choice for energy transfer is the $2 \rightarrow 3$ process where the HE particle interacts with the TB to emit a new particle. The most efficient $2 \rightarrow 3$ process of energy transfer between the OoE particles and the TB turns out be a $2 \rightarrow 3$ "splitting" process shown schematically in Fig. 1.1 [7]. The particularly efficient $2 \rightarrow 3$ splitting process is closely connected to the forward $2 \rightarrow 2$ scattering process mediated by a gauge boson; the "parent" HE particle (incoming left) can be thought of as undergoing forward elastic $2 \rightarrow 2$ scattering with TB particles (red blob) to split into two *daughter* particles each carrying a fraction of the parent particle's energy (outgoing right). Note also that, in contrast to the $2 \rightarrow 2$ processes, a splitting process simultaneously increases the number of OoE particles as expected from a successful process of thermalization.

The $2 \rightarrow 3$ splittings owe their unique role in thermalization to the fact that they can redistribute a large fraction of the parent particle's energy without relying on a large momentum transfer through the intermediate gauge boson; the small momentum transfer puts the parent particle slightly off–shell, allowing it to split into to highly *collinear* daughter particles. It is worth noting that the line of

[6] This is of course only viable so long as we are interested in a study of perturbative phenomena; nonperturbative sphaleron processes , e.g., would not be possible in a purely perturbative framework.

[7] The spin nature of the particles in the schematic diagrams in the introduction are not discussed or displayed, so that the solid lines do not correspond to fermionic species, but rather generically represent particles.

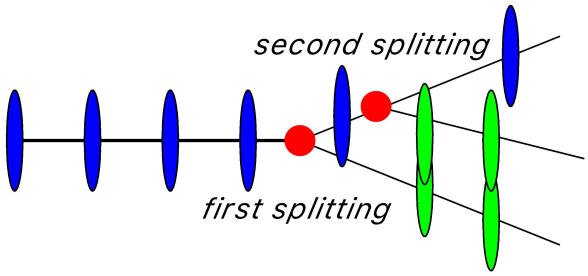

Figure 1.2: Reproduced from [37]; an intuitive explanation of the physical origin of the LPM interference; when two splittings of the incoming HE particle occur closely (i.e. within a formation time), the radiation fields (green) from the two potential splitting events overlap and interfere.

reasoning used to motivate the study of $2 \to 3$ splitting processes for the process of thermalization of HE decay products relies solely on particle physics aspects of the SM and quantum field theory (QFT); as a result, the same physics of collinear splittings can be responsible for the process of energy loss of HE particles in physical setups other than the early universe thermal plasma. Examples of these are the process of energy loss for HE cosmic–ray particles in the atmosphere or the process of thermalization for HE partons in heavy ion collision (HIC) experiments [34].

In all cases discussed above, the HE particles propagate through a *medium* of particles of lower energy. Interactions of particles with a background medium are known to affect their dynamics and interactions. One such effect is the appearance of an effective *thermal mass* for particles propagating in a thermal plasma. Another important effect, particular to particle production in a medium, is that the high degree of collinearity of the daughter particles in collinear splittings results in these processes being prone to the Landau–Pomeranchuk–Migdal (LPM) effect [35, 36]: a parametric suppression of the splitting rate as compared to that in *vacuum*. The LPM suppression results from a destructive interference among multiple coherent splitting processes associated with scatterings of the HE particles off different particles, i.e. *scattering sites*, from the medium. Fig. 1.2, reproduced from [37], shows an intuitive schematic of the interference effect among two collinear splitting processes for the case of a HE incoming (blue wave–packets) scattering off two medium particles (red blobs) to emit two new particles (green wave–packets) via the splitting; in this schematic, the finite transverse width of the wave–packets are represented by the blue and green blobs. For consecutive splittings occurring within a specific time–window (the *formation time*), the collinear radiation fields overlap and interfere, resulting in a suppression of the splitting rate.

The LPM effect was first formulated to describe the suppression of electromagnetic showering for HE cosmic rays and was only later further studied in the context of the physics of the quark–gluon plasma (QGP) and studies of HIC [38]. As highly collinear splittings also underlie the process of energy loss of HE decay products in the early universe plasma, the inclusion of the LPM effect is crucial for a correct treatment of the thermalization process. Studying the thermalization process of HE decay products in the early universe is somewhat complicated by a number of factors. A first observation is that at high temperatures of the early universe all the particles and interactions of the unbroken SM contribute to the composition and interactions of the OoE sector and the TB; in comparison, studies of thermalization in HIC experiments typically focus on photons, gluons, and light quarks. Moreover, the mass, decay rate, and decay channels of the matter component are strongly model–dependent; this results in a relatively large number of free parameters that need to be considered

in studying the thermalization process of matter decay products in early universe cosmology. The large number of parameters becomes particularly important as the study of thermalization results in equations that need to be solved numerically.

Previous works in the field [39–42] have used simplifying assumptions to study the thermalization process in order to find the properties of the OoE particles resulting from matter decays. One simplification method is to restrict one's attention to a single particle species instead of the full set of the SM particles; gluons of the non–abelian $SU(3)_C$ are the natural choice for this *single–species* treatment as they possess the largest self–couplings and gauge multiplicities in the SM. Furthermore, one may choose to find approximate analytical solutions for the energy distribution of the single–species population of OoE particles; this simplified analysis results in a spectrum of OoE particles of the form

$$\frac{\mathrm{d}n\,(p)}{\mathrm{d}p} \propto \left(\frac{p}{M}\right)^{-3/2}, \tag{1.4}$$

with $n\,(p)$ the number density of OoE particles (gluons) of energy $p < M/2$[8] ; as before, M represents the mass of the decaying matter component. The *spectrum* (1.4) shows a power–law increase in the number of OoE particles as they lose energy in the thermalization process. As mentioned before, such a spectrum can be used to study cosmological processes involving the OoE population of thermalizing decay products. While an approximate single–species solution as in (1.4) can be used to estimate and study the general behavior of cosmological processes, a precision treatment of these calls for more realistic spectra of all SM particles. This can, e.g., be well understood in the example of non–thermal DM production.

In one typical realization of the FI mechanism introduced in section 1.1, the gradual production of DM proceeds via the $2 \to 2$ scatterings of particles from the TB. Production stops once the temperature T of the TB drops below the mass of the DM; at lower temperatures, the initial states either lack the energy required for the production of DM or are suffer a strong Boltzmann suppression of their number densities. In scenarios where FI occurs during MD, the subsequent entropy production from matter decays dilutes the DM abundance as outlined in section 1.1. On the other hand, the OoE population of visible sector particles resulting from matter decays have energies larger than T prior to their full thermalization; they can, therefore, contribute to DM production via the very same $2 \to 2$ process as before, long after the regular *thermal* FI is inactive. Moreover, as the latter production from OoE particle proceeds at later times, the produced DM will experience a smaller entropy dilution. The combined effect is then that OoE particles resulting from the thermalization of HE matter decay products can play a significant role in providing the correct DM abundance; this in turn allows one to study new regions of DM model parameter space and cosmological histories involving an MD period [19].

As discussed in section 1.2, the coupling between the dark and visible sectors is strongly model–dependent. As an example, "leptophilic" DM models assume that the dark sector primarily couples to one or more generations of the SM leptons [43]. Another family of models use the "Higgs–portal" [44] to couple the dark and visible sectors; the DM candidate couples directly to the Higgs, while all SM particles with a coupling to the Higgs can contribute the production or annihilation of DM particles. These two examples showcase how studying the non–thermal FI production of DM can crucially rely on a knowledge of the OoE spectra of all SM particles.

[8] The factor of two in the limit $p < M/2$ stems from an assumption of two body decays of the matter component of mass M at rest.

In this thesis, we will work toward a description of the thermalization process involving the various particles and interactions of the SM; as we will see, even though the number of possible interactions is rather large, one can use kinematical arguments, the hierarchies of couplings, and the symmetries of the SM to reduce the number of variables in the problem.

This thesis is structured as follows: in Chapter 2 we will introduce the basic theoretical tools underlying and used throughout the thesis; these include the Friedmann–Lemaître–Robertson–Walker (FLRW) universe, physics of the thermal radiation plasma at equilibrium, and effective kinetic theory treatment of particle interactions in the presence of a thermal plasma. We will then turn to the problem of thermalization of a single species of HE particles in Chapter 3, where we will find convenient parameterization of the problem, as well as an exact numerical solution for the single–species spectrum of OoE particles. We further present an example of how our results from this chapter could be used in the study of non–thermal DM production. In Chapter 4, we find an economic path to including more SM particles in the thermalization process; we then extend our single–species parameterization and numerical solution to include these multiple species and discuss the effect of various cosmological model parameters on the spectrum of OoE particles. Finally, we summarize and exemplify how our extended results could be used in the calculation of cosmological observables, in histories involving the thermalization of HE decay products. An overall summary of the thesis is given in Chapter 5.

Parts of this thesis have previously appeared in the following articles:

- [45] Energy spectrum of thermalizing high energy decay products in the early universe
  Manuel Drees, Bardia Najjari
  e-Print: 2105.01935 [hep-ph]
  DOI: 10.1088/1475-7516/2021/10/009
  Published in: JCAP 10 (2021), 009

- [46] Multi-species thermalization cascade of energetic particles in the early universe
  Manuel Drees, Bardia Najjari
  e-Print: 2205.07741 [hep-ph]
  DOI: 10.1088/1475-7516/2023/08/037
  Published in: JCAP 08 (2023), 037

CHAPTER 2

Physics of the early universe plasma

Hot big bang cosmology describes a universe starting in a hot and dense state of relativistic particles; the universe expands and cools down to eventually form the present–day observable universe. The evolution of the universe can, therefore, be broadly thought of as resulting from the interplay of the dynamics of space–time, i.e. the expansion history, and that of the particles and fields living in that space–time. In this chapter, we will introduce the essential theoretical tools required to study the evolution of the early universe plasma in an expanding universe.

We will follow a number of textbooks and lecture notes on different subjects. For the sake of brevity, we merely cover the essential topics; the reader is advised to consult the references for in–depth discussions. We follow [15, 47] through Sections 2.1 to 2.3; our discussions of thermal field theory and coherent effects in Sections 2.4 and 2.5 closely follow [48] and [49].

Although part of the tools introduced in this chapter are also applicable to the later stages of the expansion history, we will be mainly dealing with the physics of the "early universe"; a term we often use, in this thesis, to refer to the universe prior to the onset of the *electroweak* spontaneous symmetry breaking (SSB). We will therefore be dealing with the unbroken gauge group of the SM and the massless spectrum of SM particles in vacuum. As another remark, note that the time–dependence of parameters (scale factor, Hubble parameter, etc.) is often suppressed for brevity, and also that throughout Chapter 2, we may use p to refer to both *pressure* of a cosmic fluid and *momentum* of particles; the relevant quantity will be explicitly mentioned and also clear from the context. Finally, when we are comparing or combining parameters, keep in mind that we are using natural units so that e.g. the momentum of a particle is directly comparable to its temperature.

2.1 The Friedmann–Lemaître–Robertson–Walker universe

Our modern understanding of the dynamics of spacetime is formulated by Einstein's theory of general relativity (GR). The object of interest in studying the evolution of space–time in cosmology is the *metric* tensor; a study of the evolution of space-time is, therefore, equivalent to the study of the evolution of the metric tensor. The study of the metric tensor in cosmology is greatly simplified by the observation that the observable universe appears to possess a large degree of spatial homogeneity and isotropy on finitely large length–scales. The high degree of *symmetry* restricts the allowed form to that

of the Friedmann–Lemaître–Robertson–Walker (FLRW) metric

$$\mathrm{d}s^2 = \mathrm{d}t^2 - \mathrm{d}l^2 = \mathrm{d}t^2 - a^2(t)\,\gamma_{ij}\mathrm{d}x^i\mathrm{d}x^j. \tag{2.1}$$

In eq. 2.1, t denotes the time component, $\mathrm{d}l^2$ is the spatial length element in the comoving frame further written in terms of γ_{ij}, the corresponding metric for the maximally symmetric 3-space with coordinates x^i. As conventional, we have used Latin indices to denote the three spatial coordinates and reserved Greek letters for space–time indices. In (2.1) the *comoving* coordinates have been used to write down the metric so that, if undisturbed, particles at rest in these coordinate system at one instant will remain at rest during the subsequent expansion of the universe; the form of (2.1) further implies that for stationary particles the coordinate time coincides with the proper time. Throughout this thesis, we will consider the comoving frame as the rest–frame of the content of the universe.

The information about the geometry of the FLRW metric in (2.1) is contained in the spatial metric, expressed in spherical coordinates $(r,\,\theta,\,\phi)$ as

$$\mathrm{d}l^2 = \frac{\mathrm{d}r^2}{1-kr^2} + r^2\left(\mathrm{d}\theta^2 + \sin^2\theta\,\mathrm{d}\phi^2\right), \tag{2.2}$$

where the curvature k, normalised to be $k \in \{+1, 0, -1\}$, parameterises a *closed (spherical)*, *flat (planer)*, or *open (hyperbolic)* 3-space respectively. Cosmological observations are consistent with a flat universe so that we will focus on a expanding flat universe for the remainder of this thesis [3, 15].

Finally, the time evolution of an FLRW universe is encoded in the *scale factor* parameter $a(t)$ as the only space-time dependent element of the metric. In this language, the dynamics of the expansion of the universe corresponds to the dynamics of the scale factor $a(t)$. In the case of the flat FLRW universe, the numerical value of the scale factor is unphysical; instead, the *Hubble parameter*

$$H(t) = \frac{\dot{a}(t)}{a(t)}, \tag{2.3}$$

carries a physical significance, namely that of the *expansion rate* of the universe; in eq. 2.3 we have used the convention with a dot denoting a temporal derivative with respect to the coordinate t of (2.1). As we will see shortly in Section 2.2, the rate of expansion is governed by the contents of the universe; as such, in this thesis we will often trade the scale factor for other parameters, e.g., the temperature of the thermal plasma filling up the universe.

With the form of the FLRW metric at hand, one may proceed to study the kinematics of a particle propagating in the FLRW universe; our main point of interest will be the effect of cosmological expansion on the freely propagating particles in an FLRW universe. Let us showcase this by following a massive particle of mass m, and four–velocity

$$u^\mu = \frac{\mathrm{d}x^\mu}{\mathrm{d}s}. \tag{2.4}$$

Such a particle will have a physical three momentum

$$p^i = m\,a(t)\,u^i. \tag{2.5}$$

The geodesic equation, describing the free (fall) motion of a particle in a spacetime of a given metric

reads

$$\frac{\mathrm{d}u^{\mu}}{\mathrm{d}s} + \Gamma^{\mu}_{\nu\lambda}\, u^{\nu} u^{\lambda} \;=\; 0, \tag{2.6}$$

where one then needs to calculate the Christoffel symbols

$$\Gamma^{\mu}_{\nu\lambda} = \frac{1}{2} g^{\mu\sigma} \left(\partial_{\nu} g_{\lambda\sigma} + \partial_{\lambda} g_{\nu\sigma} - \partial_{\sigma} g_{\nu\lambda} \right), \tag{2.7}$$

corresponding to the metric g of (2.1), to get the explicit form for the equation of motion

$$\frac{\mathrm{d}u^{i}}{\mathrm{d}s} + 2\frac{\dot{a}}{a}\frac{\mathrm{d}t}{\mathrm{d}s}\, u^{i} \;=\; 0. \tag{2.8}$$

One may then use eq. 2.5 and eq. 2.3 to rewrite eq. 2.8 in the form

$$\frac{\mathrm{d}p^{i}}{\mathrm{d}t} \;=\; -H\,(t)\, p^{i} \;\longrightarrow\; p^{i} \;=\; \frac{\texttt{constant}}{a\,(t)}. \tag{2.9}$$

Equation 2.9 describes how the physical momenta of massive particles *redshift* due to the growth of the scale factor $a\,(t)$ and with a rate given by the Hubble expansion parameter. As the main focus of this thesis will be following the time evolution of the momenta of various particles, the Hubble rate will often appear as a point of reference. As a side note, it should be pointed out that the same result holds for the momentum redshift of massless particles so that we will often treat the Hubble redshift of all relativistic species on the same footing.

2.2 The Friedmann Equation

In the previous section, we introduced the kinematics of the FLRW universe, dictated by the large degree of symmetry of the observable universe on large scales. The temporal evolution of spacetime and kinematics of freely propagating particles was contained in the Hubble parameter or, equivalently, in the scale factor $a\,(t)$. We now turn to the dynamics of spacetime and what determines its expansion rate. The starting point is the celebrated Einstein's equation

$$R_{\mu\nu} - \frac{1}{2} g_{\mu\nu} R \;=\; 8\pi G_{\mathrm{N}} T_{\mu\nu}, \tag{2.10}$$

where the Ricci tensor $R_{\mu\nu}$ and scalar R on the LHS are given by

$$R_{\mu\nu} = \partial_{\lambda}\Gamma^{\lambda}_{\mu\nu} - \partial_{\mu}\Gamma^{\lambda}_{\nu\lambda} + \Gamma^{\lambda}_{\mu\nu}\Gamma^{\sigma}_{\lambda\sigma} - \Gamma^{\lambda}_{\mu\sigma}\Gamma^{\sigma}_{\lambda\nu}, \qquad R \;=\; g^{\mu\nu} R_{\mu\nu}. \tag{2.11}$$

The Christoffel symbols were introduced briefly in eq. 2.7 and Newton's constant G_{N} on the RHS of eq. 2.10 is often traded for the reduced Planck mass defined as $M_{\mathrm{Pl}} \equiv 1/\sqrt{8\pi G_{\mathrm{N}}} \simeq 2.4 \times 10^{18}$ GeV; we will later use the relative large value of the Planck mass to argue for simplifying assumptions. The energy–momentum tensor $T_{\mu\nu}$ encodes the various components introduced in eq. 1.2; on cosmological scales and for our assumed homogenous and isotropic universe, this content is described by a collection of perfect fluids with energy density ρ and pressures p so that $T^{00} = \rho$ in (2.10) gives the total energy density contained within the universe; the spatial components are $T^{ij} = \frac{1}{a^2}\gamma^{ij} p$ with p being the

corresponding pressure of the cosmic fluid.

One may use eq. 2.11 to calculate the Ricci tensor and scalar corresponding to the metric (2.1) and feed them into the Einstein equation (2.10). Assuming a flat universe (see eq. 2.2) and keeping in mind that the scale factor parameter encodes the kinematics of spacetime, the evolution of the flat FLRW universe is governed by the Friedmann equation

$$H^2 = \left(\frac{\dot{a}}{a}\right)^2 = \frac{\rho}{3M_{\rm Pl}^2}. \tag{2.12}$$

Given the energy content of the universe, the Friedmann equation allows for the determination of the evolution of the scale factor $a(t)$; the single missing piece for a solution of $a(t)$ is then the time-dependence of ρ on the RHS of eq. 2.12. The latter follows from a covariant conservation law for the energy–momentum tensor corresponding to each component of the universe

$$\nabla_\mu T^{\mu 0} \equiv \partial_\mu T^{\mu 0} + \Gamma^\mu_{\mu\sigma} T^{\sigma 0} + \Gamma^0_{\mu\sigma} T^{\mu\sigma} = 0. \tag{2.13}$$

With the temporal and spatial components of T given in terms of ρ and p, the conservation law (2.13) reads

$$\dot{\rho} + 3\frac{\dot{a}}{a}(\rho + p) = 0; \tag{2.14}$$

note that the ρ and p of a given component, i.e., matter, radiation, etc., are related through the equation of state parameter ω introduced in Section 1.3 and are not independent. Combining equations 2.14 and 1.3 implies that a larger equation of state corresponds to a faster diminishing of the corresponding energy density resulting from the cosmic expansion. An important example is given for the case of radiation with $\omega = 1/3$ resulting in $\rho_{\rm R} \propto a^{-4}$; this can be nicely understood as resulting from the number density of particles in a 3–dimensional space reducing like a^{-3} along with the momentum redshift a^{-1} behavior established in eq. 2.9. It is further worth mentioning that, for a universe composed of multiple components (see eq. 1.2), the conservation relation (2.14) also holds for the individual components separately, so long as these do not interact, e.g. through the decay of a matter component into radiation.

The Friedmann equation 2.12, together with the conservation law eq. 2.14, are solved to find the expansion history of the universe, encoded in $a(t)$, and its effect on the various components residing in this universe. The masses, momenta, and interactions of these contents on the other hand determine the equation of state parameter appearing in eq. 2.14.

2.3 The Thermal Plasma

In the previous section, we introduced the dynamics of the expanding FLRW universe and the effect of the expansion on the content of the universe. We saw that the governing equation 2.10 implies an expansion rate potentially suppressed by the large Planck mass. We further established that the expansion affects the momenta of propagating particles in the form of a redshift inversely proportionate to the scale factor. We now turn our attention to a completely different class of processes affecting the momenta and number densities of particles making up the cosmic fluids of matter and radiation, namely particle interactions.

As mentioned in Chapter 1, particle interactions governed by QFT provide for very efficient

interactions among particles as compared to the non-exponential gravitational expansion of the universe after inflation. The result is that particle interactions get to bring the particles making up the cosmic fluid into a state of *thermal equilibrium* potentially for a large part of the history of the universe; the observation of the CMB, for example, provides concrete evidence for a thermal universe at the time of last scattering. As we will shortly see, thermal equilibrium allows for a system to be fully described by a few parameters so that many processes of interest in cosmology result from a departure from thermal equilibrium. Nevertheless, studying the composition and properties of a thermal plasma of particles is a key ingredient in particle cosmology, both in and out of equilibrium (OoE).

Let us consider a plasma of interacting particles of different species $s,\ s',\cdots$ undergoing a set of interactions of the form

$$s_1 + s_2 + \cdots + s_n \ \leftrightarrow\ s_1' + s_2' + \cdots + s_{n'}', \tag{2.15}$$

respecting the symmetries of the underlying particle theory; note that $n \neq n'$ so that the form (2.15) also includes number changing processes. The interactions (2.15) are local so that we may choose to look at the composition of the plasma in the *locally Lorentz frame*. If the corresponding process rate exceeds the expansion rate H, introduced in eq. 2.3, the species $s,\ s'$ are said to be in equilibrium with respect to the process (2.15). Such processes allow for an efficient exchange of momenta among the $s,\ s'$ particles, resulting in the establishment of *kinetic equilibrium*. In this case, the phase-space occupancy $f_s\ (\mathbf{p})$, describing the 3–momentum distribution of particles of species s, is given by

$$f_s(\mathbf{p}) = \frac{1}{(2\pi)^3}\frac{1}{e^{(E_s(\mathbf{p})-\mu_s)/T}\ \mp 1}, \tag{2.16}$$

where T is the temperature of the thermal plasma, and μ_s is the *chemical potential* associated with the species s; the energy E is related to the three momentum $\mathbf{p}$ via

$$E_s\ (\mathbf{p})\ =\ \sqrt{m_s^2 + |\mathbf{p}|^2}, \tag{2.17}$$

with m_s the mass of the certain species s. The choice of $\pm$ in eq. 2.16 depends on the nature of the species s, with the $+$ and $-$ signs corresponding to fermions (with Fermi–Dirac statistics) and bosons (with Bose–Einstein statistics) respectively.

In addition to kinetic equilibrium, the plasma is said to be in *chemical equilibrium* with respect to the processes 2.15. This implies a balance of the chemical potentials corresponding to the species $s,\ s'$ as

$$\mu_{s_1} + \mu_{s_2} + \cdots + \mu_{s_n}\ =\ \mu_{s_1'} + \mu_{s_2'} + \cdots + \mu_{s_{n'}'}. \tag{2.18}$$

Given a distribution function $f_s\ (\mathbf{p})$ from (2.16), the number density n_s, energy density ρ_s, and pressure p_s corresponding to the species s with g_s degrees of freedom are given by

$$\begin{aligned} n_s\ &=\ g_s \int f_s(\mathbf{p})\mathrm{d}^3p \\ \rho_s\ &=\ g_s \int E(\mathbf{p}) f_s(\mathbf{p})\mathrm{d}^3p. \\ p_s\ &=\ g_s \int \frac{|\mathbf{p}|^2}{3E} f_s(\mathbf{p})\mathrm{d}^3p \end{aligned} \tag{2.19}$$

Chemical potentials are considered to be negligibly small in the thermal plasma of the early universe due to the implications of a small Baryon asymmetry parameter; we consider $\mu_s = 0$ for all species from the thermal bath, leaving the mass m and the temperature T as the parameters of interest in the phase space density (2.16); the thermodynamics quantities (2.19) can then be calculated in the two limiting cases of relativistic *radiation* and the opposite case of non–relativistic *matter*. In this thesis, we will almost exclusively deal with a thermal bath of radiation, with $T \gg m_s$. For a relativistic species s, this will result in

$$\begin{aligned} n_s &= \begin{cases} \left(\zeta(3)/\pi^2\right) g_s T^3 & \text{(boson)} \\ (3/4)\left(\zeta(3)/\pi^2\right) g_s T^3 & \text{(fermion)} \end{cases} \\ \rho_s &= \begin{cases} \left(\pi^2/30\right) g_s T^4 & \text{(boson)} \\ (7/8)\left(\pi^2/30\right) g_s T^4 & \text{(fermion)} \end{cases} \\ p_s &= \rho_s/3 \end{aligned} \quad , \tag{2.20}$$

We will often be interested in the properties of the collective set of relativistic particles in the thermal radiation bath so that we describe a collection of species as

$$\rho = g_* \frac{\pi^2}{30} T^4, \tag{2.21}$$

where the effective number of degrees of freedom is defined as

$$g_* = \sum_{s \in \text{bosons}} g_s + \frac{7}{8} \sum_{s \in \text{fermions}} g_s, \tag{2.22}$$

where the sum is to be understood as over relativistic species of temperature T. More general definitions of g_*, where species possess different temperatures T_s also exist; we will, however, restrict our attention to relativistic bosons and fermions of a common temperature T, as appropriate for our purposes in this thesis. Similarly, as we are focusing on the physics of the early universe with the assumption of an *unbroken* SM gauge group, we will use the massless spectrum of the SM with chiral fermions. Table 2.1 summarises the SM spectrum of particles, their physical number of degrees of freedom g, and the corresponding contribution to the effective number of degrees of freedom g_*, including the gauge and generation multiplicity factors.

As explained in Chapter 1, in addition to a thermal bath of temperature T described by the distribution functions (2.16), we will also be focusing on a non–thermal distribution of particles with energies $p \gg T$. It is, therefore, often useful for our purposes to represent the particle species in the thermal bath by a single energy scale. This can be achieved by exploiting the distribution functions 2.20 to calculate the average particle energy

$$\langle p \rangle_s \equiv \frac{\rho_s}{n_s} \approx \begin{cases} 2.7 \times T & \text{(boson)} \\ 3.15 \times T & \text{(fermion)} \end{cases} \sim 3 \times T, \tag{2.23}$$

Equations 2.16 and 2.23 allow us to use the temperature T to characterise particles from the thermal bath. Notably, one may assume that typical interactions among particles from the thermal bath

Particle Species s	Degrees of freedom g_s	Contribution to g_*
B	2	2
W	2	3 (isospin) $\times$ 2
g	2	8 (color) $\times$ 2
ℓ_L	2	3 (generation) $\times$ 2 (isospin) $\times 2 \times \frac{7}{8}$
ℓ_R	2	3 (generation) $\times 2 \times \frac{7}{8}$
q_L	2	3 (generation) $\times$ 2 (isospin) $\times$ 3 (color) $\times 2 \times \frac{7}{8}$
u_R	2	3 (generation) $\times$ 3 (color) $\times 2 \times \frac{7}{8}$
d_R	2	3 (generation) $\times$ 3 (color) $\times 2 \times \frac{7}{8}$
H	2	2 (isospin) $\times$ 2
	Sum of DoF	106.75

Table 2.1: Particle content of the SM in the unbroken phase and the corresponding contribution to the effective number of degrees of freedom eq. 2.22. The mid column contains the number of degrees of freedom for an individual particle of species "s" in the corresponding Lorentz representation, excluding the gauge and flavour/generation multiplicities, which are then included to get the combined effective contribution in the right column.

occur at the energy scale $\mu \sim O(T)$; this scale is then used to study the particle physics aspects of the particle plasma. In particular, the interaction strength α_G, corresponding to a gauge group G, of particles *typically* interacting in the thermal plasma must be calculated at this energy scale i.e. $\alpha_G = \alpha_G(T)$. This observation, along with the running of the SM coupling constants, partly justifies a *weak–coupling* treatment of early universe plasmas (see Appendix A).

2.4 Thermal field theory and thermal mass

In the previous section, we looked at the thermodynamics of the thermal plasma of SM particles of temperature T. The next question one may ask is how the presence of this thermal bath of temperature T affects the properties of particles and interactions. We have already alluded to one such thermal effect, namely the restoration of the electroweak symmetry at high temperatures, in Chapter 1. Another essential effect we will often be dealing with in this thesis is the *thermal mass* of particles in the thermal bath. A systematic study of such phenomena is the subject of *thermal field theory*, a statistical mechanics formulation of QFT degrees of freedom.

In this section, we aim to outline the principal ideas and results from thermal field theory essential to this thesis. For the sake of simplicity, and following the wisdom of [48] on which this section is largely based, we will often assume a simplified particle model of a scalar ϕ^4–theory with a single mass parameter m and a single quartic coupling λ; we will however turn to the realistic case of SM gauge interactions to draw conclusions and present key results in Section 2.5.

The central object of interest in the statistical physics of a system of temperature T is the *partition*

function

$$Z = \sum_{\text{states}} e^{-\beta E} = \sum_{\text{states}} \langle E|e^{-\beta H}|E\rangle = \operatorname{tr} e^{-\beta H}, \tag{2.24}$$

where E represents energy, H is the hamiltonian of the system of interest, responsible for the time evolution of the system in QFT. The trace in eq. 2.24 runs over the corresponding Hilbert space, and $\beta \equiv \frac{1}{T}$ encodes the temperature of the system in thermal equilibrium. It will be of great interest to be able to use the developed tools and techniques of field theory for the particles making up the ensemble. The fundamental connection to the path–integral formalism follows from the assignment $\beta \to i\,t$, so that $e^{-iH\,t}$ represents the time evolution of an *imaginary–time* system. Equivalently, the evolution follows from the imaginary–time path integral

$$Z = \int [\mathcal{D}\phi] e^{-S_{\mathrm{E}}}, \tag{2.25}$$

with the *Euclidean* action S_{E} resulting from the Wick rotation of $\tau = i\,t$; in the example of a scalar ϕ^4 theory this reads

$$S_{\mathrm{E}} \equiv \int_0^\beta \mathrm{d}\tau \mathcal{L}_{\mathrm{E}} \xrightarrow{\phi^4\text{theory}} \int_0^\beta \mathrm{d}\tau \int \mathrm{d}^3x \left[\frac{1}{2}(\partial\phi)^2 + \frac{m^2}{2}\phi^2 + \frac{\lambda}{4!}\phi^4\right]. \tag{2.26}$$

In eq. 2.26 the first equality is used to define $\mathcal{L}_{\mathrm{E}}$, the Lagrangian of the Euclidean theory, resulting from the Wick rotation of the physical Lagrangian [1]. Important comments are in order regarding the Euclidean action eq. 2.26. The euclidean time parameter is confined to the interval $\tau \in (0, \beta)$ and therefore compact; periodic (anti–periodic) temporal boundary conditions are applied to bosonic (fermionic) fields to implement the trace action of eq. 2.24. For the case of the bosonic scalar theory in eq. 2.26 we therefore have

$$\phi(0, x) = \phi(\beta, x). \tag{2.27}$$

Similar to the case of real–time zero–temperature QFT, the Lagrangian eq. 2.26 allows for a derivation of a set of Feynman rules for the imaginary–time theory, subject to the boundary conditions of the form (2.27). Carrying out the Fourier transformation to move to momentum–space Feynman rules, the compactness of the virtual temporal direction results in the usual real–time energy (frequency) continuous integration, corresponding to the temporal coordinate, to be replaced by a discrete sum

$$\int \frac{\mathrm{d}^4 p}{(2\pi)^4} \to T \sum_{\nu_n} \int \frac{\mathrm{d}^3 p}{(2\pi)^3}, \qquad n \in \mathcal{Z} \tag{2.28}$$

over the *Matsubara frequencies* for integer n, i.e.

$$\begin{aligned} \nu_n &= 2\pi n/\beta = 2\pi n T && \text{(bosons)} \\ \nu_n &= 2\pi(n + \tfrac{1}{2})/\beta = 2\pi(n + \tfrac{1}{2})T && \text{(fermions).} \end{aligned} \tag{2.29}$$

Once more, the different form for the bosonic and fermionic Matsubara frequencies corresponds to symmetric and antisymmetric boundary conditions in imaginary time, as mentioned following eq. 2.26.

[1] Numerical factors in the Lagrangian (2.26) are not explicitly used in the schematic notation used in [48].

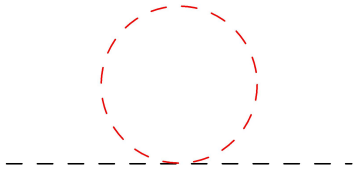

Figure 2.1: The thermal one–loop contribution to the self–energy of the ϕ^4 theory 2.26. The red color is chosen to allude to the loop representing collective effects of the thermal background as introduced in eq. 2.26.

The new Feynman rules, in association with the momentum integration 2.29 can be used to calculate processes of interest in thermal field theory; capturing the effect of the ensemble of particles in the thermal bath.

An important role in this thesis is played by the effects of a thermal bath of temperature T on a particle propagating the thermal bath; let us therefore use the procedure described above, within the simple toy ϕ^4 model of eq. 2.26. Consider the propagation of a ϕ particle through a thermal plasma of ϕ particles with the distribution function 2.16, as motivated, with vanishing chemical potential. The correspondence introduced in eq. 2.28 implies that insertions from (2.26) represent the interactions with a thermal ensemble of ϕ particles of temperature T. The self–energy diagram Fig. 2.1 results in a modification of the two–point function and an *effective* mass for the ϕ particles of the form

$$\Delta m_{\text{eff}}^2 = \frac{\lambda}{2} T \sum_{\nu} \int \frac{\mathrm{d}^3 p}{(2\pi)^3} \frac{1}{\nu^2 + p^2 + m^2}, \tag{2.30}$$

where λ is the quartic coupling of the scalar field theory 2.26 of mass parameter m. The physical significance of the Matsubara summation can be better seen by using the residue theorem to bring 2.30 into a form

$$\Delta m_{\text{eff}}^2 = \frac{\lambda}{2} \int_C \frac{\mathrm{d}\omega}{2\pi i} \int \mathrm{d}^3 p \, \frac{f_{\text{B}}(\omega)}{\omega_p^2 - \omega^2}, \tag{2.31}$$

where $\omega_p^2 \equiv p^2 + m^2$, and the Bose distribution of eq. 2.16 for the scalar field ϕ is now written in terms of the β parameter as

$$f_{\text{B}}(\omega) = \frac{1}{(2\pi)^3} \frac{1}{e^{\beta\omega} - 1}. \tag{2.32}$$

The replacement leading to (2.31) is achieved by noting that the kinetic function 2.32 has residues of T at simple poles with $\omega = i2\pi nT = i\nu_n$ as given by eq. 2.29, and using an integration contour C of the form seen in Fig. 2.2 (a). Starting from eq. 2.31, one could however take an equivalent alternate path, seen in Fig. 2.2 (b), to close integration contour C, leading to the poles along the imaginary axis to drop out of the residue theorem calculation with a vanishing winding number; one would then instead pick out residues of a size $n_{\text{B}}(\omega_p)/2\omega_p$ for the poles along the real axis (blue). Equation 2.31 can, therefore, be rewritten in the intuitive form

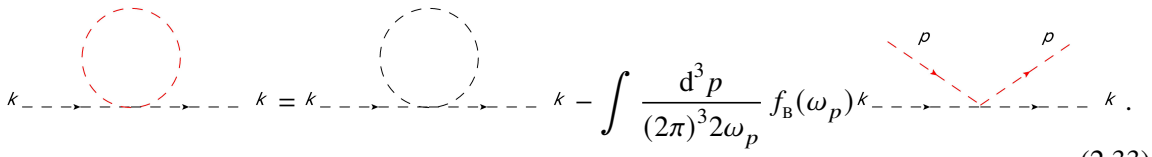

$$= \int \frac{\mathrm{d}^3 p}{(2\pi)^3 2\omega_p} f_{\text{B}}(\omega_p) \, . \tag{2.33}$$

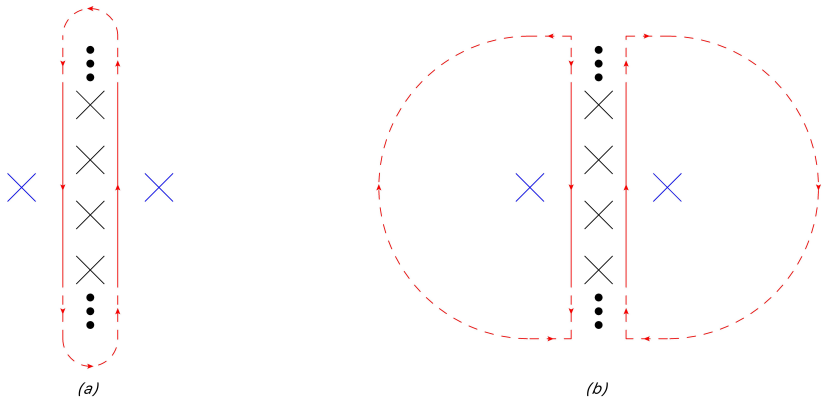

Figure 2.2: (a) pole placement corresponding to the Matsubara poles of (2.32) on the imaginary axis. (b) Alternate integration contour C relating the residue integral of eq. 2.31 to residues of poles at $\pm\omega_p$, appearing in (2.33).

In eq. 2.33, the red loop represents a thermal loop, and red external states are to be understood as particles from the thermal background plasma of temperature T. The first term on the RHS of (2.33) (black), contains the β–independent part of (2.31), and reproduces the vacuum modification to the two–point function in $T = 0$ QFT, in which we are not interested here. Additionally, note that in the shorthand notation used in (2.33), the arrows on scalar lines represent the assignment of momenta $\mathbf{k}$ and $\mathbf{p}$ to the involved particles.

The mass correction Δm^2_{eff} of eq. 2.31 can therefore be decomposed as a zero–temperature vacuum contribution of the standard QFT and a contribution arising from *forward* scatterings of particles from the thermal bath; the last term of eq. 2.33 represents a weighted phase space integrated forward–scattering amplitude λ of particles of momentum p from a thermal bath of temperature T, with a probability given by the kinetic function (2.16). Explicitly, this calculates to

$$\Delta m^2_{\text{eff}}(T) = \frac{\lambda}{24} T^2. \tag{2.34}$$

The form of effective thermal mass for the simple case of the pure scalar field theory (2.26) is rather informative. One key observation is that in the *relativistic regime* i.e. $T \gg m$, the dominant contribution to the effective mass would be provided by the thermal mass. Also, note that the latter is dominated by interactions with background particles of energies $p \sim T$. Similarly, the coupling of the theory appears through the amplitude of the thermal loop Fig. 2.1, so that in this case $\Delta m_{\text{eff}} \sim \lambda T^2$. The addition of further interaction and particles into our theory and the background plasma will, therefore, similarly contribute to the effective *thermal mass* of the ϕ field.

In a similar manner, one may proceed to calculate the effective thermal mass of gauge bosons of a gauge theory. As an example, the corresponding thermal loop diagrams contributing to the effective thermal mass of the $SU(3)_C$ gluons of the SM are seen in figure Fig. 2.3. Within the SM, gluons as well as left- and right-chiral quarks contribute to the generation of the gluon thermal mass; note further that all contributions appear at the order of g^2 in gauge coupling g so that one has a thermal mass for the gluon as

$$m^2_{\text{th}} \equiv \Delta m^2_{\text{eff}} \sim g^2 T^2, \tag{2.35}$$

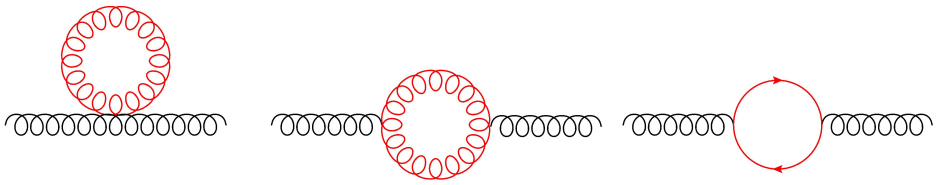

Figure 2.3: Physical thermal one–loop contributions to the self–energy of the gluon within the SM. The thermal loops is denoted as before in red, and as the only color–charged fermions in the SM, q_L and q_R run in the fermion loop on the right.

where we are disregarding the $O(1)$ group theoretic and multiplicity factors as we will often do in this chapter, to focus on the parametric role of the temperature, the momenta, and the couplings in the theory. It is reasonable to expect that the effective thermal masses of the other two gauge bosons of the SM should follow the same pattern of temperature and coupling dependence as in eq. 2.35. Throughout this thesis, we will use this approximate form for the thermal masses. More detailed results for the effective thermal mass of the SM gauge bosons in a background plasma are presented in Appendix B. For a more detailed view of the derivation of thermal masses in the SM, see [50, 51].

2.5 Coherence effects and effective kinetic theory of gauge–interactions

In the previous section, we briefly introduced the imaginary–time formulation of thermal field theory, and used it to outline the physics dictating the appearance of an effective thermal mass (2.35). The advantages of the imaginary–time formalism are best employed in the treatment of the so–called "static phenomena" within the plasma; examples include the calculation of the thermal effective mass or that of the equation of state.

The former approach however is not suited to the treatment of time–dependant phenomena, such as those occurring during the relaxation of an OoE system; examples of the latter class include viscous phenomena and dissipation [2]. To study such phenomena, one is interested in starting from the microscopic QFT interactions of particles, to describe the collective effect of a large number of interactions in the thermal plasma. The resulting machinery, known as *kinetic theory*, picks the kinetic function $f(\mathbf{x}, \mathbf{p}, t)$ introduced in (2.19) as its central object. The evolution of the kinetic function is given by the Boltzmann equation

$$\frac{\mathrm{d}f(\mathbf{p})}{\mathrm{d}t} = \frac{\partial f(\mathbf{p})}{\partial t} + \frac{\partial \mathbf{x}}{\partial t} \cdot \frac{\partial f(\mathbf{p})}{\partial \mathbf{x}} = -(\text{loss})_{\mathbf{p}} + (\text{gain})_{\mathbf{p}}\,, \tag{2.36}$$

where we have suppressed $\mathbf{x}$ and t dependence of f, and with gain and loss terms on the RHS representing the growth and depletion of states of momentum $\mathbf{p}$. Changes in the momentum of a particle in the cosmic plasma can either result from the expansion of the universe (2.9) or from particle interactions involving other plasma constituents. In the post–inflationary plasma, the latter will provide a tremendously more efficient means of momentum transfer; in Chapter 3, we will show in a specific example that the relatively short timescale of gauge–mediated particle processes allows us to disregard the Hubble expansion and treat the background FLRW universe as quasi–static. Focusing

[2] See, e.g., Section 4.1 "A failure of imaginary-time intuition" in [48].

on particle interactions leading to changes in momenta, one may then schematically rewrite (2.36) as

$$\frac{\mathrm{d}f(\mathbf{p})}{\mathrm{d}t} = -\int_{\mathbf{k},\mathbf{p}',\mathbf{k}'} \left| \begin{array}{c} p \quad p' \\ \diagup \quad \diagdown \\ \bullet \\ \diagdown \quad \diagup \\ k \quad k' \end{array} \right|^2 f_{\mathbf{p}} f_{\mathbf{k}} (1 \pm f_{\mathbf{p}'})(1 \pm f_{\mathbf{k}'}) + \int_{\mathbf{k},\mathbf{p}',\mathbf{k}'} \left| \begin{array}{c} p' \quad p \\ \diagup \quad \diagdown \\ \bullet \\ \diagdown \quad \diagup \\ k' \quad k \end{array} \right|^2 f_{\mathbf{p}'} f_{\mathbf{k}'} (1 \pm f_{\mathbf{p}})(1 \pm f_{\mathbf{k}}) + \dots \,. \tag{2.37}$$

In the schematic form of eq. 2.37, we have used the solid lines to represent generic particles, with the arrow depicting the momentum assignment, and the blob representing an interaction. The first and second terms on the RHS respectively represent the rate of removal and appearance of particles of momentum $\mathbf{p}$ (blue) from interactions of other particles in the plasma (black). Note also that for brevity, we have suppressed the integration measures in both terms on the RHS and mentioned these collectively as the integration region. Finally, the dots represents all other processes, including higher order scatterings, decays, etc. contributing to the production and removal of particles of momentum $\mathbf{p}$. The choice of sign in $1 \pm f$ terms in (2.37) depends on the bosonic/fermionic nature of the particles carrying the assigned momenta; as seen before, these Bose enhancement or Pauli blocking factors represent the spin statistics.

Boltzmann equations of the form (2.37) are widely used to calculate observables in cosmology, for example to study the evolution of DM abundance. In this thesis, we will be focusing on the process of energy loss of energetic particles, so that we will be interested in a Boltzmann equation (2.37) governing the dynamics of the kinetic function f for momenta $p = |\mathbf{p}| \gg T$. Note that we may utilise our arguments for the homogeneity and isotropy of the early–universe plasma in Section 2.1 to proceed to identify the kinetic function as $f(p,t)$, with a proper phase space averaging of the scattering processes in (2.37).

Before setting out to formulate and solve such Boltzmann equations, however, we must check the assumptions underlying the validity of the kinetic theory treatment and eq. 2.37. Taking a closer look at eq. 2.37, a first observation is that the Boltzmann formulation treats the particles classically with independent position and momenta, undergoing momentum changing interactions governed by QFT. This assumption can be justified so long as the de Broglie wavelength λ_{dB} of the particle of momentum p is small with respect to the typical separation of consecutive interactions, i.e.

$$\lambda_{\mathrm{dB}}(p) \ll \text{mean free path of particles}\,. \tag{2.38}$$

A second implicit assumption in (2.37) is that the various scattering processes are independent, as seen by the absence of interference terms; the latter requires the quantum–mechanical time–span of the scattering processes in (2.37) to be short compared to the temporal separation of these events, i.e.

$$\Delta\tau^{\text{duration}}_{\text{scattering}} \ll \text{mean free time of particles}\,. \tag{2.39}$$

Let us next examine the validity of the conditions (2.38) and (2.39) for a couple of processes we are interested in in this thesis. Consider a massless gauge–charged particle of the unbroken SM with momentum p, propagating within a plasma of temperature T. This particle will have a de Broglie wavelength of $\lambda_{\mathrm{dB}} = 1/p$, and undergoes elastic Coulomb scattering off the plasma particles of

number density (2.20) with a cross section

$$\sigma_{\text{Coulomb}} \sim \int d(q^2) \left| \frac{g^2}{q^2} \right|^2 \sim \frac{g^4}{m_{\text{th}}^2} \sim \frac{g^2}{T^2} \sim \sigma^{\text{soft}}_{\text{Coulomb}}, \tag{2.40}$$

where g is once more the corresponding gauge coupling and q denotes the momentum exchange [3]. Notably, we have used the thermal mass (2.35) to cut off the infra-red (IR) divergence of the Coulomb cross section; such *soft* scatterings with a momentum transfer $q \sim m_{\text{th}}$ dominate the cross section as can be seen by the last assignment in eq. 2.40. These soft Coulomb scatterings off the thermal background with a number density (2.20) will result in a mean free time of the order

$$\Delta\tau^{\text{mean free time}}_{\text{soft}} \sim \left(g^2 T\right)^{-1} \gg \lambda_{\text{dB}}(p) \ . \tag{2.41}$$

For the early universe plasma with $g \ll 1$, the requirement (2.38) is therefore satisfied for all OoE particles with $p \gg T$.

Next, let us look at the second condition (2.39) for the validity of the Boltzmann equation (2.37). Once again, let us start with case for $2 \to 2$ Coulomb process mediated by a SM gauge boson; as seen in (2.40), the cross section is dominated by the region of soft momentum exchange at the IR cutoff with momentum exchange $q \sim m_{\text{th}}$. Focusing for the moment on the soft elastic scatterings, the corresponding quantum mechanical *duration* for such processes is then

$$\Delta\tau^{\text{duration}}_{\text{soft}} \sim 1/m_{\text{th}} \sim 1/gT \ll \Delta\tau^{\text{mean free time}} , \tag{2.42}$$

where in the last step we have once more used the assumption of weakly coupled SM gauge theories in the early universe. With both criteria (2.38) and (2.39) met, the kinetic theory is thus safely applicable for the study of soft $2 \to 2$ processes on the RHS of eq. 2.37.

We shall go through the same checks we did above for soft $2 \to 2$ processes, also for any other process we wish to study via the Boltzmann equation 2.37. As mentioned in Chapter 1, the process of energy loss for *hard* [4] OoE particles with energy $p \gg T$ happens to be one particular example where the dominant contribution is provided by the higher order $2 \to 3$ processes. One should therefore ascertain the applicability of the Boltzmann equation 2.37 for the corresponding $2 \to 3$ processes.

Let us, however, leave the topic of energy loss of highly energetic OoE particles to Chapters 3 and 4 and, following [48], focus instead on the closely related issue of *viscosity*, where one would be interested in the modifications of the momentum vector $\mathbf{p}$ of particles with

$$p \sim T,$$

[3] Please note that we have chosen to denote the *small–angle* forward scattering processes as *soft* and the *large–anlge* scattering processes as *hard* scattering processes, to stick to the familiar terminology from the literature. This might however overburden our nomenclature of *hard* particles denoting energies of order $p \gg T$ and *soft* particles denoting particles of energy $p \sim T$ in the majority of this thesis. Please also see Footnote 4 in this regard.

[4] Readers who might be interested on consulting the referenced literature (including e.g. [48]) are advised to note a difference in nomenclature; the term "hard scale" in the QGP literature is often reserved for particles of energies $p \sim T$, while particles with $p \gg T$ are referred to as "primaries". For reasons that will become clear in Chapter 3 and conforming to the literature discussing non–thermal DM production (see e.g. [52]), we will instead use the term "hard particles" for particles with $p \gg T$; the term "primary" will also be used to refer to the first particles resulting from the decays of an OoE heavy particle.

although we will keep the p dependence of various quantities explicit, for arguments extending to higher $p \gg T$ energies to be used in the remainder of this thesis. The concepts introduced in the study of viscosity will be later used in Chapters 3 and 4 to study the process of energy loss.

In the study of viscosity, we are interested in how the interactions of a particle of energy p with the particles from the background medium result in changes in the momentum vector $\mathbf{p}$. Here, we would like to particularly focus on processes that kick a particle with $p \sim T$ out of its flow path. Above, we established that the kinetic theory treatment and the Boltzmann equation (2.37) are valid for studying the effect of soft *small-angle* elastic $2 \to 2$ processes; the used arguments can be seen to extend to the case of soft $p \sim T$ particles. It is to be expected, however, that hard *large–angle* $2 \to 2$ scattering processes also contribute to changes in particle momenta and thus to viscosity; one must therefore check if the latter processes could also be directly used in the corresponding Boltzmann equation 2.37. Consider a particle of momentum $\mathbf{p} = p\,\hat{e}_z$ with $p \gtrsim T$ and let us ask for a $\Delta\theta \sim O(1)$ change of its directions of motion, i.e., for it to develop a relative transverse momentum $p_\perp \sim O(p)$. The corresponding hard, large–angle, scattering cross section will parametrically be

$$\sigma^{\text{hard}}_{\text{Coulomb}} \sim \frac{g^4}{p_\perp^2} \sim \frac{g^4}{p^2}\,, \tag{2.43}$$

corresponding to these large angle processes occurring with a mean free time

$$\Delta\tau^{\text{mean free time}}_{\text{hard}} \sim \frac{p^2}{g^4\,T^3} \xrightarrow{\text{for } p\sim T} \sim \frac{1}{g^4 T}, \tag{2.44}$$

where in the last step, we have focused on the specific case of particles of energy $p \sim T$ in whose viscous behaviour we are interested. Note that these hard $2 \to 2$ processes with a momentum transfer $q \gg m_{\text{th}}$ occur on a shorter timescale as compared to (2.42) so that the condition (2.39) for the validity of kinetic theory treatment is met for a weakly coupled gauge theory. We had previously established that condition (2.38) is met; together, these imply that hard $2 \to 2$ processes can safely be used on the RHS of our Boltzmann equation 2.37 for particles of energy $p \gtrsim T$.

With both the hard and soft $2 \to 2$ processes eligible for being directly studied in the Boltzmann equation, one might ask how the two compare in their contribution to modifying the momentum vector $\mathbf{p}$. We saw that the mean free time (2.44) for hard processes is larger than that of the soft processes (2.41), so that a large number

$$N_{\text{soft}} \sim p^2/m_{\text{th}}^2 \tag{2.45}$$

of soft processes occur for every single hard scattering. Although dominating the Coulomb cross section 2.40, the soft processes typically result in small changes to the direction of motion of the particle traversing the thermal medium. A single soft scattering off the thermal background particles allows for a random change of $\mathbf{p}_\perp$ in the transverse XY plane; the typical size of these transverse "soft kicks" are $\delta p_\perp \sim q \sim m_{\text{th}}$, resulting in a deflection of the hard particle by an angle

$$\delta\theta \sim p_\perp/p \sim m_{\text{th}}/p\,. \tag{2.46}$$

With the fulfilment of condition (2.38), we could say these consecutive soft scatterings result in a *random walk* of $\mathbf{p}_\perp$ in the transverse XY plane, with a gradual build–up of an effective deflection angle θ. After N_{soft} (2.45) such kicks occurring during a time $\Delta\tau^{\text{hard}}_{\text{mean free time}}$ (2.44) the accumulated deflection

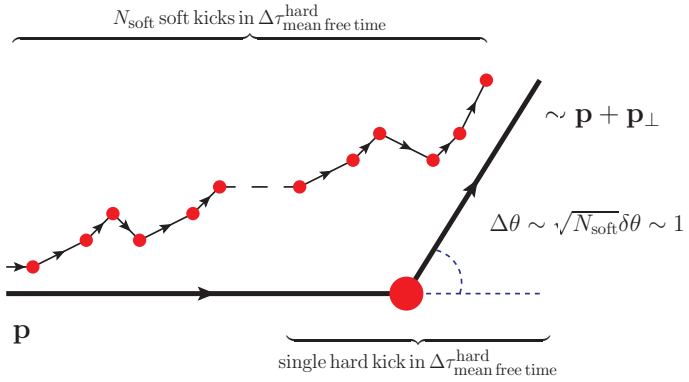

Figure 2.4: Reproduced from [48] with small changes: schematic of gauge mediated hard and soft Coulomb scatterings off the background thermal bath (red) occurring during a timescale $\Delta\tau^{\rm mean\ free\ time}_{\rm hard}$; the single hard scattering (thick/large blob) and the $N_{\rm soft}$ soft scatterings (thin/small blobs) contribute equally to modifications of the momentum vector $\mathbf{p}$ developing a transverse momentum $\mathbf{p}_\perp$. Note that the actual random walk of $\mathbf{p}_\perp$ occurs in a 2D plane.

angle will be

$$\Delta\theta \sim \sqrt{N_{\rm soft}}\,\delta\theta \sim 1\,. \tag{2.47}$$

Equation 2.47 shows that so long as one is interested in large angle changes of the the momentum vector $\mathbf{p}$, soft and hard processes contribute on the same footing to the Boltzmann equation (2.37) [5], although they do so in different number of steps; this is shown schematically in Fig. 2.4 where the thick line representing a hard scattering process encompasses $N_{\rm soft}$ soft kicks, depicted in thin lines, with the two resulting in comparable deflections after a time $\Delta\tau^{\rm mean\ free\ time}_{\rm hard}$ (2.44).

The above observation further prompts the question, what other process could competitively contribute to modifications of the momentum $\mathbf{p}$ on the same timescale as (2.44). With the case of $p \sim T$ in mind, let us next look at the $2 \to 3$ *splitting process* depicted in Fig. 2.5, and consider the special case where the initial particle of energy p splits symmetrically into two near–collinear *relatively* softer particles of energy $\sim p/2$. The near–collinear splittings indirectly contribute to the diffusion process as the resulting smaller momenta allow for more efficient diffusing as seen in (2.43) and (2.46). The process of Fig. 2.5 can be thought of as a Bremsstrahlung associated with a forward scattering of cross section (2.40), resulting in a cross section and rate of

$$\sigma_{\rm split} \sim g^2 \cdot \sigma^{\rm soft}_{\rm Coulomb}, \qquad \Gamma^{-1}_{\rm split} \sim \frac{1}{g^4 T}\,. \tag{†}$$

As seen in equations † and 2.44, for particles of energy $p \sim T$, the $\mathcal{O}(1)$ softening of the hard momenta via the splitting process would occur with the same rate as the collection of $\mathcal{O}(1)$ hard and the combined effect of soft deflections depicted in Fig. 2.4. For a consistent picture of the momentum diffusion, one therefore needs to consider the kinetic theory and Boltzmann equation of the schematic

[5] The same argument applies in fact to processes contributing to any deflection with $\Delta\theta > \delta\theta$; in Chapter 4 we will use this argument to justify the presence of the "Coulomb logarithmic" enhancement. See also the footnote 6 on Page 40.

form

$$\frac{\mathrm{d}f(\mathbf{p})}{\mathrm{d}t} = \int \left| \right|^2 + \int \left| \right|^2 + \dots , \tag{2.48}$$

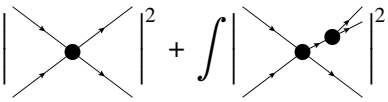

where similar to eq. 2.37, the blobs represent interactions, each contribution needs to be integrated over the appropriate phase space and include the suppressed appropriate Bose enhancement and Pauli blocking factors for the forward and backward processes, and account for the different possibilities for the assignment of momentum p to the particles involved in the interactions.

The next step would be to use the cross sections (†), (2.43) and (2.40) to formally write down the Boltzmann equation (2.48) governing momentum diffusion; before that, however, one must check the validity of the underlying kinetic treatment and the conditions (2.38) and (2.39) for the additionally considered $2 \to 3$ collinear splittings.

The addition of the $2 \to 3$ term to the Boltzmann equation (2.48) affects neither the de Broglie wavelength of the particle under study with $p \gtrsim T$, nor its mean free path dictated by soft $2 \to 2$ processes; i.e. the condition (2.38) remains intact. It is therefore the assumption of quantum decoherence among the various processes that needs to be explicitly checked.

With the intuitive image of soft $2 \to 2$ processes being a part of (†), it might be tempting to use (2.42) to deduce that, similar to the case of small angle $2 \to 2$ scatterings, condition (2.39) is met for the duration of $2 \to 3$ collinear splitting processes. This conclusion would however be *incorrect*. A closer look at (†) reveals that the propagator connecting the two bits in (†), depicted in blue in the exemplary process of Fig. 2.5 (b), is almost on–shell, calling for extra attention in the estimation of the quantum mechanical duration of the process. The duration of the near–collinear process of Fig. 2.5 is controlled by the small virtuality δE of the almost on–shell propagator as

$$\Delta\tau_{\text{split}}^{\text{duration}} \sim 1/\delta E \sim p/m_{\text{th}}^2 \sim p/g^2T^2 \sim \frac{p}{T} \cdot \Delta\tau^{\text{mean free time}} \gtrsim \Delta\tau^{\text{mean free time}} , \tag{2.49}$$

failing condition (2.39). Physically, the proximity of the intermediate state, depicted in blue in Fig. 2.5 (b), to the mass–shell allows it to *live* for a long time as an intermediate state; as the *lifetime* of this state is larger than the mean free time in the plasma, the particle gets to interact repeatedly and "coherently" with particles from the thermal medium before its demise. As a result, the soft processes (2.40) and the near–collinear processes (†), whose importance to the momentum diffusion process was established before, cannot be treated as independent in the Boltzmann equation (2.48).

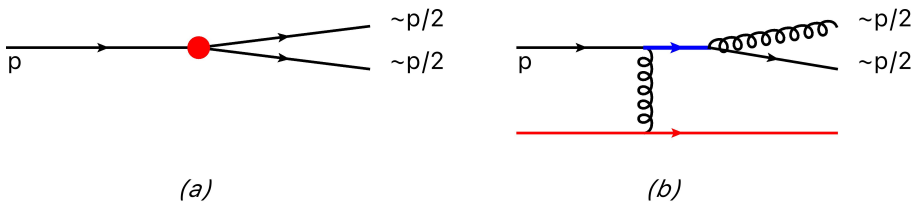

Figure 2.5: (a) Schematic of *collinear splitting* process reducing the energy carried by a an energetic particle of momentum p; the solid lines represent the flow of particles of a given momentum, and do not imply a spin. (b) Typical gauge mediated $2 \to 3$ splitting via a *bremsstrahlung* process in the case of a color charged quark, allowing for a redistribution of momentum $\mathbf{p}$. For soft gauge mediated interactions of the incoming quark with thermal bath particles (red), the mediator (blue) is slightly off–shell before splitting into two highly collinear outgoing particles, resulting in a long formation time.

In order to be able to continue using the kinetic theory and the Boltzmann equation, we must therefore coherently sum up all $2 \to 3$ splitting processes in association with different number of soft Coulomb scatterings. Schematically, one therefore needs to replace the splitting contribution in eq. 2.48 with the series

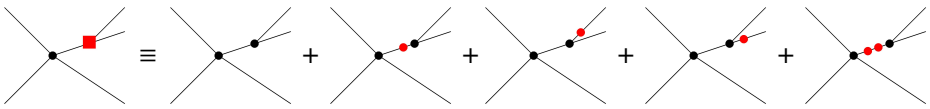

(2.50)

where we have used the red square to denote an *effective* splitting process, and where as in Fig. 2.4 red blobs are used to denote soft $2 \to 2$ interactions with particles from the background thermal bath. The rate of the "effective" splitting process, captures the effect of the interference among the individual diagrams on the RHS where applicable. Calculating the resulting effective splitting rate is a subject we will turn to in Chapters 3 and 4; as we will see, the interference will result in an effective suppression of the splitting rate in an effect known as the Landau–Pomeranchuk–Migdal (LPM) effect.

Let us for the moment assume we have summed all the contributing diagrams on the RHS of (2.50) to find the effective process on the RHS. We will then be able to use the effective LPM–suppressed rate to treat the "effective kinetic theory" of the gauge theory, by writing down the Boltzmann equation of the form

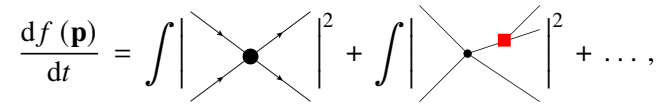

(2.51)

Equation 2.51 is consistent with the criterion (2.39) up to the order of $2 \to 3$ processes; we may, therefore, use the effective kinetic theory to study the evolution of the kinetic function f.

Before closing this section, it is worth noting once again, that although we used the sample problem of viscous behaviour of particles of energy $p \sim T$ to introduce an example of a failing kinetic treatment and the need for a resummmed effective kinetic treatment with the inclusion of coherent effects, very similar arguments will hold also for the case of interest in the remainder of this thesis; namely, for the case of highly energetic OoE particles with $p \gg T$. This can be in fact seen by comparing the timescales in equations 2.41 and 2.49 and and their dependence on the momentum scale p.

2.6 Summary and recap

Let us conclude this section by a brief summary; in Chapter 2, we started in Section 2.1 by presenting the FLRW metric of the homogeneous and isotropic expanding universe, and moved to the dynamics of the expansion governed by the Friedmann equation in Section 2.2. We then turned to the plasma filling up the universe at early times, and studied the composition of a thermal plasma of particles in Section 2.3. Next, we discussed how the presence of the thermal plasma affects the properties and interactions of particles in the early universe. In particular, we introduced the basic ideas in thermal field theory in Section 2.4 and discussed how these can be used to calculate modifications to *static* quantities, where we focused on the generation of an effective *thermal mass* for particles traversing a thermal background plasma. Going beyond static quantities, we looked at time–dependent phenomena occurring in the presence of a thermal background plasma; we introduced the kinetic theory description and how it can be used to study the temporal evolution of a kinetic function, and saw that the kinetic theory prescription is potentially invalidated for the treatment of certain problems.

The problem arises when the quantum duration of the individual processes exceeds the mean free time of the particle propagating through the background medium requiring the inclusion of potential interference among multiple processes. As a more concrete example of this break–down phenomenon we briefly looked at the process of momentum diffusion and the study of viscosity in the thermal medium. In this particular example, near–collinear splittings of particles in the plasma play a crucial role; the collinearity of the outgoing particles correspond to a "long–lived" almost–on–shell intermediate propagator. The long life–time exceeds the mean free time, calling for a coherent treatment of multiple scatterings of the OoE particle with the background plasma.

Finally, with coherent effects at the root of the breakdown of the kinetic treatment, we posited that the validity of the kinetic theory could be restored by a proper resummation of coherently interfering processes. In the presented example, the resummation leads to an effective LPM suppression in the rate of the $2 \to 3$ splitting process. One may therefore use the LPM–suppressed rates to formulate an effective kinetic theory for the OoE phenomena in the plasma. In the following chapters, we will use the LPM–suppressed rate of near–collinear splittings to write down and solve the effective Boltzmann equation governing the process of energy loss and thermalization of a highly energetic hard particle in the early universe plasma.

CHAPTER 3

Particle thermlization in the early universe: pure gauge boson treatment

In Chapter 1, we introduced the generalities of a matter–domination (MD) era and how it could affect the history of cosmological processes. In particular, we mentioned in Section 1.3 that many inflationary and non–inflationary modifications [20, 25, 53] to the standard radiation–dominated (RD) history of the universe involve a component with a matter equation of state (1.3) corresponding to $\omega = 0$. Under generic circumstances and according to eq. 2.14, this long–lived matter component dominates the energy density of the universe before decaying to *reheat* the radiation bath. A MD phase at the end of inflation, or a late matter-dominated era due to some long-lived massive particle, are viable [29, 54], well-motivated, and extensively studied realizations of such cosmological histories. In the remainder of this thesis, we will often use this context to present our analysis and results. As we will see in more detail, however, the core issues will not depend on the dominance of the matter component.

A MD era, typically ends with the massive matter particles dumping their energy density into the radiation bath via decays into lighter particles; the energy distribution and particle composition of the decay products will depend on the mass and couplings of the decaying particle and be starkly different from the equilibrium distributions of equations 2.16 and 2.19. Generically, the out of equilibrium (OoE) matter components arising in BSM scenarios will be much heavier than the light visible sector particles, so that their decay products will be highly relativistic at production. In particular, sticking to our choice of the unbroken phase of the SM, discussed in Section 2.3, the visible sector particles resulting from the decay of the matter component are massless up to the effective thermal mass (2.35) introduced in Section 2.4. Subsequent to their production, these relativistic particles will therefore need to attain kinetic and chemical equilibrium in the process of *thermalization*.

As outlined in Section 1.4, the presence of the matter component and its decay can affect cosmology beyond modifications of the expansion rate. Entropy production, (meta–)stable particle production from decays of the matter component, and changes in the composition of thermal bath particles resulting from interactions with energetic decay products are examples of such effects (see [20] and the references therein); another particularly important effect discussed in Section 1.4 is the production of (meta–)stable particles from interactions of decay products. Studying the latter two classes of phenomena via a Boltzmann equation (2.37) requires knowledge of the OoE distribution function f of decay products. To get a complete picture of how departures from a standard RD cosmological history

affect cosmological observable and processes, it is essential to study the evolution of matter decay products in the process of thermalization.

In this section, we will use the notions introduced in Chapter 2 to study the process of thermalization and the resulting distribution of OoE particles in a somewhat simplified setup. Our starting point will be to study the particle processes playing the dominant role in the kinetic theory of Section 2.5. We will argue that the dominant role in this process is reserved for the near–collinear splitting processes of the form introduced in Fig. 2.5. In order to simplify the problem, we will limit our attention to a setup with just one such allowed splitting process; within the SM, this choice corresponds to studying a non–abelian gauge theory of "pure gauge bosons" (no fermions). We will see that the resulting kinetic theory fails the decoherence condition (2.39), therefore calling for the inclusion of coherence effects. We will introduce the physics of the Landau–Pomeranchuk–Migdal (LPM) suppression effect, and further use this resummation scheme to write down a valid *effective* kinetic theory of the form introduced in eq. 2.51. We will then bring the resulting Boltzmann equation into a convenient dimensionless form and present its analytical and numerical solutions. Finally, we will conclude this chapter with an example of how the resulting distribution of OoE particles affects cosmological processes by studying the resulting non–thermal contributions to the DM abundance in certain scenarios; in order to emphasize the importance of coherence effects and the precision of numerical treatment, we will compare analytical and numerical results with those obtained without taking the LPM into account. This chapter is largely based on [45].

3.1 Formulation of the problem

3.1.1 The Basic Setup

In order to discuss the kinetic theory of energy loss in the early universe plasma more specifically, we will first present a typical setup of a non–standard cosmological history involving a decaying matter component. We will focus on the decay of a heavy, relatively long-lived "progenitor" particle with mass M into two ultra-relativistic particles whose masses are significantly smaller than the temperature of the thermal plasma; "long–lived" here means that the progenitors are not in thermal equilibrium when they decay. For the assumed two–body decay, the injection spectrum is just a delta–function at $M/2$. As we will see later in Section 3.2, the linearity of the problem allows us to write the final spectrum of non–thermal particles for any more complicated decay, or indeed for any other non-thermal injection spectrum, as a convolution of our result with the assumed initial spectrum. Finally, as we briefly motivated in Section 2.5, gauge–mediated soft scattering processes serve a special role in the physics of the particle plasma. We, therefore, assume that both the thermal bath and the injected particles take part in gauge interactions; this is true in particular for all SM particles in the unbroken phase.

Let us begin by presenting a general formulation of the relevant cosmological history. We introduce a matter component of heavy particles of mass M, and number density $n_{\rm M}$, decaying with a width $\Gamma_{\rm M}$[1] into ultra-relativistic particles of initial energy $E_{\rm i} = M/2$ and an equation of state of radiation. The evolution equations (2.14) for the radiation and matter energy densities will now need to be modified

[1] We are treating the width to be a free parameter in the model. Possible thermal effects on the decay of a scalar field have been discussed in [55–58].

to account for the conversion of matter into radiation via particle decays. The resulting equations read

$$\frac{\mathrm{d}\rho_{\mathrm{M}}}{\mathrm{d}t} + 3H\rho_{\mathrm{M}} = -\Gamma_{\mathrm{M}}\,\rho_{\mathrm{M}}\,; \tag{3.1a}$$

$$\frac{\mathrm{d}\rho_{\mathrm{R}}}{\mathrm{d}t} + 4H\rho_{\mathrm{R}} = +\Gamma_{\mathrm{M}}\,\rho_{\mathrm{M}}\,. \tag{3.1b}$$

Here H is the Hubble expansion rate (2.12) and t denotes the cosmological time of FLRW cosmology. ρ_{M} and ρ_{R} denote the energy density of the unstable matter component and the radiation component respectively. Previously, in Section 2.3, we stated that in the absence of chemical potentials the composition of the thermal radiation component is fully fixed by the temperature parameter T. In the presence of a decaying matter component in (3.1), however, the radiation component ρ_{R} is to be understood as consisting of the thermal radiation bath $\rho_{\mathrm{R}}^{\mathrm{th}}$, given by eq. 2.21, and the (typically sub-dominant) non-thermal radiation component resulting from the decays of progenitor particles prior to thermalization. Note that both components are redshifted in the same manner so that equation 3.1b is unable to distinguish between the two. Note also that eq. 3.1b is strictly correct only if the effective number of degrees of freedom (2.22) remains constant during the epoch of energy injection. In some cases this approximation can lead to significant errors in the thermal production rate of relics [59], it however suffices in this thesis, where we are mostly interested in the non–thermal radiation component, and where we consider the visible sector to consist of the unbroken SM particle spectrum.

3.1.2 The Thermalization of Energetic Particles

The process of thermalization in a (quasi-)static background has been extensively studied in the literature [39, 41, 42, 52, 60]. For a convenient formulation based on the parameters of the extended cosmological history, we will mainly rely on the results from [41, 42] to describe the energy loss of HE particles (with energy $p \gg T$) through interactions with the much more abundant particles in the thermal plasma. Throughout this thesis, we implicitly assume that such a radiation bath indeed exists. The initial thermalization process in the absence of a preexisting thermal bath, such as that occurring just after the end of inflation, has also been studied in the literature [39, 52]. The details of this initial thermalization affect the maximum temperature of the universe and therefore the cosmological history, but are not directly relevant for this thesis.

It has long been noted that in the presence of particles of energy $p \gg T$, a special role is reserved for particle interactions mediated by a massless gauge boson in the *t–channel* [61] so we will continue to focus on gauge mediated t–channel processes as in Section 2.5[2]. A key feature of the process of *energy loss* of energetic particles is that despite being the leading order process in coupling constants, $2 \to 2$ scattering processes do *not* play the dominant role; this is different from the case of momentum diffusion used in Section 2.5 to introduce the effective kinetic theory approach, and where small and large angle scatterings, as well as near–collinear splittings gave similar contributions to the diffusion process. The reason is that the $2 \to 2$ processes either suffer from a suppressed rate or offer a small momentum transfer between the high-energy states and the thermal bath. Let us look at this argument in more detail while limiting our attention to a pure–gauge theory, defined above in the introduction to Chapter 3. Consider a pure theory of non–abelian gauge bosons, e.g., the gluons of the quantum

[2] $u-$channel diagrams should be included in processes with identical particles in the initial state. See e.g. table 2 in [49] for a list of contributing matrix elements, including numerical group factors, in a gauge-mediated $2 \to 2$ process.

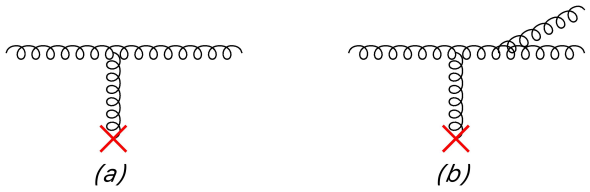

Figure 3.1: (a) The $2 \to 2$ pure non–abelian gauge scattering with a t–channel gauge boson exchange. (b) A $2 \to 3$ contribution; collinear splitting of the non–abelian gauge boson in association with a soft $2 \to 2$ scattering. The SM gluon has been used in both cases to exemplify the processes. The red crosses represent the presence and interaction with a further gauge boson of energy $p \sim T$ from the background thermal bath of temperature T.

chromodynamics (QCD). Hard gauge bosons of energy $p \gg T$ undergo various scattering processes with particles from the thermal bath. The two most dominant scattering processes are shown in Fig. 3.1, where crosses denote a coupling to a particle of energy $p \sim T$ from the thermal bath. The $2 \to 2$ processes will have a cross section in the range given by $\sigma^{\text{soft}}_{\text{Coulomb}}$ and $\sigma^{\text{hard}}_{\text{Coulomb}}$, given in eq. 2.40 and eq. 2.43 respectively. The higher order nearly collinear $2 \to 3$ process would similarly have a cross section σ_{split} given in eq. †, barring coherent effects. In the study of the energy loss process for hard OoE particles, we are predominantly interested in the rate of energy loss resulting from scatterings of hard particles on target particles from the thermal bath with a number density $n_{\text{target}} \sim T^3$ given by (2.20). The rate of energy loss will parametrically be of the form

$$\mathrm{d}p/\mathrm{d}t \sim \sigma \cdot n_{\text{target}} \cdot \delta p, \tag{3.2}$$

where δp denotes the amplitude of the momentum exchanged or rather redistributed in the process corresponding to the cross section σ. For the hard, soft, Coulomb scattering, and a symmetric splitting process, such as that of Fig. 2.5, the energy loss rate (3.2) will be

$$\left(\frac{\mathrm{d}p}{\mathrm{d}t}\right)^{\text{hard}} \sim \sigma^{\text{hard}}_{\text{Coulomb}} \cdot n_{\text{target}} \cdot p \sim \alpha^2 T^3/p \tag{3.3a}$$

$$\left(\frac{\mathrm{d}p}{\mathrm{d}t}\right)^{\text{soft}} \sim \sigma^{\text{soft}}_{\text{Coulomb}} \cdot n_{\text{target}} \cdot m_{\text{th}} \sim \alpha^{3/2} T^2 \tag{3.3b}$$

$$\left(\frac{\mathrm{d}p}{\mathrm{d}t}\right)^{\text{split}}_{\dagger} \sim \sigma_{\text{split}} \cdot n_{\text{target}} \cdot p \sim \alpha^2 pT\,. \tag{3.3c}$$

where we have switched to using the "fine–structure" α parameter to encode the coupling strength g of the gauge theory corresponding to the interactions in Fig. 3.1, to keep our notation close to the relevant literature. Note also that the splitting rate in (3.3c) has been marked with † to imply the absence of coherent effects, as in (†). Let us next look more closely at the hierarchy of energy loss rates in eq. 3.3.

The leading order processes, i.e., Coulomb $2 \to 2$ processes can reduce the energy of the incoming particle significantly only if there is a large momentum exchange through the single propagator, which implies that the exchanged particle is far off-shell, leading to a power-suppressed scattering amplitude as seen in (3.3a). On the other hand, the infrared divergence corresponding to the forward scattering limit of the hard OoE particles off the thermal bath provides a significantly larger interaction rate. The cutoff is systematically provided by the screening effects and given by thermal field theory to be the

thermal mass (2.35). As seen in eq. 3.3b the price to pay for this sizeable cross section is, however, the small momentum transfer leading to a relatively small rate of energy loss.

A second observation in eq. 3.3 is that the contribution from soft Coulomb processes dominates over the less frequent hard $2 \to 2$ scatterings. Note that this is not in contradiction with our previous statement in Section 2.5 regarding the competitive contribution of the soft and hard processes in the momentum diffusion process of Fig. 2.4. The diffusion process of Section 2.5 scales as the square root of the number of scattering events (see Fig. 2.4), whereas in eq. 3.3 the energy loss rate scales linearly with the number of scattering events. It is important to keep in mind that the soft $2 \to 2$ processes are also responsible for setting the mean free time (2.41) of particles propagating the thermal plasma and will therefore play a crucial role in the kinetic theory describing the process of energy loss. In the study of the energy loss process, we, therefore, focus on soft Coulomb $2 \to 2$ processes [3] .

For future use, and to look at these processes in more detail, let us use a slightly modified notation to write the rate of soft *elastic* processes as

$$\Gamma_{\text{el}} \sim \tilde{g}_* \alpha T \,, \tag{3.4}$$

where the factor of $\tilde{g}_*$ is introduced to account for the number of degrees of freedom in the thermal plasma that couple to the given interaction of strength α, as well as order one group factors and factors of π resulting from a detailed calculation (see e.g. Chapter 4 and footnote 2 on Page 35). Equivalently, we could say soft $2 \to 2$ processes occur on intervals of $\delta t_{\text{el}} = \Gamma_{\text{el}}^{-1}$, while allowing for a momentum transfer of the order of the effective thermal mass (2.35)

$$\delta p_{\text{el}} \sim m_{\text{th}}, \tag{3.5}$$

which we may now write as

$$m_{\text{th}} \sim \alpha^{1/2} T. \tag{3.6}$$

Going back to eq. 3.3, the large energy loss rate of collinear splitting processes in (3.3c) implies that the higher order near–collinear splitting processes of the form in Fig. 2.5 provide a by–far more efficient means of energy loss for hard OoE particles with $p \gg T$. The reason is that despite requiring an additional vertex insertion, nearly collinear splitting processes can lead to a large energy loss of order $\delta p \sim p$ without relying on large virtualities in any propagator. As first noted in [61], such splitting processes therefore dominate the rate of energy loss [41, 52]. This energy loss will be significant only if the daughter particle produced in the splitting has energies well above T. It is important to note that the splitting process also increases the number of non-thermal particles, which is crucial for thermalization both with and without a preexisting thermal bath [52, 62].

As a last remark, we should point out that the included MD era and the decays of the matter component respect the isotropy and homogeneity of the large scale universe introduced in Section 2.1. The spatial distribution of the momenta of the decay products is statistically isotropic already at the production stage; this means that thermalization can proceed through near-collinear splitting processes. In this regard, the problem at hand is different from that of thermalization of final state products in an ultra relativistic heavy ion collision, where initially a high degree of anisotropy could be present [4].

[3] As we will see in Section 3.1.3, the transverse momentum diffusion does play a role in setting the energy loss process rate by setting the LPM suppression rate; as such, hard $2 \to 2$ processes indirectly enter the leading energy loss rate, leading to the so called Coulomb logarithm enhancement factors. See also the footnote on Page 29 and the discussion in Section 4.3.

[4] For a discussion of the role of anisotropy see e.g. [34, 63].

3.1.3 Coherent interference and LPM resummation

In Section 3.1.2 we established the hierarchy of contributions to the rate of energy loss for a hard OoE particle, i.e., with $p \gg T$. Naively, our observations suggest that so long as we are interested in the energy loss process, the dominant term in the corresponding Boltzmann equation (2.48) will be given by $2 \to 3$ splitting processes. A cascade of such reactions will therefore eventually turn an initially injected particle with energy $p_{\rm i} \sim M/2$ into $O\left(p_{\rm i}/T\right)$ particles, each with energy $p \sim T$, which eventually become part of the thermal background described by eq. 2.20. Although $2 \to 3$ splitting processes can also occur in association with hard reactions, they do not require large momentum exchange between the energetic particle and the thermal bath for a sizeable energy loss. The differential cross section will then greatly prefer small momentum exchange, so that momentum redistribution proceeds chiefly via the splitting of the energetic *parent* particle into the two nearly collinear *daughter* particles with lower energies, denoted by d_1 , d_2:

$$p_{\rm i} = p_{\rm d1} + p_{\rm d2} \,. \tag{3.7}$$

In this chapter, where we are limiting our attention to a model of OoE particles consisting of merely a single species of non–abelian gauge bosons, we use the term "daughter particle" of energy $p_{\rm d}$ to refer predominantly to the particle with the smaller energy:

$$p_{\rm d} \equiv \min(p_{\rm d1}, p_{\rm d2}) = \min(p_{\rm d1}, p_{\rm i} - p_{\rm d1}) \,. \tag{3.8}$$

Let us take a closer look at the rate of the $2 \to 3$ process. As mentioned in Section 3.1.2, the zero-temperature cross section for the splitting reaction in vacuum suffers from infrared and collinear divergences. As in the case of $2 \to 2$ processes, the thermal bath regularizes infrared divergences via the thermal mass (3.6). The resulting near–collinear $2 \to 3$ splitting (3.7) can in principle proceed for a range of daughter momenta (3.8) in the interval $0 < p_{\rm d} \leq p_{\rm i}/2$; we may however use physical arguments to slightly modify the latter interval. Note that the daughter particles too will pick up an effective mass due to the presence of the background plasma. Moreover, we are not interested in the emission of daughter particles with energy $p_{\rm d} \leq \kappa T$, where κ is a constant of $O\left(1\right)$ introduced to parameterize a hard IR cutoff [5] . The latter choice is motivated by the observation that energetic particles traversing a thermal bath frequently emit and absorb such quanta; as we saw in Section 2.5, a large number of soft $2 \to 2$ processes can occur on the timescale corresponding to a near–collinear splitting.

Using the above arguments, we may limit our attention to splittings (3.7) with the daughter momentum in the range $\kappa T < p_{\rm d} \leq p_{\rm i}/2$. In line with (3.3c), the collinear emission of a gauge boson results in a differential cross section of the form

$$\frac{{\rm d}\Gamma^{\rm split}}{{\rm d}\ln p_{\rm d}} \sim \alpha\Gamma_{\rm el}, \tag{3.9}$$

suppressed by another factor of α compared to the soft elastic processes (3.4). Before incorporating the rate (3.9) to write down and solve the corresponding Boltzmann equation, however, it is imperative to consider the question of validity of the kinetic theory approach.

[5] The term *hard* here refers to the step–function form of the cut-off and is not to be conflated with the our terminology of hard particles with $p \gg T$.

In Section 2.5 we saw that the inclusion of near–collinear processes with a momentum transfer of order $\delta p_{\rm el}$ through the intermediate propagators resulted in a violation of the decoherence condition (2.39). Physically, this violation followed from near–collinear splittings occurring on timescales longer than that between consecutive soft elastic scattering events; in the language of Chapter 3, a parent particle will undergo many elastic scatterings (3.4) during its splitting process (3.9). We concluded Section 2.5 by stating that one needs to coherently resum the effect of the many soft elastic processes to get an effective rate for splitting processes in an effective kinetic theory.

For the study of energy loss via near–collinear splitting processes, the effective kinetic theory can be written down by the inclusion of the Landau–Pomeranchuk–Migdal (LPM) effect [35, 36, 49, 64–66]. The LPM effect describes the suppression of collinear emissions of particles in the presence of a background medium; the suppression is due to destructive interference between successive emissions associated with scattering reactions on the background medium during the "long" *formation time* of the emitted radiation.

As outlined in eq. 2.50, the effective theory is formally achieved by resumming a series of processes in thermal field theory [49]. Equivalently, one may use more intuitive physics arguments to derive the effective LPM–suppressed splitting rate. Following [39, 41], let us adopt the latter approach to study the suppression by focusing on the propagation of a single ultra-relativistic OoE state in the thermal medium. Without loss of generality, the unperturbed trajectory of this particle can be chosen to lie along the z axis and the time elapsed traversing the thermal bath in its rest frame as δt, so that the corresponding coordinates read

$$x^\mu = (\delta t, \delta t\, \hat{e}_z)\,. \tag{3.10}$$

We are interested in the emission of a daughter particle with momentum vector $\mathbf{k}$ corresponding to an energy $p_{\rm d}$ for the daughter particle. With the kinematics leading to eq. 3.9, this emission will be highly collinear, with the dominant component $k_\parallel \simeq p_{\rm d}$ and a small transverse momentum $k_\perp$, so that the process is not suppressed by a large momentum exchange in the intermediate state propagator. The emitted particle can then be assigned a four–momentum

$$k^\mu = (p_{\rm d},\, k\, \hat{e}_z + \theta k\, \hat{e}_\perp)\,. \tag{3.11}$$

Here θ is the emission angle, such that $\theta k = |k_\perp|$, and $p_{\rm d} \approx k(1+\theta^2/2)$. Note that whereas $p_{\rm d}$ is basically fixed by the original splitting process of interest, $k_\perp$ and so θ vary while the daughter particle traverses the thermal plasma, and should be considered to be time–dependent; as we will see shortly, the evolution of θ is closely related to our analysis of momentum diffusion in Section 2.5 and eq. 2.47.

Any destructive interference resulting from the near-collinear propagation of the parent and daughter particles in the thermal bath relies on the coherence of the parent–daughter system. Crudely, one may say that the coherence, and so the interference, persists so long as the invariant propagation phase, $\delta\phi = k\cdot x \approx 1/2\, p_{\rm d}\, \delta t\, \theta^2 \lesssim 1$, i.e. for a time

$$\delta t_{\rm coh} \simeq 1/(p_{\rm d}\,\theta^2) = p_{\rm d}/k_\perp^2\,. \tag{3.12}$$

Note that the coherence time (3.12) would coincide with the time–scale (2.49) of the splitting process, if one were to consider only a single soft elastic scattering of the splitting OoE particle off the background, with a non–dynamic $k_\perp \sim m_{\rm th}$. As shown in eq. 2.49, however, the hierarchy of timescales allows for a large number of elastic scatterings in the course of a single splitting processes, resulting in a time–dependent $k_\perp$. Therefore, the evolution of $k_\perp$ sets the timescale $\delta t_{\rm coh}$ for the coherence of the

parent–daughter system and thus for the LPM suppression of the emission process.

The evolution of $k_\perp$ in the thermal medium results from numerous individual elastic kicks by thermal bath particles. Thermal kicks of typical size δk_{el} [6] given by eq. 3.5 will occur isotropically with a rate Γ_{el}, given by eq. 3.4, resulting in $\mathbf{k}_\perp$ performing a random walk in the $x-y$ plane. The random walk should be understood as resulting from the random nature of individual elastic scatterings of the daughter particle off the background thermal bath particles. The expectation value for $k_\perp$ will then grow as the square root of the number N_s of random walk steps. For an initially collinear daughter particle one has

$$\left\langle k_\perp \right\rangle (\delta t) \simeq N_s^{1/2}\, \delta k_\perp \simeq (\delta t/\delta t_{el})^{1/2}\, \delta k_{el} \simeq \delta t^{1/2} \Gamma_{el}^{1/2} \delta k_{el} \simeq \left(\tilde{g}_* \delta t\right)^{1/2} \alpha T^{3/2}\,. \tag{3.13}$$

Combining with eq. 3.12 yields

$$\delta t_{coh} \simeq \tilde{g}_*^{-1/2} \alpha^{-1} T^{-3/2} p_d^{1/2}\,, \tag{3.14}$$

as the key quantity controlling the LPM suppression; the collective effect of N_s elastic scatterings results in the daughter particle being kicked out of equilibrium after a time given by (3.14).

An OoE particle traversing the thermal background plasma repeatedly undergoes soft Coulomb scatterings with thermal particles of number density n_{target} (2.20) at times separated by a time Γ_{el}^{-1}. In the absence of coherence effects, each such elastic scattering would result in a near–collinear splitting with a probability α, resulting in a rate (3.9) for $2 \to 3$ splittings. Coherence effects, however, prohibit such splittings for a time δt_{coh}, given by eq. 3.14. From the perspective of the hard OoE particle, coherence effects result in a reduction of the number density n_{target} of background particles by a factor

$$R_{LPM}(p_d) \simeq \delta t_{coh}^{-1} \Gamma_{el}^{-1} \simeq \left(\frac{T}{\tilde{g}_* p_d}\right)^{1/2}\,, \tag{3.15}$$

suppressing collinear splittings rate (3.9) by a factor $R_{LPM}(p_d)$. The resulting LPM–suppressed splitting rate is thus

$$\frac{\mathrm{d}\Gamma_{LPM}^{split}}{\mathrm{d}p_d} \simeq \frac{\mathrm{d}\Gamma^{split}}{\mathrm{d}p_d} R_{LPM}(p_d) \simeq \alpha^2 \left(\frac{T}{p_d}\right)^{3/2} \sqrt{\tilde{g}_*}\,. \tag{3.16}$$

The LPM–suppressed splitting rate (3.16) therefore resums the series of contributing diagrams to yield the effective rate of splitting (2.50) and allows us to write down an *effective kinetic theory* for the process of energy loss.

A critical question would then be whether a suppressed rate $2 \to 3$ splittings would affect the hierarchy of rates in eq. 3.3; i.e. whether splitting processes continue to provide the dominant contribution to the energy loss rate of an OoE hard particle. The total energy loss rate for a parent particle with energy p_p can be derived from eq. 3.16 as an integral over all possible splittings with different daughter energies p_d.[7]

[6] In Section 2.5 and Fig. 2.4, we discussed the comparable contribution of soft and hard elastic Coulomb processes to the momentum diffusion of hard momenta. One may therefore ask if one should add up the effects of all elastic processes in the evolution of $k_\perp$; the answer is positive and as we will see in Chapter 4, allowing for the combined effect of progressively harder elastic processes results in a logarithmic enhancement in the evolution rate for $k_\perp$ and consequently the LPM suppression effect.

[7] Note that we are treating the coupling α as a constant, independent of the energy of the daughter particles. This should be

$$\left(\frac{\mathrm{d}p_{\mathrm{p}}}{\mathrm{d}t}\right)^{\mathrm{split}}_{\mathrm{LPM}} = \int_T^{p_{\mathrm{p}}/2} dp_{\mathrm{d}} p_{\mathrm{d}} \frac{\mathrm{d}\Gamma^{\mathrm{split}}_{\mathrm{LPM}}}{\mathrm{d}p_{\mathrm{d}}} \simeq 2\alpha^2 T^{3/2}\sqrt{p_{\mathrm{p}}\tilde{g}_*}\,. \tag{3.17}$$

This new LPM–suppressed rate replaces our previous naive estimate in (3.3c); comparing to the energy loss rate provided by $2 \to 2$ processes in (3.3a) and (3.3b) clearly shows that near–collinear splitting processes still have the upper hand, despite suppression due to coherence effects.

To conclude this section, and with the form of our key results at hand, we may go back to check the validity of some of the assumptions we have so far made. First, with the form of the LPM–suppressed splitting rate (3.16) at hand we may now motivate the choice of p_{d} in eq. 3.8. In a splitting process, the destructive interference ends once a daughter state picks up a sufficiently large transverse momentum via interactions with the thermal bath. This is always first realized for the softer of the two daughter states in eq. 3.7, whose energy p_{d} thus determines the LPM suppression factor. Moreover, equation 3.12 shows that there is no LPM suppression of non-collinear splitting processes if the initial $k_\perp$ is so large that $\delta t_{\mathrm{coh}} < \delta t_{\mathrm{el}}$, i.e. for $k_\perp^2 > \alpha\tilde{g}_* p_{\mathrm{d}} T$. However, the rate for such processes is suppressed by a factor $1/p_{\mathrm{d}}$. Since R_{LPM} only scales like $1/\sqrt{p_{\mathrm{d}}}$, nearly collinear splitting reactions still dominate.

Next, we may circle back to validate our treatment of the temperature parameter T as being constant throughout the thermalization process; this assumption is for example central to our formulation of the Boltzmann equation (2.51) in Section 2.5; note the LHS contains time–derivatives of the kinetic function while we have parameterised the RHS in terms of a single time–independent temperature parameter T; more explicitly, we disregarded the momentum redshift due to the expansion (2.9). This should be a good approximation if thermalization occurs on a timescale much shorter than the Hubble time, setting the rate of change of T. The validity of this assumption depends on thermalization processes occurring much faster than the Hubble time $t_{\mathrm{H}} \equiv H^{-1}$. With (3.17) as the dominant process, a particle with initial energy $p_{\mathrm{i}} \gg T$ can be thought to thermalize in a time

$$t_{\mathrm{therm}} \simeq \frac{\sqrt{p_{\mathrm{i}}}}{2\alpha^2 T^{3/2}\sqrt{\tilde{g}_*}} = \Gamma^{\mathrm{therm}\,-1}_{\mathrm{LPM}}\left(p_{\mathrm{i}}\right). \tag{3.18}$$

To compare against the expansion rate, we write the total energy density $\rho_{\mathrm{tot}} = \rho_{\mathrm{R}} + \rho_{\mathrm{M}} \equiv r\,\rho_{\mathrm{R}}$. The (time-dependent) quantity r describes the contribution of the heavy decaying particles, so that for a matter-dominated era we expect $r \geq 2$. Using eq. 3.18 with $p_{\mathrm{i}} \simeq M/2$ (the mass of the decaying particle), we have

$$H t_{\mathrm{therm}} \simeq \frac{\pi\sqrt{MT/20}}{6\alpha^2 M_{\mathrm{Pl}}}\sqrt{r g_*/\tilde{g}_*} \sim 5\cdot 10^{-8}\frac{\sqrt{MT}}{10^{10}\ \mathrm{GeV}}\left(\frac{0.1}{\alpha}\right)^2\sqrt{r}\,. \tag{3.19}$$

Evidently, the thermalization time will be many orders of magnitude smaller than the Hubble time, unless M is close to the reduced Planck mass, $M_{\mathrm{Pl}} = 2.4\cdot 10^{18}$ GeV, or ρ_{M} exceeds ρ_{R} by many orders of magnitude. However, even if this is the case initially, $H t_{\mathrm{therm}} \ll 1$ will hold for the majority of energy injection Hubble eras. As long as $r \gg 2$[8], ρ_{R} will only decrease like t^{-1}, while ρ_{M} decreases

reasonable since, as we saw above, a large energy loss in a splitting process is possible without any large momentum transfer. The argument of the relevant beta functions should therefore be of order T, and not p_{d}; further considerations can be taken into account if one includes subleading large angel scatterings (see footnote 6). We further ignore a logarithmic enhancement, namely the remnant of the collinear enhancement of the splitting process in vacuum.

[8] In this case, the decay products produced per Hubble time dominate over the properly redshifted thermal background

like t^{-2}, so that $\sqrt{Tr} \propto t^{-5/8}$. Note also that the density of relics produced in the early stage of the epoch of energy injection gets diluted by entropy production if initially $r \gg 1$; moreover, most of the massive particles will decay near the end of that epoch (see Section 3.4). Therefore the non-thermal production of relics, either directly from the decay of the massive particles or in the collisions of their decay products prior to thermalization, dominantly occurs in the later stages of energy injection; here eq. 3.19 clearly implies $Ht_{\rm therm} \ll 1$ so that the formulation (2.51) of the Boltzmann equation is permitted.

3.2 The thermalization cascade and the Boltzmann equation

In Section 3.1, we established the role of near–collinear splitting processes in the process of energy loss of a single species of non–abelian gauge bosons and used physical arguments to calculate the LPM–suppressed splitting rate required for the effective kinetic theory treatment. We now wish to write down the corresponding Boltzmann equation governing the spectrum of the hard OoE particles. Let us start by taking a closer look at the role of various splittings (3.7) in the process of energy loss.

The total energy loss rate in eq. 3.17 is dominated by contributions from near the upper limit of integration corresponding to nearly symmetric splitting where $p_{\rm d} \sim p_{\rm i}/2$; that is in fact why we have used symmetric splittings to estimate the energy loss rate induced by near collinear splittings in eq. 3.3c. On the other hand, it is clear from (3.16) that the process rate favors softer daughter particles, so for every symmetric splitting in the thermal bath there will be numerous asymmetric splittings producing one daughter particle with $T < p_{\rm d} \ll p_{\rm i}$, while the second daughter has energy near $p_{\rm i}$. It is important to note that many of the daughter particles still have energy $p_{\rm d} \gg T$, which means that they undergo further splittings. An energetic particle thus triggers a cascade of splittings, generating a non-thermal spectrum of daughter particles. Let us denote this spectrum by

$$\tilde{n}(p) \equiv \frac{{\rm d}n(p)}{{\rm d}p} \quad \text{such that} \quad \int_T^M \tilde{n}(p)dp = n, \tag{3.20}$$

so that n denotes the physical number density of all OoE particles in the plasma. The distinction between the dominant energy loss process and the dominant rate process in the thermalization cascade has, in some cases, been neglected in the literature; as a result, the spectrum of the high energetic states has been assumed to result from the dominant symmetric splitting, yielding a spectrum of $n \propto p^{-1}$. Similarly, the presence of the natural cut–off at $O(T)$ for the cascade of splitting processes has been in some cases ignored; this is partly due to the fact that even in the absence of an IR cutoff, the rate of energy loss (3.17) will be finite. The same is however not true for the spectrum in (3.20). Our objective is to find a more accurate estimate of the non-thermal spectrum $\tilde{n}(p)$ resulting from LPM-suppressed gauge interactions of energetic particles injected into a thermal plasma, including the thermal IR cutoff in the splitting process. In the following subsection, we will describe how to tackle this problem.

The spectrum $\tilde{n}(p)$ provides a convenient non–equilibrium parameterization of the kinetic function $f(p)$ as seen , e.g., in eq. 2.19. The success of standard BBN suggests that the period of injection of energetic decay products must have ended well before the onset of BBN [67], when the universe was

existing at the beginning of this Hubble time. The energy density of relativistic particles at any given time is nevertheless dominated by the thermal contribution.

still essentially isotropic. Moreover, we can safely assume that the energetic particles were injected isotropically; if these energetic particles originated from the decay of very massive matter particles, as in (3.1), this assumption can only be violated if these progenitors were polarized along the same direction, which seems highly implausible. Further, we argued in Section 3.1.3, that the efficiency of $2 \to 3$ process allows one to treat all splittings of the thermalization cascade as occurring within one Hubble era, and therefore as corresponding to a certain temperature T. The spectrum (3.20) should, therefore, be implicitly understood and sufficiently describable as $\tilde{n}\,(p, T)$ depending on the magnitude of the three momentum p as well as the temperature T.

3.2.1 The quasi–static Boltzmann equation

In Section 3.1, we introduced the expansion history of a universe involving a decaying matter component (3.1). We further established the LPM–suppressed rate (3.16), required for the formulation of the effective kinetic theory of the process of the energy loss. Finally, we introduced the phase space density parameter $\tilde{n}\,(p)$ (3.20) to describe the population of OoE particles as they are produced from the decays of the matter component (3.1a) and evolve to form a thermal radiation bath with $\rho_{\mathrm{R}} \propto T^4$ in (3.1b).

Let us start studying the evolution of the phase space distribution of OoE particles by looking at the generic Boltzmann equation for a homogenous isotropic distribution:

$$\frac{\partial}{\partial t}\tilde{n}(p,t) - 3Hp\frac{\partial}{\partial p}\tilde{n}(p,t) = +C_{\mathrm{inj}}(p,t) - C_{\mathrm{dep}}(p,t). \tag{3.21}$$

The LHS of eq. 3.21 contains the temporal variations of the phase space distribution function $\tilde{n}$, as well as the Hubble friction term capturing the effect of expansion on momenta. The "collision terms" on the RHS of this equation correspond to the loss and gain terms schematically introduced in (2.36) and capture the particle interactions affecting the phase space distribution $\tilde{n}$. The first of these terms, $C_{\mathrm{inj}}(p,t)$, represents the injection processes adding particles of momentum p; in our case, this includes the primary injection, which we assume to be due to the two-body decay of some massive particle resulting in a δ-function at $p = M/2$, as well as "feed-down" from particles with momentum $k > p$ through the thermalization splitting cascade. The second collision term, $C_{\mathrm{dep}}(p,t)$, represents the depletion processes removing particles of momentum p when they themselves initiate an energy loss cascade.

The generic form (3.21) can be further simplified using the arguments presented in Section 3.1.3 and the discussion ensuing eq. 3.19. We saw that, for most epochs of energy injection, the decay products thermalize on a timescale much less than a Hubble time. This leads to two further simplification of our Boltzmann equation. First, as advertised in Section 2.5, we can safely neglect the second term on the LHS of eq. 3.21, representing the Hubble expansion. Second, since the rate of change of the temperature is given by the Hubble time, we can also neglect the change of the temperature of the thermal bath over the time needed for any one cascade to develop and fade away. Of course, the temperature will likely change over the entire epoch of energy injection. However, we can safely assume that the phase space distribution of the non-thermal component is quasi-static, i.e. a time dependence should only exist via the time temperature function $T(t)$ as well as the time dependence of the density of decaying particles $n_{\mathrm{M}}(t)$. The phase space density distribution function in eq. 3.21 can therefore be written as $\tilde{n}\,(p, T)$ and be thought of as representing the distribution of OoE particles in a certain Hubble era.

A quasi-static solution, i.e. steady state solution within each Hubble time, exists only if the injection and depletion terms cancel in the Boltzmann equation 3.21, that is

$$C_{\rm inj}(p) = C_{\rm dep}(p)\,, \tag{3.22}$$

which for the case of the splitting cascade of a single non–abelian gauge boson can be written as

$$2n_{\rm M}\Gamma_{\rm M}\delta(p - M/2) + \int_{p+\kappa T}^{M/2} \tilde{n}(k)\frac{d\Gamma^{\rm split}_{\rm LPM}(k \to p)}{dp}dk = \int_{\kappa T}^{p/2} \tilde{n}(p)\frac{d\Gamma^{\rm split}_{\rm LPM}(p \to k)}{dk}dk\,. \tag{3.23}$$

Here $\Gamma^{\rm split}_{\rm LPM}(p \to p')$ denotes the splitting rate (3.16) for a process where a parent particle of energy p results in daughters with energy p' and $p - p'$. In accordance with the discussion in Section 3.1.3, here we only consider emission of daughter particles with energy above κT, where κ of $O(1)$ parameterizes our IR cutoff. The first term on the LHS is due to the direct injection of decay products from decaying particles of mass M and number density $n_{\rm M}$ into the plasma; the factor of two is due to the assumption that each parent M decays to two daughter particles of momentum $M/2$.[9] The remaining terms describe the feed-down from particles with momentum $k > p$ and the loss of particles with momentum p due to emission of a daughter with momentum k, respectively. The latter term, appearing on the RHS of eq. 3.23, is directly described by the differential splitting rate given in eq. 3.16. Note that the upper integration limit is set to $p/2$; this is because the splitting rate is symmetric under the exchange of k and $p - k$. Another key point is that here the unknown function $\tilde{n}(p)$ can be pulled in front of the integral, i.e. the loss term can be written as $\tilde{n}(p)\Gamma^{\rm split}_{\rm LPM}(p)$, with

$$\Gamma^{\rm split}_{\rm LPM}(p) = 2\alpha^2\sqrt{\tilde{g}_*}T\left(\frac{1}{\sqrt{\kappa}} - \sqrt{\frac{2T}{p}}\right)\,. \tag{3.24}$$

Physically, this simply reflects the fact that the rate of depletion of particles of energy p depends solely on the number density of these same particles.

The first integral in eq. 3.23 sums over all possible splittings of a parent of momentum k which lead to one of the two daughters having a momentum p; the latter may be either the more or the less energetic daughter particle. One may split the integral to more easily treat these two possibilities:

$$\begin{aligned}\int_{p+\kappa T}^{M/2} \tilde{n}(k)\frac{d\Gamma^{\rm split}_{\rm LPM}(k \to p)}{dp}dk &= \int_{2p}^{M/2} \tilde{n}(k)\frac{d\Gamma^{\rm split}_{\rm LPM}(k)}{dp}dk + \int_{p+\kappa T}^{2p} \tilde{n}(k)\frac{d\Gamma^{\rm split}_{\rm LPM}(k-p)}{dp}dk \\ &= \alpha^2\sqrt{\tilde{g}_*}T^{3/2}\left(\int_{2p}^{M/2} \tilde{n}(k)p^{-3/2}dk + \int_{p+\kappa T}^{2p} \tilde{n}(k)(k-p)^{-3/2}dk\right)\,.\end{aligned} \tag{3.25}$$

The first term on the RHS of (3.25) describes the case where the softer of the two daughters is of momentum p, while the second term captures the other case, where the more energetic daughter carries momentum p. In these integrals, the unknown function $\tilde{n}(k)$ can not be pulled out of the integral. The steady-state condition (3.23) is thus an integral equation; no analytical solution is known to us and we will, therefore, look for approximate and numerical solutions in the following sections.

[9] For decays into $n > 2$ daughter particles one would have to replace $2\delta(p - M/2)$ by the initial decay spectrum $\frac{1}{\Gamma_{\rm M}}\frac{d\Gamma_{\rm M}(p)}{dp}$. It is worth noting that such higher order decays may in fact contribute independently to the cosmological process of interest, e.g. DM production [30, 68, 69].

Before setting ourselves to the task of solving the Boltzmann equation, let us comment on the validity of the approximations used to derive the simple form in eq. 3.23. Compared to the form of the generic Boltzmann equation introduced in Section 2.5, our treatment of the injection and depletion terms in (3.23) disregards the Bose enhancement and Pauli Blocking factors. The validity of this approximation is partly closely tied to the efficiency of splitting processes as compared to the Hubble expansion discussed in eq. 3.19; in the language of eq. 2.36, the small kinetic functions of OoE particles with $p \gg T$ will allow one to approximate $1 \pm f \approx 1$.

As discussed in Section 3.1.3, we further limit our attention to emission of particles with $p > \kappa T$. This determines the integration boundaries in eq. 3.23; we are using κT as an infrared cutoff. This is, strictly speaking, an oversimplification. In particular, our approach will not work for $p \simeq T$, or for $M/2 - p \simeq T$; for example, our loss term vanishes for $p < 2\kappa T$, see also (3.24), and our Boltzmann equation will not generate particles with momenta between $M/2 - \kappa T$ and $M/2$. Ideally, instead of the hard cutoff, one would consider the full set of competing processes at the scale of the thermal bath $p_{\rm d} \sim T$. However, the *total* density of particles with $p \simeq T$ will in any case be dominated by the thermal bath, and it is difficult to envision a process where it matters whether an incident particle has momentum $M/2 \gg T$ or momentum $M/2 - T$. Furthermore, although our treatment in (3.17) resummed soft $2 \to 2$ Coulomb processes, disregarding the full set of $2 \to 2$ processes is an approximation we have taken up. Efficient soft $2 \to 2$ scatterings with a momentum exchange given in (3.5) are further arguments for an $O(T)$ cutoff of soft daughter particles in $2 \to 3$ splittings. Our default choice will be $\kappa = 1$; we will comment on the κ dependence of our numerical results later on in Section 3.3.2. As we will see, the cutoff will allow for an exact solution of the resulting Boltzmann equation 3.23.

3.2.2 Model parameters and the dimensionless Boltzmann equation

Before proceeding to solve the Boltzmann equation, it is useful to reduce the number of model parameters affecting $\tilde{n}$; as we will see, this will not only allow us to use a single solution in many cosmological scenarios but will also be rather helpful in gaining an intuition for the form of the solution. Let us first focus on the parameters in the first term in eq. 3.23, i.e., the initial rate of OoE particle injection. It is physically clear that the normalization of the spectrum of non-thermal particles will be proportional to the product $n_{\rm M}\Gamma_{\rm M}$: if the injection of energetic particles were to suddenly stop either due to the absence of matter particles ($n_{\rm M} \to 0$) or due to the absence of decays ($\Gamma_{\rm M} \to 0$), we would be left with a thermal radiation bath in a time of the order of the thermalization time (3.18) with $p_{\rm i} \to M/2$. Moreover, at $p = M/2$ the first integral in (3.23) vanishes so that our steady-state condition can be solved directly:

$$\tilde{n}(M/2) = \frac{2n_{\rm M}\Gamma_{\rm M}\delta(p - M/2)}{\Gamma^{\rm split}_{\rm LPM}(M/2)} \equiv \widetilde{N}_{\rm M}\delta(p - M/2)\,, \tag{3.26}$$

where $\Gamma^{\rm split}_{\rm LPM}(M/2)$ is given by (3.24) with $p = M/2$. Physically $\tilde{n}(M/2)$ should be understood as $\tilde{n}(p)$ in the immediate neighborhood of $M/2$. Of course, for $p < M/2$ the first term in eq. 3.23 does not contribute. The dependence on $n_{\rm M}\Gamma_{\rm M}$ can now be absorbed by defining

$$\bar{n}(p) \equiv \frac{\tilde{n}(p)}{\widetilde{N}_{\rm M}}\,. \tag{3.27}$$

Note that the homogeneous part of eq. 3.23, which describes the spectrum for $p < M/2$, is invariant under arbitrary changes of the normalization of $\tilde{n}$. The solution for $\bar{n}(p)$ can now only depend on M and T; this will later allow us to more easily present our results in Section 3.3. In fact, we will later see that solutions for $\bar{n}$ essentially depend only on the ratio of these two quantities. This can be seen by defining the dimensionless momentum (energy) variable

$$x \equiv \frac{p}{T} ; \tag{3.28}$$

with the maximal value

$$x_{\mathrm{M}} \equiv \frac{M}{2T} . \tag{3.29}$$

We also introduce the new number density distribution function

$$\tilde{n}(x) \equiv \frac{dn(x)}{dx} = T\tilde{n}(p) \implies \tilde{n}(x_{\mathrm{M}}) = \widetilde{N}_{\mathrm{M}}\delta(x - x_{\mathrm{M}}) . \tag{3.30}$$

Recalling that $\tilde{n}(p)$ has units of squared energy, eq. 3.30 implies that $\tilde{n}(x)$ has units of $[E]^3$. We finally arrive at a dimensionless function describing the spectrum of non-thermal particles by a normalization analogous to eq. 3.27:

$$\bar{n}(x) = \frac{\tilde{n}(x)}{\widetilde{N}_{\mathrm{M}}} \implies \bar{n}(x_{\mathrm{M}}) = \delta(x - x_{\mathrm{M}}) . \tag{3.31}$$

In order to derive the final integral equation describing the steady state condition we divide eq. 3.23 by $\Gamma^{\mathrm{split}}_{\mathrm{LPM}}$ of eq. 3.24:

$$\tilde{n}(p) = \widetilde{N}_{\mathrm{M}}\delta\left(p - \frac{M}{2}\right) + \int_{p+\kappa T}^{M/2} \tilde{n}(k) \frac{\sqrt{T}}{2\left(1/\sqrt{\kappa} - \sqrt{2T/p}\right)} \min(p,\, k-p)^{-3/2}\, dk , \tag{3.32}$$

where we have used eq. 3.26. In terms of the dimensionless variable introduced in eq. 3.28 and the normalized distribution introduced in eq. 3.31 this finally yields:

$$\bar{n}(x) = \int_{x+\kappa}^{x_{\mathrm{M}}} \bar{n}(x') \frac{\min(x, x'-x)^{-3/2}}{2\left(1/\sqrt{\kappa} - \sqrt{2/x}\right)} dx' + \delta(x - x_{\mathrm{M}}) . \tag{3.33}$$

We have therefore managed to reduce the number of free parameters in our treatment of the Boltzmann equation to two; the ratio parameter x_{M} of (3.29) describing the ratio of scales characterizing the matter and component ratios, and the cutoff parameter κ. In the next section, we will devote our attention to solving the dimensionless Boltzmann equation (3.33).

3.3 Solution of the Boltzmann equations

We are now ready to discuss solutions to the Boltzmann equation (3.23), or its normalized, dimensionless version given in eq. 3.33. As already stated, we do not know of an exact analytical solution to this equation; we can however use the forms (3.23) and (3.33) along with physical arguments to deduce the features the solution is expected to exhibit. The latter can be in turn used to make attempts at an

analytical approximate solution for the Boltzmann equation. This will be the focus of Section 3.3.1.

In the absence of an analytical solution, we will then proceed to treat the Boltzmann equation (3.33) numerically in Section 3.3.2, where now we will have to restrict our attention to a limited number of physics scenarios with fixed values for the parameters $x_{\rm M}$ and κ as discussed in Section 3.2.2. Finally, in Section 3.3.3, we will analytically parameterize our numerical solutions of Section 3.3.2 so that we may generalize these to other cosmological scenarios with a different $x_{\rm M}$.

3.3.1 Generic features and approximate solutions

In Section 3.2.1 we saw that the quasi–static distribution of OoE particles is governed by a detailed balance (3.22) of the number of hard particles entering and leaving a certain energy interval around p with $M/2 > p > T$. Let us consider the chain of splittings available to the initial decay products of energy $p = M/2$, and the subsequent daughter particles.

As we saw in eq. 3.26, the Boltzmann equation can be used to find the normalization of the solution at $p = M/2$. We may now ask how the spectrum $\tilde{n}(p)$ behaves in the vicinity of $p = M/2$. A naive expectation would be for the spectrum $\tilde{n}$ to rise towards smaller momenta as the thermalization process is expected to increase the number of OoE particles via consecutive splittings. A closer look, however, implies that one should instead expect a decay of the solution at high$-p$ and in the vicinity of $p = M/2$; one way to see that is to consider two neighboring momentum intervals $I_1 = [p, p - \kappa T]$ and $I_2 = [p - \kappa T, p - 2\kappa T]$, in the immediate neighborhood of $p \lesssim M/2$. Now any population of particles in I_2 will necessarily have to had originated in I_1, whereas the states originating from I_1 are allowed to split into any state of momentum $p' < p$. That results in only a fraction of the states in I_1 ending up in I_2, and hence the quick decay of $\bar{n}$ at high$-p$. Note that while the differential rate of the splitting process (3.16) favors splittings into softer -and therefore neighboring- daughter momenta, the preference does not compensate the presence of numerous available splitting chains.

Evidently, the spectrum of OoE particles needs to rise towards the radiation temperature T, to provide the large number of particles required by the process of thermalization; this is achieved when the decay behavior at high p is balanced out by the presence of many I_1-like intervals at $p > P$ from which a given I_2 interval can be populated. One, therefore, expects a flattening behavior as we move away from the high$-p$ region towards lower momenta. The same cumulative effect can further be expected to finally give rise to a monotonic rise of the spectrum $\tilde{n}(p)$ at lower momenta.

In Section 3.3.2 we will use the behavior described above as a cross–check for the performance of our numerical solution. Before we proceed to the numerical treatment of the problem, however, we may also look for possible approximate analytical solutions to the Boltzmann equation (3.23). Motivated by our discussion above, it is reasonable to expect that any such approximate solution will be more accessible, away from the "boundaries" and in the intermediate regions of the solution domain, i.e. with $M \gg p \gg T$.

In what follows, we will follow and expand upon the discussion in [41] to obtain an analytic approximate solution, with minimal changes to the therein used notation for consistency. [10] A key starting observation is the analytical form of the Boltzmann equation is somewhat complicated by the presence of the cutoff parameter κ. Even though this cutoff is necessary for a numerical treatment free of divergence, one may take the limit $\kappa \to 0$ for an analytic treatment. [11] Let us follow this advice and

[10] For the original notation, see equations 10 – 15 and Appendix A in [41].

[11] The divergent contributions from $\kappa \to 0$ can be expected to cancel out from the detailed balance, corresponding to

rewrite the Boltzmann equation 3.23 with a vanishing cutoff as

$$2n_{\mathrm{M}}\Gamma_{\mathrm{M}}\,\delta\left(p-M/2\right)+\int_{2p}^{M/2}\mathrm{d}k\,\frac{\mathrm{d}\Gamma^{\mathrm{split}}_{\mathrm{LPM}}}{\mathrm{d}p}(p)\tilde{n}\left(k\right)\quad+\quad\int_{0}^{p}\mathrm{d}k\,\frac{\mathrm{d}\Gamma^{\mathrm{split}}_{\mathrm{LPM}}}{\mathrm{d}k}(k)\tilde{n}\left(p+k\right). \tag{3.34}$$

$$=\quad\int_{0}^{p/2}\mathrm{d}k\,\frac{\mathrm{d}\Gamma^{\mathrm{split}}_{\mathrm{LPM}}}{\mathrm{d}k}(k)\tilde{n}\left(p\right) \tag{3.35}$$

with the LHS and RHS corresponding to the injection and depletion terms in (3.22) respectively. In (3.34), the LPM–suppressed splitting rate is given by eq. 3.16 and the integration domains have once more been chosen for convenient treatment of the daughter momentum. For brevity, the process rates can be written as[12]

$$\frac{\mathrm{d}\Gamma^{\mathrm{split}}_{\mathrm{LPM}}}{\mathrm{d}k}(k)=-\frac{1}{2}Ak^{-3/2}\rightarrow A\equiv k^{1/2}\Gamma^{\mathrm{therm}}_{\mathrm{LPM}}(k)=\text{constant}. \tag{3.36}$$

with the thermalization rate (3.18).

We may further simplify the form of the Boltzmann equation if we were to confine our attention to the intermediate region of momenta; in particular for the region of momenta with $p > M/4$, any emission of a particle of momentum p will necessarily involve a second softer particle. Equation 3.34 therefore takes the form

$$2n_{\mathrm{M}}\Gamma_{\mathrm{M}}\delta\left(p-M/2\right)=\frac{1}{2}A\left[\int_{0}^{p/2}\frac{\mathrm{d}k}{k^{3/2}}\tilde{n}(p)-\int_{0}^{p}\frac{\mathrm{d}k}{k^{3/2}}\tilde{n}(p+k)\right],\ \text{for}\ p\geq M/4, \tag{3.37}$$

$$A\left[\int_{0}^{p/2}\frac{\mathrm{d}k}{k^{3/2}}\tilde{n}(p)-\int_{2p}^{M/2}\frac{\mathrm{d}k}{p^{3/2}}\tilde{n}(k)-\int_{0}^{p}\frac{\mathrm{d}k}{k^{3/2}}\tilde{n}(p+k)\right]=0,\ \text{for}\ p<M/4. \tag{3.38}$$

Note that the amplitude pre–factor A of the process rates does not affect the form of the solution in (3.38). The rate of the splitting processes, instead, sets the normalization of the spectrum via its relative size compared to the initial injection rate in (3.37); it then follows that a solution of (3.38) will, by itself, not suffice to fix the normalization of the spectrum $\tilde{n}\left(p\right)$. Regardless, let us focus on the momentum distribution for the intermediate region $p \ll M$ and make an ansatz

$$\tilde{n}(p)\propto p^{-n},\qquad n\in\mathbb{R}^{+} \tag{3.39}$$

divergences in the injection and depletion terms in eq. 3.23 (see [70]). Following [41], we will be disregarding the Bose enhancement and Puli blocking factors, despite the vanishing cutoff parameter.

[12] Please note that in the notation used in [41] (equation A5-A6) the quantity $\Gamma_{\mathrm{split}}\left(k\right)$ is not the total splitting rate (3.24) resulting from the integration $\int\mathrm{d}k\,\frac{\mathrm{d}\Gamma_{\mathrm{split}}(k)}{\mathrm{d}k}$; note also that the total splitting rate (3.24) is not well–defined in the limit $\kappa\rightarrow 0$. Instead, to the best of our understanding, the authors use the notation $\Gamma_{\mathrm{split}}\left(k\right)$ to denote the thermalization rate of a *parent* particle of energy k, given by $\Gamma_{\mathrm{therm}}=t^{-1}_{\mathrm{therm}}$ given in eq. 3.18. Furthermore, in this sense, the parameter k in equations A5 and A6 of [41] corresponds to the two momenta of daughter (p_{d}) and parent (p_{p}) particles respectively.

Equation eq. 3.38, therefore, reduces to

$$\underbrace{-\int_0^{p/2} \frac{\mathrm{d}k}{k^{3/2}} p^{-n}}_{\text{(I)}} + \underbrace{\int_{2p}^{M/2} \frac{\mathrm{d}k}{p^{3/2}} k^{-n}}_{\text{(II)}} + \underbrace{\int_0^{p} \frac{\mathrm{d}k}{k^{3/2}} (p+k)^{-n}}_{\text{(III)}} = 0. \tag{3.40}$$

Multiplying eq. 3.40 by $p^{n+1/2}$ simplifies the $p-$dependence and allows for the equation to be written as

$$\underbrace{-\mathrm{B}_{1/2}\left(-1/2, 1\right)}_{\text{(I)}} + \underbrace{\frac{1}{n-1}\left((2p/M)^{n-1} - 2^{1-n}\right)}_{\text{(II)}} + \underbrace{\exp\left(i\,3\pi/2\right)\,\mathrm{B}_{-1}\left(-1/2, 1-n\right)}_{\text{(III)}} = 0. \tag{3.41}$$

where $\mathrm{B}_a\left(c, d\right)$ are incomplete Beta functions (see Appendix C). Note that the terms (I) and (III) do not depend on the momentum p, implying a solution of the form (3.39) can only exist in the region

$$p \ll M, \quad n > 1 \tag{3.42}$$

where the momentum dependence in (II) also vanishes; this is fine for a solution of (3.38). Finally, as can be seen from equations 3.40 and 3.41, the expression (II), corresponds to splittings with a soft daughter momentum p and is therefore finite. (I) and (III), on the other hand, involve singularities at integration boundaries. A cancellation of the divergent parts of (I) and (III) and subsequently the finite contribution from (III), together with (3.42) puts the best solution at (see Appendix C)

$$n \,=\, 3/2\,. \tag{3.43}$$

The authors in [41] therefore write the approximate solution of eq. 3.38 in the region $p \ll M$ as

$$\tilde{n}(p) \simeq \frac{n_{\mathrm{M}}\Gamma_{\mathrm{M}}}{A} M p^{-3/2}. \tag{3.44}$$

The coefficient $n_{\mathrm{M}}\Gamma_{\mathrm{M}}/A$ is included as it appears as the prefactor of the source term in eq. 3.37; the factor of M is *chosen* by *dimensional analysis*; as mentioned before, a solution to eq. 3.38 does not, in itself, allow for a determination of the normalisation in (3.44).

The normalisation of the the approximate solution (3.44) can be either estimated by matching to a solution of the spectrum in the $p > M/4$ region and (3.37), or by extending the validity of (3.44) to lower momentum regions and using energy conservation arguments [41]; the latter relies on the expectation that independent of the combination of splittings (3.7) through which the thermalization process proceeds, The energy M should be deposited at lower energies $p \ll M$ in the form of $O\left(M/p\right)$ particles. One should, however, keep in mind that solutions to (3.34) at $p \sim T$ are expected to differ from the more physical solutions of (3.23).

In the next section, we will instead numerically solve the IR–regularised Boltzmann equation (3.23) over the entire range of momenta p; the resulting solution will therefore be free of ambiguities; we will check to see if the expected behaviour introduced in Section 3.3.1, and the approximate form of (3.44) in the region $M \gg p \gg T$ will be observed in the numerical solution.

3.3.2 Numerical solution

As discussed in Section 3.2.2, the normalized and dimensionless formulation of the integral equation has two free model parameters, namely x_{M} and the cutoff parameter κ, and better allows for a numerical treatment; we will be presenting results for a limited number of numerical values for these parameters.

Before going on to the numerical solution for each specific case, let us first address the presence of the delta function, as this could be thought to be problematic in the numerical treatment. The presence of the delta function in the physical description of the Boltzmann equation 3.33 is clearly an approximation to a narrow distribution in energy. Since the decaying progenitor particles have a finite lifetime, the uncertainty relation implies a width of the initial peak at $x = x_{\mathrm{M}}$ given by Γ_{M}/T. Much more importantly, as discussed at the end of Section 3.2.1, soft $2 \to 2$ interactions with the thermal plasma will smear out the initial momentum, creating a width of the order of $\delta k_{\mathrm{el}}/T \sim \alpha^{1/2}$, at time scales considerably shorter than that of the splitting reactions described by our Boltzmann equation 3.33. It would therefore not be amiss if we were to smoothen out the delta function to get a numerically tractable injection term in the vicinity of x_{M}.

Moreover, any contribution to the solution at low x will depend on all higher values of x via integration, therefore picking out the coefficient of the source term delta function. At least for $x_{\mathrm{M}} - x \gg \kappa$ the precise shape of the source term at x_{M} is immaterial; recall that our hard IR cutoff implies that the shape of our solution for $x_{\mathrm{M}} - x \lesssim \kappa$ will in any case not be reliable. As a result, for the purpose of a numerical solution, we can simply set

$$\bar{n}(x_{\mathrm{M}}) = 1/\kappa\,, \tag{3.45}$$

with the understanding that this represents a bin around x_{M} of width κ. We will adopt this shorthand notation so that our solutions will always start at a finite $O(1)$ value at $x = x_{\mathrm{M}}$.

Interpreting $\bar{n}\left(x_{\mathrm{M}}\right)$ to represent the range from $x_{\mathrm{M}} - \kappa$ to x_{M} also solves the problem that this range can, strictly speaking, not be populated by our evolution equation, since we do not allow the emission of daughter particles with momentum less than κT. As already noted, physically it should not matter whether a non-thermal particle has energy $M/2 \gg T$ or $M/2 - \kappa T$. Similarly, the interval $[1, 1+\kappa]$ will be populated from splittings at higher x, without a possibility to split further down to $x \leq 1$. This should not reduce the usefulness of our solution either, since we expect our non-thermal contribution to be well below the thermal one at least for $x \leq 3$ or so. Note that, as discussed in Section 2.3 and in particular eq. 2.23, the expectation value of the energy of a relativistic thermal distribution is $\sim 3T$ for both the bosonic and the fermionic degrees of freedom. Moreover, the total number density in the thermal plasma is much higher than that of the non-thermal radiation component due to OoE particles.

With these points in mind, we can move on to the numerical solutions of eq. 3.33. Since $\bar{n}(x)$ only depends on $\bar{n}\left(x' \geq x + \kappa\right)$ the procedure is in principle straightforward: One starts with $\bar{n}\left(x_{\mathrm{M}}\right) = 1/\kappa$ and gradually works down to smaller values of x. In practice we divide the interval $[1+\kappa, x_{\mathrm{M}} - \kappa]$ into equal steps; inside the integral we evaluate $\bar{n}(x')$ by linear interpolation. This simple algorithm leads to numerically stable results as long as the step size $\mathrm{d}x \leq \kappa$.[13]

Numerical solutions for the choice of $\kappa = 1$ and $x_{\mathrm{M}} = 10^2$, 10^3 and 10^4 are presented in Fig. 3.2.

[13] A cubic spline interpolation of solution points also allows for a slight improvement in convergence behavior for the numerical integration. My simple use of log-spaced steps turned out to make the numerics less stable. The authors in [70] subsequently use a coarse-grained discretisation grid for a solution of the integral Boltzmann equation by a refinement of the derivative calculation (see in particular equation 4.4 and the ensuing discussion in [70]); this allows for a significantly faster numerical solution.

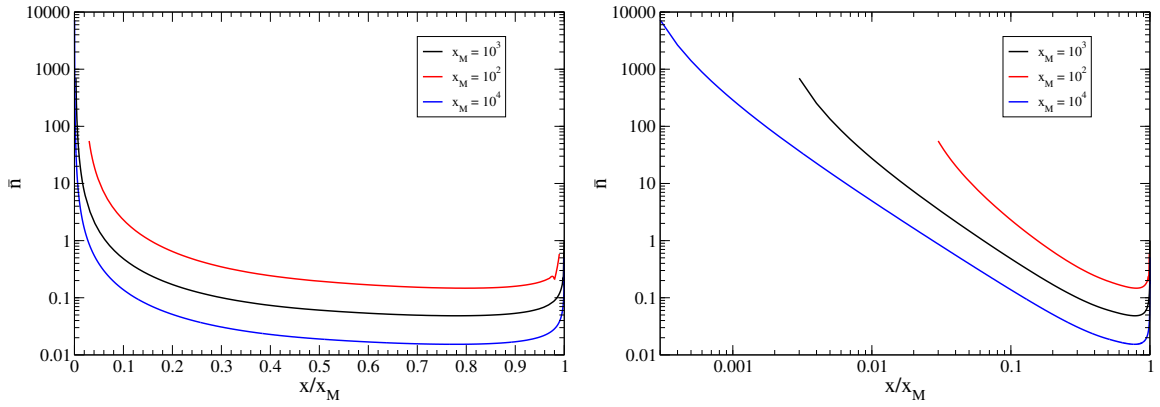

Figure 3.2: Numerical results for $\bar{n}(x)$ vs the ratio $x/x_{\rm M}$, computed from the Boltzmann equation (3.33) for three cases $x_{\rm M} = 10^2$ (red, top), 10^3 (black, middle), and 10^4 (blue, bottom). The left frame uses a linear scale for the x-axis, whereas the right frame uses logarithmic scales on both axes. The IR regulator has been set to $\kappa = 1$.

Note that, for reasons we will turn to in Section 3.3.3, we will often present the solutions in plots against $x/x_{\rm M}$. As can be seen in these three cases in Fig. 3.2, the overall shape and features of the curves appear to be independent of $x_{\rm M}$. Starting at $x = x_{\rm M}$ the solution at first drops quickly; this part of the curves can better be seen in the left frame, which uses a linear scale for the x-axis. Initially this decline simply reflects the $(x_{\rm M} - x)^{-3/2}$ dependence of the integration kernel applied to the δ-function at $x = x_{\rm M}$. However, this contribution becomes sub-leading already at $x \leq x_{\rm M} - 3$, where iterated emission processes become important, and lead to a flattening of the spectrum. This agrees well with the expected behavior mentioned in Section 3.3.1.

Perhaps somewhat counter-intuitively, the $\sqrt{2/x}$ term in the denominator of the Boltzmann eq. 3.33 is quite important even in the large–x region; without this term, the spectrum would reach a (much lower) minimum at $x \lesssim x_{\rm M}/2$. Instead, via the cumulative effect of the small variation due to the square root, the curves in Fig. 3.2 reach their minimum at $x_- \simeq 0.78 x_{\rm M}$; to a very good approximation, the minimum of the spectra in the three cases is reached at a fixed *ratio* of $x/x_{\rm M}$, showing a scaling behavior we will turn to in Section 3.3.3.

Figure 3.2 further shows that the spectrum rises again towards smaller values of x, once again in agreement with the expected behavior discussed in Section 3.3.1. This low–x part of the spectrum is more readily studied using a logarithmic scale for the x-axis (right frame). We see that for $10 \leq x \leq x_-/2$ the spectrum can be described by a falling power of x. The numerical value of this power is close to $-3/2$. This reflects the $p_{\rm d}^{-3/2}$ dependence of the LPM splitting rate, see eq. 3.16, and agrees with (3.44), and therefore among others with the results in [41, 63, 71]. Finally, for $x \leq 10$ the spectrum bends upwards, as the x'–independent denominator in eq. 3.33 develops a strong x–dependence.

These features of the spectrum mentioned so far are relatively independent of $x_{\rm M}$. However, the absolute value of the spectrum at fixed x, or fixed ratio $x/x_{\rm M}$, clearly does depend on $x_{\rm M}$. In fact, to a good approximation, the solution $\bar{n}$ at fixed $x/x_{\rm M}$ scales like $1/\sqrt{x_{\rm M}}$, unless $x \leq 10$ where the low–x rise described above becomes pronounced. This can be understood from the observation that the

thermalization time of eq. 3.18 scales like $\sqrt{M} \propto \sqrt{x_{\rm M}}$: the total number of non-thermal particles should be proportional to the thermalization time; since the spectrum is spread out over a wider energy range when M increases, the differential spectrum at fixed $x/x_{\rm M}$ should scale like $t_{\rm therm}/M \propto 1/\sqrt{x_{\rm M}}$. In Section 3.3.3 we will use this observation to parameterize an approximate solution to the Boltzmann equation.

The above observation, namely that the overall normalization of the spectrum scales as $1/\sqrt{x_{\rm M}}$, further helps explain why the spectrum scales linearly in $x_{\rm M}$ at fixed small x. The overall normalization of the spectra at fixed $x/x_{\rm M} \propto 1/\sqrt{x_{\rm M}}$ is over-compensated by the $(x/x_{\rm M})^{-3/2}$ behavior at fixed x (well below the location of the minimum) to give the linear behavior observed in the $x \sim \mathcal{O}(1)$ region in Fig. 3.2.

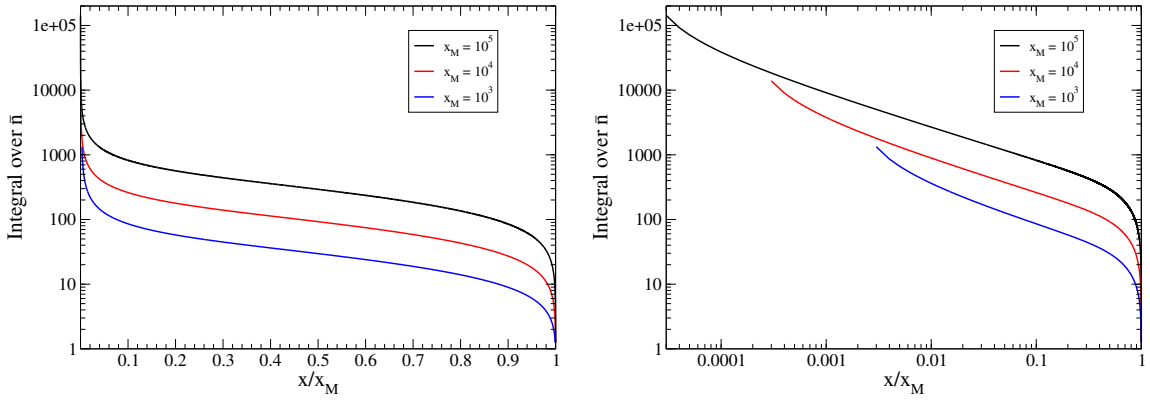

Figure 3.3: Numerical results for $\int_x^{x_{\rm M}} \bar{n}(x')\,dx'$ vs. the ratio $x/x_{\rm M}$, computed from the Boltzmann equation (3.33) for three cases $x_{\rm M} = 10^5$ (black, top), 10^4 (red, middle), and 10^3 (blue, bottom). The left frame uses a linear scale for the x-axis, whereas the right frame uses logarithmic scales on both axes. The IR regulator has been set to $\kappa = 1$.

We may further understand the behavior of the solution in Fig. 3.2 by looking at the number density, i.e. the integrated spectrum, of OoE particles. As mentioned in Section 1.4, OoE particles of energy $p' \gtrsim p$ could for example contribute to production of particles of mass $m \sim p$. In Fig. 3.3 we, therefore, show results for the integral $\int_x^{x_{\rm M}} \bar{n}(x')\,dx'$, again as function of the ratio $x/x_{\rm M}$, for three values of $x_{\rm M}$ now extending to $x_{\rm M} = 10^5$. We see that the integral quickly increases when x is reduced from $x_{\rm M}$; this reflects the spike at large x seen in Fig. 3.2. This is followed, in the vicinity of the broad minimum of $\bar{n}$, by a rather flat plateau where the integral increases relatively slowly (note, however, the logarithmic scale of the y-axis). At smaller x the integral increases $\propto (x/x_{\rm M})^{-1/2}$. This power-law behavior, which is again better seen with a logarithmic x-axis (right frame), evidently reflects the $(x/x_{\rm M})^{-3/2}$ behavior of $\bar{n}$ noted above. The upturn at $x \leq 10$ is again due to the x-dependence of the factor in front of the integral in eq. 3.33.

The behavior of the number density in Fig. 3.3 is further closely related to energy conservation. As expected from the above discussion of the thermalization time, the value of the integral at fixed $x/x_{\rm M}$ increases $\propto \sqrt{x_{\rm M}}$ as long as $x \gtrsim 10$. Together with the $1/\sqrt{x}$ dependence of the integral at fixed $x_{\rm M}$ this implies that the total number of non-thermal particles, i.e., the integral starting at $x = 3$ (or a similar

fixed, low value), increases essentially linearly with $x_{\rm M}$. This is in line with our expectation of the thermalization process turning a single progenitor matter particle of mass M into $O\left(M/T\right) = O\left(x_{\rm M}\right)$ thermal particles.[14]

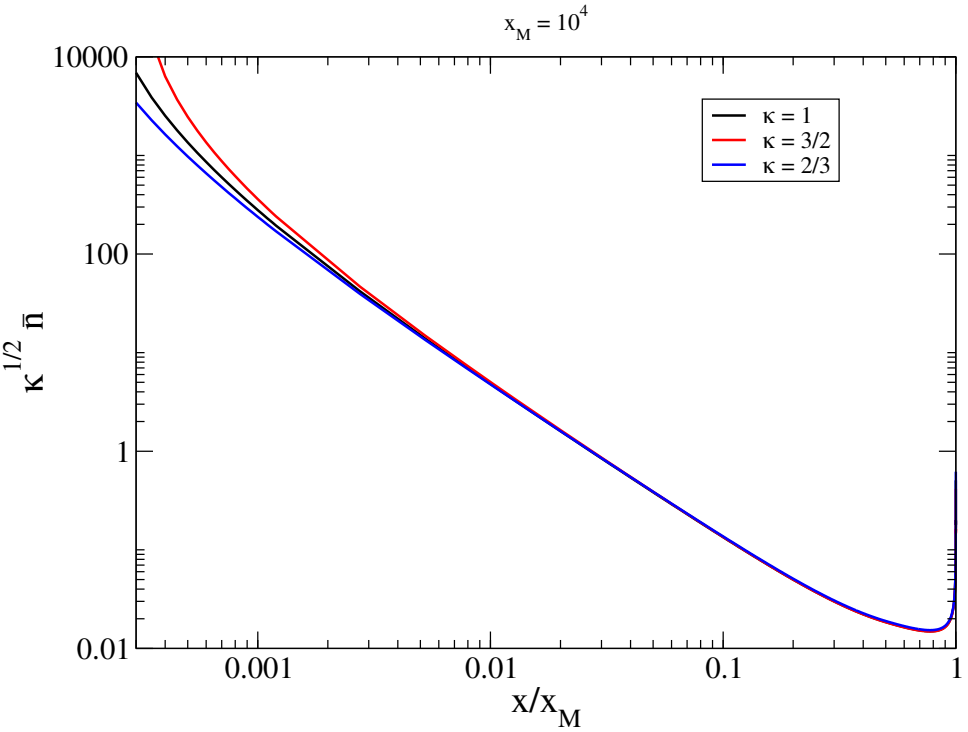

Figure 3.4: Numerical results for $\sqrt{\kappa}\cdot\bar{n}(x)$ vs the ratio $x/x_{\rm M}$, computed from the Boltzmann equation (3.33), with $x_{\rm M} = 10^4$ and three different values of the IR regulator κ: 1 (black), 3/2 and 2/3 (blue). $\bar{n}$ has been multiplied with $\sqrt{\kappa}$ in order to remove the κ-dependence of the normalization factor $\widetilde{N}_{\rm M}$ defined in eq. 3.26. The three curves essentially lie on top of each other for $x/x_{\rm M} \gtrsim 0.01$, i.e. $x \gtrsim 100$.

As stated earlier, the dimensionless formulation of our Boltzmann equation 3.33 involves a physical parameter $x_{\rm M}$, and a cutoff choice κ. The results presented so far have focused on the role of $x_{\rm M}$ and have been obtained with our default choice for the IR regulator $\kappa = 1$. We may now address the effects of the choice of κ. It is reasonable to expect the *physical solution* to be fairly independent of the specific choice of thermal cutoff. The physical (non–normalized) density of particles in the thermal spectrum is proportional to $\widetilde{N}_{\rm M}\cdot\bar{n}$ and so, using (3.26), proportional to $\bar{n}/\Gamma^{\rm split}_{\rm LPM}$. Furthermore, we know from (3.24) that $\Gamma^{\rm split}_{\rm LPM} \propto 1/\sqrt{\kappa}$ for $\sqrt{x_{\rm M}} \gg 1$. Hence we can expect the combination $\sqrt{\kappa}\bar{n}$ to be κ-independent.

In Fig. 3.4 we present results for $\sqrt{\kappa}\cdot\bar{n}$, with a fixed $x_{\rm M} = 10^4$ as an example, using three different values of κ. The agreement among different solutions implies that the physical density computed from our formalism is indeed almost independent of κ, except for the region $x \lesssim 10$ where an increase

[14] In this respect the thermal bath behaves like the calorimeter of a particle physics experiment.

of κ begins to significantly increase the time needed to complete the thermalization; recall that we do not admit emission of daughter particles with energy below κT. We checked numerically that the results indeed depend on κ significantly only for $x \lesssim 10$, independent of the value of $x_{\rm M}$. This is also well expected, as it is an effect of the saturation exclusively due to the presence of the thermal bath of temperature T. As expected from our discussion in Section 3.3.2 and as can be directly seen from eq. 3.7, there is a corresponding dependence on κ for the high$-x$ region $x_{\rm M} - x \lesssim 5$, although this effect will again be fairly unimportant and also difficult to spot in Fig. 3.4. We will therefore continue to present and use results corresponding to $\kappa = 1$ in the remainder of Chapter 3, as well as in Chapter 4 thereafter.

3.3.3 Analytical parameterization of the numerical solution

We saw in Section 3.3.2 and Fig. 3.2 that solutions to the Boltzmann equation 3.33 for different $x_{\rm M}$'s enjoy common features; we further physically motivated the dependence of the relative overall scaling of these solutions on $x_{\rm M}$. In this section, we wish to find an analytical approximation to the exact numerical solution. A simple fitted function would obviously be much easier to compute; this can be very advantageous in numerical applications, e.g., when many values of $x_{\rm M}$ need to be investigated. Note that $x_{\rm M} = M/(2T)$ in general changes during the epoch of energy injection, since T decreases as $\propto t^{-1/2}$ ($t^{-1/4}$) if $\rho_{\rm M} \ll \rho_{\rm R}$ ($\rho_{\rm M} \gg \rho_{\rm R}$).

Let us first exploit our understanding of the properties of the solution to narrow down candidates for the fitting function. Clearly, an approximation will be more accessible if it only depends on the ratio $x/x_{\rm M}$, rather than on x and $x_{\rm M}$ separately. In the previous subsection we saw that $\bar{n}$ indeed has a rather similar shape for different values of $x_{\rm M}$; we also saw that the value of $\bar{n}$ at fixed $x/x_{\rm M}$ scales like $1/\sqrt{x_{\rm M}}$ if $x \gg 1$. This motivates us to "factor out" the explicit dependence on $x_{\rm M}$ to get a function with a *scaling behavior*, i.e., depending on the ratio $x/x_{\rm M}$. As can be seen in Fig. 3.5, this is achieved if the solution of the Boltzmann equation 3.33 (*without* the δ-function at $x = x_{\rm M}$, which is always normalized to unity) is multiplied with the function

$$f(x, x_{\rm M}) = \sqrt{x_{\rm M}} \frac{\left(1 - \sqrt{2/x}\right)^{5/4}}{1 - 2/\sqrt{x_{\rm M}}} \,. \tag{3.46}$$

Let us look at the structure of the function (3.46) more closely. The factor of $\sqrt{x_{\rm M}}$ has already been remarked upon; the denominator in (3.46) removes the $x_{\rm M}$ dependence that results from $\Gamma^{\rm split}_{\rm LPM}$. The numerator further somewhat compensates the prefactor $1/(1 - \sqrt{2/x})$ of the integral in the Boltzmann equation (3.33), where the power $5/4$ has been adjusted to make the curves in Fig. 3.5 approximately coincide.

As discussed in Section 3.3.2, the delta function at $x = x_{\rm M}$, is already analytically available and can be included in our analytical formulation of the numerical solution. Further, the inclusion of the delta function will further imply that in the immediate neighborhood of $x_{\rm M}$ one should have

$$\bar{n}(x)|_{x \simeq x_{\rm M}} \simeq \frac{1}{2} \int_{x+1}^{x_{\rm M}} \delta(x' - x_{\rm M})(x' - x)^{-3/2} dx' = \frac{1}{2}(x_{\rm M} - x)^{-3/2} \,. \tag{3.47}$$

However, (3.47) merely includes the contribution of a single splitting starting from $x = x_{\rm M}$. The numerical analysis shows that this becomes inadequate already at $x_{\rm M} - x \simeq 3$; recall that for $x_{\rm M} - x \lesssim 3$

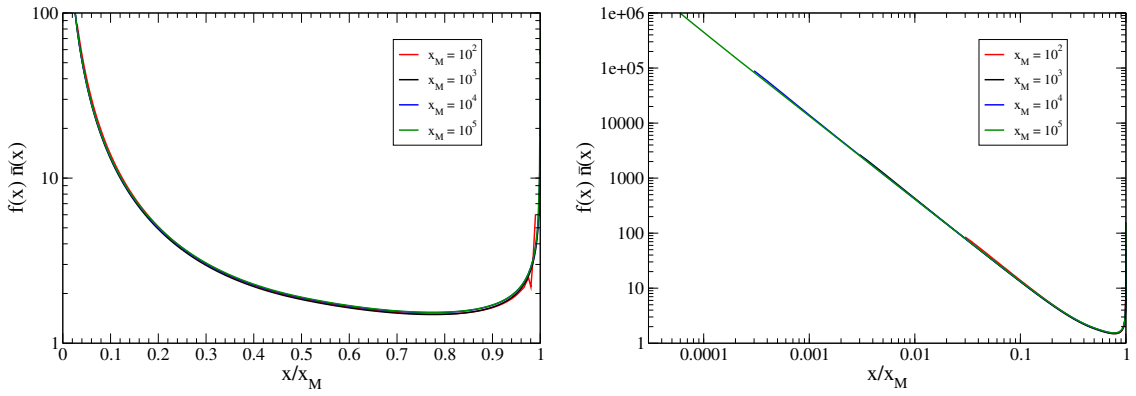

Figure 3.5: Numerical results for $f(x) \cdot [\bar{n}(x) - \delta(x - x_{\rm M})]$ vs the ratio $x/x_{\rm M}$. $\bar{n}$ has been computed from the Boltzmann equation 3.33 for four values of $x_{\rm M}$, with IR regulator $\kappa = 1$. The function $f(x)$ as defined in eq. 3.46 has been chosen such that the four curves almost fall on top of each other. The left (right) frame uses a linear (logarithmic) scale for the x-axis.

our solution is in any case not reliable, due to the dependence on the hard IR cutoff κ. Nevertheless, the numerical results clearly show that the spectrum initially falls off with decreasing x, corresponding to the expected "falling" behavior introduced in Section 3.3.1. The inclusion of further splittings results in a departure from the $(x_{\rm M} - x)^{-3/2}$ behavior, but we can parameterize the falling behavior through a negative power in $(x_{\rm M} - x)^{-b}$ where b is a positive constant.[15] On the other, hand we found in Section 3.3.1, that the spectrum basically scales as $x^{-3/2}$ for $1 \ll x \ll x_{\rm M}$; Fig. 3.5 shows that after multiplying $\bar{n}(x)$ with the function $f(x)$ this scaling holds for *all* $x \ll x_{\rm M}$.

Together, the above considerations suggest the ansatz

$$f(x, x_{\rm M}) \cdot \left[\bar{n}(x, x_{\rm M}) - \delta(x - x_{\rm M})\right] = a \left(\frac{x}{x_{\rm M}}\right)^{-3/2} \left(1 - \frac{x}{x_{\rm M}}\right)^{-b} + c\,, \tag{3.48}$$

where the constant c has been introduced in order to improve the description of the numerical result near the minimum, and a parameterizes the normalization of the universal function resulting in Fig. 3.5. Our final fitting function for the spectrum of non-thermal particles is thus:

$$\bar{n}(x, x_{\rm M}) = \delta(x - x_{\rm M}) + \frac{\left[a \left(x/x_{\rm M}\right)^{-3/2} \left(1 - x/x_{\rm M}\right)^{-b} + c\right] \left(1 - 2/\sqrt{x_{\rm M}}\right)}{\sqrt{x_{\rm M}} \left(1 - \sqrt{2/x}\right)^{5/4}}\,. \tag{3.49}$$

As an example, in the case of $x_{\rm M} = 10^5$, the following choice of parameters leads to an average

[15] One could also start with an initial solution of the form $(x_{\rm M} - x)^{-3/2}$ and iteratively obtain higher–order analytical approximations to the solution for $\bar{n}\,(x)$; the result from a couple of iterations could, however, not compete with the fit in (3.49).

deviation between the numerical result and the fit of about 2%:

$$a = 0.39,\ b = 0.48,\ c = 0.37\,. \tag{3.50}$$

In fact, for values of $0.35 \leq a\,, b\,, c \leq 0.45$ the numerical results can be reproduced by a solution of the form (3.48) within 3% average error, across four orders of magnitude.

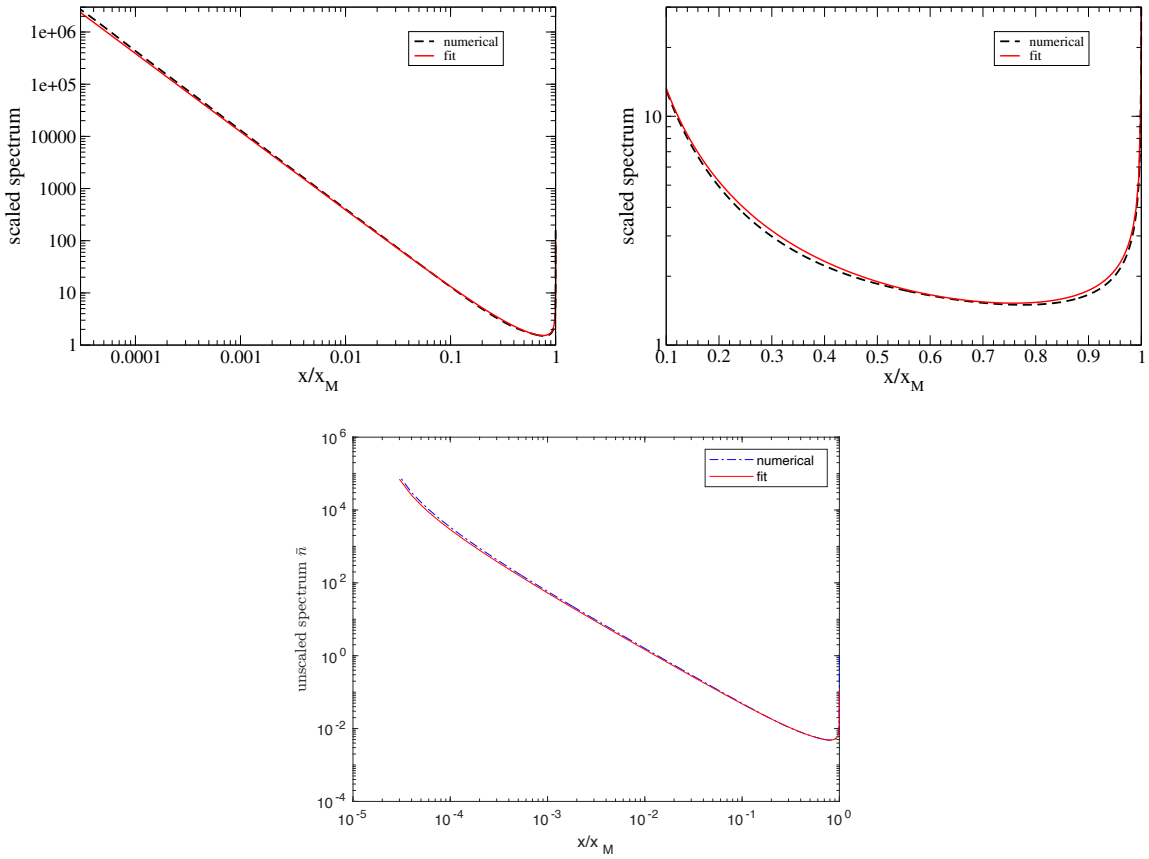

Figure 3.6: Fit (solid, red) of the form (3.48) and (3.49) compared to the numerical result (dashed, black) for the scaled spectrum $f(x, x_{\rm M})\bar{n}(x, x_{\rm M})$ (top left and top right) and non-scaled spectrum $\bar{n}(x, x_{\rm M})$ (bottom). The numerical results are for IR regulator $\kappa = 1$ and $x_{\rm M} = 10^5$, however, the results shown in the top figures practically only depend on the ratio $x/x_{\rm M}$ as long as $x \geq 1$.

In Fig. 3.6 we compare the fit function with the exact numerical result for the rescaled spectrum $f \cdot \bar{n}$; the latter has been computed for $x_{\rm M} = 10^5$, but we saw above that the rescaled spectrum practically only depends on the ratio $x/x_{\rm M}$ as long as $x \geq 1$. Similarly, the bottom frame in Fig. 3.6 shows the agreement between the numerical results and fits of form (3.49) to the numerical solution. We see that the fit not only describes the overall behavior well (left frame) but also the spike at $x \simeq x_{\rm M}$ as well as the minimum at $x \simeq 0.78 x_{\rm M}$ (right frame). Recall that these results hold for IR cutoff $\kappa = 1$, but we saw at the end of Section 3.3.2 that taking a different $O(1)$ value for κ only affects the solution at $x \lesssim 10\kappa$ and $x_{\rm M} - x \lesssim 10\kappa$.

As advertised earlier, an analytical expression of the form (3.49) allows for a much faster estimation of the spectra of OoE particles resulting from the thermalization cascade. Note that for a given Hubble era of temperature T of cosmological history involving a MD era, the soltuion (3.49) can be directly translated to a physical number density (3.20) by reintroducing the dimensionful parameters as outlined in Section 3.2.2. The importance of this accessibility can be better understood in applications in cosmology where the spectrum of OoE particles needs to be repeatedly calculated for multiple cosmological eras of different temperature T or correspondingly different x_{M}; this will be the focus of the next section.

3.4 Applications of the spectrum of out–of–equilibrium particles: an example

In Chapter 3 we set out to find the spectrum of OoE particles resulting from the splitting cascade of a single species of non–abelian gauge bosons. To conclude this chapter, we will briefly review an example for the applications of a spectrum of type (3.49) in calculating quantities of interest in cosmology. We will further quantitatively examine the importance of the inclusion of the LPM effect, as introduced in Section 3.1.3, and the performance of the approximate analytic solution of Section 3.3.1. To that end, we will adopt the notations and results from [52] along with results from [41] for comparison. Note that in Section 3.4, and for the sake of clarity, we will refrain from including the † symbol, as in (3.3c) for expressions in need of correction with coherent effects.

For an era where the decay products dominate the radiation bath (see (3.1)), authors in [52] use the (bulk) number density of *hard* primary decay products (progenitors) of energy $M/2$, given by

$$n_{\mathrm{h}}(T) \sim \rho_{\mathrm{R}}/M \sim 0.3\, g_* T^4/M, \tag{3.51}$$

with g_*, given by (2.22), being the effective number of DoF. As discussed in Section 3.3.1, the authors in [41] instead suggested an analytical solution of the form

$$\tilde{n}_{\mathrm{An}}(p) = \frac{n_{\mathrm{M}}\Gamma_{\mathrm{M}}M}{\sqrt{\tilde{g}_*}\alpha^2 T^{3/2}} p^{-3/2}, \tag{3.52}$$

for the spectrum of thermalizing decay products. In equation 3.44, the dependence on the effective interacting degrees of freedom $\tilde{g}_*$ can be assumed to have been absorbed by a redefinition of α, including other order one group factors. Here in (3.52) we have reintroduced these factors for a clearer comparison of results. In this setup of decay–dominated radiation bath, one may further identify $\Gamma_{\mathrm{M}} \cdot n_{\mathrm{M}} \cdot M \cdot t_{\mathrm{H}} \approx \rho_{\mathrm{R}}(T)$ to fix $\tilde{N}_{\mathrm{M}}$ in (3.27), and so the normalization of the solution $\tilde{n}(p)$ in (3.32) as well as (3.52) for a given cosmological temperature T.

In order to outline the consequences of the presence and form of a spectrum of energetic particles as in (3.49) and (3.52), we will revisit our discussion of Section 1.4, i.e., the production of *heavy* (meta-)stable particles χ prior to reheating in a matter-dominated universe, and point out further possible consequences for cosmology. We are once more studying a universe with a decaying matter component, described by equation 3.1; without loss of generality, we may trade the decaying rate of the matter component Γ_{M} for the cosmological reheating temperature T_{RH}, where the latter describes

the temperature of the radiation bath (3.1b) at times $t \sim \Gamma_{\rm M}^{-1}$, so that

$$T_{\rm RH} \simeq \left(\frac{90}{8\pi^3 g_*}\right)^{1/4} \sqrt{\Gamma_{\rm M} M_{\rm Pl}} \sim \sqrt{\Gamma_{\rm M} M_{\rm Pl}}. \tag{3.53}$$

Let us assume we are interested in the production of a heavy species χ with a mass $m_\chi \gg T_{\rm RH}$. The high mass of species χ implies that, in addition to processes among *soft* particles in the thermal bath, χ production via interactions of the hard OoE thermalizing decay products with the soft thermal particles (hard–soft processes), or other OoE particles (hard–hard processes), can become important. As discussed in Section 3.1.3, the efficiency of the thermalization process results in the OoE particles possessing a number density much smaller than that of the thermal radiation bath at any given time. It then follows that any physical process will be dominated by the contribution of initial states from the thermal bath, so long as this is kinematically and chemically allowed. When this condition fails, one or both initial states can be thought of as belonging to the hard OoE particles. Following the literature, we will therefore classify the various possible heavy particle production processes as soft–soft, hard–soft, and hard–hard according to the energy composition of the $2 \to n$ process. As mentioned above, we are primarily interested in the production of heavy particles inaccessible to soft–soft production.

In one of the earlier studies of the process of thermalization of decay products in cosmology, the authors in [52] have used $2 \to 3$ splitting processes with a massless gauge boson as the t-channel propagator to calculate a *slow-down* (thermalization) rate of

$$\Gamma_{\rm slow} \simeq 3\alpha^3 T \left(\frac{g_*}{200}\right)^{1/3}. \tag{3.54}$$

To regulate the process rate (3.54), the IR cutoff has been chosen as $n_{\rm R}^{1/3}(T)$, with $n_{\rm R}$ given by the contributions in (2.20), corresponding to the average spacing of particles in the thermal bath; notably, this choice of the IR cutoff points to disregarding phenomena occurring on length–scales *longer* than the average particle spacing. As such, the hallmark energy-dependence of the LPM effect (3.18), resulting from the coherent contribution of interactions with multiple scattering cites in the background plasma, is absent from (3.54). Note also that despite the different choice of IR cutoff, the rate (3.54) represents the very same physics resulting in the non–suppressed $2 \to 3$ energy loss rate in eq. 3.3c.

In [52], the primary decay products (3.51) are assumed to constitute the highly energetic OoE particles contributing to χ production. In this simplified picture of thermalization, the OoE particles consist solely of energy $p = M/2$ which get replaced by thermal particles of energy $p \sim T$ after a time $\Gamma_{\rm slow}^{-1}$. The hard–soft production rate, resulting from the interactions of an OoE particle of energy $M/2$ with a thermal particle of energy T, takes the form

$$\Gamma_\chi^{\rm hs} \sim 0.2 \left(\frac{\alpha_\chi^2}{TM} + \frac{\alpha\alpha_\chi^2}{\beta m_\chi^2}\right) T^3. \tag{3.55}$$

In equation 3.55, the coupling of χ to a single species of the thermal bath is parameterized via α_χ; we will continue using the same notation in the remainder of this thesis. The two terms in the parentheses in eq. 3.55 correspond to a $2 \to 2$ and a $2 \to 3$ process respectively; note that the inclusion of the $2 \to 3$ production channel for χ represents processes where the $2 \to 2$ rate suppression due to the high ($O(M/2)$) energy of the OoE particles is circumvented by a collinear emission of χ's in a higher

order process. Moreover, we have introduced the kinematic threshold parameter β of $O(1)$ to set the kinematic production threshold[16]; this is merely to unsure that phase–space suppressions do not limit the χ production process in a given model, in principle, the parameter β could be absorbed into the parameterisation of m_χ.

As can be seen from the denominators of (3.55), the hard–soft cross section for the number density (3.51) of primary decay particles of energy $M/2$ will either suffer from large Center of mass (CoM) energy suppression, or will have to resort to radiating away the extra energy at the cost of an extra power of α, resulting in a number density for χ's reading

$$n_\chi^{\rm hs}(T) \sim n_{\rm h} \cdot \frac{\Gamma_\chi^{\rm hs}}{\Gamma_{\rm slow}} \sim 4 \left(\frac{g_*}{200}\right)^{2/3} \frac{\alpha_\chi^2}{\alpha^2} \left(\frac{T^5}{\alpha M^2} + \frac{T^6}{M\beta m_\chi^2}\right). \tag{3.56}$$

In line with (3.51), equation 3.56 should be understood as representing the number density of χ's produced during a Hubble time $t_{\rm H}$ with temperature T; as we will see shortly, the total abundance of χ produced in a cosmological history results from properly adding up the contribution from the relevant Hubble eras.

Next, let us redo the same calculation of $n_\chi^{\rm hs}(T)$ using the spectra of OoE particles, as introduced in Sections 3.3.1 and 3.3.3. The splitting cascade underlying the spectra (3.49) and (3.52) affects the production rate in more than one way. As we saw in Section 3.1.3, the LPM suppression factor (3.15) increases the number density of OoE particles parametrically. Moreover, the splitting cascade provides particles with energies lower than $M/2$, so that the $\chi-$production rate will be suppressed neither by a too–large CoM energy nor by extra factors of α. A particle of energy $p \gg T$ from the thermalization cascade may contribute to production of χ's in $2 \to 2$ processes with a rate

$$\Gamma_\chi^{\rm hs}(p) \sim 0.2 \frac{\alpha_\chi^2}{pT} T^3 \mathcal{H}\left(pT - p_{\rm thr} T\right). \tag{3.57}$$

Here we have introduced the kinematic threshold parameter $p_{\rm thr} = \beta m_\chi^2/T$ and the Heaviside step function $\mathcal{H}$ to enforce a cutoff at the kinematic threshold of βm_χ^2; note that the momentum threshold depends on the temperature of the radiation bath in a Hubble era of temperature T. The rate (3.57) results in a number density

$$n_\chi^{\rm hs}(T) \;=\; t_{\rm H} \int_{p_{\rm thr}}^{M/2} \Gamma_\chi^{\rm hs}(p)\, dn(p) = t_{\rm H} \int_{p_{\rm thr}}^{M/2} \Gamma_\chi^{\rm hs}(p)\, \tilde{n}(p)\, dp. \tag{3.58}$$

of χ particles produced via hard–soft processes. A comparison with (3.56) shows, that the yield in (3.58) can be parametrically larger as advertised above eq. 3.57.

A finer comparison is between the hard–soft yield resulting from the two numeric (3.49) and

[16] With the particle spectra having power-law forms, as in (3.59), production will be most active near the threshold, so that the precise value of the cutoff can lead to an order of magnitude variation in the resulting abundance; we therefore consistently use a threshold of $\beta = 8$ to have results directly comparable to [52].

analytic (3.52) solutions for a certain $x_{\rm M}$. To that end, let us first rewrite the two spectra as

$$\left.\begin{matrix}\tilde{n}_{\rm Num}(p)\\ \tilde{n}_{\rm An}(p)\end{matrix}\right\} = \left(\frac{\tilde{N}_{\rm M}}{T}\right) \times \begin{cases}\bar{n}_{\rm Num}\,(x)\\ \bar{n}_{\rm An}\,(x) = \dfrac{2}{\sqrt{x_{\rm M}}}\left(x/x_{\rm M}\right)^{-3/2}\end{cases}, \tag{3.59}$$

where $\bar{n}_{\rm Num}\,(x)$ is given in (3.49), and we have used (3.30) to relate $\tilde{n}\,(p)$ and $\tilde{n}\,(x)$. Motivated by the form of (3.58) and the relative sensitivity to near–threshold energies $p_{\rm thr}$ for a heavy χ, we may directly compare the two spectra using the integrated weighted spectrum

$$n_{\chi}^{\rm hs}\,(T) \propto \frac{t_{\rm H} n_{\rm R} \alpha_{\chi}^2}{T} \int_{p_{\rm thr}}^{M/2} \frac{\tilde{n}\,(p')}{p'}\,dp' = \left(\frac{t_{\rm H} n_{\rm R} \alpha_{\chi}^2 \tilde{N}_{\rm M}}{T^2}\right) \int_{x_{\rm thr}}^{x_{\rm M}} \frac{\bar{n}\,(x')}{x'}\,dx', \tag{3.60}$$

appearing on the RHS. Fig. 3.7 (top-left) shows the integrated weighted spectra, as a function of x, from the two forms in (3.59), and the corresponding relative error of an analytical approximation compared to a full numerical solution for the two cases $x_{\rm M} = 10^3$ and 10^5. The figure on the right further shows that an error of $\mathcal{O}(1)$ is expected by using the monotonic form of the particle spectrum $\tilde{n}_{\rm An}$. As explained in our discussion following eq. 3.44, one could, however, in principle modify the numerical prefactors of the analytical solution for a better fit.

In scenarios where m_{χ} is large enough so that at the end of reheating $p_{\rm thr} \gg M$, the hard–soft channel of production might be either kinematically forbidden, or highly suppressed due to subsequent entropy production via the matter decay process. In such cases, interactions among the less abundant HE particles contribute to the production of χ's. Once again we will begin by presenting the *hard–hard* yield using the initial number density of particles of energy $M/2$ in the setup from [52].

Previously, we introduced the initial number of hard OoE particles resulting from decays of the matter component during a Hubble time in eq. 3.51. In the case of hard–hard production, only a small fraction of OoE particles will be available at any instant in time; one, therefore, cannot directly use the initial number density of hard particles $n_{\rm h}\,(T)$, and the transient nature of out-of-equilibrium states implies one should use the instantaneous number density. Specializing again to a case where M decays dominate the thermal bath of a Hubble era of temperature T, one can write

$$n_{\rm h}^{\rm inst}\,(T) \sim \frac{H}{\Gamma_{\rm slow}} n_{\rm h}\,(T) \sim H g_* T^4 / 3\Gamma_{\rm slow} M, \tag{3.61}$$

to represent the fraction of initial decay products present during a time $\Gamma_{\rm slow}^{-1}$. Within a Hubble time of temperature T, the number density (3.61) leads to a χ number density [52]

$$n_{\chi}^{\rm hh}(T) \sim n_{\rm h}^{\rm inst} \Gamma_{\chi}^{\rm hh} t_{\rm H} \quad \text{with, } \Gamma_{\chi}^{\rm hh} = \sigma_{\chi}^{\rm hh} n_{\rm h}^{\rm inst} = \left(\frac{\alpha_{\chi}^2}{M^2} + \frac{\alpha \alpha_{\chi}^2}{\beta m_{\chi}^2}\right) n_{\rm h}^{\rm inst}. \tag{3.62}$$

Note that the target density in (3.62) one again reflects the transient nature of the hard–hard process. Furthermore, the second term in the cross section would *radiatively return* the CoM energy to the production threshold of χ particles, similar to what we had in eq. 3.55.

Next, let us turn to the calculation of the hard–hard yield in the presence of a continuous spectrum

of OoE particles as in (3.49) and (3.52); the resulting number density can be estimated as

$$n_{\chi}^{\mathrm{hh}}(T) \sim \int_{T}^{M/2}\int_{T}^{M/2} \tilde{n}\left(p\right)\tilde{n}\left(p'\right)\sigma_{\chi}^{\mathrm{hh}}\left(p,p'\right)dp\,dp'\,t_{\mathrm{H}}, \quad \sigma_{\chi}^{\mathrm{hh}}\left(p,p'\right) = \frac{\alpha_{\chi}^{2}}{pp'}\mathcal{H}\left(pp'-\beta m_{\chi}^{2}\right). \tag{3.63}$$

Here, we have once more used the step function $\mathcal{H}$ and the kinematic cutoff parameter β to shut down χ production at low CoM energy. The integral is in general calculated numerically for a spectrum as in (3.49). In the case m_{χ} is sufficiently smaller than M, however, the dominant contribution to $n_{\chi}^{\mathrm{hh}}(T)$ will originate from the region $p \ll M$ and we may use the approximation $\tilde{n}(p \ll M) \propto p^{-3/2}$ to put the solution in the form of eq. 3.62, but where we are looking at an instantaneous population $n_{\mathrm{h}}^{\mathrm{inst}}(T)$ of particles of energy $\sqrt{\beta}m_{\chi}$ with

$$n_{\mathrm{h}}^{\mathrm{inst}}(T) \sim \frac{H}{\Gamma_{\mathrm{LPM}}^{\mathrm{therm}}\left(\sqrt{\beta}m_{\chi}\right)}\cdot\frac{\rho_{\mathrm{R}}}{\sqrt{\beta}m_{\chi}} \sim Hg_{*}T^{4}/\Gamma_{\mathrm{LPM}}^{\mathrm{therm}}\left(\sqrt{\beta}m_{\chi}\right)\sqrt{\beta}m_{\chi}, \quad \text{and} \quad \sigma_{\chi}^{\mathrm{hh}} = \frac{\alpha_{\chi}^{2}}{\beta m_{\chi}^{2}}, \tag{3.64}$$

resulting in a sizeable enhancement as compared to (3.62) [17]. The enhancement results from precisely the same effects explained above eq. 3.56 for the case of hard–soft production; the replacement of Γ_{slow} of (3.54), with the LPM–suppressed thermalization rate of (3.18) leads to a relatively larger population of OoE particles, while more HE particles with energies close to the production threshold further boost the resulting χ yield with respect to (3.62).

One can also employ eq. 3.63 to find how large an effect differentiates the two spectra in (3.59) in case of hard–hard production of χ's. This is shown in Fig. 3.7 (bottom), where we plot the resulting number density for a range of χ masses between $T_{\mathrm{RH}}\cdot 10^{2}$ and $M/2$, and have again factored out the prefactors in (3.63) as

$$n_{\chi}^{\mathrm{hh}}(T) \sim \left(t_{\mathrm{H}}\,\alpha_{\chi}^{2}\,\tilde{N}_{\mathrm{M}}^{2}/T^{2}\right)\iint_{1}^{x_{\mathrm{M}}}\frac{\bar{n}\left(x\right)\bar{n}\left(x'\right)}{x\,x'}\mathcal{H}\left(xx'-x_{\mathrm{thr}}^{2}\right)dx\,dx', \tag{3.65}$$

to better capture the effect of the two spectra. Similar to what we did on the RHS of (3.60), in (3.65) we have rewritten the kinematic cutoff as $x_{\mathrm{thr}}^{2} = \beta x_{\chi}^{2} = \beta m_{\chi}^{2}/T^{2}$. Figure 3.7 (bottom) shows that while the combination of low- and high-x parts of the spectrum in (3.65) flattens the resulting spectrum as compared to (3.49), an order of magnitude effect is observed, similar to the case of hard–soft production.

Finally, we can use the $\Omega-$ parameter to translate the number densities n_{χ}^{hh} and n_{χ}^{hs} into energy density fraction today $\left(\Omega h^{2}\right)_{\chi}$, to make easier contact with the observed quantities (1.1). The contribution of $n_{\chi}(T)$ from an era of temperature T to the omega parameter today can be written as

$$\left(\Omega h^{2}\right)_{\chi}(T) \sim \frac{n_{\chi}(T)}{s(T)}\frac{T_{\mathrm{RH}}^{5}}{T^{5}}\frac{m_{\chi}}{T_{0}}\left(\Omega h^{2}\right)_{\mathrm{R}}, \tag{3.66}$$

with $T_{0} = 0.24$ meV denoting the radiation temperature today, and $\left(\Omega h^{2}\right)_{\mathrm{R}} = 4.3\cdot 10^{-5}$ [52] (see also

[17] In bringing (3.63) into the form of (3.62), as we have done in (3.64), we are disregarding a logarithmic enhancement factor stemming from various combinations of $pp' = \beta m_{\chi}^{2}$. This does not however affect our main point.

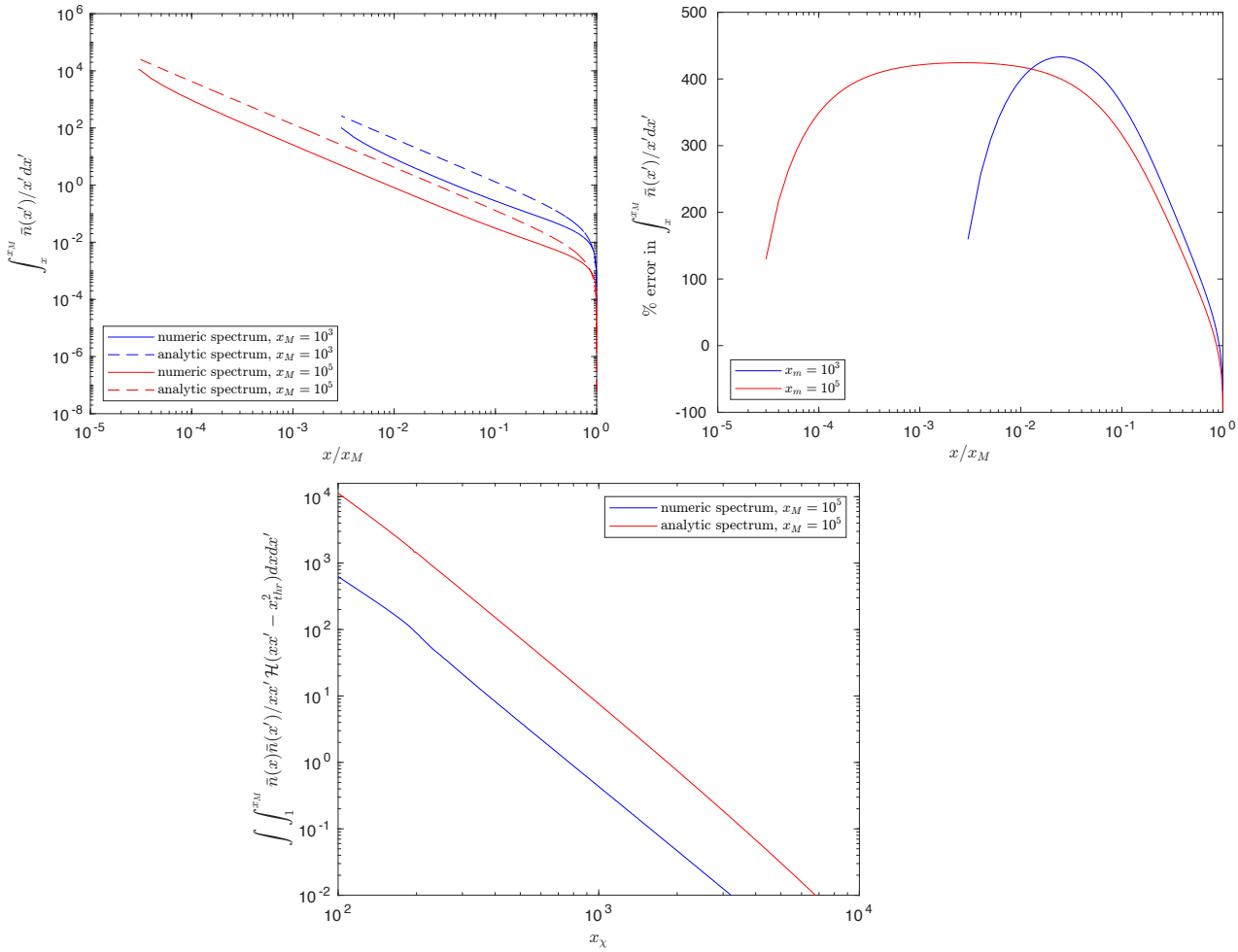

Figure 3.7: (Top-left) Scaled integrated weighted spectrum (3.60), resulting from the the two spectra from (3.59) versus x/x_{M} for two cases with $x_{\mathrm{M}} = 10^3$(blue), and 10^5(red). (Top-right) The relative error in (3.60) stemming from a monotonic spectrum. (Bottom) Scaled hard–hard yield from (3.65), resulting from the two spectra in (3.59) and the case of $x_{\mathrm{M}} = 10^5$.

[1]). Equation 3.66 can be used to compare the contribution of different production channels, and from Hubble eras of temperature T, to the overall χ yield.

The resulting temperature dependence of the diluted hard–soft yield implies that the dominant contribution results from the lowest temperature available for productions of χ

$$T_{\mathrm{thr}} = \max(\beta m_\chi^2/M, T_{\mathrm{RH}}). \tag{3.67}$$

Equation 3.67 simply expresses that hard–soft production stops either when the temperature of the thermal bath is so low that the CoM energy falls short of the threshold, or when matter decays stop at reheating. The opposite is true in the case of hard–hard production, where the diluted yield from a Hubble era grows with the temperature T; the result will, therefore, be set by the maximum temperature available to the thermal bath T_{max} [52]. The temperature and composition of the universe at earliest

times, corresponding to highest temperatures, is by nature somewhat model dependent. In addition to the cosmological model at these early times, an estimation of $T_{\rm max}$ and its consequences is closely related to the thermalization mechanism underlying the reheating phase and the thermalization of the decay products (see e.g. [39, 72]). As this is not the topic of our study, here we use the estimate from [52], reading

$$T_{\rm max} \sim T_{\rm RH} \left(\alpha^3 \left(\frac{g_*}{3} \right)^{1/3} \frac{M_{\rm Pl}}{M^{1/3} T_{\rm RH}^{2/3}} \right)^{3/8} , \tag{3.68}$$

in order for the different estimations of (3.66) to be comparable in Fig. 3.8.

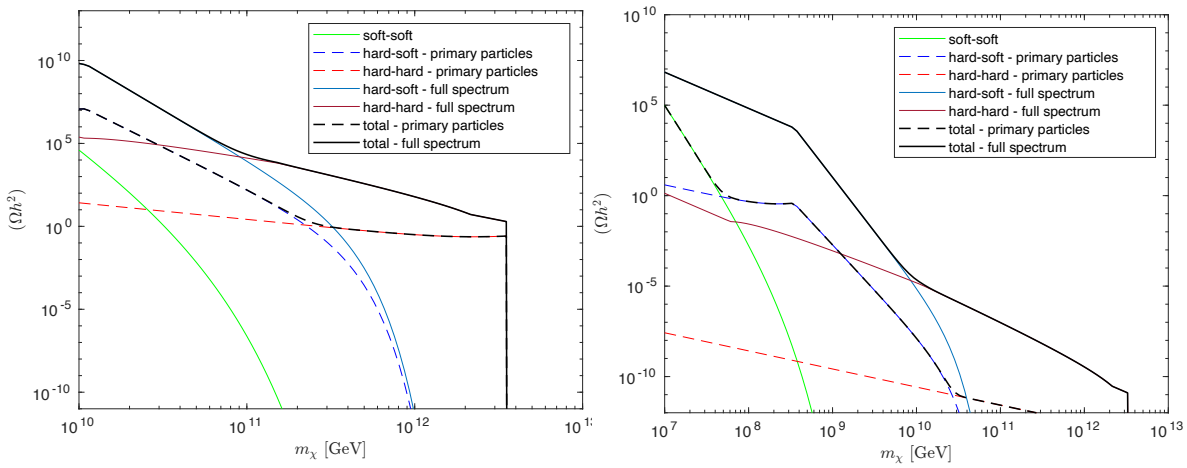

Figure 3.8: Energy density fraction parameter $\left(\Omega h^2\right)_\chi$ resulting from hard–soft (3.56, 3.58), hard–hard (3.62, 3.63), and thermal soft–soft (3.69) contributions with $\alpha_\chi = 0.01$, $\alpha = 0.05$, $M = 10^{13}$ GeV, and $T_{\rm RH} = 10^8$ GeV ($T_{\rm RH} = 10^5$ GeV) on the left (right). The dashed lines represent the resulting contribution from the primary number density of decay products [52] (see Fig. a & b), while the solid lines correspond to production via the spectrum (3.49). The resulting hard–soft yield agrees with results in [41] within the errors discussed in Fig. 3.7 after accounting for the choice of production threshold energy, and the number of target species in the thermal bath. The knee-shaped effect at low m_χ region in the case of $T_{\rm RH} = 10^5$ GeV signifies of a change in $T_{\rm thr}$ (3.67).

Fig. 3.8 shows examples of the various contributions to $\left(\Omega h^2\right)_\chi$, given by using a number density of initial decay products as in [52] along those resulting from the corresponding processes using the full spectrum (3.49) for $x_{\rm M} = 10^5$ (left) and $x_{\rm M} = 10^8$ (right). For completeness, the total abundance includes the sub–leading soft–soft production given by [73]

$$\left(\Omega h^2\right)_\chi^{\rm ss} \sim \left(\frac{200}{g_*} \right)^{3/2} \alpha_\chi^2 \left(\frac{2000 T_{\rm RH}}{m_\chi} \right)^7 . \tag{3.69}$$

This contribution results from interactions of the particles from the thermal bath with the composition (2.19); note that if the coupling α_χ in (3.69) is to be identified with those in the hard–soft and hard–hard productions (3.56, 3.60, 3.62, 3.63), the form (3.69) implicitly assumes that χ couples uniformly to all particles in thermal bath. For convenient comparison, we use the latter assumption

along with the approximation that the entirety of the OoE spectrum consists of a single non–abelian gauge boson species.

In Fig. 3.8 the hard–hard and hard–soft processes are shut down by an exponential suppression above $T_{\rm max}$ for simplicity [18]. The dark coupling $\alpha_\chi = 0.01$ is chosen so as to reproduce the results in [52] for comparison. Slight deviation from a power low behavior in the intermediate regions of m_χ for $\left(\Omega h^2\right)_\chi^{\rm hh}$ can be understood as resulting from contributions from a larger set of combinations of p and p' in (3.63) (see also footnote 17); In the intermediate region $T \ll p \ll M$ with the approximate form of the spectrum (3.52), one can express this enhancement as an $O(1)$ logarithmic factor [42].

To summarise, a sizable gain in particle production is evident in Fig. 3.8 when considering the full spectrum of the thermalization cascade (3.59). The given choice of α_χ is in fact seen to lead to an overproduction of the species χ; this could rather be understood as a suppression of the dark coupling α_χ required to reproduce a certain abundance for the species χ. Note that in a general analysis, there could be other contributions from direct branching of the scalar field decays [30, 68, 69]. If sizeable, these channels will further increase the abundance or correspondingly lead to a further suppression of the dark coupling α_χ.

3.5 Summary

As introduced in Chapter 1, the high energetic decay products resulting from the decay of heavy out-of-equilibrium states are used for a plethora of applications in cosmology, including entropy production, the production of (meta-)stable relics (e.g. DM particles), baryogenesis, modifications of the expansion history and structure formation. While some of these applications rely solely on the presence of an extra contribution to the energy density content of the universe or the thermal bath, others depend critically on the energy distribution of the decay products prior to their complete thermalization.

In Chapter 3 we studied the energy spectrum of the chain of $2 \to 3$ near–collinear splitting processes involved in the thermalization process. We have adopted the framework of thermalization via LPM–suppressed $2 \to 3$ splittings of a single species of non–abelian gauge boson introduced in [41], paying special attention to the natural cutoffs and regulations of splitting rate divergences provided by the thermal plasma. These rely on the fact that particles exchange energies of order T (gT) with the thermal bath relatively efficiently, via both emission and absorption processes and elastic scatterings. Therefore only the emission of particles with energy above κT needs to be included in the hard kernel of integral equations governing the momentum dispersion, with κ acting as an IR cutoff parameter of order unity. The inclusion of an IR cutoff allows us to derive an unambiguous numerical solution for the spectrum of hard OoE particles involved in the thermalization cascade.

We showed in the discussion around eq. 3.19 that the thermalization time is typically much smaller than a Hubble time so that the thermalization process can be treated as occurring at a fixed temperature T. This leads to a quasi–steady state spectrum, described by the integral equation 3.23. Dividing out normalization factors, and introducing the dimensionless momentum (or energy) variable $x = p/T$ (see eq. 3.28), we can instead deal with the equivalent dimensionless Boltzmann equation 3.33. The latter can be solved numerically by straightforward integration. The numerical solution exhibits

[18] Note that for $M \gg m_\chi$, hard–hard production can proceed prior to the formation of a thermal bath of temperature $T_{\rm max}$, see e.g. the discussion in Section III B in [52].

the features and approximate behaviour predicted by the analytical form of the Boltzmann equation introduced in Section 3.3.1.

After further normalization (see eq. 3.46), the numerical solution is seen to depend, to excellent approximation, only on the ratio $x/x_{\rm M} = p/(2M)$, with M denoting the mass of the decaying particle. This allowed us to find a simple, yet very accurate analytical fit function, given in eq. 3.49 which describes the numerical result to about 3% accuracy. This analytical approximation for the numerical solution to $\bar{n}(x)$ can easily be converted back to the original form using equations 3.27, 3.30 and 3.26. In this manner, our analytical fit results in a solution for the intermediate region $\tilde{n}$ ($T \ll p \ll M$) that is to very good approximation given by

$$\tilde{n}_{\rm Num}(p \ll M) = \frac{\widetilde{N}_{\rm M}\,\bar{n}(x \ll x_{\rm M})}{T} = 0.4\frac{n_{\rm M}\Gamma_{\rm M}}{\sqrt{MT}\Gamma^{\rm split}_{\rm LPM}(M/2)} \cdot \left(1 - \sqrt{2T/p}\right)^{-5/4} (p/M)^{-3/2}\,. \tag{3.70}$$

Similar to (3.52), the leading power–law dependence of this solution is consistent with (3.43). However, our solution contains an additional p-dependent factor. Moreover, our complete solution (3.49) contains another factor which generates a minimum at $p \simeq 0.4M$, followed by a spike as $p \to M/2$ further consistent with our arguments in Section 3.3.1, that the spectrum of non–thermal particles must be a rising function of p near $p = M/2$. Note that the analytical solution (3.52) based on cancellation of divergences in $\kappa \to 0$ suggested in [41] and further used in [42] shows a monotonous behavior in the entirety of the solution domain $M/2 \le p \le T$. Moreover, the normalization of our solution (3.70) differs from that of (3.52) by the factor $a/\sqrt{\tilde{g}_*}$, which may be partly absorbed into the coupling parameter α. Note that the dependence on $\tilde{g}_*$ appears via the normalization factors (3.26) and is, therefore, absent in the normalized form of eq. 3.33. In Chapter 4, we will use this property to simplify the form of our equations for a splitting cascade involving multiple particles.

Both solutions (3.52) and (3.49) lead to

$$\int_0^{M/2} \tilde{n}(p) p\,dp \propto \rho_{\rm M} \cdot \Gamma_{\rm M} \cdot t_{\rm therm}(M/2) \tag{3.71}$$

with $t_{\rm therm}$ given by (3.18). This can be understood as the total energy of hard OoE particles contained within the thermalization cascade at each instant being directly proportionate to the rate of energy injection and inversely proportionate to the rate of thermalization; we would like to emphasize the distinction of the latter to the splitting time given by the inverse of (3.24).

For $b = 0.5$, close to the best-fit value of 0.48, and ignoring the x-dependence in the denominator of eq. 3.49, the energy density integral of (3.71) can be computed analytically; the numerical value of the proportionality coefficient on the RHS of (3.71) is then $a\pi + c/2 \simeq 1.4$, which is of order 1 as expected. Note further that the contribution due to the δ-function at $p = M/2$ to the integral in (3.71) is subdominant: this can be seen by noting that the latter contribution is set by the timescale $\propto t_{\rm split} = 1/\Gamma^{\rm LPM}_{\rm split} = t_{\rm therm}\sqrt{T/M}$, leading to a suppression of contributions from the $x \to x_{\rm M}$ region by a relative factor of $1/x_{\rm M}$. Finally, eq. 3.70 shows that a solution of the form (3.49) does indeed approach a growth $\propto M$ of the number density $dn/d\ln p$ at fixed p, as required by energy conservation (see also eq. 3.64).

With our numerical solution (3.49) established, we then moved on to present an example of how this spectrum of hard OoE particles affects observables in cosmology. To that end, we looked at the production of *heavy* DM from hard–hard and hard–soft scatterings. The inclusion of the LPM

effect results in a parametrically larger DM abundance, while our numerical results unambiguously fix the spectrum and the corresponding DM yield within an order of magnitude of previous analytical estimations. A sizeable suppression of the dark coupling α_χ discussed in Section 3.4 allows for an earlier kinetic decoupling of the species χ following production, as is the case for FIMP scenarios [19].

We mentioned in Chapter 1 that one may discuss other potential consequences of considering the full spectrum of thermalizing OoE particles. As discussed in the literature, non-relativistic and kinetically decoupled DM perturbations grow linearly in the EMD or IMD era, potentially affecting the matter spectrum of the late universe [74–76]. While difficult to preserve in scenarios where the bulk of (relativistic) DM is generated thermally or directly via matter decays at the end of reheating era [74], viable scenarios might be realized using non–thermal production, e.g. via near-threshold production of DM from hard–hard scatterings. Note that after production at the threshold, the resulting abundance could then be rendered non-relativistic as a result of the Hubble expansion. Finally, a population of long–lived χ's and its subsequent decay, can contribute to realizing cosmological processes, e.g. via formation of a later IMD eras and/or late entropy production, generation of the baryon asymmetry (see e.g. [77] with superparticle decays), and dilution of preexisting abundances [15, 19, 78].

In all the cases mentioned above, detailed knowledge of the spectra of OoE particles is integral to studying the corresponding processes. We may, therefore, ask if we may further improve our study of the OoE thermalizing particles. Even though we believe our numerical result of Chapter 3 to be more accurate and include more features than what was previously available in the literature, it clearly has some limitations. The most obvious issue is the inclusion of a single species of particles in the splitting cascade of thermalization. Note that in our treatment the Boltzmann equation (3.23), we have so far defined a single function $\tilde{n}(p)$ for the OoE spectrum of thermalizing particles. Similarly, we have assumed the presence of a single coupling constant α responsible for all processes involved in the splitting cascade, as well as the soft interactions responsible for the generation of thermal masses and the LPM suppression. Another closely related approximation we have used in Eq. (3.23) is the use of a single splitting kernel [79], given by eq. 3.16. The leading $E_{\rm d}^{-3/2}$ dependence on the energy $E_{\rm d}$ of the softer daughter particle results from a combination of the form of the vacuum rate for the emission of a near–collinear gauge boson and the corresponding LPM factor introduced in eq. 3.15, both of which depend on the nature of the parent and daughter particles.

Given the fact that the SM and a large number of BSM extensions include multiple coupled particles with different gauge couplings, gauge group representations, multiplicities, and spins, we may expect the relatively simple form of our current single–species analysis to be insufficient for describing the physics of thermalization in the early universe. In particular, the form of energy dependence in the splitting kernel will depend on the individual species; the emission of a gluon from a quark has a somewhat different kernel than that from another gluon. In addition, different species and interactions will in general, appear in the solution with different overall factors. The formalism developed here could be understood to hold for a suitable average over particle species. Considering the inevitable degeneracies in parameter combinations[19] and the limited accuracy of a single–species analysis, our results in Chapter 3 should suffice for constraining model parameters on a logarithmic scale. In a more precise treatment, one has to differentiate between different species of particles in the cascade, i.e. our single integral Boltzmann equation will have to be replaced by a set of coupled integral equations.

[19] Note, , e.g., that an $O(1)$ change of the splitting rate $\Gamma^{\rm split}_{\rm LPM}$ can be compensated by a change in the decay width $\Gamma_{\rm M}$ of the parent particle, without invalidating (3.70)

This will be the subject of Chapter 4.

To conclude this chapter, let us briefly note that we believe the presence of the hard IR cutoff, parameterized by the $O(1)$ parameter κ not to be particularly problematic (see also the discussion of IR cutoffs in [70]). We showed in Section 3.3.2 that the choice of κ only affects the spectrum of OoE particles with momenta which are either not much larger than T (where the non-thermal spectrum gets swamped by the thermal contribution anyway), or where $M/2 - p$ is of order T (where the difference between p and $M/2$ should be immaterial for all practical applications). More realistically, however, one should recognize that at very low energies, there is an eventual smooth crossover into the regime where elastic processes in the thermal bath become competitive as an energy transfer mechanism. As we will later see in Chapter 4, $2 \to 2$ processes could further be crucial in establishing the chemical equilibrium (see eq. 2.18). These processes, however, continue to be relatively unimportant so long as we are interested in the spectrum of HE particles with $p \gg T$; we will therefore continue to use the same framework of a cascade of splitting processes with a hard IR cutoff in the next chapter.

CHAPTER 4

The Standard Model of particle physics and thermalization cascades in the early universe

4.1 A cascade of Standard Model particles

In Chapter 1, we motivated studying the dynamics leading to the equilibration of highly energetic out of equilibrium (OoE) particles in the early universe plasma and how such a study could prove crucial to our understanding of other cosmological observables [80–83], e.g. the abundance of DM [18, 19, 28, 30, 41, 42, 52, 68, 73, 84–95]. The hard non–thermal particles can most generically result from the decay of scalar fields abundant in top–down approaches to the history of the universe; examples include theories of inflation or additional "moduli" fields. Such scalar fields are initially displaced from their low energy minima around which they oscillate at later times; if the potential around the minimum can be described by a quadratic function, the oscillating field corresponds to a non–relativistic (matter) component [15, 20, 25, 53], resulting in a universe described by the energy densities of eq. 3.1. Given enough time, a matter component will grow to dominate the energy density of the universe prior to its decay, which is bound to occur before the onset of BBN at a temperature of about 1 MeV [29, 54, 96].

The success of the BBN points [15] to the universe having been dominated by a bath of relativistic radiation in thermal equilibrium. In Chapter 2, we discussed the composition and properties of this thermal bath and its effect on gauge–interacting particles propagating through the thermal medium. We saw that subsequent forward scattering interactions with particles from the thermal plasma can be thought of as resulting in an effective thermal mass for the particle traversing the thermal bath. We further saw that for certain processes involving interactions with particles from the background plasma, individual interactions with medium particles cannot be treated as independent and one needs to coherently add multiple contributions to the corresponding matrix element. This phenomenon was then formulated in the form of an *effective kinetic theory*. In case of the kinetic theory of collinear splittings of gauge–interacting particles, the effective theory is achieved by the inclusion of the LPM resummation [35, 36] resulting in a parametric suppression of the collinear splitting rate.

In Chapter 3, we turned to the process of thermalization of gauge–interacting OoE hard particles. Highly collinear gauge–mediated $2 \to 3$ splittings were identified as the leading contribution [39, 41, 42, 45, 52, 61], allowing for a growth of the number density of high energy particles and simultaneously reducing the average energy of the out of equilibrium particles. We then used our knowledge from

Chapter 2 to deduce that coherent multiple scatterings with the background plasma play a key role in setting the rate of these splitting processes. We saw that the destructive interference between coherent interactions of the parent and daughter particles with the background thermal plasma leads to a parametrically suppressed splitting and therefore thermalization rate, increasing the number density of hard OoE particles. To simplify the problem for a first step study, we limited our attention to the thermalization of a mono–energetic injection of initial decay products consisting and proceeding via interactions of a single species of non–abelian gauge bosons; in the symmetric phase of the SM, these could be identified with either weak gauge bosons or gluons. We then used the corresponding LPM–suppressed splitting rates to write down the Boltzmann equations for the effective kinetic theory of thermalization. After reducing the number of model–dependent parameters via a convenient dimensionless formulation of the Boltzmann equations, we proceeded to the numerical solution. We could further use the latter to deduce a parametric fit function describing the properties of the solution spectrum of OoE particles in the entirety of the solution domain. We concluded Chapter 3 by outlining an example of the application of a spectrum of the form (3.49) in calculating cosmological observables such as the DM abundance; we reaffirmed that the parametric LPM–suppression of the thermalization rate, along with the gradual growth in the number density of OoE particles through particle creation, allows for sizeable non–thermal production of *heavy* relics.

The "pure–gauge approximation" of Chapter 3 was partly motivated by the fact that, as we will see in more detail in Chapter 4, gauge boson emissions in a plasma are typically favoured by a combination of larger $\mathcal{O}(1)$ group factors, gauge boson emission enhancements, and in some cases statistical enhancement and blocking factors [97]. This general picture, together with our results in Chapter 3, already allow us to speculate about the composition of the OoE particles when we allow for the presence of other SM species. The dominance of the $SU(3)_C$ interactions by gauge coupling strength and the larger number of available gauge bosons, allows one to conjecture that irrespective of the initial decay products, the energy density of the plasma of thermalising particles can be expected to flow towards the colored sector and in particular to gluons. In this regard, thinking of our single–species spectrum of OoE particles from Chapter 3 as a pure gluon plasma is a better approximation than that of $SU(2)$ gauge bosons.

It is, nonetheless, evident that the simplicity of a thermalization cascade consisting of a single species of non–abelian gauge bosons severely restricts the precision and applicability of our results from Chapter 3. In particular, even for an initial population of non–abelian gauge bosons resulting from decays of the matter component, fermions are expected to appear in the thermalization cascade via splittings of a gauge boson to a fermion pair. In the case of reheating after inflation, while gauge bosons could be produced efficiently at early stages of reheating in some scenarios, the completion of the energy transfer from the inflation field to the visible sector can typically involve decays to fermions; the latter is also true for other scenarios of a matter component mentioned in Chapter 1 (see e.g. Section 2.1 of [20]).

Our single–species spectrum from Chapter 3 is further insufficient when used to calculate cosmological observables, such as DM abundance. Evidently, BSM scenarios can be sensitive to the presence of particles other than gauge–bosons; in particular, we expect the DM to be a singlet under the SM gauge group and not to directly coupled to the SM gauge bosons. The calculation in Chapter 3 does not answer the question of how quickly the *chemical* composition[1] of the plasma flows towards the

[1] As motivated in Section 2.3, will always assume vanishing chemical potential in this work; by the chemical composition we merely mean the relative abundance of various species. Consequently, we will not distinguish between particles and

colored QCD gauge bosons, nor does it yield other subdominant contributions to the total OoE number density. Our exemplary calculation in Section 3.4 should, therefore, be understood as merely allowing for the production of DM from gauge bosons and via higher order processes, severely limiting the precision and applicability of the spectrum (3.49).

In this chapter, we will seek to address the above shortcomings by expanding our analysis to include other SM particles and interactions. This will require us to consider additional interactions, both among the HE particles, as well as with the background thermal plasma. We need to use the correct form for different vacuum splitting kernels, and include the variations in the LPM suppression factor corresponding to the different Abelian and non–Abelian interactions of the charged particles involved in the splitting process. Fortunately, this task is somewhat simplified by adopting the results developed in the literature for the study of a quark–gluon plasma (QGP) for our purpose of studying the cosmic plasma of massless SM particles.

The process of energy loss of energetic gauge interacting particles in the presence of a thermal background has been extensively studied in the context of heavy ion collision (HIC) and the thermalization of the resulting QGP [49, 63, 79, 98, 99]. Here, the thermalization procedure evolves the initial non–thermal spectrum of energetic partons traveling mostly along the beam directions towards a thermal distribution of quarks and gluons. As color exchange is the dominant interaction in the QGP, studies in this area typically focus on colored matter and $SU(3)_C$ interactions. Additionally, as the photon spectrum serves as a probe of the QGP, the emission of photons from the QGP and from electromagnetic plasmas have also been studied using the same machinery [64–66]. We will use these to extend the relevant process rates and LPM suppression factors to the case of chiral $SU(2)_L$ and $U(1)_Y$ interactions fit for our purpose of studying the process of thermalization in the unbroken phase of the SM.

The analogy between cosmological thermalization and thermalization at colliders is not universal, but rather well motivated. As mentioned in Chapter 1, both the maximum temperature of the cosmic plasma and the mass scale of the decaying component in the early universe are largely model–dependant and can be in a range of several orders of magnitude. Similarly, the reheating temperature can be as low as a few MeV [96] or as high as 10^{15} GeV [3]. For a majority of possible cosmological histories with a reheating temperature above that of the electroweak phase transition at $T_c = \mathcal{O}(100\,\text{GeV})$, the electroweak symmetry and therefore the entire standard model gauge group is intact. As a result, there is an increased similarity to the case of thermalization in HIC where $SU(3)_C$ and $U(1)_{\text{EM}}$ interactions are considered and, although potentially on a very different energy scale, the physics of thermalization following matter decay is expected to be realized via the very same mechanisms as in the case of quark gluon plasma resulting from HIC experiments [100].

In this chapter, we will use this analogy to extend the analysis in Chapter 3 to include all non–scalar species of the standard model in the thermalization cascade of energetic particles resulting from the decay of a cosmological matter component. This chapter is organised as follows. In Section 4.2 we review the framework of thermalization via gauge mediated collinear splitting processes including the LPM effect, with a focus on allowing for the individual particles involved in the splitting process possessing different gauge interactions with the background thermal medium following in Section 4.3. Section 4.4 includes a formulation of the Boltzmann equations governing the number density of the various species we include in our analysis. The resulting set of Boltzmann equations will be numerically solved and their results presented and discussed in Section 4.5. In Section 4.6 we

antiparticles.

exemplify the application of our results by sketching how to compute the production of massive particles in annihilation reactions involving particles from the thermal bath and the HE thermalization cascade. We then conclude in Section 4.7 with a summary and some final remarks.

4.2 Thermalization via a splitting cascade of multiple particles

In Section 3.1.2 we established the role of gauge mediated $2 \to 3$ splitting processes in the process of thermalization of a gauge interacting HE particle. We limited our attention to interactions of a single species of non–abelian gauge bosons, so that all particles in the splitting cascade will interact similarly with particles from the background thermal plasma. These interactions were responsible for *kicking out of coherence* the daughter particles in a splitting process via momentum transfers typically of the order of the thermal mass of the non-abelian gauge boson. In this setup, we saw that the LPM suppression factor was governed by the softer of the two daughter particles.

Our first task in this chapter will be to retrace our steps from Chapter 3 and account for the presence of different SM particles and interactions. Assuming the existence of a thermal bath of temperature T, we will be focusing on the thermalization of energetic particles of species s and energy $p \gg T$, via interactions with the bath. As outlined in Section 3.1.2, the large energy of OoE particles suppresses the cross section for $2 \to 2$ interactions except for $t-$ and $u-$channel forward scattering via exchange of a massless gauge boson [61]. Notably, the arguments for the dominant rate of the these processes relies on the Lorentz structure of the cross section and not the couplings; they therefore extend naturally to the case with multiple particles and interactions. The vacuum cross section for the forward scattering process involving the exchange of massless gauge bosons is IR–divergent and this divergence is regulated by the thermal mass, which can be approximated by

$$m_G^{\text{th}}(T) \approx g_G T \,. \tag{4.1}$$

In this approximation, $G \in \left\{C = SU(3)_C, W = SU(2)_L, Y = U(1)_Y\right\}$ denotes the gauge group corresponding to the dominant interaction in the scattering process; despite slight differences in group factors, this simple choice provides a very good approximation for our purpose here (see Appendix B). Fig. 4.1 shows schematically such elastic processes, with time flowing from left to right and the cross denoting a coupling to a particle in the thermal bath as introduced in Fig. 3.1. As outlined in Chapter 3,

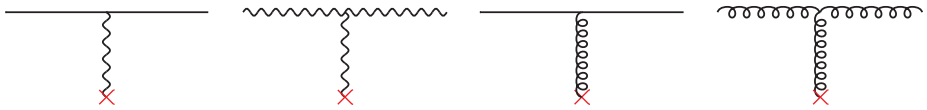

Figure 4.1: Examples of scattering processes of energetic particles from the SM, on the thermal bath mediated by a gauge boson; the former is denoted by the line on top while the latter is represented by the cross at the bottom. The intermediate gauge boson should be considered as having acquired the thermal mass (4.1).

forward scattering is an inefficient means of energy loss for the HE parent particles. In the presence of a thermal bath, typical elastic scattering reactions will have $|t| \sim \left(m_G^{\text{th}}\right)^2$, and hence a momentum exchange

$$\delta k_G^{\text{el}} = m_G^{\text{th}} \,. \tag{4.2}$$

with a rate

$$\Gamma^s_{\text{el}} \approx \tilde{g}^s_* \alpha_G T \equiv 1/t^s_{\text{el}}\,, \tag{4.3}$$

where, parallel to what we had in Eq. (3.4), the factor $\tilde{g}^s_*$ is introduced to include the order unity group factors for the elastic scattering of species s. Similarly, t^s_{el} denotes the timescale between successive elastic scatterings of a particle of species s. By themselves, these soft elastic processes would need $O\left(p/m^{\text{th}}_G\right)$ scatterings, i.e. the thermalization time would scale as $1/p$. The same issue disfavours hard elastic scattering reactions (3.3a), which can lead to much larger energy transfer in a single scattering event, but whose rate is similarly suppressed by $1/p$.

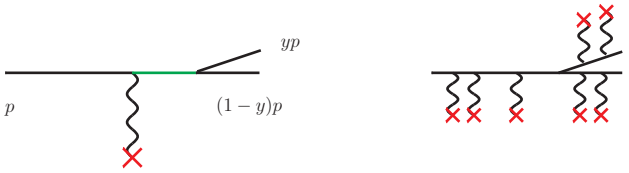

Figure 4.2: (Left) Schematic of splitting processes after scattering on the thermal bath mediated by a gauge boson. Here the solid lines represent fermions or gauge bosons. The parent particle can lose a significant fraction y of its momentum p, see eq. 4.4. The small momentum transferred by the intermediate boson implies that the connecting propagator – depicted in green – is close to the mass shell. (Right) Multiple couplings of the particles involved in the splitting process to the thermal bath of temperature T; many soft processes are required for the loss of collinearity and consequently coherence of the splitting process.

Despite their small momentum transfer, we saw in Chapter 3 that soft elastic processes play a key role in the energy loss process of hard OoE particles, by kicking the scattering particle off the mass shell so that the outgoing particle can then lose up to half its energy in a $1 \to 2$ (or $2 \to 3$) splitting process. Fig. 4.2 (left) shows such a splitting reaction, and defines our convention for the momenta of participating particles. In contrast to elastic processes, the maximal energy loss is not restricted by the virtuality of either the exchanged gauge boson or of the scattered particle. The daughter particles can carry away a large fraction

$$y \equiv k/p \tag{4.4}$$

of the parent's energy, while the virtuality of the intermediate gauge boson is still of the order of its thermal mass given in Eq. (4.1).

With the introduction of multiple particle species, a first deviation from our analysis in Chapter 3 comes about by realising that the collinear splitting process giving rise to the daughter particles could proceed via a different interaction, with a coupling $\alpha_{G'} \leq \alpha_G$, than that of the dominant $t-$channel gauge boson exchange. Consider as an example, the process of energy loss for a SM quark traversing the thermal plasma. In this example, the dominant contribution to the quark thermal mass would be due to interactions of the $G = SU(3)_C$ group; splitting processes in this case could proceed via the emission of $SU(3)_C$, $U(1)_Y$, or $SU(2)_L$ depending on the chirality state of the quark. The most frequent splitting processes are those involving the largest coupling, favouring the emission of gluons in this case.

The arguments we made in Section 3.1.1 regarding the hierarchy of timescales for the elastic and splitting processes are nevertheless still valid in the presence of multiple gauge groups. In the absence of coherent effects, the collinear splitting rates can be thought of to be suppressed by a factor $\alpha_{G'}$ relative to the dominant elastic scattering. These higher order processes nevertheless dominate the

energy loss since only $O(\log(p/T))$ of these reactions are required for the thermalization of the parent particle. Were we to ignore medium effects, we would get the so–called Bethe–Heitler differential rate for these processes:

$$\frac{d\Gamma^{\mathrm{BH}}_{\mathrm{split}}}{d\log k} \sim \alpha_{G'}\Gamma^{s}_{\mathrm{el}} \leq \alpha_G^2 T\,, \tag{4.5}$$

corresponding to a time between subsequent splitting reactions $t_{\mathrm{BH}} \equiv \Gamma^{\mathrm{BH}\ -1}_{\mathrm{split}}$. The corresponding formation time for the splitting process is, as before, connected to the virtuality of the intermediate state. In the rest frame of the thermal medium this is of order $p/(m^{\mathrm{th}}_{\mathrm{G}})^2$, which is much longer than the time between successive soft elastic scatterings of eq. 4.3.

One should therefore coherently add up all possible contributions to a splitting process, schematically depicted on the right in Fig. 4.2. A bit more caution is warranted in interpreting Fig. 4.2: in this schematic representation, not only does the interaction responsible for the splitting process potentially differ from that of gauge interactions with the plasma, but these interactions are also potentially different for the parent and daughter particles involved in the scattering. In our previous example of a HE quark losing energy via collinear emissions of gauge bosons, the emission of an abelian $U(1)_Y$ boson from the quark would imply the resulting abelian gauge boson not to have any gauge–mediated interactions with the background plasma particles. Despite the extra complication introduced by the presence of multiple species and interaction, the coherent effect of multiple interactions with the background plasma leads, as discussed in Chapter 3, to a reduced splitting rate; this LPM suppression effect is the topic of Section 4.3.

4.3 The LPM effect for multiple species and interactions

As we saw in Section 2.5, and more specifically in eq. 2.50, the formal inclusion of the LPM effect requires coherently summing the many diagrams corresponding to thermal interaction insertions of Fig. 4.2. The formal procedure may also be reformulated as a variational problem that is more readily numerically tractable [64, 66]. Alternatively, one may use physical arguments like the ones we used in Chapter 3 to deduce the generic form of the LPM suppression factors for splitting processes involving different types of particles. We will therefore begin by retracing our steps from Section 3.1.3 while keeping the species-dependence of the various rates and momentum transfers explicit.

Remember that the LPM suppression of collinear splittings results from the destructive interference among multiple splitting matrix elements, or equivalently, from the fact that the HE particle is unable to physically distinguish multiple scattering sites in the background medium so long as they lie within the coherence region of one another for a specific splitting process. The key parameter setting the magnitude of the rate suppression is therefore the *coherence*, which can be understood to last as long as the phase factor accumulated in successive soft scattering reactions is small. Equivalently, the suppression can be thought to last so long as the cumulative effect of multiple soft processes kick the outgoing collinear particles out of coherence.

We will stick to our notation from Section 3.1.3 and work in the rest frame of the thermal bath, which in our application corresponds to the cosmological rest frame. We use coordinates where the parent particle propagates along the z axis, and the splitting occurs at $x^{\mu}_{\mathrm{split}} = 0$. Denoting the time elapsed traversing the thermal bath by δt, the trajectory of the emitting particle and the 3−momentum

of a daughter particle of energy $k \gg T$ are then given by

$$\vec{x}(\delta t) \simeq \delta_t (\sin\theta\, \hat{e}_\perp + \cos\theta\, \hat{e}_z)\,, \quad \vec{k} \simeq (k_\parallel\, \hat{e}_z + k_\perp \hat{e}'_\perp)\,, \tag{4.6}$$

where $\hat{e}_\perp$ and $\hat{e}'_\perp$ are (in general independent) unit vectors in the (x, y) plane. Recall that we are interested in collinear splitting. The transverse momentum $k_\perp \ll k$ of the daughter particle, as well as the deviation $\theta \ll 1$ of the emitter from the initial z direction therefore only result from the soft interactions of the form shown in Fig. 4.1. We can therefore approximate $\sin\theta \simeq \theta$, $\cos\theta \simeq 1 - \theta^2/2$ and $k_\parallel \simeq k - k_\perp^2/(2k)$.

Crudely, one may say that the coherence, and hence the interference, persists as long as the accumulated phase satisfies

$$\delta\phi = k \cdot x \simeq \delta t \left(-k_\perp \theta\, \hat{e}_\perp \cdot \hat{e}'_\perp + k\frac{\theta^2}{2} + \frac{k_\perp^2}{2k} \right) \leq 1\,. \tag{4.7}$$

Note that, compared to our previous account in Section 3.1.3 (see discussion before eq. 3.12), eq. 4.7 now retains information about the individual momenta of the daughter particles in the form of independent evolutions for the transverse momenta $k_\perp$ and the deviation angle θ. This is because we are looking to allow for independent evolution of momenta of particles with different interactions with the thermal background plasma.

So long as (4.7) is satisfied, further splittings are not possible due to the destructive interference reducing the "effective" background plasma density as perceived by the HE particles undergoing energy loss via collinear splittings. The angle $\theta\,(\delta t)$ similarly encodes the evolution of a transverse momentum as

$$\theta(\delta t) \simeq p_\perp(\delta t)/p\,. \tag{4.8}$$

The accumulated phase is therefore of order

$$\delta\phi \sim \delta t \left(\frac{k_\perp p_\perp}{p} \oplus \frac{k p_\perp^2}{2p^2} \oplus \frac{k_\perp^2}{2k} \right)\,. \tag{4.9}$$

The $\oplus$ symbol in eq. 4.9 should be understood as indicating that the comprising terms should be added in quadrature, reflecting the statistical nature of the random walk of the transverse momentum vectors in the transverse direction; this is also in line with the quadratic addition rule used for the single random walk of $k_\perp$ in Section 3.1.3. Here, however, both the emitter and emitted particles undergo a random walk through multiple scatters on the thermal background. In this intuitive picture, the evolution of the transverse momenta of the two outgoing collinear particles occurs via random soft kicks from the thermal background.

During a time δt, there will be $\delta t/\delta t_{\rm el}$ "steps", with "step size" $\delta k_{\rm el}$ for each particle with its respective interactions. The hierarchy of the different contributions in (4.9) will then depend on the specifics of the splitting process, including the interactions and momenta.

Let us first look at the case where both emitted particles interact with particles from the background

plasma with similar strength. In this case we will have for the transverse momenta

$$\left\langle k_{\perp}\right\rangle (\delta t) \simeq \left\langle p_{\perp}\right\rangle (\delta t) \simeq \sqrt{\frac{\delta t}{\delta t_{\rm el}}}\,\delta k_{\rm el} \simeq \delta t^{1/2}\Gamma_{\rm el}^{1/2}\delta k_{\rm el}\,. \tag{4.10}$$

In this case, the accumulated transverse momenta are comparable for the two daughter particles; therefore, for hard (symmetric) splittings, where $k \sim p$, all three terms in eq. 4.9 will be of the same order. On the other hand, if one of the particles is much softer than the other, say $k \ll p$, the third term will dominate the evolution of the accumulated phase. As discussed in Chapter 3, such emissions of a soft particle are more likely as the dominance of the third term of (4.9) reflects the fact that a softer emitted particle will be kicked out of coherence more easily; furthermore, the soft emissions will be further enhanced due to the soft emission enhancement we have disregarded in our calculations.

For the case where all particles that participate in the splitting have roughly equal coupling strength to the thermal bath, we can thus approximate the phase $\delta\phi \sim \delta t k_{\perp}^2/k$, with the understanding that k denotes the momentum of the softer daughter particle. The coherence time, defined by $\delta\phi(t_{\rm coh}) = 1$, is given by

$$\delta t_{\rm coh} \sim \sqrt{\frac{k}{\Gamma_{\rm el}\delta k_{\rm el}^2}}\,. \tag{4.11}$$

Recall that the next splitting reaction can only happen at $t > \delta t_{\rm coh}$; this can be described by reducing the plasma density and therefore the interaction rate by a factor

$$R_{\rm LPM}(k) \simeq \delta t_{\rm coh}^{-1}\delta t_{\rm el} = \sqrt{\frac{\delta k_{\rm el}^2}{k\Gamma_{\rm el}}}\,, \tag{4.12}$$

in agreement with our discussion in Section 3.1.3, where both daughter particles were of the same species and therefore had similar interactions with the background plasma.

Let us now turn to the case where the particles involved in the splitting process differ in their interactions with the thermal plasma. To emphasise the effect of different interactions, let us next look at the special case where the emitted particle basically does not couple to the thermal bath via $t-$ channel gauge–mediated processes, as in $q \to \gamma q$, where γ represents the SM photon [2]. In the particular case of an Abelian gauge boson, the absence of $t-$channel soft scattering processes on the thermal bath implies that its momentum, originating from the splitting process itself, can be considered a constant within our framework. We can then choose its direction, rather than that of the parent particle, to define the z axis, i.e. $k_{\perp} = 0$.

Going back to eq. 4.9, an absence of soft transverse kicks to the photon implies that only the second term survives. Defining once gain the coherence time via $\delta\phi(\delta t_{\rm coh}) = 1$ and using eq. 4.10 for the evolution of $p_{\perp}$, we have

$$\delta t_{\rm coh} \sim \sqrt{\frac{p^2}{k\Gamma_{\rm el}(\delta k_{\rm el})^2}}, \quad R_{\rm LPM}(k) \sim \sqrt{\frac{k\delta(k_{\rm el})^2}{p^2\Gamma_{\rm el}}}. \tag{4.13}$$

[2] We will be facing the $U(1)_Y$ gauge boson B in our setup of thermalization in the unbroken phase of the SM; the arguments, however, remain the same and here we use the photon merely for convenience.

Let us take a moment to compare (4.13) to the LPM suppression in the symmetric case (4.12). A first, rather obvious lesson we learn from the comparison is the confirmation that the form of the LPM suppression depends on the interactions of individual particles involved in a splitting process with the background particles in the thermal plasma. In fact, the suppression in (4.13) favors the emission of harder photons, in apparent contrast to what we had in (4.12) for gluon emission. Both cases, however, can be seen to stem from the same underlying physics. Additionally, the emission of a harder Abelian photon in (4.13) implies a softer second daughter particle, whose existing soft elastic scatterings with the plasma can therefore result in a faster growth of θ and hence earlier loss of coherence.

Before we move on to presenting explicit expressions for LPM–corrected rates calculated in the literature for the many available processes of the standard model fermions and gauge bosons, we may summarize the results of our physical arguments for the LPM suppressed splitting rate as follows. The rate for a process can be decomposed as the result of the splitting rate in vacuum, using the thermal gauge boson mass (4.1) as infrared regulator, and the corresponding suppression factor:

$$\frac{d\Gamma^{\text{split}}_{\text{LPM}}\left(s(p)\rightarrow s'(k)+s''(p-k)\right)}{dk}=\frac{d\Gamma^{\text{split}}_{\text{vac}}\left(s(p)\rightarrow s'(k)+s''(p-k)\right)}{dk}\times R_{\text{LPM}}\left(k,s'\right)\,, \tag{4.14}$$

where

$$R_{\text{LPM}}\left(k\right)\propto\begin{cases}\sqrt{\dfrac{kT}{p^2}} & s'=\texttt{Abelian GB}\\ \sqrt{\dfrac{T}{\min\left(k,p-k\right)}} & \texttt{others}\end{cases}\,. \tag{4.15}$$

Here s is the parent particle and s', s'' are the two daughter particles.

Even though it helps establish the physical significance, the heuristic derivation given here does not allow to derive exact numerical factors for the LPM–suppressed rates. In particular, we have assumed that the transverse momenta evolve exclusively by the cumulative effect of "soft" kicks of δk_{el}. Although the latter assumption is based on soft kicks occurring most often, we saw in Section 2.5 that the less frequent harder elastic processes also contribute to the random walk evolution of the transverse momenta. The inclusion of processes with momentum transfer $q > \delta k_{\text{el}}$ enhances the final splitting rate by a so–called Coulomb logarithm of order $\ln(p/T)$ (see Fig. 2.4). Similarly, in the general case, the magnitude of the various contributions to decoherence via (4.9) could be comparable, so that the suppression factor will have a more complicated form. This, we will turn to in Section 4.3.1; as we will see, the results of careful calculations indeed reproduce the behavior given by eq. 4.14 and 4.15 in the corresponding regimes.

4.3.1 LPM suppressed splitting rates in leading logarithmic approximation

As mentioned earlier, the study of relativistic heavy ion collisions requires knowledge of various elastic $2 \rightarrow 2$ scattering as well as splitting processes, where the inclusion of coherence effects is crucial. Additionally, the relative accessibility of the QCD plasma in an experimental setup allows for precision observations, and has therefore called for detailed calculation of process rates [65, 100]. The process of energy loss of highly energetic OoE colored plasmas has therefore been studied in the literature using thermal field theoretical methods briefly introduced in Section 2.3, and to different levels of precision for QCD [101]. However, as the processes of interest are gauge interactions, process

rates can be expressed in terms of the couplings and group–theoretical factors; this in turn allows for straight–forward generalization of these formal results to other gauge groups and gauge interactions of the SM.

This is the path we will follow here. We limit our attention to the gauge interactions of the SM and mostly rely on the results obtained in [79], whose notation we also largely adopt; we, however, use physical arguments similar to what was presented in Section 4.3 to generalise the results to allow for two separate gauge groups being responsible for the splitting process and the gauge-mediated scattering of the three particles involved in a splitting off the thermal bath. We will discuss the proper choice of parameters corresponding to each of these two gauge groups shortly.[3]

Generically, the LPM corrected rate for the various splitting reactions can be written as

$$\frac{d\Gamma^{\text{split}}_{\text{LPM}}\left(s(p) \to s'(k) + s''(p-k)\right)}{dy} = \frac{(2\pi)^3}{p\nu_s^{G'}}\,\gamma_{s\to s's''}\left(p, yp, (1-y)p\right)\,. \tag{4.16}$$

Here y is the momentum fraction carried by the species s' as previously used in (4.4), and the averaging factor $\nu_s^{G'}$ is the number of spin degrees of freedom for the species s times $d_s^{G'}$, the dimension of its gauge representation under the gauge group G'. For example, a gluon has $\nu_g^{SU(3)} = 2\times 8 = 16$ and for a quark $\nu_q^{SU(3)} = 6$; note also that the assignment of $\nu_s^{G'}$ also depends on the gauge group G' so that an $SU(2)_L$ –charged quark also has $\nu_q^{SU(2)} = 4$.[4]

The bulk of information about the splitting process is encoded the in the LPM–corrected *splitting functions* $\gamma_{s\to s's''}(p; yp, (1-y)p)$. Here s, s' and s'' stand for either a fermion F or a gauge boson A. Therefore, equations 4.17a, 4.17b and 4.17c respectively describe pure gauge splittings like $g \to gg$ or $W \to WW$, gauge boson emission from a fermion like $q \to gq$ or $l \to Wl$, and splitting of a gauge boson to a fermion antifermion pair like $g \to q\bar{q}$ or $W \to l\bar{l}$. Note that $\gamma_{A\to AA} = 0$ for $U(1)$ interactions.

[3] Note that we are interested in the splitting rate per parent particle, while in the literature the total emission rate of daughter particles is often reported per unit time and volume of a thermal plasma [64–66]; care must be taken when adopting results from the literature for comparison in these cases. Moreover, as motivated in Chapter 3 (see discussion following (3.25)) we neglect all Bose enhancement and Fermi blocking factors; this is justified since we are only interested in particles with energy much above T, which have very low occupation numbers.

[4] Once electroweak interactions are included one has to distinguish between fermions of different chirality, since in the SM only left–handed fermions and right–handed antifermions have $SU(2)$ interactions. We will comment in the next subsection on the required changes to our expressions.

To leading logarithmic approximation, the corrected splitting functions are given by [79][5]:

$$\gamma_{A\to AA}(p;yp,(1-y)p) = \frac{d_A^{G'}C_A^{G'}\alpha_{G'}}{(2\pi)^4\sqrt{2}}\frac{1+y^4+(1-y)^4}{y^2(1-y)^2} \cdot \left[m_{\rm th}^2\hat{\mu}_\perp^2(1,y,1-y;A,A,A)\right]_G ; \tag{4.17a}$$

$$\gamma_{F\to AF}(p;yp,(1-y)p) = \frac{d_F^{G'}C_F^{G'}\alpha_{G'}}{(2\pi)^4\sqrt{2}}\frac{1+(1-y)^2}{y^2(1-y)} \cdot \left[m_{\rm th}^2\hat{\mu}_\perp^2(1,y,1-y;F,A,F)\right]_G ; \tag{4.17b}$$

$$\gamma_{A\to FF}(p;yp,(1-y)p) = \frac{d_F^{G'}C_F^{G'}\alpha_{G'}}{(2\pi)^4\sqrt{2}}\frac{y^2+(1-y)^2}{y(1-y)}\times N_{\rm fl} \cdot \left[m_{\rm th}^2\hat{\mu}_\perp^2(1,y,1-y;A,F,F)\right]_G . \tag{4.17c}$$

Let us take a moment to elaborate on the structure and notation of (4.17). Firstly we have again labeled with G the gauge group responsible for the (dominant) scattering processes on the thermal background, while gauge group G' is responsible for the splitting process $s \to s's''$. Note that assigning a single gauge group G to the soft elastic interactions implies we neglect subdominant contributions to the soft scattering; e.g. we will assume the evolution of the transverse momenta of HE quarks results from gluon–mediated soft elastic scatterings , i.e., soft processes mediated by an $SU(2)_L$ gauge boson are ignored in this approximation. The gauge group G' on the other hand, is uniquely determined by the identity of the involved gauge boson(s) in the splitting process $s \to s's''$.

The first term in each splitting function captures the physics of the splitting process without the plasma effects, and thus loosely corresponds to $\Gamma_{\rm vac}$ in (4.14). The representation dimension $d_s^{G'}$ was introduced below (4.16), and the remaining parameter $C_s^{G'}$ is the quadratic Casimir corresponding to the gauge group G'; these group and $O(1)$ factors correspond to what we subsumed into the constant $\sqrt{\tilde{g}_*}$ in Chapter 3 (see e.g. eq. 3.16).

Within the SM, with the fermions and bosons in fundamental and adjoint representations respectively, we have for the group $SU(N)$:

$$C_F = \left(N^2-1\right)/2N\,, \qquad C_A = N\,, \qquad d_F = N\,, \qquad d_A = N^2-1, \tag{4.18}$$

while for a $U(1)$, we have

$$C_F^s = Y_s^2, \qquad C_A = 0\,, \qquad d_F = 1, \qquad d_A = 1\,, \tag{4.19}$$

with Y_s denoting the $U(1)_Y$ charge of the corresponding fermion.

The second term in the set of equations 4.17 are the fragmentation functions, encoding the preference of the splitting reaction in redistributing the momentum of the parent particle into the two daughter particles. The y–dependence of the different fragmentation functions is determined by the structure of the relevant three–point vertex; up to a factor $1/[y(1-y)]$ it is the same as that of the splitting functions appearing in the Dokshitzer–Gribov–Lipatov–Altarelli–Parisi (DGLAP) equations [102–104]. The parameter $N_{\rm fl}$ in eq. 4.17c quantifies the number of indistinguishable Dirac fermions that the gauge boson A can split into. For the $SU(2)$ and $U(1)_Y$ gauge bosons splitting into $q\bar{q}$ pairs this will always

[5] As mentioned before, results from the literature and in particular [79] deal with the case $G = G' = SU(3)_C$.

include a color factor of 3; $N_{\rm fl}$ may be considered to be larger if several quarks (of different generations, say) are considered indistinguishable, as we will do shortly.

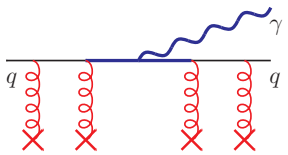

Figure 4.3: Photon bremsstrahlung (blue, $G' = U(1)_{\rm EM}$) from a quark interacting strongly with colored plasma particles (red, $G = SU(3)_C$). The resulting rate is of order $\alpha_G \alpha_{G'}$.

The third set of terms in eq. 4.17, denoted by the brackets and the subscript $[\ldots]_G$, can be thought of as representing the background plasma of temperature T, describing the scattering target density, the momentum transfer for the $2 \to 3$ scattering process, as well as the LPM suppression effects. As mentioned earlier, although SM matter fields can be charged under several gauge groups, one simplifying assumption is to consider only the dominant interaction of each species with the background plasma and for the assignment of G.

Consider once more, in the broken phase of the SM, the process of emission of a photon from a QGP via the splitting process $q \to \gamma q$ depicted in Fig. 4.3. In the first term of eq. 4.17, we assigned $G' = U(1)_{\rm EM}$ as the gauge group responsible for the emission of the photon, corresponding to the blue sections of Fig. 4.3. This splitting process however relies on interactions with the hot plasma and the same interactions also provide the coherent suppression effect, shown in red in Fig. 4.3. As can be seen, the latter class of processes will be dominated by the strong interactions of the colored quarks, so that $G = SU(3)_C$. In this formulation, the non–colored photon comes with a corresponding group factor of $C_\gamma = 0$. Our approximate treatment therefore implies that we will neglect the electroweak interactions of the quarks with the background plasma; similarly, we ignore hypercharge interactions of $SU(2)$ doublet leptons with the background particles.

In the formulation of [79] the effect of the number density of the thermal background plasma particles and momentum exchange amplitude via soft elastic processes is expressed via the thermal mass $m_G^{\rm th}$. In these terms, the function $\hat{\mu}_\perp^2$ on the RHS of eq. 4.17 can, in leading log approximation, be universally written as

$$\hat{\mu}_\perp^2(y_1, y_2, y_3; s_1, s_2, s_3) \simeq \frac{g_G T}{m_G^{\rm th}} \left[\frac{2}{\pi}\, y_1 y_2 y_3\, \frac{p}{T}\right]^{1/2} \left\{\left[\tfrac{1}{2}(C_{s_2} + C_{s_3} - C_{s_1}) y_1^2 + \tfrac{1}{2}(C_{s_3} + C_{s_1} - C_{s_2}) y_2^2 + \tfrac{1}{2}(C_{s_1} + C_{s_2} - C_{s_3}) y_3^2\right] \ln(\sqrt{p/T})\right\}^{1/2}. \tag{4.20}$$

Equation (4.20) encodes the LPM effect for a splitting process $s_1 \to s_2 s_3$; the various Casimir factors originate from the coupling of the three particles involved in the thermal plasma to the thermal bath. The coupling constant g_G cancels in eq. 4.20 due to $m_G^{\rm th}$ appearing in the denominator.

We are now in a position to see how the explicit form of eq. 4.20 reproduces our physically motivated results in equations 4.12 and 4.13 as advertised. Consider, first, the photon emission process discussed in section 4.3. As emphasized above, the photon has $C_{s2} = C_A = 0$, while $C_{s1} = C_F = C_{s3} = 4/3$ for

the colored quarks, so that

$$\hat{\mu}_\perp^2(1,y,1-y;q,\gamma,q) \propto \left[\frac{2}{\pi}\,y(1-y)\,\frac{p}{T}\right]^{1/2}\left\{\frac{4}{3}y^2\ln(\sqrt{p/T})\right\}^{1/2}. \tag{4.21}$$

On the other hand, for gluon emission from a quark, $q \to gq$, we have $C_{s2} = C_A = 3$, and $C_{s1} = C_F = C_{s3} = 4/3$, so that

$$\hat{\mu}_\perp^2(1,y,1-y;q,g,q) \propto \left[\frac{2}{\pi}\,y(1-y)\,\frac{p}{T}\right]^{1/2}\left\{\left[\frac{4}{3}y^2+3\left(1+(1-y)^2\right)\right]\ln(\sqrt{p/T})\right\}^{1/2}. \tag{4.22}$$

For small y, where the term in the second square parentheses in eq. 4.22 approaches a constant, equations 4.21 and 4.22 differ by factor $y = k/p$, reproducing the relation between equations 4.12 and 4.13. Finally, the appearance of the Coulomb logarithm is, as mentioned before, the result of including all processes with a momentum transfer larger than m_{th}, which occur at a rate smaller than that of eq. 4.3 (see Fig. 2.4 and footnote 5 on Page 29).

So far, we have refrained from including simultaneous contributions of multiple interactions to the LPM suppression rate; e.g. in the case of a gluon splitting to a colored quark pair, that would mean we neglected the contribution of weak and/or hypercharge interactions to the growth of the transverse momenta of the quarks; we deemed this approximation acceptable as all particles involved in the splitting process were colored and therefore comparably coupled to the thermal background plasma with $SU(3)_C$ interactions as the dominant interaction. Before concluding this subsection, we comment on processes where this approximation is not as well justified. Recalling that we assign $C_A = 0$ when treating the emission of a $U(1)_Y$ gauge boson, which cannot scatter on the background by $t-$channel exchange of a gauge boson, the only[6] such processes within the SM involve two $SU(2)_L$ doublet quarks and an $SU(2)_L$ gauge boson; here, two participants carry color but the third one only undergoes weaker non–Abelian interactions so that the involved particles couple to the background plasma with different strengths.

The $q \to Wq$ splitting is described by eq. 4.17b with $G' = SU(2)_L$, $G = SU(3)_C$. In this example, assigning a $C_A = 0$ will be disregarding the non–Abelian W interactions contributing to the loss of coherence, although the relevant $SU(2)_L$ coupling strength is smaller than that of $SU(3)$. The discussion at the end of Section 4.3 showed that the scattering of the W might terminate coherence if it has much less energy than the parent quark. We treat this by assigning $C_A = (\alpha_W/\alpha_S)^2 C_A^W$ to the W boson in the splitting process; the rationale for this assignment could be best understood from eq. 4.17 where the relative strength of the thermal kicks from a gauge group is represented by the corresponding thermal mass m_G^{th}. This may be a crude approximation, but is well justified for an exploratory work, so long as we are looking to assign a single interaction to the loss of coherence.[7]

[6] You may have noticed that the scalar part of the SM has so far not been mentioned in the discussion of the splitting functions. This is a simplifying choice we have made in our studies, as will be explained in Section 4.3.2. As such, we are also disregarding other splittings such as $q \to Hq$ that would also involve particles with different interactions with the background plasma.

[7] We do not know of a study focusing on the calculation of explicit LPM suppression factors involving multiple non–Abelian gauge groups; although, one can rely on the same physical arguments we used in Section 4.3 to deduce a summation rule for multiple contributions to coherence loss.

4.3.2 Particle content and the treatment of chirality

Equations (4.17) and (4.20) provide the rate of all splitting processes involving SM fermions and gauge bosons within the approximations discussed in Section 4.3.1. As mentioned before, the form in (4.17) is developed and used mainly within the study of QGP and the vector–like QCD. Before we move on to composing the system of Boltzmann equations, therefore, we should address some technicalities regarding the applicability of the splitting rates to various processes that stem from the presence of chirality and the multitude of SM particles while we keep track of the chiralities of the fermions in the splitting cascade.

Since we always sum or average over the spins of the participating gauge bosons, we do not need to change the y dependence of any splitting function. Moreover, the $1/2$ factors in the normalization of ν in eq. 4.16 and of d_F in eq. 4.17b cancel out so that no change is required for the case of gauge boson emission off a chiral fermion. However, since $N_{\rm fl}$ in eq. 4.17c counts the number of indistinguishable Dirac fermions, it should include a factor of $1/2$ when considering splittings to species of chiral (or Weyl) fermions. Note that this does not change the total splitting rate of the corresponding gauge boson for $SU(3)_C$ and $U(1)_Y$.

Next, let us turn our attention to the population of (anti-)particles of a certain chirality. Note that gauge boson vertices are chirality conserving; the relaxation of any preexisting net [8]chiral charge via $2 \to 2$ or $1 \to 2$ processes will therefore either rely on bare fermion mass insertions [105–107], which are absent in the unbroken $SU(2)_L$-phase, or involve emission or exchange of a scalar Higgs boson; the latter processes are highly suppressed compared to gauge processes, by the small Yukawa couplings of most SM fermions, as well as by a factor of $y^2/2$ in the splitting function relative to that for the emission of a gauge boson [108, 109]. In what follows, we will therefore neglect such processes and treat the chiralities of fermions as conserved quantities, keeping track of evolution of their populations separately; i.e. we will present separate spectra for left– and right–chiral fermions $f_{L/R}$. A further advantage of this approximation is that eq. 4.17 economically contains all splitting functions required for the study of our thermalization cascade; if we wanted to include the Higgs doublet ϕ among the parent or daughter particles, we would need to include several additional[9] splitting functions for processes involving spin−0 bosons [108, 109]. Since ϕ does not have strong interactions, and describes a rather small number of degrees of freedom within the SM, we ignore these processes in our treatment. This should be a good approximation, unless Higgs bosons feature prominently among the original parent particles.

With chirality under control, let us next turn our attention to gauge multiplicities of particles in the thermal cascade. Somewhat trivially, one does not need to distinguish between the members of a given representation of the gauge group. As an example, in the phase of unbroken $SU(2)_L$ we would not, and in fact cannot, distinguish between an up–type and a down–type left–chiral fermion. Even if we fix the gauge (so that "up–type" is well defined), $2 \to 2$ scattering processes on the thermal background induce changes between these states at the high rate $\Gamma_{\rm el}$, , i.e., these states are not well–defined over the duration of a splitting process which we saw contains many spans of $t_{\rm el}$ (4.3). The same is also true for the color of a quark, so that the quark undergoing a splitting process in Fig. 4.2 cannot be considered to have a well–defined color even in a fixed gauge.

[8] As we will see in Section 4.5, the relative chiral asymmetry is strongly diluted by the fact that the thermalization cascades increases, manifold, the number of fermion pairs, a majority of which will be the result of chiral symmetric $SU(3)_C$ and $U(1)$ gauge boson splittings.

[9] This is subsequently done explicitly in [70]; see in particular the set of splitting functions in Section 2.4 of [70].

The same is, however, not true for right–chiral particles and different right–chiral fermions f_R are, at least in principle, physically distinct particles. For example, u_R and d_R have different $U(1)_Y$ charges. Different $U(1)_Y$ charges mean, via eq. 4.17, differing thermalization times and splitting rates for the emission of further $U(1)_Y$ gauge bosons; one would therefore in principle need to track the populations of the f_R separately. However, as it is difficult to imagine physical scenarios where we would need to distinguish between the up and down type f_R, and to further reduce the number of species tracked in our thermalization cascade, we will simply treat both these species as possessing an average squared charge in (4.19), using

$$Y_{q_R}^2 = \frac{1}{2}\left(Y_{u_R}^2 + Y_{d_R}^2\right) . \tag{4.23}$$

Our choice for the approximation to leave out the Higgs boson out of our cascade of SM particles allows for a further simplifying step. With the presence of only gauge interactions in (4.17), we will not need to distinguish between fermions of different generations; this allows us to further limit the number of species whose evolution we need to track in the thermalization cascade.

All the above simplifications still leave us with seven distinct particle species:

$$s \in \left\{q_L,\, q_R,\, \ell_L,\, \ell_R,\, g,\, W,\, B\right\} \equiv \mathbb{S}, \tag{4.24}$$

whose number densities we will track via Boltzmann equations, as we did in Chapter 3 for a single species.

Finally, note that we assume equal production of particles and antiparticles, grouping them together in (4.24). This is true if the original M particles always decay into $s\bar{s}$ pairs, which we assume to be the case as a matter of convenience. Treating more fermion species as distinguishable is in principle straightforward. However, this would increase the number of coupled Boltzmann equations that need to be solved, and also the number of terms in some of these equations. The choice (4.24) should be sufficient to illustrate the main effect of the appearance of particles with very different interaction strengths in this first, exploratory analysis.

4.4 System of Boltzmann equations

We established that $2 \to 3$ processes play a significant role in the redistribution of energy, and in the growth of number density, towards a thermal distribution. These processes can be understood as quasi–elastic scattering processes that leave the energy p of the parent particle almost unchanged, followed by $1 \to 2$ splittings which distribute the energy of the parent among two daughter particles of energy k and $p - k$, respectively. Focusing on gauge interactions of the SM, the differential rate of the relevant $2 \to 3$ processes for a representative set of species $\mathbb{S}$ (4.24) introduced in Section 4.3.2, was given in eq. 4.16.

Our final goal is to find the number densities of all OoE particles in $\mathbb{S}$, developing throughout the thermalization process. These densities are governed by a set of Boltzmann equations; similar to what we had in Chapter 3. Let us therefore recap our treatment of Chapter 3 while emphasising on the choice of a single species s and a single splitting process $s \to ss$, now to be extended to include the species and interactions in (4.3.2) and eq. 4.17. Recall that in Chapter 3 we invoked the well–motivated assumptions of homogeneity and isotropy to conclude that the phase space or number

density depends solely on the magnitude p of the 3−momentum and on the cosmological time t. Splittings of the species s to other particles of the same species s, generated a non–thermal spectrum of non-abelian gauge bosons s, which we denoted by

$$\tilde{n}_s\,(p) \equiv \frac{dn_s(p)}{dp} \quad \texttt{such that} \quad \int_T^{p_{\max}} \tilde{n}_s(p)dp = n_s\,. \tag{4.25}$$

We established in Section 3.1.3 (see eq. 3.19) that, in almost all scenarios of interest, the initial particles thermalize within a period much shorter than a Hubble time, so that the temperature of the thermal bath can be considered as constant within the thermalization time; despite differences in the form of the splitting function and, therefore, the parametric form of thermalization time via different splitting processes, the same conclusion naturally extends to the individual processes in eq. 4.17 so that the appearance of the background temperature T in the various elements is well defined. Recall that the efficiency of the splitting processes moreover meant that one could look for a quasi–static solution to the Boltzmann equation 3.22.

The exchange symmetry of the two daughter states for the case of $A \to AA$ splittings (see eq. 4.17a) allowed us to write eq. 3.22 as [10]

$$\begin{aligned} 2n_{\rm M}\Gamma_{\rm M}\delta(p - M/2) + \int_{p+\kappa T}^{M/2} \tilde{n}_s(k)\frac{d\Gamma^{\rm split}_{\rm LPM}(s(k) \to s(p)s(k-p))}{dp}dk \\ = \int_{\kappa T}^{p/2} \tilde{n}_s(p)\frac{d\Gamma^{\rm split}_{\rm LPM}(s(p) \to s(k)s(p-k))}{dk}dk\,. \end{aligned} \tag{4.26}$$

Here, as before, $n_{\rm M}$ and $\Gamma_{\rm M}$ denote the number density and decay rate of the long–lived matter particle, and the splitting rates on both LHS and RHS are given by eqs.(4.16) and (4.17a). Moreover, as discussed in Section 3.3.2, the cutoff scale κT, with κ of order unity[11] , effectively deals with the IR divergence from soft emissions in the rate (4.17a) and subsequently in the Boltzmann equation (4.26). The choice of such an IR cutoff is reasonable since the much faster $2 \to 2$ scattering reactions allow momentum exchange of order T; moreover, the total spectrum of particles with energy $\leq 3T$ is in any case dominated by the thermal contribution. Finally, we saw that the precise choice of κ does not affect the physical result, so that we may choose $\kappa = 1$ for convenience.

With a numerical solution directly accessible after the introduction of the cutoff, we facilitated our treatment of the Boltzmann equation (4.26) by grouping and renaming the involved quantities to get the normalized number density parameter

$$\widetilde{N}_{\rm M} = \frac{2n_{\rm M}\Gamma_{\rm M}}{\Gamma^{\rm split}_{\rm LPM}(M/2)}\,, \quad \bar{n}_s\,(p) = \frac{\tilde{n}_s\,(p)}{\tilde{N}_{\rm M}}, \tag{4.27}$$

in eq. (3.26 and 3.27), and further by using introducing the dimensionless parameters

$$x = \frac{p}{T} \implies \bar{n}_s\,(x) = T\bar{n}_s\,(p)\,, \tag{4.28}$$

[10] In Chapter 3 an approximation of eq. 4.17a was used, where the y−dependence was approximated as $1/y^{3/2}$ for $y \leq 1/2$, and the region $y > 1/2$ was treated via the $y \leftrightarrow 1 - y$ exchange symmetry. Since this approximates the full result to better than 10% for $y < 0.4$ (and hence for $y > 0.6$ as well), this did not change the solution qualitatively.

[11] See also footnote 13 on Page 50.

in eq. (3.28 – 3.31). Treating the gauge couplings as constants, the spectrum $\bar{n}(x)$ could then only depend on the single parameter $x_{\rm M}$ defined in eq. 3.29 as

$$x_{\rm M} = \frac{M}{2T} \,.$$

The Boltzmann equation (4.26) could, as such, be written as

$$\bar{n}_s(x; x_{\rm M}) = \int_{x+\kappa}^{x_{\rm M}} \frac{\bar{n}_s(x')}{\Gamma^{\rm split}_{\rm LPM}\left(s(x) \to ss\right)} \frac{d\Gamma^{\rm split}_{\rm LPM}\left(s(x') \to s(x)s(x'-x)\right)}{dx} dx' + \delta(x - x_{\rm M}) \,, \tag{4.29}$$

where $\Gamma^{\rm split}_{\rm LPM}\left(s(x) \to ss\right)$ is the total (integrated) rate for a particle of dimensionless momentum x to undergo a splitting process. As discussed in Chapter 3, the advantage gained by switching to $\bar{n}$ could be understood as follows: the splitting rate appears in both the numerator and denominator of eq. 4.29, so that numerical factors like $\sqrt{\tilde{g}_*^{\,s}}$ of eq. 3.16, or equivalently the numerical factors of eq. 4.17a, as well as the coupling strength α_G do not affect $\bar{n}_s\,(x)$; they appear in the final, physical spectrum only via the normalization factor $\tilde{N}_{\rm M}$.

The numerical solution to the relatively compact form of eq. 4.29 could, as we saw in Section 3.3.3, be well approximated by an analytical expression (3.49):

$$\bar{n}_s(x; x_{\rm M}) = \delta(x - x_{\rm M}) + \frac{\left[a\left(x/x_{\rm M}\right)^{-3/2}\left(1 - x/x_{\rm M}\right)^{-b} + c\right]\left(1 - 2/\sqrt{x_{\rm M}}\right)}{\sqrt{x_{\rm M}}\left(1 - \sqrt{2/x}\right)^{5/4}} \,,$$

with $a,\ b,\ c \approx 1/2$. The form of the single species solution (3.49) further showed that for $x_{\rm M} > x \gg 1$, the solution is proportional to the function

$$f\left(x/x_{\rm M}\right) \equiv \left[a\left(x/x_{\rm M}\right)^{-3/2}\left(1 - x/x_{\rm M}\right)^{-b} + c\right] \,, \tag{4.30}$$

which exhibits a *scaling* behavior in x, i.e. depends only on the ratio $x/x_{\rm M}$. In Section 4.5 we will use this latter feature, and the pure–gauge solution (3.49) to present the results of the splitting cascade involving all species $s \in \mathbb{S}$.

So far we have assumed that the parent particle of species s can only split into two daughter particles of the same species, as is the case for a pure Yang–Mills gauge theory. The splitting of a gluon into two gluons is indeed the fastest splitting reaction in the SM, and is expected to dominate the evolution of the system produced in heavy ion collisions, at least at central rapidities [97]. However, as discussed in Section 4.1, one expects other particles to develop within the cascade of thermalizing OoE particles. The multiplicity of accessible fermion flavors appearing in (4.17c) suggests that a sizable population of fermionic daughters may develop in the splitting cascade. Since SM quarks are charged under several gauge groups, eventually electroweak gauge bosons, and hence leptons, will become part of the cascade even when starting from a parent gluon.

The need for a more inclusive treatment of the thermalization cascade of OoE particles becomes even more pronounced when the matter particles, whose decays feed the cascade, primarily decay to colorless species; our expectation of the flow of the OoE plasma towards coloured particles calls for the inclusion of other SM species. A third line of reasoning in favor of including other SM species in

the thermalization cascade follows from the applications of the spectrum of HE particles. Recall, that our purpose in computing the spectrum of particles in the cascade triggered by the primary decay is to compute rates for processes that leave observable relics, e.g. dark matter particles. These reactions may involve preferentially, or even only, colorless particles in the initial state so that the population of a specific species directly affects the observables, as outlined in Section 3.4.

We will therefore extend our previous analysis in Chapter 3 by formulating and solving the coupled system of Boltzmann equations governing the energy spectrum of all particles listed in eq. 4.24 during a LPM–suppressed thermalization cascade. As in the case of pure–gauge treatment in Chapter 3, we will be interested in the quasi steady–state solution so that the starting point will once again be the steady–state balancing equation 3.22, equating gain and loss terms for particles to and from a specific energy.

A multi species analysis therefore means that we should consider various decay and splitting process involving particles $\mathbb{S}$ (4.24) contributing to the balancing in (3.22). Expanding (4.26), the spectrum of particles of a species $s \in \mathbb{S}$ is then determined by the integral equation

$$\begin{aligned} 2n_{\mathrm{M}}\Gamma_{\mathrm{M}}Br_s \cdot \delta(p - M/2) \quad &+ \quad \sum_{s',s''} \int_{p+\kappa T}^{M/2} \tilde{n}_{s'}(k). \frac{d\Gamma^{\mathrm{split}}_{\mathrm{LPM}}(s'(k) \to s(p)s''(k-p))}{dp} dk \\ &= \quad \sum_{s',s''} \int_{\kappa T}^{p-\kappa T} \tilde{n}_s(p) \frac{d\Gamma^{\mathrm{split}}_{\mathrm{LPM}}(s(p) \to s'(k)s''(p-k))}{dk} dk \ . \end{aligned} \tag{4.31}$$

Here $2Br_s$ is the average number of s particles produced in a given two–body decay of an M particle with branching ratio Br_s, and it is implied that $s', s'' \in \mathbb{S}$. As noted earlier, we assume equal production of fermions and antifermions, and the density n_s should be thought to include both s and $\bar{s}$ particles in case these are distinct [12]. In the rate $\Gamma^{\mathrm{split}}_{\mathrm{LPM}}\left(s(p) \to s'(k)s''(p-k)\right)$, within the SM, the particle type of s'' is often fixed once s and s' have been specified; this is true in particular if s and/or s' denote a gauge boson. However, if s and s' are both fermions (which implies $s = s'$), several types of gauge boson might be possible for s''. In the example of $q_L \to q_L$ splitting, the $\sum_{s''}$ in (4.31) will run over all three species of gauge bosons of the SM in $\mathbb{S}$.

Similar to the narrative we followed at the beginning of Section 4.4, we may now move on to simplifying the set of Boltzmann equation. In eq. 4.31 most dependence on high–scale physics has been factored into the first term. As noted in Chapter 3, any effects from interactions of the decaying particles and their decay products is encoded in Γ_{M} and the branching ratios Br_s (see also footnote 1 on Page 34); in particular, the product $n_{\mathrm{M}}\Gamma_{\mathrm{M}}$ only affects the overall normalization of all spectra. In contrast, the splitting rates can be computed within a theory, here identified with the unbroken SM, that is valid at energy scales well below M. The second and third terms in eq. 4.31, which determine the shapes of the various spectra and also affect their relative normalization, therefore, depend on high–scale physics only through the upper limit of integration of the first integral.

As in the case of the single particle pure gauge cascade, it is useful to make these dependencies

[12] If only decays of the type $M \to s\bar{s}$ are allowed, Br_s is the branching ratio for one such mode. However, if $M \to ss'$ with $s \neq s'$ decays are possible, the corresponding branching ratio would appear as Br_s in the equation for $\tilde{n}_s$, and as $Br_{s'}$ in the equation for s'.

explicit by using (4.28) to rewrite (4.31) in the dimensionless form

$$\begin{aligned}\bar{n}_s(x) &= \frac{\Gamma^{\text{split}}_{\text{LPM}}\left(s^*, x_{\text{M}}\right)}{\Gamma^{\text{split}}_{\text{LPM}}\left(s, x_{\text{M}}\right)} Br_s \cdot \delta\left(x - x_{\text{M}}\right) \\ &+ \sum_{s',s''} \int_{x+\kappa}^{x_{\text{M}}} \frac{\bar{n}_{s'}\left(x'\right)}{\Gamma^{\text{split}}_{\text{LPM}}\left(s, x\right)} \frac{d\Gamma^{\text{split}}_{\text{LPM}}\left(s'(x') \to s(x)s''(x'-x)\right)}{dx} dx' \,. \end{aligned} \tag{4.32}$$

Here we have generalized the procedure of eq. 4.27 for single species, by normalizing the spectra of all species in (4.31) using the total rate of $2 \to 3$ reactions of some single specific reference species $s^* \in \mathbb{S}$:

$$\widetilde{N}^*_{\text{M}} = \frac{2n_{\text{M}}\Gamma_{\text{M}}}{\Gamma^{\text{split}}_{\text{LPM}}(s^*, M/2)} \,, \quad \bar{n}_s(x) = T\bar{n}_s\left(p\right) = T\frac{\tilde{n}_s\left(p\right)}{\tilde{N}^*_{\text{M}}} \,, \tag{4.33}$$

with

$$\Gamma^{\text{split}}_{\text{LPM}}(s,x) = \sum_{s',s''} \int_{\kappa}^{x-\kappa} \frac{d\Gamma^{\text{split}}_{\text{LPM}}\left(s(x) \to s'(x')s''(x-x')\right)}{dx'} dx' \,. \tag{4.34}$$

We use the particle with the largest total rate, i.e. the gluon $s^* = g$, for the normalization; although a matter of taste, this particular choice is somewhat better motivated as we expect the composition of the OoE cascade to move towards a QGP plasma, as discussed in Section 4.1. Note that even for gluon species $s = g$, this implies a normalization slightly different from that of a pure–gluon cascade as we would have in Section 3.2.2 by identifying the gauge boson species as the gluon, as the normalization in (3.2.2) would not include the contribution from splittings to fermion pairs present in eq. 4.34.

Equation 4.32 implies an evolution similar to the case in eq. 4.29, but with new features resulting from the couplings among the different species. In a single particle cascade, e.g., increasing the coupling strength increases the total rate for $2 \to 3$ reactions which *reduces* the overall normalization of the spectrum. The reason is that a larger rate of splitting reactions decreases the thermalization time, i.e. the particle spends less time in the cascade. In the case at hand, this is true only if all couplings are increased by the same factor. In contrast, increasing some coupling relative to that of the reference particle (i.e. relative to the strong coupling, for our choice $s^* = g$) still reduces the normalization of the first term in eq. 4.32, but it also *increases* the probability that s will be produced later in the cascade, as seen by the appearance of the splitting rate in the numerator in (4.32).

4.5 Numerical calculation of the spectra

The numerical solution of eq. 4.32 proceeds essentially in the same way as in the case of a single particle cascade, outlined in Section 3.3.2. One starts at $x = x_{\text{M}}$, regularizing the δ function, and successively works down to lower x. Of course, now we actually need to solve seven such equations, for the species $\mathbb{S}$ in (4.24).

The integrand in eq. 4.32 is computed from equations (4.16) and (4.17), using (4.18) and (4.19) for the coupling parameters; we use three generations of massless leptons and quarks, and include extra factors of $1/2$ for splitting of gauge bosons to chiral fermion pairs in (4.17) as discussed in Section 4.3.2. Note that we use the parameter x of eq. 4.28 in the Boltzmann equations, while the fragmentation functions are written in terms of the momentum fraction y of eq. 4.4; the two are related by $y = k_{\text{daughter}}/p_{\text{parent}} = x_{\text{daughter}}/x_{\text{parent}}$. The use of the exact (leading order) splitting functions (4.17)

implies that the total rates $\Gamma^{\text{split}}_{\text{LPM}}(s,x)$ in eq. 4.34 also have to be computed numerically, whereas the approximation we used in Section 3.2.1 allowed the integral in eq. 3.24 to be calculated analytically. The contributing splitting reactions, corresponding to species $s \in \mathbb{S}$ are depicted in Fig. 4.4.

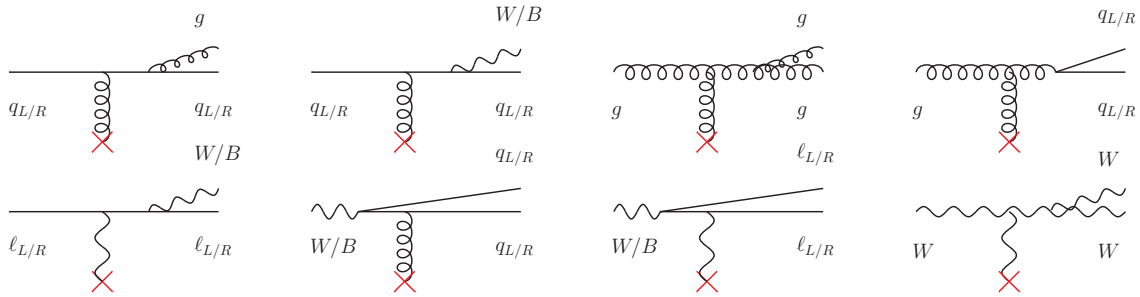

Figure 4.4: Splitting processes for the species in $\mathbb{S}$ that can proceed via soft interactions with the thermal background. The red crosses again denote couplings to particles in the thermal bath via many soft exchanges. We only include the $t-$channel gauge boson which has the largest possible coupling, as discussed in Section 4.3.1; e.g. the process $B \to \ell_L \ell_L$ is mediated by an $SU(2)$ gauge boson W. Note also that W bosons only couple to left–handed fermions q_L, ℓ_L.

To deal with the presence of several species and the branching ratios Br_s in our numerical treatment of eq. 4.32, we will assume that only one of the seven species $I \in \mathbb{S}$ is produced in primary M decays, i.e. $Br_I = 1$, in which case the first term in eq. 4.32 is absent for the other species, $Br_s = 0\ \forall s \neq I$; we denote the scaled number densities developing in such a scenario as $\bar{n}^I_s(x)$. Scenarios where more than one Br_s is nonzero can be treated by weighted sums of our results with the branching ratios serving as weights. If only primary decays of the kind $M \to ss$ are allowed[13], this sum reads:

$$\bar{n}_s\left(x, x_{\text{M}}\right) = \sum_{I \in \mathbb{S}} Br_{\text{I}}\, \bar{n}^{\text{I}}_s\left(x, x_{\text{M}}\right) \ . \tag{4.35}$$

Note also that the total rates $\Gamma^{\text{split}}_{\text{LPM}}(s, x_{\text{M}})$ in eq. 4.32 are independent of the cosmological parameters, so they need to be calculated only once for every species s and given value of x_{M}.

4.5.1 Solutions for $x_{\text{M}} = 10^4$

In the previous sections, we formulated the Boltzmann equations for the evolution of the OoE particles in the thermalization cascade, and brought these into a form better numerically tractable. We are now ready to present some numerical results. As noted, we will assume $Br_I = 1$, but we will show results for all seven possible choices of I so that spectra for more general primary decays can be computed using the weighted sum in eq. 4.35. In this subsection we choose $x_{\text{M}} = 10^4$; the dependence on x_{M} will be discussed in Section 4.5.2. Throughout our numerical treatment, we assume a temperature of $T = 100$ TeV, where the $SU(2)_L \times U(1)_Y$ symmetry is still unbroken so that the (bare) masses of all particles in the cascade vanish. [14]

[13] Recall that s describes antiparticles as well.

[14] As explained above, the efficiency of the thermalization process allows for a well–defined temperature for all splitting processes occurring on a HE particle's path in the thermalization cascade. With a fixed temperature, we can further choose the appropriate gauge coupling; since all relevant vertices involve at least one particle with virtuality of order

The results of the numerical solutions to (4.32) are spectra of number densities for the species $s \in \mathbb{S}$ (4.24). In the following figures, spectra of particles charged under $SU(3)_C$ (g, q_L, q_R) are shown in green; spectra of colorless particles that are charged under $SU(2)_L$ (W, ℓ_L) are shown in red; and spectra of particles that have only $U(1)_Y$ interactions (B, ℓ_R) are shown in blue. We use solid lines for gauge bosons, while left– and right–chiral fermions are represented by dashed and dotted lines respectively. One may be interested in the evolution of the total number of HE particles in the thermalization cascade. The black lines in the upcoming figures, therefore, additionally show the total spectrum of thermalizing OoE particles, $\bar{n}_{\text{tot}}(x) = \sum_s \bar{n}_s(x)$; note that in eq. 4.33 $\bar{n}_s$ are related to the physical spectra $\tilde{n}_s$ by a factor common among the different species. Finally, we show for comparison the pure gluonic (single species) solution of eq. 4.29 in dark green. As we expect and will see, this pure gluon solution serves as an attractor for the gluon number density, irrespective of the matter decay branching ratios Br_I.

Following our discussion in Section 3.3.2, it is reasonable to terminate the solution curves at $x = 3$ i.e. $p = 3T$, which approximates the average energy of particles in the thermal bath; this will be reflected in the following figures containing the spectra of OoE particles. Recall that due to the relative efficiency of the thermalization process for gauge interacting particles and the assumed long lifetime of the decaying matter particles, the number density, and so the total flux of particles, can be expected to be dominated by thermal particles, out to energies considerably larger than the temperature T; for practical applications, therefore, the region close to this cutoff is likely not of interest. Note further that the computed OoE spectra become independent of the choice of the IR cut–off κ, only for $x \geq 10 \leftrightarrow x_{\text{M}} - x \geq 10$, roughly coincident with the scale at which the elastic $2 \to 2$ processes get to compete with the inelastic processes, further restricting the precision of results for $x \leq 10$.

- $\boldsymbol{I \in \{B, \ell_R\}}$**:**
  As mentioned in Section 4.1, we expect our pure gauge treatment in Chapter 3 to better approximate a pure gluon plasma. To best showcase the interplay among different particles species and the evolution of the composition of OoE particles in the thermalization cascade, let us therefore begin with a plasma with stark differences to the case of pure gluons; i.e. we begin with the case of an initial injection of particles that have only $U(1)_Y$ interactions, B and ℓ_R. The resulting spectra are shown in Fig. 4.5 and, as expected, can be readily seen to contain more dynamics with rising and falling populations of different particles.

  A first observation in both cases depicted in Fig. 4.5 is that for large x the spectra of B and ℓ_R lie well above the single species pure gluon spectrum. This can be easily understood as resulting from the less efficient splittings of B and ℓ_R as compared to gluons, and is reflected in (4.32) in the form of the coefficient in front of the δ function being considerably larger than unity. Physically, this translates to OoE particles lingering longer than they used to in the case of HE gluons, resulting in a denser plasma of OoE particles at the highest energies $p \sim M/2$.

  Apart from the enhancement with respect to the pure gluon spectrum, the relative size of the B and ℓ_R can be similarly understood from eq. 4.32. Note that B can split into quarks with a rate of order $\alpha_S \alpha_Y$ in couplings, corresponding to the vacuum and LPM contributions

gT, we use running couplings taken at that scale. We saw in examples in Section 3.4 that in applications in cosmology, one could be dealing with multiple Hubble eras with the temperature being orders of magnitudes apart. Variations in temperature, however, affect the couplings only logarithmically. In the particular example of DM production we reviewed in Section 3.4, it is therefore reasonable to expect that the correct choice of temperature will not be critical for finding the Hubble era with the dominant contribution to the DM abundance.

discussed in Section 4.3, with α_S and α_Y being the fine structure constants for $SU(3)_C$ and $U(1)_Y$, respectively. On the other hand, the only splitting reaction for ℓ_R is the emission of a B boson with a rate of order α_Y^2 in couplings. The difference in process rates contributing to the thermalization of B and ℓ_R is further enhanced by the large color, generation and flavor final–state multiplicity factors (see eq. 4.17c) in the case of B splittings to quarks. Moreover, due to the LPM suppression factor of the Abelian B in eq. 4.21, the differential rate for $\ell_R \to B\ell_R$ splittings only scales like $1/\sqrt{y}$ at small y, just like the LPM suppressed differential rate for $B \to ff$ splittings does. As a result, the total splitting rate is considerably higher for B than for ℓ_R. The combination of these effects explains why, at large x, the spectra for $I = B$ (left frame) lie well below those for $I = \ell_R$ (right frame).

In addition to differences in interaction rates and LPM suppression factors among species, a further peculiarity of the case of $I = B$ is that the first splitting of the original B completely depletes its spectrum, trading it for a weighted sum of fermion spectra to which the B splits. Although the splitting processes are statistical in nature, leading to a left–over population of red–shifted B bosons, the relative efficiency of splitting processes with respect to the gravitational expansion (see Section 3.1.3) allows us to safely ignore this statistical process and speak of a depletion of B into fermionic species; i.e. in all relevant situations we have $H \ll \Gamma_{\text{split}}$, in which case the density of these redshifted particles is exponentially small. As such, the evolution of the spectra for the case of $I = B$, ℓ_R is directly proportionate to the relative hierarchy of splittings of B in their first splittings; these production processes are, as before, weighted out against the thermalization rates to give the spectra of the individual fermionic species resulting from B, ℓ_R splittings.

Let us first discuss the couplings involved in these splittings. The relative rates of fermionic splittings of the B are proportional to the sum of squared hypercharges of the resulting fermion species s; including color factors, these are 5 for q_R, 3 for ℓ_R, 3/2 for ℓ_L and 1/2 for q_L. Of course, the effect of couplings also comes in via the thermal mass parameter, and the factor m_{th}^2 in eq. 4.17c is larger for quarks compared to that of the leptons by α_S/α_W (α_S/α_Y) for the left (right) chirality, reflecting the observation that the quarks scatter more readily off the thermal background. The larger production rate is, however, overcompensated by the larger total splitting rate of quarks, which appears in the denominator in eq. 4.32. The net effect is , e.g., that the quark spectra in the left frame of Fig. 4.5 are suppressed by a factor of order α_Y/α_S compared to that of ℓ_R.

Similar arguments can be used to analyse the relative spectra of different chiralities of a given dirac fermion. In the case of colored quarks, there is a relative factor of 10 larger hypercharge-squared for right–chiral quarks appearing in the production reaction; on the other hand, the left– and right–chiral quarks have almost identical splitting rates appearing in the denominator of eq. 4.32 due to the dominant contribution of $SU(3)_C$-mediated splittings in both cases. The combined effect is a larger q_R spectrum compared to that of q_L seen in Fig. 4.5. With arguments following that for the quarks, the ℓ_L spectrum is suppressed by α_Y/α_W, compared to that of ℓ_R; the subdominant spectrum for ℓ_L is once again the result of an overcompensation of the relatively larger LPM–suppressed production rate by the $SU(2)_L$ driven thermalization of the left–chiral leptons.

In addition to the couplings and multiplicities, the momentum–dependence of the splitting rates

from (4.17) and (4.20) also play a role in setting the rates and the corresponding populations. In particular, the differential rate for $F \to AF$ splittings scales like $1/y^{3/2}$ if A is a non–Abelian gauge boson, and like $1/\sqrt{y}$ for an Abelian A. The total splitting rates for quarks and ℓ_L leptons, at a momentum scale x, are therefore enhanced by a factor $\sqrt{x}$ relative to that of ℓ_R. This difference in the functional form explains why the flux of ℓ_R is by far the dominant one at large x.

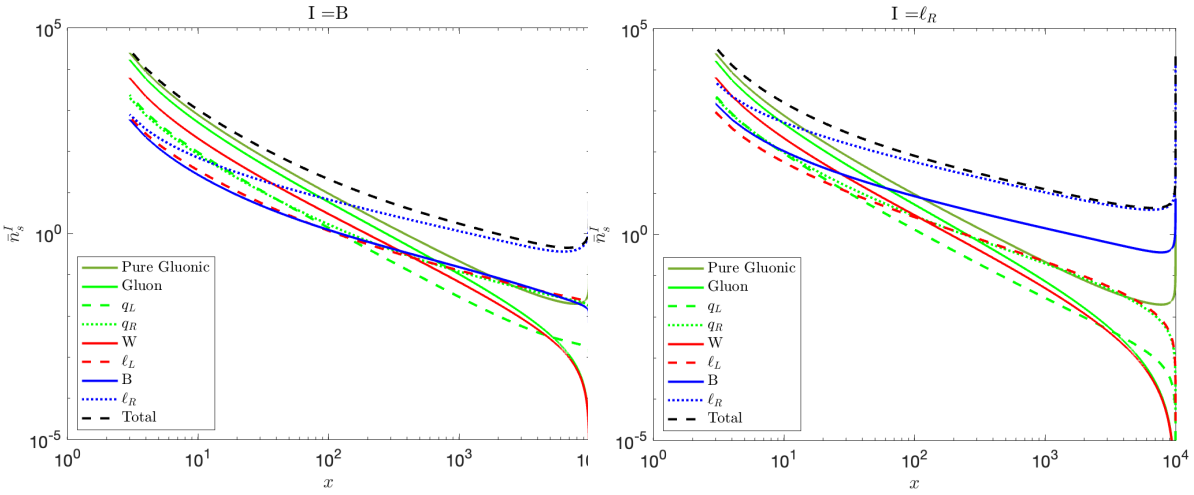

Figure 4.5: Scaled number density functions $\bar{n}_s^I(x)$ of eq. 4.35, for the various particles $s \in \mathbb{S}$, with $I = B$ (left) and $I = \ell_R$ (right); we use $x_{\rm M} = 10^4$ for both cases.

The right frame in Fig. 4.5 shows the spectra of species resulting from an initial ℓ_R injection. As already noted, the single splitting channel for the $SU(2)_L$ singlet leptons is the emission of a B boson, where the LPM effect partially counteracts the vacuum preference for a soft B, due to its lack of gauge–mediated interactions with the thermal bath particles. Other species of fermions are in turn produced later in the cascade, via splittings of the B, hence their relative ordering can be understood as in the case of initial B injection. The other gauge bosons can, at the earliest, be produced in tertiary splitting reactions, e.g., $\ell_R \to B \to q_L \to g\,/W$, hence their spectra fall off fastest as $x \to x_{\rm M}$.

A look at the low–x tail of the spectra in Fig. 4.5 shows that, despite the discussed relatively later production in the splitting cascade, strongly interacting particles eventually dominate the non–thermal cascade of OoE particles. For an initial injection of B bosons, where quarks and gluons are already among the products of primary and secondary splitting reactions, this occurs for $x/x_{\rm M} < 10^{-2}$, while for the case of $I = \ell_R$ right–chiral leptons dominates the total flux down to $x/x_{\rm M} > 10^{-3}$. Nevertheless, at $x \ll x_{\rm M}$ the gluon number density approaches that of the pure gluon solution as advertised and argued for before.

While the eventual dominance of particles with the strongest interactions in the cascade seems intuitively reasonable, within our formalism the realization of this dominance is actually rather subtle, relying on the interplay of various charge assignments, couplings, and group factors. Let us compare, as an example of this interplay, the spectrum of gluons to that of W bosons. In Fig. 4.5 these two spectra are very similar as $x \to x_{\rm M}$; let us further focus on the case of initial B

injection; the case of initial ℓ_R injection is similar, except that one more cascade step is required to produce W or g, as noted above. Starting from an initial population of B bosons, we saw above that the quark spectra at large x are suppressed relative to the ℓ_L spectrum by a factor α_W/α_S, reflecting the larger total splitting rate for q compared to that of the ℓ_L. As we are interested in the population of the $SU(2)_L$ gauge boson, we should also note that the population of q_L resulting from B splittings is an order of magnitude smaller than that of q_R due to the hypercharge assignment. Nevertheless, the LPM suppression factor induced order α_s/α_w larger splitting rate of $q_L \to W$ compared to $\ell_L \to W$ splittings results in both processes contributing to W production parametrically at the same order in couplings in the RHS of eq. 4.32. The gluon spectrum on the other hand, receives contributions from the quark spectra, suppressed relative to ℓ_L by a factor of α_w/α_s; given that both the production (off quark splittings) and thermalization of gluons are of order α_s^2 in couplings, the α–suppressed population of quarks would result in a subdominant gluon spectrum at high x, if not for the relatively large q_R population. These arguments show how the coincidence of the gluon and W spectra at high x in the case of initial B injection relies on the interplay of various charge assignments, group factors, and couplings.

In the above argument leading to the comparison of the spectra for g and W in initial B injections, we have implicitly assumed that the total splitting rate of non–Abelian gauge bosons is dominated by $A \to AA$ splittings, disregarding the contribution from splittings to fermions. This is in fact correct for $x \gg 1$, since this rate scales like $1/y^{3/2}$ for $y \ll 1$ while the rate for $A \to FF$ only scales like $1/\sqrt{y}$ (see the dependence on momentum fractions y in equations 4.17 and 4.20), hence this contribution to the total splitting rate is suppressed by a factor $1/\sqrt{x}$ relative to that from $A \to AA$ splitting. Another detail worth taking note of in neglecting the $A \to ff$ splittings in our argument above, is that in case of the W, the soft gauge boson enhancement of $W \to WW$ is only partly compensated by the relative enhancement factor α_S/α_W reflecting the larger scattering rate of quarks on the thermal background for the $W \to q_L q_L$ process. In contrast, both the weaker coupling in the splitting matrix element and the somewhat stronger LPM suppression disfavor $q_L \to q_L W$ relative to $q \to qg$ splittings. The combined effect is, therefore, a net flow from exclusively weakly interacting to strongly interacting particles.

- $I \in \{\ell_L, W\}$:
  Next, we turn to the injection of color singlet particles with $SU(2)_L$ interactions, where the stronger $SU(2)_L$ interactions then dominate their scattering off the thermal background compared to potential $U(1)_Y$ mediated scatterings. The resulting particle spectra are seen in Fig. 4.6. Some general observations can be made on a first look. One could see that the overall normalization at large x in Fig. 4.6 lies in between that of the pure gluon case and the case where the injected particles have only $U(1)_Y$ interactions, as we saw in Fig. 4.5. Moreover, we once again see that, at sufficiently small x, colored particles begin to dominate the number density of OoE particles in the thermalization cascade.

  In detail, let us first consider the case of W injection (top frames). With a look at Fig. 4.5 for comparison, one observes that the flow towards the dominance of colored states is considerably slower than for the injection of B bosons. This is partly because $SU(2)_L$ interactions in the SM are stronger than $U(1)_Y$ interactions and thus closer to the strong $SU(3)_C$ processes, but mostly because $SU(2)_L$ is a non–Abelian group, allowing $A \to AA$ splittings; eq. 4.17 shows that the splitting rate to vector bosons is larger by a factor $1/[y(1-y)]$ relative to that of

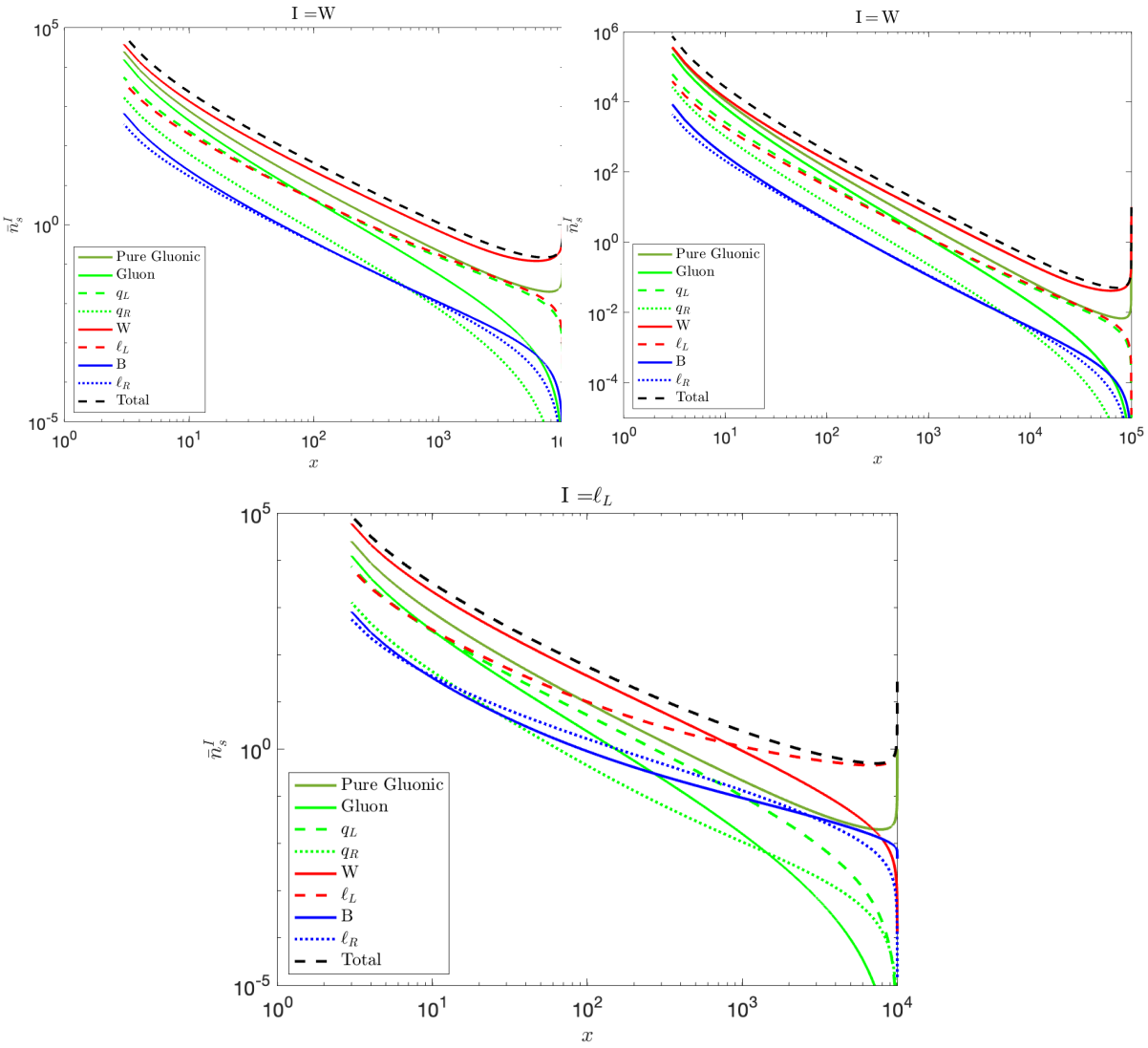

Figure 4.6: Scaled number density functions $\bar{n}_s^I(x)$ of eq. 4.35 for the various particles $s \in \mathbb{S}$, with $I = W$ (top) and $I = \ell_L$ (bottom); we use $x_{\rm M} = 10^5$ in the top–right frame in order to show that an extra decade in x allows the composition of thermalizing particles to approach domination by colored particles, in particular gluons. The top–left and bottom frames are for $x_{\rm M} = 10^4$.

$A \to FF$ splittings. The initial and subsequent W bosons, therefore, strongly prefer to emit additional W bosons, rather than splitting into quark–antiquark pairs necessary for a transition to colored particles. The same physical argument also explains why the flux of non–Abelian gauge bosons eventually overtakes that of $SU(2)_L$−charged fermions in the case of fermion injection in the lower frames of Fig. 4.6: the only splitting process contributing to the growth of ℓ_L are $A \to FF$ splittings with no soft gauge boson emission enhancement. Both $A \to AA$ and $F \to AF$ splittings on the other hand increase the number of gauge bosons; note that the rate for the latter process is still enhanced by a factor $1/y$ relative to that for $A \to FF$.

Due to the high efficiency of $W \to WW$ splitting and the relatively slower flow of the OoE spectra towards colored particles, the gluon flux can be seen to eventually catch up with, but not overtake, the W flux in the case of $x_{\mathrm{M}} = 10^4$ in the top left frame of Fig. 4.6. We've therefore made the exercise of extending the thermalization cascade development by another decade; setting $x_{\mathrm{M}} = 10^5$, it can be seen in the top frame of Fig. 4.6 that gluons do indeed begin to dominate at the smallest values of x[15]. Note once again that particle changing $2 \to 2$ processes, occurring at competitive rates at low-x have been neglected in the current analysis.

The small rate of $A \to FF$ splittings relative to non–Abelian $A \to AA$ also explains why the spectrum of $SU(2)$ doublet fermions, which can in principle be produced in the first splitting of the original W bosons, does not spike as $x \to x_{\mathrm{M}}$, in contrast to what we observed earlier in the case of $U(1)_Y$ gauge boson injection in Fig. 4.5. The spectra of the fermions follow once more from a balancing of production and thermalization processes. Production of colored q_L in W-splittings is enhanced by the color factor and a LPM induced relative factor of $\alpha_{\mathrm{s}}/\alpha_{\mathrm{W}}$ compared to the rate of splittings to ℓ_L. This enhancement, however, is balanced out by the more efficient thermalization of quarks relative to ℓ_L, leading to very similar amplitudes of these two spectra at large x. At much smaller x, the flux of q_L (and, for $x_{\mathrm{M}} \gg 10^4$ eventually q_R) overtakes that of ℓ_L, due to quark production in (tertiary) gluon splitting. A last observation in the top frames in Fig. 4.6 is that the population of all $SU(2)_L$ singlet fermions fall off rapidly as $x \to x_{\mathrm{M}}$, corresponding to early splittings in the thermalization cascade; this is to be expected as the appearance of the $SU(2)_L$ singlet fermion from the initial W particles requires at least three splittings, e.g. $W \to \ell_L \to B \to \ell_R$.

The bottom frame of Fig. 4.6 shows the spectra of OoE particles resulting from the injection of $SU(2)_L$ doublet leptons ℓ_L. Here, the two possible primary splittings are the emission of a W or B boson. Since the corresponding differential rates scale like $1/[y^{3/2}\sqrt{1-y}]$ and $1/\sqrt{y(1-y)}$ respectively (see equations 4.21 and 4.22), the emitted gauge bosons are predominantly soft, while a larger fraction of the momentum is carried off by the remaining fermion; this is why the gauge boson spectra do not spike as $x \to x_{\mathrm{M}}$. Following our discussion of the LPM effect on the emission of abelian and non-abelian gauge bosons in equations 4.21 and 4.22, the soft gauge bosons are even more strongly favored in case of W emission, which explains the difference between the behaviors of the W and B spectra as $x \to x_{\mathrm{M}}$. In comparison to what we had in the case of initial W injection, the $SU(2)_L$ singlet fermions can, in the case of initial ℓ_L injection, be already produced in the second step of their cascade, so their spectra at large x lie well above those shown in the top frames in Fig. 4.6. Gluons, on the other hand, require at least three splitting reactions to be produced; combined with their very short thermalization time, this explains why gluons have by far the smallest spectrum as $x \to x_{\mathrm{M}}$. The gluon flux in the thermalization cascade remains below the flux of W bosons even for the smallest x shown in the bottom frame of Fig. 4.6; however, the arguments made earlier for the case of W injection imply that also in the case of ℓ_L injections gluons will eventually dominate the cascade if $x_{\mathrm{M}} \gg 10^4$ (see footnote 15).

Finally, it is worth noting that although the dominant contribution to initial stages of the thermalization cascade for both W and ℓ_L is the emission of Ws, the resulting W spectrum in the

[15] The results for higher $x_{\mathrm{M}} = 10^{12}$ from [70], obtained via a more efficient discritization method (see footnote 13 on Page 50) similarly result in a gluon crossover at $x/x_{\mathrm{M}} \sim \mathcal{O}\left(10^{-5}\right)$.

W injection scenario (top frames of Fig. 4.6) differs slightly from that of the ℓ_L spectrum in the bottom frame. This is due to the fact that the rate for $A \to AA$ splittings is enhanced by a factor $1/(1-y)$ relative to that for $F \to AF$ splittings (see eq. 4.17). This relative enhancement factor allows for more emissions of relatively harder W bosons from an initial W, speeding up the loss of very energetic Ws in the cascade. The latter is further enhanced by $A \to FF$ splittings which, while comparatively rare, further reduce the number of gauge bosons in the cascade. In contrast, emission off fermions favors very soft gauge bosons, leading to smaller energy loss; note also that no splitting process can reduce the number of fermions in the cascade. These two effects combine to produce a pronounced minimum in the W spectrum for the case of W injection, at $x \sim x_{\mathrm{M}}/2$, whereas the ℓ_L spectrum for the case of ℓ_L injection reaches its minimum closer to x_{M}, and rises more slowly for smaller x. The x dependence of the denominator in eq. 4.32 also plays a role in determining the shape of the spectra near their minima.

- $I \in \{g, q_L, q_R\}$

  We saw above that starting from an initial population of HE color–singlet particles, the thermalization cascade develops toward an OoE plasma dominated by the colored quarks and gluons. Let us therefore finally focus on the case where the injected particles are themselves charged under $SU(3)_C$. The resulting spectra are shown in Fig. 4.7 for injected gluons (top left), $SU(2)_L$ doublet quarks (top right), and $SU(2)_L$ singlet quarks (bottom).

  A first observation here could be, as already discussed in the context of Fig. 4.5 and Fig. 4.6, that the shape of the spectrum of the injected particle at large x depends partly on whether the species is a fermion or gauge boson. A second expectable observation in Fig. 4.7 is that, in all three initial injection cases, colored particles remain the dominant species in the spectrum, with the gluons eventually ending up on top. If gluons are the injected particles, their spectrum (light green) is quite close to that of a pure gluon cascade (dark green) for all x; the reason for that echoes closely our explanation for the persistence of the W spectra in the case of W injection in Fig. 4.6, namely, the relative efficiency of the $A \to AA$ splittings. Compared to the allowed splittings of the W, this efficiency is even more pronounced in the case of $g \to gg$ as both the $A \to AA$ and the $A \to FF$ splittings are comprised of $SU(3)_C$–charged particles, whereas the $W \to q_L q_L$ splitting enjoyed relatively larger color and smaller LPM suppression factors.

  A closer look at the gluon and pure gluon spectra in the top frame of Fig. 4.7 also shows a slight reduction of the actual gluon normalization, relative to the pure gluon spectrum. This is to be expected due to the loss of a fraction of gluons from splitting into quarks at every step of the splitting cascade, further reflected in the larger total splitting rate in eq. 4.34 compared to the pure gluon case in eq. 4.29. The consecutive fractional loss of gluons to quarks in the thermalization cascade is then of course balanced out by the predominant emission of gluons from the resulting quarks, resulting in a gluon spectrum closely following that of the pure gluon analysis.

  The $g \to qq$ splittings do not distinguish between left– and right–chiral quarks, whose spectra are therefore very similar in the top left frame of Fig. 4.7. The latter two almost identical spectra of q_L and q_R will further source electroweak gauge bosons and leptons, appearing first in the second and third step of the cascade, respectively. Radiations of B from the quarks will favor harder Bs as discussed above, resulting in a sharper rise of the B spectrum at $x \to x_{\mathrm{M}}$ as compared to that of Ws. The W spectrum overtakes that of the B at lower x despite a larger

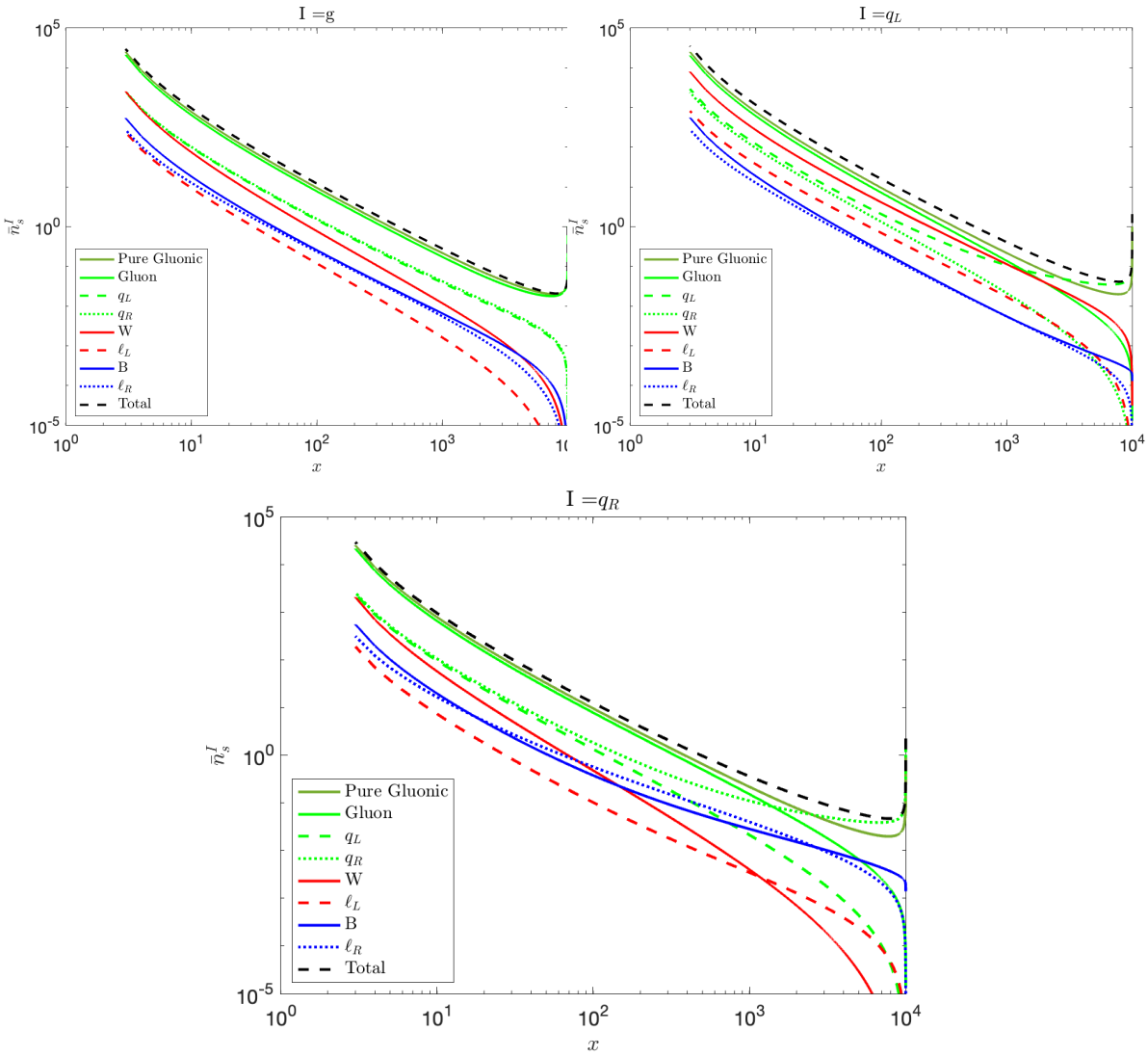

Figure 4.7: The scaled number density functions $\bar{n}_s^I(x)$ of eq. 4.35 for the various particles $s \in \mathbb{S}$, with $I = g$ (top Left), $I = q_L$ (top right) and $I = q_R$ (bottom); we use $x_{\rm M} = 10^4$ for all three cases.

thermalization rate (mainly due to $W \to WW$ splittings), and despite being sourced by q_Ls only. This should again not come as a surprise, as the Bs disappear after each splitting, while the splittings of Ws predominantly lead to extra W bosons. Let us next turn to the tertiary fermions; as before, the ℓ_R population is exclusively sourced by, and therefore tracks, that of the B, with the former winning gradually over the sourcing population of Bs as a result of ℓ_Rs being conserved in their thermalization cascade splittings. Compared to the ℓ_R, the ℓ_L population receives an additional contribution from the splittings of the W. These Ws however, will be predominantly sourcing the W and q_L spectra; only a small fraction of all W bosons splits into ℓ_L pairs. Together with having a larger thermalization rate compared to that of ℓ_R, this makes the ℓ_L spectrum subdominant in the top frame of Fig. 4.7.

Next, let us take a closer look at the case of quark–injection, with the results shown in the top right and bottom frames of Fig. 4.7. For an initial injection of both q_L and q_R, gluons dominate the cascade only for $x < x_{\rm M}/10$, but then the gluon spectrum again quickly approaches that of a pure gluon cascade. Sizeable differences are seen in the relative ordering of the spectra of the two quark chiralities at large x. If q_L are injected, q_R production requires at least two splitting reactions, and vice versa; as a result, the q_L and q_R spectra are seen to converge only for $x \leq 10^{-2} x_{\rm M}$. The chirality of the initially injected quarks is further reflected in the large gap between the W and B populations. For an initial injection of q_L, all electroweak gauge bosons can be produced in the first step of the cascade, albeit with significantly smaller rates than gluons. On the other hand, for initial q_R injection, W bosons can only be produced in the third step,e.g. $q_R \to g \to q_L \to W$. As a result, in the bottom frame, W bosons have the smallest flux at large x.

Through the difference in population of $SU(2)_L$ and $U(1)_Y$ gauge bosons discussed above, the chirality of the initially injected quarks also leaves an imprint on the spectra of the leptons. Due to their smaller hypercharge, ℓ_L pairs are less often produced in the splittings of B; additionally, the ℓ_L spectrum is further affected by a larger thermalization rate due to eventual emissions of the non–Abelian W bosons. On the other hand, relatively more efficient $W \to q_L q_L$ splittings could contribute to the q_L spectrum to tip the balance. With the population of the W subdominant to B in the case of initial q_R injection, however, the ℓ_L population remains below that of $SU(2)_L$ singlet leptons over the entire range of x shown in the bottom frame of Fig. 4.7.

Figures 4.5, 4.6 and 4.7 show that for x not much below $x_{\rm M}$ both the shape and the normalization of the spectra quite strongly depend on the identity of the injected particle, i.e. on the branching ratios of the long–lived matter particles. However, these differences diminish as x becomes smaller; hence with increasing $x_{\rm M}$ a larger and larger part of the spectrum will be largely independent of the high–scale $Br_{\rm I}$ parameters; the role of $x_{\rm M}$ is what we turn to next.

4.5.2 The role of $x_{\rm M}$ and scaling behavior

In Section 4.5.1 we presented solutions to the set of Boltzmann equations (4.32), assuming a decay of the matter component resulting in an initial population of a single species I. Here we focused on setups with cosmological eras of temperatures T, and energy injection via two–body mono–energetic decays of a non–relativistic particle of mass M giving rise to an initial population of HE particles of energy $M/2$, such that the dimensionless parameter $x_{\rm M}$, defined in eq. 3.29 has a fixed value of $x_{\rm M} = 10^4$. We saw that the spectra of SM particles develop via a cascade of splittings towards lower energies with $x \ll x_{\rm M}$. We further observed that the relative amplitudes of the spectra develop towards an attractor solution, where the colored particles are the dominant species in the OoE plasma. A larger span of $x_{\rm M}$ means therefore a larger number of splitting processes occurring throughout the thermalization cascade; we observed that in certain cases (see Fig. 4.6), a larger $x_{\rm M}$ allows the thermalization cascade to develop further towards a dominant population of $SU(3)_C$ charged particles.

In previous chapters in Section 3.4, we presented examples of how a spectrum of OoE particles could be used to study its potential effects cosmological observables. We saw that even for a given mass M of the particle feeding the radiation bath with monochromatic two–body decays, the consideration of different cosmological eras i.e. Hubble eras with different temperatures T, gave rise to a need for an understanding of the spectrum of OoE particles corresponding to different $x_{\rm M}$ values. Additionally, as

discussed in our introduction in Chapter 1, the mass, branching ratios, and the energy spectrum of the initial decay products resulting from e.g. the decays of a matter component depend on the high–scale model and are, therefore, often treated as unknown parameters when calculating observables [69]. As we discussed earlier in the context of eq. 4.35, the introduction of branching ratios does not complicate the OoE spectra beyond the need for a linear combination of a set of pure initial state injection solutions $\bar{n}_s^I(x)$. The remainder of the unknown factors, however, imply a need for the availability of the OoE spectra of different species for different values of the parameter $x_{\rm M}$.

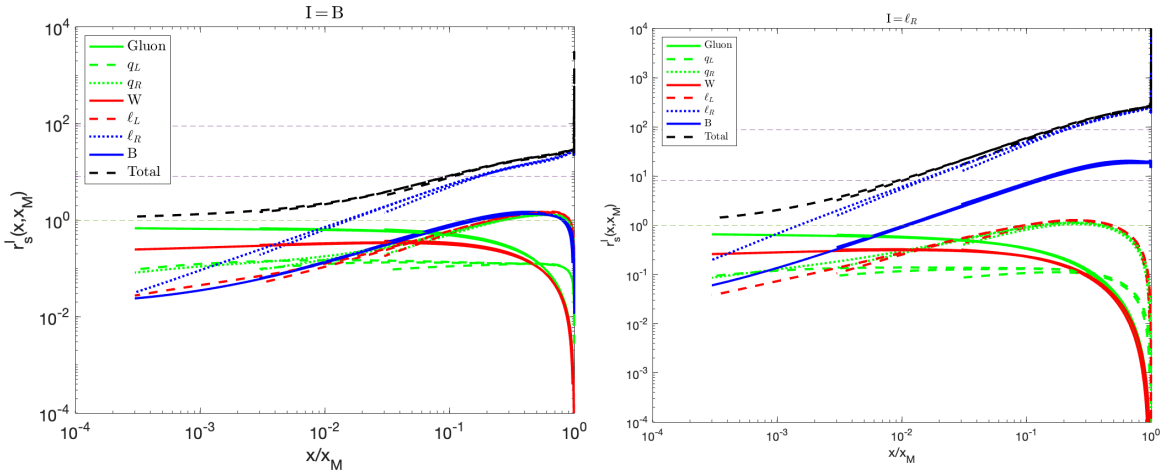

Figure 4.8: Ratios $r_s^I(x, x_{\rm M})$ of eq. 4.36, for initial populations: $I = B$ (left), ℓ_R (right). Results for $x_{\rm M} = 10^2, 10^3, 10^4$ are overlaid. The dark green horizontal dashed line marks $r = 1$. The two purple dashed lines represent the typical normalization of a would–be pure gauge boson ratio curve with coefficients from $W \to WW$ and $B \to \ell_R \ell_R$ splittings.

In this subsection we, therefore, quantitatively analyze the role of $x_{\rm M}$ in the normalization and shape of the OoE spectra resulting from the Boltzmann equations 4.32, and of the set of species $\mathbb{S}$ introduced in eq. 4.24. For a pure gauge boson cascade in Chapter 3, we saw in eq. 3.49 that the normalized spectrum is essentially given by $1/\sqrt{x_{\rm M}}$ times the function (4.30) (see also equations 3.50 and 3.48) which only depends on the ratio $x/x_{\rm M}$, with minor corrections. If this behavior also holds for the entirety of the solution domain [16] for the multi–species cascade we are analyzing here, the ratios

$$r_s^{\rm I}(x, x_{\rm M}) = \frac{\bar{n}_s^I(x, x_{\rm M})}{\bar{n}_{gg}^g(x, x_{\rm M})} \tag{4.36}$$

should to good approximation only depend on the ratio $x/x_{\rm M}$; here $\bar{n}_{gg}^g$ denotes to the dark green curve in the figures in Section 4.5.1, and denotes the pure gluon solution of (4.29), using the full splitting rate of eq. 4.17a. The results are shown in Figs. 4.8 to 4.10 for the different initial injection of species

[16] Scaling behavior in the low–x power–law tail of the particle spectra has previously been observed both in approximate analytical solutions of our pure gluon Boltzmann equations [41], in a somewhat different context in kinetic theory studies of QGP (see e.g. [110] and references therein). Subsequently, this scaling behaviour is also observed in the multi–species coupled set of Boltzmann equations 4.32 in [70]; in line to what we see in Figs. 4.6 and 4.9, the scaling solution is harder to attain for the case of an initial injection of W and ℓ_L (see particularly section 4.2, and the "scaling regime" solution therein).

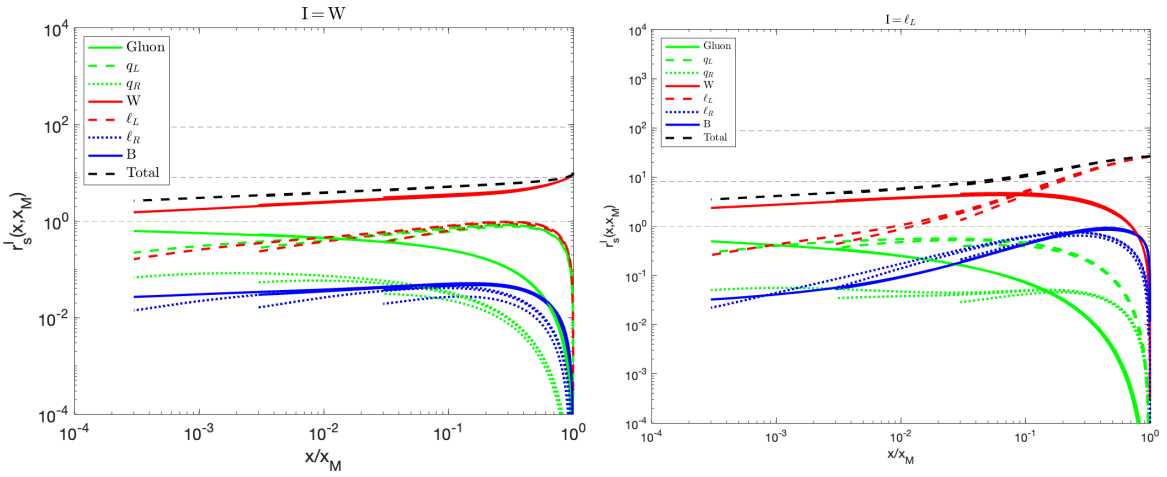

Figure 4.9: Ratios $r_s^I\left(x, x_{\mathrm{M}}\right)$ of eq. 4.36, for initial populations: $I = W$ (left), ℓ_L (right). Results for $x_{\mathrm{M}} = 10^2$, 10^3, 10^4 are overlaid. The dark green horizontal dashed line marks $r = 1$. The two purple dashed lines represent the typical normalization of a would–be pure gauge boson ratio curve with coefficients from $W \to WW$ and $B \to \ell_R \ell_R$ splittings.

$I \in \mathbb{S}$, grouped based on the strongest available interaction as we did in Section 4.5.1. Each figure contains the overlaid $r_s^{\mathrm{I}}\left(x, x_{\mathrm{M}}\right)$ curves for three values of $x_{\mathrm{M}} = 10^2,\ 10^3,$ and 10^4. As guides for the eyes, the dark green horizontal dashed line marks $r = 1$, corresponding to a population $\bar{n}_s^I\left(x, x_{\mathrm{M}}\right)$ coinciding with that of the pure gluon cascade; additionally, the two purple dashed lines show the ratios of the prefactors (see the y-independent terms in eq. 4.17a and 4.17c) for the $W \to WW$, and $B \to \ell_R \ell_R$ [17], relative to that of the $g \to gg$ splitting. Recall that, as seen in eq. 4.32 the normalization of the spectra at $x \to x_{\mathrm{M}}$ is inversely proportionate to the splitting rate.

Looking at the resulting overlaid curves in Figs. 4.8 to 4.10, a first observation is that, within an order of magnitude, a scaling behavior is indeed observed for all species and all cases of initial injection. We further see that the rescaled spectra of gauge bosons typically show a higher degree of this scaling behavior, i.e. are well approximated by a function of x/x_{M}, as compared to the fermionic particles. Note that, the observation of the scaling behavior in the gluon spectra in Figs. 4.8 to 4.10, does not trivially follow from the same observation in the pure gluon treatment in Chapter 3, as the governing Boltzmann equations 4.32 are coupled. Looking at the curves for r_g for example, it is worth emphasising that the scaling behavior is seen even in the case of ℓ_R injection in Fig. 4.8 where gluons are generated in tertiary splittings via e.g. $\ell_R \to B \to q_L \to g$.

In the case of the W boson, we saw in the discussion of Fig. 4.5 that, apart from the relative ratios of the $A \to AA$, $A \to FF$ and $F \to AF$ processes, the evolution equations are quite similar to those of the g. It might, therefore, not be surprising that the rescaled W spectra r_W in Figs. 4.8 to 4.10 do not show a strong dependence on x_{M}, and become relatively flat at $x \ll x_{\mathrm{M}}$ in Figs. 4.8 and 4.10. The evolution equation for Abelian B bosons is, however, quite different due to the absence of $B \to BB$ splitting and the strong LPM suppression of $F \to BF$ splitting. It is therefore also not surprising that

[17] As an Abelian gauge boson the B does not, of course, posses a $B \to BB$ splitting. As such, the prefactor for the $B \to \ell_R \ell_R$ process is used to represent the typical strength of B splittings in comparison to the prefactors of $g \to gg$ and $W \to WW$, merely as a reading aid.

r_B can have quite a different shape than r_W, e.g. in the case of q_R injection. Correspondingly, it seems even less trivial to justify the observation that r_B, to very good approximation, depends on $x_{\rm M}$ only via the ratio $x/x_{\rm M}$, based on the scaling behavior of the pure gluons observed in Chapter 3. It is worth mentioning that the spectra of the various gauge bosons are coupled through the fermions, and in our results in Figs. 4.8 to 4.10, the rescaled fermion spectra do in fact show some residual dependence on $x_{\rm M}$.

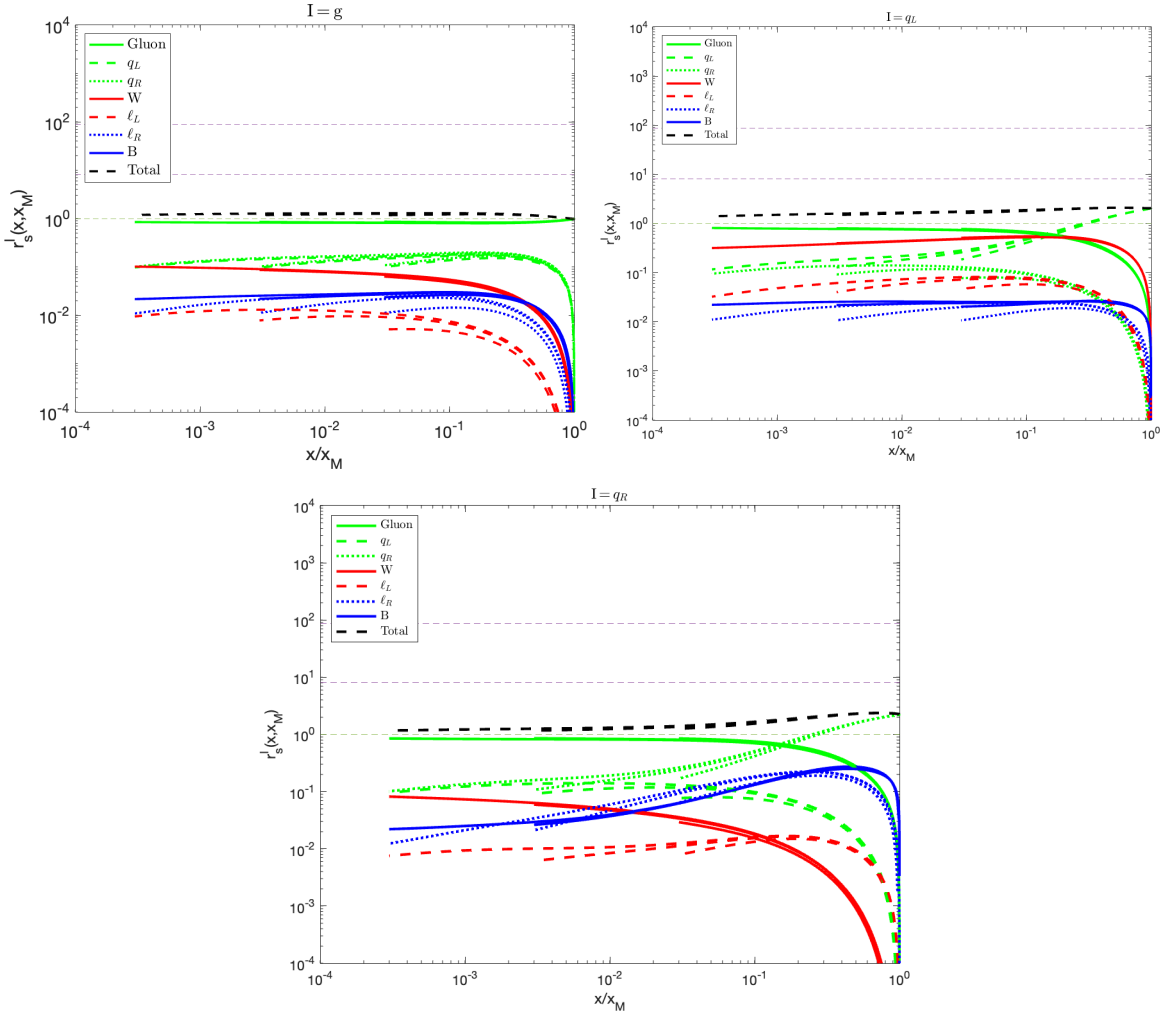

Figure 4.10: Ratios $r_s^I\left(x, x_{\rm M}\right)$ of eq. 4.36, for three initial populations: $I = g$ (top left), q_L (top right), and q_R (bottom). Results for $x_{\rm M} = 10^2$, 10^3, 10^4 are overlaid. The dark green horizontal dashed line marks $r = 1$. The two purple dashed lines represent the typical normalization of a would–be pure gauge boson ratio curve with coefficients from $W \to WW$ and $B \to \ell_R \ell_R$ splittings.

The departure from the scaling behavior in case of fermions is, as seen in Figs. 4.9 and 4.10, most pronounced for r_{ℓ_R}, whose sole means of energy loss in the set of processes we are considering is via the emission of B bosons. Recall that, as we saw in Section 4.5.1 and specifically in Fig. 4.5, a population of B bosons, primarily sources a spectrum of ℓ_R fermions; note also that the B boson ratio curve for an initial W injection in (4.9) does primarily depend on $x/x_{\rm M}$. On the other hand, however,

the differential splitting rate for the B emission off the ℓ_R's only scales like $1/\sqrt{y}$ for small y, while all rates for emitting a non–Abelian gauge boson scale like $1/y^{3/2}$ in that limit. ℓ_R therefore typically emits more energetic gauge bosons, leading to a significantly shorter cascade[18] and hence a stronger dependence on the boundary conditions; that could explain the departure from the scaling behavior and the apparent dependence on $x_{\rm M}$. Moving on to the other fermions in $\mathbb{S}$, the rescaled spectra explicitly depend on $x_{\rm M}$ mostly at relatively small x. This may reflect the effect of $A \to FF$ splitting on the total splitting rate of A which, as we saw above, becomes more competitive at smaller x.

Similar to what was discussed in Section 4.5.1, Figs. 4.8 to 4.10 also illustrate the flow towards an OoE plasma dominated by gluons and quarks, irrespective of the initial injection. In particular, in the case of gluon injection, the ratio functions settle quickly into their asymptotic values, so that the particle ratios depend only weakly on x for $x \leq 0.1 x_{\rm M}$. At least for this scenario, and for the given values of the gauge couplings, one should therefore be able to predict the various ratio functions for $x_{\rm M} > 10^4$ quite accurately by extrapolating the numerical results of the bottom frame of Fig. 4.10, without the need for new numerical solutions of eq. 4.32; recall that the gauge couplings depend on the temperature only logarithmically.

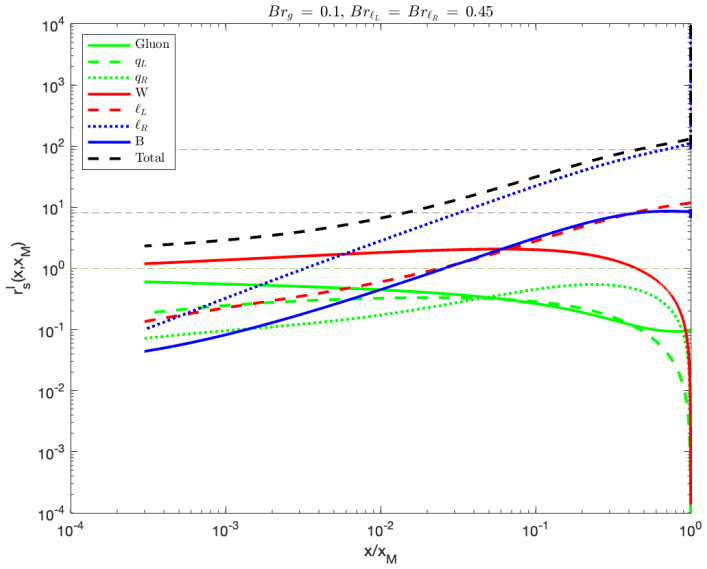

Figure 4.11: Ratios $r_s\left(x, x_{\rm M}\right)$ for a scenario where several species are injected, with branching ratios $Br_g = 0.1$, $Br_{\ell_L} = Br_{\ell_R} = 0.45$, with $x_{\rm M} = 10^4$. The dark green horizontal dashed line marks $r = 1$. The two purple dashed lines represent the typical normalization of a would–be pure gauge boson ratio curve with coefficients from $W \to WW$ and $B \to \ell_R \ell_R$ splittings.

Finally, let us take a moment to explicitly check if our numerical solutions indeed exhibit the earlier advertised linearity in the initial decay branching ratios in eq. 4.32. As depicted in eq. 4.35, once computed, the set of solutions $\bar{n}_s^I(x)$ could be used to deduce the spectrum of OoE particles for any given set of branching ratios Br_I. One such example is shown in Fig. 4.11, where we assumed $Br_g = 0.1$, $Br_{\ell_L} = Br_{\ell_R} = 0.45$ with $x_{\rm M} = 10^4$; we checked explicitly that a direct numerical solution of (4.32) gives the same result within numerical accuracy. The OoE spectra remain dominated by ℓ_R

[18] More exactly, a cascade containing fewer splittings, which nevertheless takes more time, due to the small total splitting rate of l_R.

for most of the range of x, reflecting the slower thermalization of the HE ℓ_R population, as discussed previously for Fig. 4.5.

4.6 Example of applications: Revisiting non–thermal production of heavy dark matter

In Chapter 3, we introduced the machinery allowing us to numerically study the chain of the most efficient splitting processes responsible for the kinetic equilibration of a single species of highly–energetic (HE) non–Abelian gauge bosons, initially appearing as decay products of a matter component comprised of "particles" of mass M and decay width $\Gamma_{\rm M}$. After obtaining a numerical solution and a corresponding analytical approximation in Section 3.3.2, we proceeded to present an example of how such a spectrum of HE particles could be used to calculate further quantities of interest in a given cosmological history. We had briefly introduced the topic of non–thermal (NT) DM production in Chapter 1; in Section 3.4 we revisited the question of the NT production of "heavy" DM particles (χ) resulting from the interactions of OoE particles in the thermalization cascade amongst themselves, as well as with the background thermal plasma of SM particles.

Now that we have worked our way to a multi–species description of the thermalization process, allowing for both the injection and the development of a set of particles (4.24) in the splitting cascade, let us conclude this chapter by repeating the exercise we did in Section 3.4. We would in this case like to know how the more detailed picture of the composition of the OoE plasma of particles in the thermalization cascade can be incorporated into calculating a non–thermal (hard–hard) and semi–thermal (hard–soft) contribution to the population of a *heavy* species χ, which could potentially be a stable DM candidate.

Let us, therefore, first consider the hard–soft production of heavy particles χ via two–body annihilation reactions involving one OoE particle and one particle from the thermal bath. To present an example, let us once again simplify the model–dependence of the matter decay process and the cosmological history to assume that the long–lived particles, with mass M and decay width $\Gamma_{\rm M}$, whose decays are ultimately responsible for the spectra of OoE particles, dominate the energy density of the universe prior to its decay.

Let us quickly recap our results from Section 3.4. The long–lived very massive M particles dominated the energy density as long as the temperature is above the reheating temperature (3.53), approximated by

$$T_{\rm RH} \sim \sqrt{\Gamma_{\rm M} M_{\rm Pl}}\,, \tag{4.37}$$

where $M_{\rm Pl}$ is the reduced Planck mass (see eq. 3.1 and 2.10). We further saw in Fig. 3.8, that the thermal ("soft–soft") contribution to χ production became competitive as $m_\chi \to T_{\rm RH}$. If $m_\chi \lesssim T_{\rm RH}$, total χ pair production through renormalizable interactions will be dominated by reactions only involving thermalized particles, so the resulting χ density will be insensitive to the details of the spectra of nonthermal particles. On the other hand, if $m_\chi \gg T_{\rm RH}$ (e.g. $m_\chi > 20 T_{\rm RH}$ in the case of WIMPs), thermal production of χ particles will effectively cease at temperature $T_{\rm TP} \gg T_{\rm RH}$ ($T_{\rm TP} \sim \mathcal{O}\left(0.05 m_\chi\right) > T_{\rm RH}$ for the famous WIMPs in an RD universe). Any thermal contribution to the χ density will then be diluted by the entropy production between $T_{\rm TP}$ and $T_{\rm RH}$. In this case the final χ

density may be dominated by the semi–thermal processes of the kind

$$s\, s' \longrightarrow \chi\, \chi\,, \tag{4.38}$$

where $s' \in$ SM denotes a "soft" particle from the thermal bath, but the "hard" $s \in \mathbb{S}$ is taken from the spectra (4.31) of OoE particles, with momentum $p_s \gg T$. Denoting the corresponding production cross section by $\sigma_\chi^{\rm hs}$ and incorporating the ratio function (4.36), we can rewrite eq. 3.58 for the χ number density n_χ anew to get

$$\begin{aligned} \frac{dn_\chi^{\rm hs}(T)}{dt} + 3Hn_\chi^{\rm hs} &= \sum_{s,\,s'} \int n_{s'}(T)\, \langle \sigma_\chi^{\rm hs} v \rangle_{s,\,s'}(p,T)\, \tilde{n}_s(p,T)\, dp \\ &= \sum_{s,\,s'} \int n_{s'}(T)\, \langle \sigma_\chi^{\rm hs} v \rangle_{s,\,s'}(p,T)\, r_s(p,T)\, \tilde{n}_{gg}^{g}(p,T)\, dp\,. \end{aligned} \tag{4.39}$$

Here, $n_{s'}(T) = c_{s'}\zeta(3) g_{s'} T^3/\pi^2$ with $c_{s'} = 1\ (3/4)$ for bosonic (fermionic) s' is the thermal number density (2.20) of the species s' with $g_{s'}$ degrees of freedom, $\langle \sigma_\chi^{\rm hs} v \rangle_{s,\,s'}$ denotes the appropriate "thermal average" of the production cross section for the process 4.38, including the correct averaging over the gauge and spin degrees of freedom. The ratio functions r_s are used to write $\tilde{n}_s(p,T)$ in terms of the pure gluon solution of eq. 4.29.

Similar to what we had in Section 3.4, the form of the Boltzmann equation 4.39 implies a number of assumptions. We are focusing on a case where the lifetime of the produced χ's is much larger than $1/\Gamma_{\rm M}$, so that we can treat them as stable; this is certainly true if we are interested in χ directly as a DM candidate. We have further assumed that n_χ remains small enough so that χ annihilation processes are negligible. Despite these approximations, the incorporation of the ratios r_s in eq. 4.39 now allows for a much more precise calculation for the production rate of the process (4.38) compared to what was previously possible in Section 3.4.

Recall further that for a complete picture we need to consider the Boltzmann equation 4.39, as an approximation to the population of χ particles produced during a given Hubble era, for various eras of different temperatures T. We saw in Section 3.4 that depending on the ratios of masses and the temperature T of the thermal bath, the dominant contribution to the final χ abundance could be provided by different cosmological eras; the additional involvement of the ratio functions 4.36 in eq. 4.39 introduces further dependence on the initial branchings of the decaying M particles, as well as new forms of momentum dependence for the production rate. Pair production of χ (4.38) is only possible if the CoM energy exceeds $2m_\chi$ (see footnote 16 on Page 59). Since the average energy of a particle in the thermal bath is around $3T$ and the spectrum of OoE particles quickly increases with decreasing momentum (see Figs. 4.5 to 4.7), the dominant contribution to the integral in eq. 4.39 typically comes from a threshold $p \sim m_\chi^2/T$ for an era of temperature T. Looking at Figs. 4.8 to 4.10, the variation of the ratio functions 4.36 are seen to be slower than $1/x$ for $x \leq 0.1 x_{\rm M}$, so that in the absence of numerical calculations, dominant production at $p \sim m_\chi^2/T$ could be assumed to hold for a typical production (4.38).

Together with the fact that $n_{s'} \propto T^3$ in eq. 4.39, the above production at threshold implies that the χ production rate quickly increases with increasing T. However, the entropy dilution of $(T_{\rm RH}/T)^5$, occurring due to further decays between this higher temperature T and the end of reheating at $T_{\rm RH}$, implies that the biggest contribution to the final χ density often comes from temperature $T \simeq T_{\rm RH}$,

unless $m_\chi^2 > T_{\rm RH} M$ [19]. If $m_\chi^2 \ll T_{\rm RH} M$ the, hard–soft production rate will be dominated by particles with energy $p \ll M$, whose spectrum is less dependent on the decay branching ratios of our heavy matter particles. In contrast, for $m_\chi^2 \gtrsim T_{\rm RH} M$, very energetic particles with $p \sim M/2$, corresponding to the region $x \geq 0.1 x_{\rm M}$ will make sizable or even dominant contributions to the hard–soft production of χ's. As we saw in Figs. 4.5 to 4.7 the spectra of the OoE initial states in this case do strongly depend on the initial branching ratios; Figs. 4.8 to 4.10 further imply the strong momentum dependence of the ratio functions should also be taken into account in eq. 4.39.

In Section 3.4, we further introduced $T_{\rm max}$ (3.68), the maximal temperature the thermal plasma in the EMD. We saw that so long as $m_\chi^2 < T_{\rm max} M$, χ particles will be produced down to a threshold temperature $T_{\rm Thr}$ (3.67) via the hard–soft process. For sufficiently heavy χ's, however, we will have $T_{\rm Thr} \gg T_{\rm RH}$, so that the subsequent entropy production due to M decays between $T_{\rm Thr}$ and $T_{\rm RH}$ dilutes the produced χ population, leading e.g. to a suppressed hard–soft DM yield. Moreover, for even heavier χ particles with $m_\chi^2 \gtrsim T_{\rm max} M$, hard–soft processes fail the kinematic threshold, so that χ production will be available solely through the hard–hard processes, where *both* initial particles in the reaction (4.38) belong to the OoE spectra (4.32). In such scenarios, χ production from HE particles from the thermalization cascade accumulate for Hubble eras with $T_{\rm RH} \leq T$. The corresponding evolution of number density of χ's during a Hubble era of temperature T is then given by

$$\frac{dn_\chi^{\rm hh}(T)}{dt} + 3Hn_\chi^{\rm hh} = \sum_s \int dn_s(p,T)\, \Gamma_{s\to\chi}^{\rm hh}(p,T) \tag{4.40}$$

$$= \sum_{s,\,s'} \iint r_s(p,T)\, r_{s'}(p',T)\, \tilde{n}_{gg}^g(p,T)\, \tilde{n}_{gg}^g(p',T)\, \sigma_{s\,s'\to\chi\chi}^{\rm hh}(p,p')\, dp\, dp'. \tag{4.41}$$

Similar to what we had in (4.39), in eq. 4.40, the cross section $\sigma_{s\,s'\to\chi\chi}^{\rm hh}$, can once again be assumed to include the appropriate normalization factors for combinations of s and s' species allowed by the process (4.38). If we were, for example, to rely on a flavor diagonal gauge-neutral $q_R + \bar{q}_R \to \chi + \chi$ production, one should include a factor $1/(2\times 3\times 6)$ in association with using r_{q_R} as each element of the population s need to pick up the right color, and flavor out of the s' spectrum; the remaining factor of $1/2$ accounts for the thermalization cascade including equal parts in particles and antiparticles as discussed in Section 4.3.2. For apparent reasons, and as reflected in the double presence of the ratio function (4.36), the hard–hard production of heavy species χ is more sensitive to the details of the OoE spectra resulting from the thermalization cascade. Our results in Section 4.5 will therefore play an even more important role in the case of hard–hard production for calculations such as those done in Section 3.4 or [41, 42, 52].

4.7 Summary and discussion

Cosmological histories including an EMD or IMD epoch, where the energy density of the universe is dominated by a long–lived matter component of mass M and decay width $\Gamma_{\rm M}$, are well motivated and widely studied. The inclusion of such a period has been shown to potentially affect various aspects

[19] As discussed in Section 4.5.2, the ratio functions are, to a good approximation, a function of $x/x_{\rm M}$ and therefore independent of the temperature T and will not directly affect our argumentation here.

of cosmology, including the production of DM or the baryon asymmetry. Since we know that the universe was dominated by the SM radiation bath at the latest at the onset of BBN, any sizeable matter component should decay and eventually (predominantly) thermalize into the thermal bath.

The thermalization procedure entails the splitting of initial decay products of energy $p_i \gg T$ into $O\left(p_i/T\right)$ particles of energy $O\left(T\right)$, and has been studied in the literature both in cosmological contexts and in the context of HIC. So long as the OoE particles are gauge charged, the dominant process of thermalization is known to be the $1 \rightarrow 2$ near collinear splittings of the energetic particles made possible via soft $t-$channel interactions with the thermal bath, mediated by gauge bosons with thermal mass $O\left(gT\right)$, g being the relevant gauge coupling. The collinearity of the splitting then calls for a careful inclusion of the LPM effect resulting from consecutive interactions of the particles with the plasma during the formation time of the splitting process. The LPM suppressed rate of pure–gauge splittings $g \rightarrow gg$ had already been studied analytically and numerically in the literature, and was the subject of Chapter 3 in this thesis; these studies are motivated by the fact that the QCD sector, and in particular gluons, can be expected to dominate the spectrum of nonthermal particles, at least for momenta $p \ll p_i$; this expectation is in fact verified by our current analysis in Chapter 4, in a majority of cases.

In Chapter 4, we extend the previous works, and our analysis of Chapter 3, by including the full set of chiral SM fermions and gauge bosons in the splitting cascade of an initial population of energetic particles of energy $p_i = M/2$; M here denotes the mass of a heavy decaying matter component. Our choice of particles to study, allows us to limit our attention to three classes of splitting events: pure gauge boson splittings, gauge boson radiation off fermions, and finally fermion pair productions in gauge boson splittings. The functions describing the emission of a gauge boson in vacuum have similar functional forms, but the process rates can have different coupling strengths, flavor multiplicity factors, and numerical LPM suppression factors; evidently these processes increase the number of gauge bosons. In contrast, the splitting of a gauge boson into an $f\bar{f}$ pair is suppressed by a factor p_d/p_p, where p_d and p_p denote the momentum of the softer daughter and parent particle, respectively; it increases the number of fermions, but reduces the number of gauge bosons. Note also that this is the only splitting process available to Abelian gauge bosons.

We use the explicitly calculated results for LPM suppressed splitting rates corresponding to an $SU(N)$ gauge group from the literature, and use physical arguments to deduce the rate for processes involving species charged under different gauge groups, see equations 4.16 to 4.19. The resulting Boltzmann equations can be written in terms of the dimensionless ratio $x = p/T$, see eq. 4.32; in this form the equations depend only on $x_{\mathrm{M}} = M/2T$ rather than on M and T separately. Of course, the decay branching ratios of the matter particles into the various SM species are also important, but due to the linearity of the problem, we only need to consider the limiting cases where decay into a single species dominates. The corresponding numerical results are shown in Figs. 4.5 to 4.7.

We find that spectra of individual species can have order of magnitude deviations from that of the pure–gluon solution, derived in Chapter 3, over several decades of momentum, i.e. for $1 \lesssim x/x_{\mathrm{M}} \lesssim 10^4$. We treat the fermion chiralities separately, since only left–chiral fermions (and right–chiral antifermions) have $SU(2)_L$ interaction. In scenarios with an initial chiral asymmetry in the matter decay products, the latter persists for several decades in x (see e.g. Fig. 4.7). On the other hand, an approximate scale invariant behavior is observed for the ratios of the various species (4.36), which for $x \ll x_{\mathrm{M}}$ asymptotically approach unique solutions independent of the branching ratios.

Our treatment in Chapter 4 concludes the arc introduced in Chapter 1 and should suffice for many practical purposes, greatly improving the precision of the calculation of cosmological processes

involving OoE particles. The validity of the results is, however, limited by the approximations we made; let us review these briefly. In writing the Boltzmann equations (4.32), we disregard the role of hard $2 \to 2$ processes, similar to what we did in our simpler analysis of Chapter 3. This should be a good approximation so long as $x \gg 1$[20], but the low$-x$ tail of our result could be affected. On the other hand, these results for the ratios of spectra, together with the pure gluon solution, should serve as a good approximation for $x \gg 1$ regions even for cases with $x_{\mathrm{M}} \gg 10^4$, as we argued in section 4.5. Recall also that the total flux of particles with momentum $p \lesssim 10T$ will in any case be dominated by the thermal component.

Another reasonable approximation we have incorporated in our analysis is that of a quasi–static Boltzmann equation (4.31). As motivated in eq. 3.19 and Chapter 3, the gravitational Hubble expansion can be neglected in comparison to the much faster gauge–mediated particle processes, unless one is interested in cosmological eras with a very large temperature with a very large matter to radiation ratio $\rho_{\mathrm{M}}/\rho_{\mathrm{R}} \gg 1$, corresponding, e.g., to very early stages of reheating; it should also be noted that at these very early stages of reheating, a thermal background radiation bath of temperature T could be absent. The relevant timescale for the initial formation of a thermal radiation bath has been previously studied in the literature, is however not the subject of this work [21]; this timescale affects the maximum temperature attained in the universe (3.68), which we used to identify a cosmological history in Section 3.4 and Section 4.6.

Finally, a notable simplifying assumption we used to limit the number of coupled integral equations to be solved, was to limit our attention to a subset $\mathbb{S}$ (4.24) of the SM particle content, excluding the scalar Higgs and its interactions with the species in $\mathbb{S}$. In Section 4.3.2 we argued that we may safely leave out the SM Higgs doublet in our analysis, but this may be different in models with extended Higgs sectors (with more degrees of freedom, and often also enhanced couplings to some fermions). Scalars, and Majorana gauginos, will certainly be important if one wishes to analyze a supersymmetric cascade. Results for medium induced scalar–scalar–gauge boson splittings have been published in the literature [66]; these would need to be augmented with splitting functions involving Yukawa interactions; this is subsequently included in the analysis in [70], where the third generation quarks are treated separately to account for large Yukawa interactions. It is worth mentioning that the same machinery introduced and used here in Chapter 4, could in principle be used to study models with extended particle content; e.g. extension of the SM involving SUSY. Such scenarios will admit a larger number of splitting processes, compared to Fig. 4.4, and would require us to keep track of a larger set of particles (4.24).

[20] Another implicit approximation is the use of a single form of the LPM suppression factor over several orders of magnitudes in x; interpolation schemes have been suggested [111] to smoothly cross over to the unsuppressed Bethe–Heitler regime of eq. 4.5.

[21] In scenarios where there is no preexisting thermal radiation bath, e.g. at the onset of reheating after inflation, the energetic decay products can only interact with each other. The critical process will then be the formation of a *seed* of soft particles, on which later energetic decay products can scatter [52, 61]. This is somewhat similar to the initial stages of HIC [62, 63]. The details of this process, and in particular the critical timescale of seed formation, set the *maximal* temperature of the radiation bath [39, 52]. We will not be dealing with these very early stages of thermalization. Note that in possible post–inflationary epochs, where energetic particles are injected, the existence of a thermal bath is guaranteed.

CHAPTER 5

Summary

Theories of GR and QFT are used to formulate models for the observable universe and its content. The ΛCDM and the SM, are two such models, that can be broadly said to capture our understanding of the evolution (expansion) history of the universe, and the interactions of its contents [1]. The so called "standard" cosmological histories of the universe typically involve an initial *inflationary* expansion era, followed by a *reheating* phase through which the universe is filled up with relativistic *radiation* which subsequently cools down via the expansion of the universe. Observations corresponding to the BBN imply that the universe has indeed been RD at temperatures $\sim 3\,\mathrm{MeV}$ [2]. The subsequent expansion of the universe then leads to a MD era and finally, to the present day state of accelerated expansion.

The standard history can, however, be modified to include, e.g. , additional EMD or IMD periods; in fact, such MD eras often arise naturally in models and cosmological histories studied in the literature [20]. Irrespective of their origin, observational constraints require such MD eras to end, and for the energy contained in the matter component to be converted to thermal radiation. Particles comprising the matter component can have masses that are larger than the temperature of the TB at the time of their decay by many orders of magnitude. The particles resulting from the decay of the matter component, therefore, have a non–thermal distribution of energy, with energies much larger than the temperature of the thermal radiation bath; moreover, while the composition of elementary particles resulting directly from the decay of the matter component particles is controlled by its mass and couplings to lighter particles, the composition of the TB is solely controlled by the temperature.

A process of *thermalization* is therefore required to convert the initial OoE distribution of HE particles, to a population of particles belonging to the TB. Assuming the decaying matter particle to have a mass M much larger than the temperature T of the TB, the thermalization process is responsible for generating $\mathcal{O}\left(M/T\right)$ new particles and redistributing the energy of the initial HE particles among these to ensure a thermal distribution of energy, as well as the thermal particle composition. Changes in the particle composition, generation of new particles, and the redistribution of energy all rely on particle interactions that could potentially occur among the HE particles from the OoE decay products, and particles from the TB. In this thesis, we study the process of thermalization of HE particles, in a background of particles from a thermal radiation bath.

We start in Chapter 2 by introducing the thermal radiation bath and its composition; focusing on a TB of unbroken SM particles, we review the particle composition of a radiation bath of temperature T. We then move on in Section 2.4 to introduce some concepts in *thermal field theory*, in particular the "thermal mass" capturing the effect of forward scatterings of a particle traversing the TB off the

particles it contains. This is followed by a brief introduction to *kinetic theory* in Section 2.5, a tool to study the evolution of the composition of an ensemble of particles; we introduce the Boltzmann equation, governing the evolution of phase–space distribution functions due to the expansion of the universe and particle interactions. We then point out that the validity of the kinetic theory treatment hinges on a number of criteria, which could be violated for specific processes of interest, calling for the formulation of an "effective kinetic theory" capturing the effects which would otherwise render the kinetic theory invalid [49]. We provide an example of a case, where the quantum mechanical duration of a process exceeds the mean–free time of the particle under study in the thermal plasma, therefore failing one of the validity conditions for the kinetic theory treatment [48]. We further allude to how this particular failure could be remedied by a reformulation in terms of an effective kinetic theory treatment.

In Chapter 3, we start applying the lessons from Chapter 2 to the problem of thermalization of HE particles of energy of $\mathcal{O}(M)$, resulting from decays of particles of mass M, in a thermal background plasma of temperature $T \ll M$. We realise that the large energy of the decay products typically suppresses the rate of interactions for the OoE particles, so that we may focus on the process of energy loss (kinetic equilibration), as the initial stage to be accomplished before chemical equilibrium can be reached [52]. Taking up the simplifying assumption that we are dealing with a single species of non–Abelian gauge bosons A, only capable of generating new particles from its own species, we study the particle interactions that could contribute to the process of energy loss of A particles propagating in the TB. While this is a simplifying assumption, within the SM, the $SU(3)_C$ or $SU(2)_L$ gauge bosons could be thought to take up the role of A.

In Section 3.1.2 we find that nearly–collinear *splittings* of the form $A \to AA$, in association with a forward scattering of the A particles off the particles in the TB, provide the most efficient means of energy loss for the HE A particles [61]. A closer look at this process, however, shows that directly incorporating it into the Boltzmann equation would lead to a violation of the validity of kinetic theory treatment. The root cause of the issue can be traced back to the long "formation time" associated with the near–collinear splitting process $A \to AA$; quantum mechanical contributions from splitting process associated with scatterings off multiple scatterers in the TB interfere as a result of the "long" formation time, and can therefore not be treated as independent contributions in the Boltzmann equation. The effective kinetic theory treatment required to deal with this issue is achieved in Section 3.1.3 by including the LPM suppression factor associated with the $A \to AA$ splitting process [39]. Physically, the LPM suppression factor encodes the *fraction* of splitting processes that are not suppressed by quantum interference.

Knowing the form of the effective kinetic theory of nearly–collinear splittings for a non–Abelian gauge boson in a thermal background, we proceed in Section 3.2 to study the process of energy loss of HE A particles resulting from two–body decays of a decaying matter component, with particles of mass M. Using the dimensionless parameter $x \equiv p/T$, with p denoting the momentum (energy) of the relativistic particles, and defining away the dependence of the equation on the number density and decay rate of the matter component, we bring the Boltzmann equation into a form better suited for analytical and numerical treatment. The resulting Boltzmann equation 3.33, can be thought of as yielding the number density distribution $\bar{n}(x)$ (3.31) of OoE A particles resulting from the cascade of splittings of a single A particle injected into the TB at dimensionless energy $x_{\mathrm{M}} \equiv M/2T$ directly via two–body M decays. We present an approximate analytical solution (3.44) introduced in the literature [41] in Section 3.3.1, and further proceed to numerically solve the Boltzmann equation in Section 3.3.2. To do so, we motivate and introduce an IR–cutoff (see eq. 3.45), representing the

minimum energy a "daughter" particle can carry away in a splitting process.

Solving (3.33) for different values of x_{M} and choices of the cutoff parameter, we first observe that the physical energy distribution of OoE particles is independent of the choice of the cutoff parameter, which can therefore be set to $p = T \rightarrow x = 1$ without loss of generality. We further observe that the resulting energy spectrum of HE A particles exhibits the behavior we expect; assuming a monochromatic injection of initial decay products at dimensionless energy x_{M}, the spectrum quickly diminishes in the immediate vicinity of x_{M}, before flattening out at $x_{\_} \sim 0.8\, x_{\mathrm{M}}$; this falling behavior reflects the fact that there are "few" particles splitting in the upstream (i.e. $x > x_{\_}$) energy interval, and on the other hand a "large" number of splitting combinations available to the upstream particles. The combined effects of further splitting subsequently leads to a growth of the spectrum towards lower x so that for a large intermediate region, $1 \ll x \ll x_{\mathrm{M}}$, the dimensionless spectrum will have a form $\propto x^{-3/2}$, consistent with the analytical approximation in the same x region. The growth of $\bar{n}\,(x)$ towards lower x results in the normalised OoE spectrum approaching a value $\bar{n}\,(x) \sim x_{\mathrm{M}}$, as would be expected from energy conservation.

After obtaining numerical solutions of $\bar{n}\,(x)$ for several values of x_{M}, we proceed in Section 3.3.3 to find a new analytical approximate solution (3.49), describing the numerical solution in the entire x region. In Section 3.4 examples are presented of how the spectrum of HE particles can be used to calculate contributions to the production of χ particles, too heavy ($m_{\chi} \gg T$) to be produced efficiently via interactions among particles from the TB, via interactions of the OoE particles among themselves and with the TB particles. Results from the numerically calculated spectrum of OoE A gauge bosons show an $O\,(1)$ improvement relative to the previous analytical estimations; this improvement is further reflected, in this example, in the resulting yield of heavy χ particles (see Fig. 3.7).

Having established a framework to formulate and solve the Boltzmann equation for the effective kinetic theory of energy loss of a single species of non–Abelian gauge bosons, we move in Chapter 4 to lift the simplifying assumption that the energy loss cascade consists exclusively of particles of species A. In Section 4.3 we revisit the formulation of an effective kinetic theory of nearly collinear splitting processes. We motivate the form of LPM suppression factors corresponding to nearly–collinear splittings of the type $s \rightarrow s's''$, where s, s', and $s'' \in \mathbb{S}$ (see eq. 4.24) represent potentially different species from the SM [79]; this is necessary because the differences in interaction rate from particle species s, s', and s'' with the background thermal plasma result in differences in contribution to the momentum diffusion behavior setting the formation time. We pay particular attention to the distinction between the momentum diffusion process for HE Abelian and non–Abelian gauge bosons.

Leaving out the only scalar species in the SM, i.e. $H \notin \mathbb{S}$, we use the set of LPM–suppressed rates (4.16, 4.17) for nearly–collinear splittings $A \rightarrow AA$, $A \rightarrow FF$, and $F \rightarrow AF$, with A, $F \in \mathbb{S}$ representing the gauge bosons, and fermions of the SM respectively. In Section 4.4 we use these rates to write down a set of coupled Boltzmann equations governing the OoE spectra of particles developing via cascades of $s \rightarrow s's''$ splittings subsequent to initial decays of the matter complement of mass M. We once again use the x parameter, along with a an appropriate form of normalization (4.33), to bring the Boltzmann equations to a form (4.32) suitable for numerical treatment. Using the numerical method developed in Chapter 3, we can solve for the normalised spectra $\bar{n}_s\,(x)$ for $s \in \mathbb{S}$; similar to what we had before, $\bar{n}_s\,(x)$ is proportional to the number of particles of species s resulting from the initial decay of a single M particle to particles from $\mathbb{S}$ and of dimensionless energy $x_{\mathrm{M}}/2$.

With the introduction of multiple species $I \in \mathbb{S}$, the branching ratios Br_{I} of the matter component M into the different initial decay products also enter the calculation of the spectra $\bar{n}_s\,(x)$. Motivated by the linearity of the Boltzmann equation 4.32 in Br_{I}, we therefore solve for the spectra $\bar{n}^{\mathrm{I}}_s\,(x)$, each time

assuming $Br_{\rm I} = 1$, for a single species I. The results, presented in Section 4.5, and particularly as seen in Figs. 4.5 to 4.7, show that the spectra of different species s can be orders of magnitude apart, both at high and low–x regions. We further see that the inclusion of several species s, and the appearance and disappearance of species in $s \to s's''$ processes, as well as the dependence on the initial decay products I, lead to stark differences in the x–dependence of the spectra $\bar{n}^{\rm I}_s(x)$; the observations here are notably different from the behavior seen in the high–x region of the single–species spectrum obtained in Section 3.3, reflected e.g. in eq. 3.49. This departure is consistent with the spectra $\bar{n}^{\rm I}_s(x)$ in Figs. 4.5 to 4.7 flowing towards a universal hierarchy of the spectra $\bar{n}_s(x)$ at low–x regions, with the QCD plasma dominating the OoE plasma [60]; in other words, depending on the composition of initial decay products $Br_{\rm I}$, the spectra $\bar{n}_s(s)$ must flow differently towards a common QCD–dominated plasma. Comparisons of the spectra $\bar{n}_s(x)$ for different values of $x_{\rm M}$ in Section 4.5.2, and particularly Figs. 4.6 and 4.8 to 4.10, show that larger $x_{\rm M}$ values allow for a longer flow towards the QCD plasma; this is further seen in the results in following studies [70].

We analyse the hierarchy of the spectra in Figs. 4.5 to 4.7, based on the couplings, multiplicities and symmetries of the SM, and find that these agree with our understanding and expectations. As in the case of a single species spectrum discussed in Chapter 3, the kinetic equilibration process based on $s \to s's''$ splittings converts the energy M in a single matter decay event to $\mathcal{O}(M/T)$ particles of energy $\sim T$. We further use the linearity of the Boltzmann equation 4.32 in $Br_{\rm I}$ to cross check the validity of our numerical solution. Calculating the resulting spectra $\bar{n}_s(x)$, once directly, and once using a linear combination of $\bar{n}^{\rm I}_s(x)$, the comparison can be seen in Fig. 4.11.

Similar to what we had in Chapter 3, we conclude our multi–species study of the OoE thermalization spectra $\bar{n}^{\rm I}_s(x)$, by exemplifying how these could be used for relevant calculations in cosmology. In Section 4.6 we revisit the problem of the production of heavy ($m_\chi \gg T$) particles, via interactions of the HE particles from the thermalization cascade with those of the TB, and among themselves. As seen in equations 4.39 and 4.40, a more precise knowledge of the OoE spectra directly translates to a better control over the resulting yield of χ particles. We conclude this thesis by a summary of our findings in Section 4.7, where we also comment on potential next steps in the study of the thermalization process after the injection of HE gauge–interacting particles into a background thermal plasma.

APPENDIX A

Running of the coupling constants, and the treatment of couplings for the SM

Throughout Chapters 2 to 4, we have assumed the existence of an unambiguous coupling constant, or equivalently α_G corresponding to the gauge group G. From QFT, however, we know the coupling constants of the SM to be scale dependant, with the evolution given by the beta functions (see e.g. [112]). At energy scale μ, the renormalization group equations imply

$$\alpha_G^{-1}(\mu) - \alpha_G^{-1}(\mu_0) = -\frac{b_G}{4\pi} \ln \frac{\mu^2}{\mu_0^2}, \tag{A.1}$$

with μ_0 denoting a reference scale, and $\alpha_G(\mu_0)$ the corresponding fine structure constant. The coefficient b_G, representing the contributing loop diagrams, can be written as

$$b_G = \begin{cases} 41/6 & G = U(1)_Y \\ -19/6 & G = SU(2)_L \\ -7 & G = SU(3)_C \end{cases}. \tag{A.2}$$

Equation A.2 involves the contribution of the full SM particles to the running of the couplings which, as explained in Chapter 2, is relevant for our purpose of studying the unbroken "massless" SM.

Equation A.1 therefore allows relating the couplings g_G, at a given scale μ, to those of a reference scale μ_0. For the latter, we may use the values from [1], noting that the values for $\alpha_{U(1)_Y}$ and $\alpha_{SU(2)_L}$ may be obtained from that of the $\alpha_{U(1)_{\mathrm{EM}}}$ via the Weinberg angle θ_W.

$$\sin^2(\theta_W) \approx 0.231, \qquad m_Z = 91.2\,\mathrm{GeV}, \qquad \alpha_{U(1)_{\mathrm{EM}}}(m_Z) \approx 1/128, \tag{A.3}$$

as

$$\alpha_{SU(3)_C}(m_Z) \approx 0.118, \quad \alpha_{SU(2)_L}(m_Z) = \sin^{-2}\theta_W \alpha_{U(1)_{\mathrm{EM}}}(m_Z) \approx 0.0338, \tag{A.4}$$

$$\alpha_{U(1)_Y}(m_Z) = (1 - \sin^2\theta_W)^{-1} \alpha_{U(1)_{\mathrm{EM}}}(m_Z) \approx 0.0102. \tag{A.5}$$

The question that remains to be addressed will then be that of the scale μ appropriate for our purpose of studying the soft, hard, and splitting processes in the thermalization cascade. We saw in Chapter 2

(see Fig. 2.4) and Chapter 4, that $2 \to 2$ processes with different magnitude of momentum exchange contribute constructively to the momentum diffusion, or the growth of the transverse momenta $k\perp$ of the collinearly emitted particles. The logarithmic form of eq. A.1, however, implies that although we formally need to treat the gauge coupling as depending on the momentum exchange scale, this dependence can be disregarded for a simplified treatment, leading to a Coulomb logarithmic description of the combined effect of soft to hard $2 \to 2$ processes (see footnote 6 on page Page 40). A more detailed view, allowing for a scale–dependent treatment of couplings leading to equations 4.20, can be found in Section VI of [79].

As discussed in Chapters 2 to 4, we use the thermal mass scale gT, with g denoting the coupling constant of the dominant gauge group $G \in SU(3)_C \times SU(2)_L \times U(1)_Y$ for a particle $s \in$SM, to cutoff the IR divergencies of the forward $2 \to 2$ scattering process. The latter we further use to deduce the coherence time for the LPM suppression effect. As such, we find gT to be a reasonable choice of scale for representing the various processes central to the study of thermalization of HE particles in the presence of a background plasma.

As the coupling constant g appears in the choice of the scale $\mu = gT$, at which we wish to estimate g, I decided to use a recursive approach to the calculation of $g\ (\mu = gT)$. Since we take the coupling strength g to also represent processes at energies $p \gg gT$, I have used the temperature T to directly calculate a first set of couplings $g_G\ (T)$, which are then further used for an estimation of the couplings as

$$\alpha_G\left(\mu = g_G \cdot T\right) \approx \alpha_G(\mu = g_G\ (T) \cdot T). \tag{A.6}$$

Note that the amplitude for α_G, only affects the overall scaling for the spectrum of a single species of OoE particles, as discussed in Chapter 3; in the case of multiple species in Chapter 4, however, ratios of different coupling strengths potentially affect the shape and development of the spectra.

I have therefore used the approximation (A.6), together with Eqs. (A.1) to (A.3) to estimate

$$\alpha_{SU(3)_C}\left(g_{SU(3)_C}T\right) \approx 0.063, \quad \alpha_{SU(2)_L}\left(g_{SU(2)_L}T\right) \approx 0.027, \quad \alpha_{U(1)_Y}\left(g_{U(1)_Y}T\right) \approx 0.001, \tag{A.7}$$

in the numerical treatment of the coupled Boltzmann equations (4.31) in Chapter 4.

APPENDIX B

Standard Model gauge boson thermal masses

In Chapter 2 we reviewed the physics of thermal field theory, giving rise to an effective "thermal mass" for particles traversing a thermal background plasma of temperature T (see Section 2.4). We established that the gauge bosons, corresponding to the gauge group $G \in$SM pick up a thermal mass of the order of gT, where g is the coupling strength corresponding to the gauge group G.

We further see, in Chapter 3, that a different value for the coupling constant and/or the thermal mass, would change the overall scaling of the spectrum of OoE particles; this is however no longer the case, once we switch to the multi–species thermalization cascade in Chapter 4. Similar to the role of the ratios of the coupling constants alluded to in Appendix A, the ratios of the thermal masses of the various gauge bosons could affect the hierarchy of the spectra in the case of a cascade involving several species from the SM. Let us therefore take a closer look these ratios to evaluate the approximation made in Chapter 4 and (4.1).

$$m_G^{\text{th}}(T) \approx g_G T\,. \tag{B.1}$$

As mentioned in Chapter 2, the full form of the thermal mass calculation would involve all contributions, similar to what we had in Fig. 2.3, with particles from the thermal bath (red) running in the thermal loop. The couplings of the gauge boson to these bosonic and fermionic particles will therefore come with different multiplicities and group–theoretic factors. The details of the calculation of SM gauge boson thermal masses can be found in the literature (see e.g. [50, 51]); for our purposes, however, it will suffice to look at the form and amplitude of the thermal mass expressions. For the unbroken phase of the SM, we will have two thermal masses corresponding to the $SU(N)$ gauge group, with the thermal mass given by

$$m_G^{\text{th}}(T) = \frac{g^2 T^2}{3}\left(C_A^G + \sum_{f\,\in\,\text{Dirac fermions}} t_f^G + \sum_{s\,\in\,\text{scalars}} t_s^G\right). \tag{B.2}$$

In equation B.2, C_A is the quadratic Casimir corresponding to the non–Abelian gauge boson A of the gauge group G, introduced in (4.18); additionally, we have used $t_{f/s}^G$ to represent the trace normalization coefficient for the representation $R_{f/s}^G$ in which the fermions and scalars transform under the action of the gauge group G; for the fundamental representation of the $SU(N)$, the latter reads $1/2$. Finally, note that the form in (B.2) assumes a Dirac fermion, calling for the insertion of a factor $1/2$ in case chiral fermions are instead used.

For the case of the gluon thermal mass with $G = SU(3)_C$, we will have three generations of up and down type Dirac fermions contributing to the thermal mass. For the case of the W boson, with $G = SU(2)_L$, this is slightly more complicated, with 3 generations of left–chiral leptons, $3 \times 3 = 9$ colored chiral quarks of three generations, and a single scalar Higgs doublet. We thus have a thermal mass of

$$m_g^{\text{th}}(T) = 2g^2T^2 \tag{B.3}$$

$$m_W^{\text{th}}(T) = \frac{11}{6}g^2T^2, \tag{B.4}$$

for the weak and strong gauge bosons traversing a thermal bath of temperature T.

In the case of an Abelian ($U(1)_{\text{EM}}$ or $U(1)_Y$) gauge group, the thermal mass picked up by the gauge boson can be expressed as

$$m_{U(1)}^{\text{th}}(T) = \frac{g^2T^2}{3}\left(\sum_{f\,\in\,\text{Dirac fermions}} q_f^2 + \sum_{s\,\in\,\text{scalars}} q_s^2\right), \tag{B.5}$$

with q representing the $U(1)$ charge. The charge assignment for the $U(1)_Y$ in the case of SM reads

	ℓ_R	ℓ_L	u_R	d_R	q_L	ϕ
$q_{U(1)_Y}$	-1	$-1/2$	$2/3$	$-1/3$	$1/6$	$1/2$

This allows for a calculation of the thermal mass for the $U(1)_Y$ gauge boson as

$$m_B^{\text{th}}(T) = \frac{11}{6}g^2T^2. \tag{B.6}$$

A comparison of equations B.3 and B.6, clearly shows that a simplifying approximation (B.1) does not adversely affect the ratios of spectra of the species (4.24) calculated in Chapter 4; the single overall normalization of the spectra could be affected via the difference in prefactors in Appendix B and Eq. (B.6) of $O(1)$, in line with other approximations we have made throughout this thesis.

APPENDIX C

Analytic approximate solution the single–species splitting driven spectrum

In Chapter 3, we derive the Boltzmann equation (3.23) governing the evolution of the spectrum of a single species of non–Abelian gauge boson thermalizing via near–collinear splittings to further gauge bosons. In an effort to come with an approximate analytical solution, and following [41], we start by disregarding the presence of an IR cutoff in the presence of thermal bath in Section 3.3.1, focusing on an in intermediate region of momenta $M \gg p \gg T$. The resulting equation 3.38, then reads

$$\int_0^{p/2} \frac{\mathrm{d}k}{k^{3/2}} \tilde{n}(p) - \int_{2p}^{M/2} \frac{\mathrm{d}k}{p^{3/2}} \tilde{n}(k) - \int_0^{p} \frac{\mathrm{d}k}{k^{3/2}} \tilde{n}(p+k) \; = 0. \tag{C.1}$$

In eq. C.1 $\tilde{n}\,(p)$ defined in (3.20) represents the spectrum of OoE non–Abelian gauge bosons, and M represents the mass of the decaying particle, and therefore defines the energy scale at which new particles are injected into the thermalization cascade. An ansatz

$$\tilde{n}(p) \propto p^{-n}, \qquad n \in \mathbb{R}^{+} \tag{C.2}$$

was proposed to solve eq. C.1, where the exponent n is to be determined. Plugging the ansatz (C.2) in (C.1), and multiplying with powers of p, we get

$$\underbrace{-\,\mathrm{B}_{1/2}\,(-1/2,1)}_{\text{(I)}} + \underbrace{\frac{1}{n-1}\left((2p/M)^{n-1} - 2^{1-n}\right)}_{\text{(II)}} + \underbrace{\exp\left(i\,3\pi/2\right)\,\mathrm{B}_{-1}\,(-1/2,1-n)}_{\text{(III)}} = 0, \tag{C.3}$$

where $B_a\,(c,d)$ is an (analytically continued) incomplete Beta function defined as

$$B_a(c,d) = \int_0^a t^{c-1}(1-t)^{d-1} dt. \tag{C.4}$$

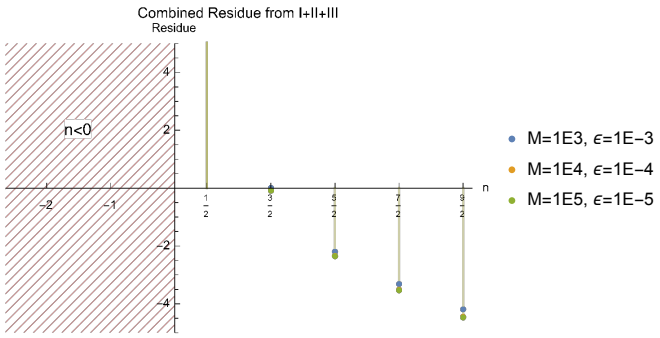

Figure C.1: Residue of an approximate Boltzmann equation (C.5) for the single–species thermalization cascade for choices of ansatz (C.2), using a numerical cutoff ϵ to manifest the cancellation of divergencies.

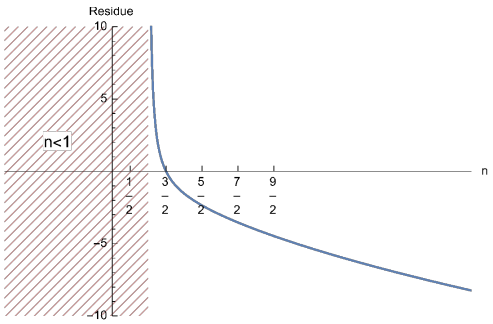

Figure C.2: Residue of a reformulated approximate Boltzmann equation (C.6) for the single–species thermalization cascade for choices of ansatz (C.2), using an analytical regulation and cancellation of the divergencies.

The form in (C.1) and (C.3), imply a cancellation of the divergencies resulting from the lower bound of the integration interval. Let us therefore, digress to replace these in (C.1) with an $\epsilon \ll 1$

$$\int_{\epsilon}^{p/2} \frac{\mathrm{d}k}{k^{3/2}} \tilde{n}(p) - \int_{2p}^{M/2} \frac{\mathrm{d}k}{p^{3/2}} \tilde{n}(k) - \int_{\epsilon}^{p} \frac{\mathrm{d}k}{k^{3/2}} \tilde{n}(p+k) \; = 0, \tag{C.5}$$

and ask for a choice of momentum $p \equiv 10^{-3} M$ and $\epsilon = 1/M$ The resulting expression can then be calculated e.g. using Mathematica. The LHS in (C.5) can then be calculated for a set of choices n in eq. C.2. Fig. C.1 shows depicts that for set of choices $n \in \{1/2 \ldots 9/2\}$. The residue can be seen to approach a smallest value for $n \to 3/2$, compatible with the conclusion in [41].

Having observed Fig. C.1, cancellation of the divergencies in Eq. (C.3), can be treated more directly by reordering and grouping and restricting our attention to the region $n > 1$. Multiplying by powers of p as done in Section 3.3.1, and defining $u = k/p$, we can group terms I and III in the region $k \in [0, p/2] \equiv u \in [0, 1/2]$ to rewrite (C.3) as

$$\int_0^{\frac{1}{2}} \left(u^{-3/2} (u+1)^{-n} - u^{-3/2} \right) du + \int_{\frac{1}{2}}^{1} u^{-3/2} (u+1)^{-n} \, du + \frac{2^{(1-n)}}{n-1} = 0. \tag{C.6}$$

In eq. C.6, the second and third terms are finite contributions so long as $n > 1$. The integrals can be

further computed, e.g. using Mathematica, to yield a compact form

$$-2\,{}_2F_1\left(-\frac{1}{2}, n; \frac{1}{2}; -1\right) + \frac{2^{1-n}}{n-1} + 2\sqrt{2} = 0 \tag{C.7}$$

In eq. C.7, ${}_2F_1\,(a, b; c; z)$ is the hypergeometric function [113]. Fig. C.2 once again depicts the residue of eq. C.7, and points to the ansatz (C.2) with $n = 3/2$ as the best solution.

Bibliography

[1] R. L. Workman et al., *Review of Particle Physics*, PTEP **2022** (2022) 083C01 (cit. on pp. 2–6, 62, 107, 111).

[2] R. H. Cyburt, B. D. Fields, K. A. Olive and T.-H. Yeh, *Big bang nucleosynthesis: Present status*, Rev. Mod. Phys. **88** (1 2016) 015004, URL: https://link.aps.org/doi/10.1103/RevModPhys.88.015004 (cit. on pp. 2, 107).

[3] N. Aghanim et al., *Planck 2018 results. I. Overview and the cosmological legacy of Planck*, Astron. Astrophys. **641** (2020) A1, arXiv: 1807.06205 [astro-ph.CO] (cit. on pp. 2, 3, 16, 71).

[4] M. Drees, *Dark Matter Theory*, 2018, arXiv: 1811.06406 [hep-ph] (cit. on pp. 2, 4).

[5] M. Cirelli, A. Strumia and J. Zupan, *Dark Matter*, (2024), arXiv: 2406.01705 [hep-ph] (cit. on pp. 2, 4).

[6] V. C. Rubin and W. K. Ford Jr., *Rotation of the Andromeda Nebula from a Spectroscopic Survey of Emission Regions*, Astrophys. J. **159** (1970) 379 (cit. on p. 3).

[7] G. Bertone and D. Hooper, *History of dark matter*, Reviews of Modern Physics **90** (2018), ISSN: 1539-0756, URL: http://dx.doi.org/10.1103/RevModPhys.90.045002 (cit. on p. 3).

[8] G. R. Blumenthal, S. M. Faber, J. R. Primack and M. J. Rees, *Formation of Galaxies and Large Scale Structure with Cold Dark Matter*, Nature **311** (1984) 517, ed. by M. A. Srednicki (cit. on p. 3).

[9] S. W. Allen, A. E. Evrard and A. B. Mantz, *Cosmological Parameters from Observations of Galaxy Clusters*, Ann. Rev. Astron. Astrophys. **49** (2011) 409, arXiv: 1103.4829 [astro-ph.CO] (cit. on p. 3).

[10] F. Zwicky, *Die Rotverschiebung von extragalaktischen Nebeln*, Helv. Phys. Acta **6** (1933) 110 (cit. on p. 3).

[11] S. W. Randall, M. Markevitch, D. Clowe, A. H. Gonzalez and M. Bradac, *Constraints on the Self-Interaction Cross-Section of Dark Matter from Numerical Simulations of the Merging Galaxy Cluster 1E 0657-56*, Astrophys. J. **679** (2008) 1173, arXiv: 0704.0261 [astro-ph] (cit. on p. 3).

[12] P. Shah, P. Lemos and O. Lahav, *A buyer's guide to the Hubble constant*, Astron. Astrophys. Rev. **29** (2021) 9, arXiv: 2109.01161 [astro-ph.CO] (cit. on p. 3).

[13] T. Zimmermann, J. Alvey, D. J. E. Marsh, M. Fairbairn and J. I. Read, *Dwarf galaxies imply dark matter is heavier than* $\mathbf{2.2 \times 10^{-21}}$ **eV**, (2024), arXiv: 2405.20374 [astro-ph.CO] (cit. on p. 4).

[14] E. Armengaud, N. Palanque-Delabrouille, C. Yèche, D. J. E. Marsh and J. Baur, *Constraining the mass of light bosonic dark matter using SDSS Lyman-α forest*, Mon. Not. Roy. Astron. Soc. **471** (2017) 4606, arXiv: 1703.09126 [astro-ph.CO] (cit. on p. 4).

[15] E. W. Kolb and M. S. Turner, *The Early Universe*, vol. 69, 1990, ISBN: 978-0-201-62674-2 (cit. on pp. 4, 15, 16, 66, 69).

[16] G. Arcadi et al., *The waning of the WIMP? A review of models, searches, and constraints*, Eur. Phys. J. C **78** (2018) 203, arXiv: 1703.07364 [hep-ph] (cit. on p. 4).

[17] L. J. Hall, K. Jedamzik, J. March-Russell and S. M. West, *Freeze-In Production of FIMP Dark Matter*, JHEP **03** (2010) 080, arXiv: 0911.1120 [hep-ph] (cit. on p. 5).

[18] G. L. Kane, P. Kumar, B. D. Nelson and B. Zheng, *Dark matter production mechanisms with a nonthermal cosmological history: A classification*, Phys. Rev. D **93** (2016) 063527, arXiv: 1502.05406 [hep-ph] (cit. on pp. 5, 69).

[19] R. T. Co, F. D'Eramo, L. J. Hall and D. Pappadopulo, *Freeze-In Dark Matter with Displaced Signatures at Colliders*, JCAP **12** (2015) 024, arXiv: 1506.07532 [hep-ph] (cit. on pp. 5, 11, 66, 69).

[20] R. Allahverdi et al., *The First Three Seconds: a Review of Possible Expansion Histories of the Early Universe*, (2020), arXiv: 2006.16182 [astro-ph.CO] (cit. on pp. 6, 7, 33, 69, 70, 107).

[21] R. R. Caldwell, R. Dave and P. J. Steinhardt, *Cosmological imprint of an energy component with general equation of state*, Phys. Rev. Lett. **80** (1998) 1582, arXiv: astro-ph/9708069 (cit. on p. 6).

[22] M. Abdul Karim et al., *DESI DR2 Results II: Measurements of Baryon Acoustic Oscillations and Cosmological Constraints*, (2025), arXiv: 2503.14738 [astro-ph.CO] (cit. on p. 6).

[23] K. D. Lozanov and M. A. Amin, *Equation of State and Duration to Radiation Domination after Inflation*, Phys. Rev. Lett. **119** (2017) 061301, arXiv: 1608.01213 [astro-ph.CO] (cit. on p. 6).

[24] S. Antusch, D. G. Figueroa, K. Marschall and F. Torrenti, *Energy distribution and equation of state of the early Universe: matching the end of inflation and the onset of radiation domination*, Phys. Lett. B **811** (2020) 135888, arXiv: 2005.07563 [astro-ph.CO] (cit. on p. 7).

[25] G. Kane, K. Sinha and S. Watson, *Cosmological Moduli and the Post-Inflationary Universe: A Critical Review*, Int. J. Mod. Phys. D **24** (2015) 1530022, arXiv: 1502.07746 [hep-th] (cit. on pp. 7, 33, 69).

[26] T. Banks, D. B. Kaplan and A. E. Nelson,
Cosmological implications of dynamical supersymmetry breaking,
Phys. Rev. D **49** (2 1994) 779,
URL: https://link.aps.org/doi/10.1103/PhysRevD.49.779 (cit. on p. 7).

[27] E. Hardy and J. Unwin, *Symmetric and Asymmetric Reheating*, JHEP **09** (2017) 113,
arXiv: 1703.07642 [hep-ph] (cit. on p. 7).

[28] G. Kane, J. Shao, S. Watson and H.-B. Yu,
The Baryon-Dark Matter Ratio Via Moduli Decay After Affleck-Dine Baryogenesis,
JCAP **11** (2011) 012, arXiv: 1108.5178 [hep-ph] (cit. on pp. 7, 69).

[29] G. F. Giudice, E. W. Kolb and A. Riotto,
Largest temperature of the radiation era and its cosmological implications,
Phys. Rev. D **64** (2001) 023508, arXiv: hep-ph/0005123 (cit. on pp. 8, 33, 69).

[30] G. B. Gelmini and P. Gondolo,
Neutralino with the right cold dark matter abundance in (almost) any supersymmetric model,
Phys. Rev. D **74** (2006) 023510, arXiv: hep-ph/0602230 (cit. on pp. 8, 44, 64, 69).

[31] N. Bernal, J. Rubio and H. Veermäe, *UV Freeze-in in Starobinsky Inflation*,
JCAP **10** (2020) 021, arXiv: 2006.02442 [hep-ph] (cit. on p. 8).

[32] S. Schlichting,
Non-equilibrium dynamics and thermalization of weakly coupled non-Abelian plasmas,
PhD thesis: U. Heidelberg (main), 2013 (cit. on p. 9).

[33] E. Braaten and M. H. Thoma, *Energy loss of a heavy fermion in a hot plasma*,
Phys. Rev. D **44** (1991) 1298 (cit. on p. 9).

[34] S. Schlichting and D. Teaney, *The First fm/c of Heavy-Ion Collisions*,
Ann. Rev. Nucl. Part. Sci. **69** (2019) 447, arXiv: 1908.02113 [nucl-th]
(cit. on pp. 10, 37).

[35] A. B. Migdal, *Bremsstrahlung and pair production in condensed media at high-energies*,
Phys. Rev. **103** (1956) 1811 (cit. on pp. 10, 39, 69).

[36] L. D. Landau and I. Pomeranchuk, *Limits of applicability of the theory of bremsstrahlung electrons and pair production at high-energies*, Dokl. Akad. Nauk Ser. Fiz. **92** (1953) 535
(cit. on pp. 10, 39, 69).

[37] G. D. Moore, "Transport coefficients in hot QCD",
6th International Conference on Strong and Electroweak Matter, 2005 82,
arXiv: hep-ph/0408347 (cit. on p. 10).

[38] D. Besak, *Thermal particle production in the early universe*,
PhD thesis: U. Bielefeld (main), 2010 (cit. on p. 10).

[39] K. Harigaya and K. Mukaida, *Thermalization after/during Reheating*, JHEP **05** (2014) 006,
arXiv: 1312.3097 [hep-ph] (cit. on pp. 11, 35, 39, 63, 69, 106, 108).

[40] K. Mukaida and M. Yamada,
Thermalization Process after Inflation and Effective Potential of Scalar Field,
JCAP **02** (2016) 003, arXiv: 1506.07661 [hep-ph] (cit. on p. 11).

[41] K. Harigaya, M. Kawasaki, K. Mukaida and M. Yamada,
Dark Matter Production in Late Time Reheating, Phys. Rev. D **89** (2014) 083532,
arXiv: 1402.2846 [hep-ph]
(cit. on pp. 11, 35, 37, 39, 47–49, 51, 57, 63–65, 69, 98, 104, 108, 115, 116).

[42] K. Harigaya, K. Mukaida and M. Yamada,
Dark Matter Production during the Thermalization Era, JHEP **07** (2019) 059,
arXiv: 1901.11027 [hep-ph] (cit. on pp. 11, 35, 64, 65, 69, 104).

[43] P. J. Fox and E. Poppitz, *Leptophilic Dark Matter*, Phys. Rev. D **79** (2009) 083528,
arXiv: 0811.0399 [hep-ph] (cit. on p. 11).

[44] N. Bernal, F. Elahi, C. Maldonado and J. Unwin,
Ultraviolet Freeze-in and Non-Standard Cosmologies, JCAP **11** (2019) 026,
arXiv: 1909.07992 [hep-ph] (cit. on p. 11).

[45] M. Drees and B. Najjari,
Energy spectrum of thermalizing high energy decay products in the early universe,
JCAP **10** (2021) 009, arXiv: 2105.01935 [hep-ph] (cit. on pp. 13, 34, 69).

[46] M. Drees and B. Najjari,
Multi-species thermalization cascade of energetic particles in the early universe,
JCAP **08** (2023) 037, arXiv: 2205.07741 [hep-ph] (cit. on p. 13).

[47] D. S. Gorbunov and V. A. Rubakov, *Introduction to the Theory of the Early Universe*,
World Scientific Publishing Company, 2011,
eprint: https://www.worldscientific.com/doi/pdf/10.1142/7874,
URL: https://www.worldscientific.com/doi/abs/10.1142/7874 (cit. on p. 15).

[48] P. B. Arnold, *Quark-Gluon Plasmas and Thermalization*, Int. J. Mod. Phys. E **16** (2007) 2555,
ed. by D. Peres Menezes, M. Chiapparini, M. J. Menon and S. dos Santos Avancini,
arXiv: 0708.0812 [hep-ph] (cit. on pp. 15, 21, 22, 25, 27, 29, 108).

[49] P. B. Arnold, G. D. Moore and L. G. Yaffe,
Effective kinetic theory for high temperature gauge theories, JHEP **01** (2003) 030,
arXiv: hep-ph/0209353 (cit. on pp. 15, 35, 39, 71, 108).

[50] N. Haque and M. G. Mustafa, *Hard Thermal Loop—Theory and applications*,
Prog. Part. Nucl. Phys. **140** (2025) 104136, arXiv: 2404.08734 [hep-ph]
(cit. on pp. 25, 113).

[51] M. G. Mustafa, *An introduction to thermal field theory and some of its application*,
Eur. Phys. J. ST **232** (2023) 1369, arXiv: 2207.00534 [hep-ph] (cit. on pp. 25, 113).

[52] R. Allahverdi and M. Drees,
Thermalization after inflation and production of massive stable particles,
Phys. Rev. D **66** (2002) 063513, arXiv: hep-ph/0205246
(cit. on pp. 27, 35, 37, 57–64, 69, 104, 106, 108).

[53] R. Allahverdi, R. Brandenberger, F.-Y. Cyr-Racine and A. Mazumdar,
Reheating in Inflationary Cosmology: Theory and Applications,
Ann. Rev. Nucl. Part. Sci. **60** (2010) 27, arXiv: 1001.2600 [hep-th] (cit. on pp. 33, 69).

[54] J. T. Giblin, G. Kane, E. Nesbit, S. Watson and Y. Zhao,
Was the Universe Actually Radiation Dominated Prior to Nucleosynthesis?,
Phys. Rev. D **96** (2017) 043525, arXiv: 1706.08536 [hep-th] (cit. on pp. 33, 69).

[55] J. Yokoyama,
Fate of oscillating scalar fields in the thermal bath and their cosmological implications,
Phys. Rev. D **70** (2004) 103511, arXiv: hep-ph/0406072 (cit. on p. 34).

[56] Y.-K. E. Cheung, M. Drewes, J. U. Kang and J. C. Kim,
Effective Action for Cosmological Scalar Fields at Finite Temperature, JHEP **08** (2015) 059,
arXiv: 1504.04444 [hep-ph] (cit. on p. 34).

[57] M. Drewes, *On finite density effects on cosmic reheating and moduli decay and implications for Dark Matter production*, JCAP **11** (2014) 020, arXiv: 1406.6243 [hep-ph]
(cit. on p. 34).

[58] C. M. Ho and R. J. Scherrer, *Cosmological Particle Decays at Finite Temperature*,
Phys. Rev. D **92** (2015) 025019, arXiv: 1503.03534 [hep-ph] (cit. on p. 34).

[59] M. Drees, F. Hajkarim and E. R. Schmitz,
The Effects of QCD Equation of State on the Relic Density of WIMP Dark Matter,
JCAP **06** (2015) 025, arXiv: 1503.03513 [hep-ph] (cit. on p. 35).

[60] A. Kurkela and E. Lu, *Approach to Equilibrium in Weakly Coupled Non-Abelian Plasmas*,
Phys. Rev. Lett. **113** (2014) 182301, arXiv: 1405.6318 [hep-ph] (cit. on pp. 35, 110).

[61] S. Davidson and S. Sarkar, *Thermalization after inflation*, JHEP **11** (2000) 012,
arXiv: hep-ph/0009078 (cit. on pp. 35, 37, 69, 72, 106, 108).

[62] R. Baier, A. H. Mueller, D. Schiff and D. T. Son,
'Bottom up' thermalization in heavy ion collisions, Phys. Lett. B **502** (2001) 51,
arXiv: hep-ph/0009237 (cit. on pp. 37, 106).

[63] A. Kurkela and G. D. Moore, *Thermalization in Weakly Coupled Nonabelian Plasmas*,
JHEP **12** (2011) 044, arXiv: 1107.5050 [hep-ph] (cit. on pp. 37, 51, 71, 106).

[64] P. B. Arnold, G. D. Moore and L. G. Yaffe, *Photon emission from ultrarelativistic plasmas*,
JHEP **11** (2001) 057, arXiv: hep-ph/0109064 (cit. on pp. 39, 71, 74, 78).

[65] P. B. Arnold, G. D. Moore and L. G. Yaffe,
Photon emission from quark gluon plasma: Complete leading order results,
JHEP **12** (2001) 009, arXiv: hep-ph/0111107 (cit. on pp. 39, 71, 77, 78).

[66] P. B. Arnold, G. D. Moore and L. G. Yaffe, *Photon and gluon emission in relativistic plasmas*,
JHEP **06** (2002) 030, arXiv: hep-ph/0204343 (cit. on pp. 39, 71, 74, 78, 106).

[67] E. Holtmann, M. Kawasaki, K. Kohri and T. Moroi,
Radiative decay of a longlived particle and big bang nucleosynthesis,
Phys. Rev. D **60** (1999) 023506, arXiv: hep-ph/9805405 (cit. on p. 42).

[68] Y. Kurata and N. Maekawa, *Averaged Number of the Lightest Supersymmetric Particles in Decay of Superheavy Particle with Long Lifetime*, Prog. Theor. Phys. **127** (2012) 657,
arXiv: 1201.3696 [hep-ph] (cit. on pp. 44, 64, 69).

[69] A. Banik and M. Drees, *Non-thermal WIMP production from higher order moduli decay*, JCAP **12** (2023) 032, arXiv: 2308.15380 [hep-ph] (cit. on pp. 44, 64, 98).

[70] K. Mukaida and M. Yamada, *Cascades of high-energy SM particles in the primordial thermal plasma*, JHEP **10** (2022) 116, arXiv: 2208.11708 [hep-ph] (cit. on pp. 48, 50, 67, 82, 94, 98, 106, 110).

[71] A. Kurkela and U. A. Wiedemann, *Picturing perturbative parton cascades in QCD matter*, Phys. Lett. B **740** (2015) 172, arXiv: 1407.0293 [hep-ph] (cit. on p. 51).

[72] S. Passaglia, W. Hu, A. J. Long and D. Zegeye, *Achieving the highest temperature during reheating with the Higgs condensate*, Phys. Rev. D **104** (2021) 083540, arXiv: 2108.00962 [hep-ph] (cit. on p. 63).

[73] D. J. H. Chung, E. W. Kolb and A. Riotto, *Production of massive particles during reheating*, Phys. Rev. D **60** (1999) 063504, arXiv: hep-ph/9809453 (cit. on pp. 63, 69).

[74] C. Miller, A. L. Erickcek and R. Murgia, *Constraining nonthermal dark matter's impact on the matter power spectrum*, Phys. Rev. D **100** (2019) 123520, arXiv: 1908.10369 [astro-ph.CO] (cit. on p. 66).

[75] J. Fan, O. Özsoy and S. Watson, *Nonthermal histories and implications for structure formation*, Phys. Rev. D **90** (2014) 043536, arXiv: 1405.7373 [hep-ph] (cit. on p. 66).

[76] A. L. Erickcek and K. Sigurdson, *Reheating Effects in the Matter Power Spectrum and Implications for Substructure*, Phys. Rev. D **84** (2011) 083503, arXiv: 1106.0536 [astro-ph.CO] (cit. on p. 66).

[77] G. Kane and M. W. Winkler, *Baryogenesis from a Modulus Dominated Universe*, JCAP **02** (2020) 019, arXiv: 1909.04705 [hep-ph] (cit. on p. 66).

[78] K. Harigaya, A. Kamada, M. Kawasaki, K. Mukaida and M. Yamada, *Affleck-Dine Baryogenesis and Dark Matter Production after High-scale Inflation*, Phys. Rev. D **90** (2014) 043510, arXiv: 1404.3138 [hep-ph] (cit. on p. 66).

[79] P. B. Arnold and C. Dogan, *QCD Splitting/Joining Functions at Finite Temperature in the Deep LPM Regime*, Phys. Rev. D **78** (2008) 065008, arXiv: 0804.3359 [hep-ph] (cit. on pp. 66, 71, 78–80, 109, 112).

[80] A. Berlin, D. Hooper and G. Krnjaic, *PeV-Scale Dark Matter as a Thermal Relic of a Decoupled Sector*, Phys. Lett. B **760** (2016) 106, arXiv: 1602.08490 [hep-ph] (cit. on p. 69).

[81] A. Berlin, D. Hooper and G. Krnjaic, *Thermal Dark Matter From A Highly Decoupled Sector*, Phys. Rev. D **94** (2016) 095019, arXiv: 1609.02555 [hep-ph] (cit. on p. 69).

[82] Y. Hamada and K. Kawana, *Reheating-era leptogenesis*, Phys. Lett. B **763** (2016) 388, arXiv: 1510.05186 [hep-ph] (cit. on p. 69).

[83] T. Asaka, H. Ishida and W. Yin, *Direct baryogenesis in the broken phase*, JHEP **07** (2020) 174, arXiv: 1912.08797 [hep-ph] (cit. on p. 69).

[84] B. S. Acharya et al., *Non-thermal Dark Matter and the Moduli Problem in String Frameworks*, JHEP **06** (2008) 064, arXiv: 0804.0863 [hep-ph] (cit. on p. 69).

[85] J. Hasenkamp and J. Kersten, *Dark radiation from particle decay: cosmological constraints and opportunities*, JCAP **08** (2013) 024, arXiv: 1212.4160 [hep-ph] (cit. on p. 69).

[86] K. Ishiwata, *Axino Dark Matter in Moduli-induced Baryogenesis*, JHEP **09** (2014) 122, arXiv: 1407.1827 [hep-ph] (cit. on p. 69).

[87] M. Dhuria, C. Hati and U. Sarkar, *Moduli induced cogenesis of baryon asymmetry and dark matter*, Phys. Lett. B **756** (2016) 376, arXiv: 1508.04144 [hep-ph] (cit. on p. 69).

[88] H. Kim, J.-P. Hong and C. S. Shin, *A map of the non-thermal WIMP*, Phys. Lett. B **768** (2017) 292, arXiv: 1611.02287 [hep-ph] (cit. on p. 69).

[89] S. Hamdan and J. Unwin, *Dark Matter Freeze-out During Matter Domination*, Mod. Phys. Lett. A **33** (2018) 1850181, arXiv: 1710.03758 [hep-ph] (cit. on p. 69).

[90] M. Drees and F. Hajkarim, *Dark Matter Production in an Early Matter Dominated Era*, JCAP **02** (2018) 057, arXiv: 1711.05007 [hep-ph] (cit. on p. 69).

[91] M. A. G. Garcia and M. A. Amin, *Prethermalization production of dark matter*, Phys. Rev. D **98** (2018) 103504, arXiv: 1806.01865 [hep-ph] (cit. on p. 69).

[92] M. Drees and F. Hajkarim, *Neutralino Dark Matter in Scenarios with Early Matter Domination*, JHEP **12** (2018) 042, arXiv: 1808.05706 [hep-ph] (cit. on p. 69).

[93] P. Chanda, S. Hamdan and J. Unwin, *Reviving Z and Higgs Mediated Dark Matter Models in Matter Dominated Freeze-out*, JCAP **01** (2020) 034, arXiv: 1911.02616 [hep-ph] (cit. on p. 69).

[94] C. Maldonado and J. Unwin, *Establishing the Dark Matter Relic Density in an Era of Particle Decays*, JCAP **06** (2019) 037, arXiv: 1902.10746 [hep-ph] (cit. on p. 69).

[95] M. A. G. Garcia, K. Kaneta, Y. Mambrini and K. A. Olive, *Reheating and Post-inflationary Production of Dark Matter*, Phys. Rev. D **101** (2020) 123507, arXiv: 2004.08404 [hep-ph] (cit. on p. 69).

[96] S. Hannestad, *What is the lowest possible reheating temperature?*, Phys. Rev. D **70** (2004) 043506, arXiv: astro-ph/0403291 (cit. on pp. 69, 71).

[97] A. Kurkela and A. Mazeliauskas, *Chemical equilibration in weakly coupled QCD*, Phys. Rev. D **99** (2019) 054018, arXiv: 1811.03068 [hep-ph] (cit. on pp. 70, 85).

[98] S. Jeon and G. D. Moore, *Energy loss of leading partons in a thermal QCD medium*, Phys. Rev. C **71** (2005) 034901, arXiv: hep-ph/0309332 (cit. on p. 71).

[99] M. C. Abraao York, A. Kurkela, E. Lu and G. D. Moore, *UV cascade in classical Yang-Mills theory via kinetic theory*, Phys. Rev. D **89** (2014) 074036, arXiv: 1401.3751 [hep-ph] (cit. on p. 71).

[100] J. Berges, M. P. Heller, A. Mazeliauskas and R. Venugopalan,
QCD thermalization: Ab initio approaches and interdisciplinary connections,
Rev. Mod. Phys. **93** (2021) 035003, arXiv: 2005.12299 [hep-th] (cit. on pp. 71, 77).

[101] P. Arnold, T. Gorda and S. Iqbal,
The LPM effect in sequential bremsstrahlung: nearly complete results for QCD,
JHEP **11** (2020) 053, [Erratum: JHEP 05, 114 (2022)], arXiv: 2007.15018 [hep-ph]
(cit. on p. 77).

[102] V. N. Gribov and L. N. Lipatov, *Deep inelastic e p scattering in perturbation theory*,
Sov. J. Nucl. Phys. **15** (1972) 438 (cit. on p. 79).

[103] Y. L. Dokshitzer, *Calculation of the Structure Functions for Deep Inelastic Scattering and e+ e- Annihilation by Perturbation Theory in Quantum Chromodynamics.*,
Sov. Phys. JETP **46** (1977) 641 (cit. on p. 79).

[104] G. Altarelli and G. Parisi, *Asymptotic Freedom in Parton Language*,
Nucl. Phys. B **126** (1977) 298 (cit. on p. 79).

[105] A. Boyarsky, V. Cheianov, O. Ruchayskiy and O. Sobol,
Evolution of the Primordial Axial Charge across Cosmic Times,
Phys. Rev. Lett. **126** (2021) 021801, arXiv: 2007.13691 [hep-ph] (cit. on p. 82).

[106] A. Boyarsky, V. Cheianov, O. Ruchayskiy and O. Sobol,
Equilibration of the chiral asymmetry due to finite electron mass in electron-positron plasma,
Phys. Rev. D **103** (2021) 013003, arXiv: 2008.00360 [hep-ph] (cit. on p. 82).

[107] D. Bödeker and D. Schröder, *Equilibration of right-handed electrons*, JCAP **05** (2019) 010,
arXiv: 1902.07220 [hep-ph] (cit. on p. 82).

[108] E. Reya, *Perturbative Quantum Chromodynamics*, Phys. Rept. **69** (1981) 195 (cit. on p. 82).

[109] H. Abramowicz et al., *Tests of QCD and Nonasymptotically Free Theories of the Strong Interaction by an Analysis of the Nucleon Structure Functions Xf(3), F(2), and $\bar{q}$*,
Z. Phys. C **13** (1982) 199 (cit. on p. 82).

[110] A. Mazeliauskas and J. Berges,
Prescaling and far-from-equilibrium hydrodynamics in the quark-gluon plasma,
Phys. Rev. Lett. **122** (2019) 122301, arXiv: 1810.10554 [hep-ph] (cit. on p. 98).

[111] J. Ghiglieri and M. Laine, *Smooth interpolation between thermal Born and LPM rates*,
JHEP **01** (2022) 173, arXiv: 2110.07149 [hep-ph] (cit. on p. 106).

[112] P. Langacker, *The standard model and beyond*, 2010, ISBN: 978-1-4200-7906-7
(cit. on p. 111).

[113] E. W. Weisstein, *Hypergeometric Function*, From MathWorld–A Wolfram Web Resource,
Accessed: 2025-02-02, 2025,
URL: https://mathworld.wolfram.com/HypergeometricFunction.html
(cit. on p. 117).

List of Figures

1.1 Schematic of a splitting process of a highly energetic particle via interactions with thermal bath particles. . . . 9
1.2 Schematic of the collinearity of splittings of a HE particle, leading to the coherent interference of consecutive emissions. . . . 10

2.1 Self–energy diagram contributing to the thermal mass of the scalar theory. . . . 23
2.2 Complex-plane integration contour corresponding to the Matsubara sums and eq. 2.31. 24
2.3 Physical self–energy diagrams contributing to the thermal mass of the SM gluon. . . 25
2.4 Soft and hard Coulomb scattering contributions to gauge mediated momentum diffusion. 29
2.5 Schematic of a typical $2 \to 3$ contribution to gauge mediated momentum diffusion and the near on–shell propagator in case of collinear splittings. . . . 30

3.1 Typical $2 \to 2$ and $2 \to 3$ processes involved in the energy loss process for a pure non–abelian gauge theory with momentum exchange in the t–channel. . . . 36
3.2 Numerical results for $\bar{n}(x)$ of eq. 3.33 for $x_{\mathrm{M}} = 10^2$, 10^3, and 10^4. . . . 51
3.3 Numerical results for the integrated spectrum $\int_x^{x_{\mathrm{M}}} \bar{n}(x')\,dx'$ vs. the ratio x/x_{M}, computed from the Boltzmann equation 3.33 for three cases $x_{\mathrm{M}} = 10^3$, 10^4 and 10^5. . 52
3.4 The scaling of the spectrum $\sqrt{\kappa} \cdot \bar{n}(x)$ and the effect of the choice of cutoff parameter κ. 53
3.5 Rescaled numerical results for numerical solutions to the dimensionless Boltzmann equation resulting in a universal function of x/x_{M}. . . . 55
3.6 Performance of the fit function (3.48) in reproducing the numerical solution to the Boltzmann equation (3.33). . . . 56
3.7 Comparison of the integrals in hard–soft and hard–hard yield calculation resulting from the numerical and analytical approximate solutions (3.59). . . . 62
3.8 $\left(\Omega h^2\right)_\chi$ resulting from hard–soft, hard–hard, and thermal soft–soft contributions. . . 63

4.1 Examples of $2 \to 2$ scattering processes off particles in the thermal bath, with gauge boson exchange in the t– or u– channel. . . . 72
4.2 Schematic of gauge mediated splitting processes leading to energy loss of highly energetic particles. . . . 73
4.3 Photon bremsstrahlung from a quark interacting strongly with colored plasma particles. 80
4.4 Splitting processes for the species s of eq. 4.24 that can proceed via soft interactions with the thermal background. . . . 88
4.5 Scaled number density functions resulting from initial decays to $I = B\,\ell_R$ for $x_{\mathrm{M}} = 10^4$. 91
4.6 Scaled number density functions resulting from initial decays to $I = W\,\ell_L$ for $x_{\mathrm{M}} = 10^4$ and $x_{\mathrm{M}} = 10^5$. . . . 93

4.7 Scaled number density functions resulting from initial decays to $I = g\, q_L$ and q_R for $x_{\rm M} = 10^4$. 96
4.8 Ratios $r_s^I\left(x, x_{\rm M}\right)$ for initial populations: $I = B$ (left), and ℓ_R (right). 98
4.9 Ratios $r_s^I\left(x, x_{\rm M}\right)$ for initial populations: $I = W$ (left), and ℓ_L (right). 99
4.10 Ratios $r_s^I\left(x, x_{\rm M}\right)$ for initial populations: $I = g$ (top left), q_L (top right), and q_R (bottom) 100
4.11 Ratios $r_s\left(x, x_{\rm M}\right)$ for a generic branching scenario of the decaying M particles to $g\, \ell_L and \ell_R$. 101

C.1 Residue of an approximate Boltzmann equation (C.5) for choices of ansatz (C.2) using a numerical cutoff. 116
C.2 Residue of a reformulated approximate Boltzmann equation (C.6) for choices of ansatz (C.2) using analytical cancellation. 116

List of Tables

2.1 Effective number of degrees of freedom from the SM. 21

Acronyms

ΛCDM Λ cold dark matter. 1–3, 5, 6

BBN big–bang nucleosynthesis. 1, 6, 7, 42, 43, 69, 104

BSM physics beyond the standard model. 2–4, 6, 7, 33, 66, 70

CMB cosmic microwave background radiation. 1–3, 5, 7, 18

CoM Center of mass. 59–62, 103

DGLAP Dokshitzer–Gribov–Lipatov–Altarelli–Parisi. 79

DM dark matter. 2–5, 7, 8, 11, 26, 27, 34, 44, 64–66, 69–71, 89, 102–104

DoF degrees of freedom. 5, 57

EMD early matter–dominated era. 6–8, 66, 104

FI freeze in. 4, 5, 7, 11

FIMP feebly interacting massive particle. 4, 5, 66

FLRW Friedmann–Lemaître–Robertson–Walker. 11, 15–18, 25, 31, 35

FO freeze out. 4, 5, 7

GR general relativity. 15

HE highly–energetic. 7–12, 35, 60, 61, 67, 71, 72, 74, 75, 79, 86, 88, 89, 95, 97, 102, 104, 108, 123

HIC heavy ion collision. 9, 10, 71, 105

IMD intermediate matter–dominated era. 6, 7, 66, 104

IR infra-red. 26, 27, 38, 42, 44, 49–53, 55, 56, 58, 64, 67, 72, 84, 89, 108, 111

LPM Landau–Pomeranchuk–Migdal. 9, 10, 30, 31, 34, 37, 39–43, 48, 51, 57–59, 61, 64–66, 69–72, 74, 77, 78, 80, 81, 86, 89–92, 94, 95, 99, 105, 106, 108

LSP lightest supersymmetric particle. 4

MD matter–domination. 6–8, 11, 33, 37, 57

NT non–thermal. 102

OoE out of equilibrium. 7–12, 18, 25–27, 31, 33, 34, 36–40, 42, 43, 45, 47, 50, 52, 57–61, 64–67, 69–73, 77, 83, 85–89, 91, 92, 94, 95, 97, 98, 101–105, 108, 109, 111

PBH primordial black hole. 3, 4, 7

QCD quantum chromodynamics. 35, 71, 77, 82, 105

QFT quantum field theory. 9, 18, 21, 22, 24–26, 107

QGP quark–gluon plasma. 10, 27, 71, 80, 82, 87, 98

RD radiation–dominated. 1, 6, 33, 102

RH reheating. 6

SM standard model. vi, 1–11, 15, 20, 21, 24–27, 33–36, 66, 70–73, 76, 78–83, 85, 86, 92, 97, 102–110, 123

SSB spontaneous symmetry breaking. 15

SUSY supersymmetry. 4, 106

TB thermal bath. 8–11

WIMP weakly interacting massive particle. 4, 5, 102